NOTE TO USERS

INTEGRATED COASTAL ENGINEERING MODELING

USAMA M. SAIED

M.Sc. (Ain Shams University)
B.Sc. (Ain Shams University)

A thesis submitted in conformity with the requirements for the degree of
Doctor of Philosophy

McMaster University

INTEGRATED COASTAL ENGINEERING MODELING

Doctor of Philosophy (2004)
(Civil Engineering)

McMaster University
Hamilton, Ontario

TITLE: Integrated Coastal Engineering Modeling

AUTHOR: Usama M. Saied
M.Sc. (Ain Shams University)
B.Sc. (Ain Shams University)

SUPERVISOR: Professor I.K. Tsanis

NUMBER OF PAGES: xviii, 289

ABSTRACT

An Integrated Coastal Engineering model (ICEM) has been developed, which models the waves, the coastal circulation and the rates of bed level changes simultaneously. The wave model simulates the combined effect of refraction, diffraction, shoaling, reflection and breaking and the circulation model simulates the wave driven currents in the coastal zone. Finally, the morphological model simulates the sediment transport loads and the morphological changes after solving the combined wave current boundary layer. The waves, currents and sediment transport loads are recalculated for every so-called morphological time step. The ICEM is capable of modeling both the short and long term effects of coastal structures such as groins, detached breakwaters, seawalls, etc.

The ICEM is calibrated and verified using field data in the Mediterranean coast of Egypt. The model is applied to similar areas in Crete, where the wave climate and bathymetric data are available. The best protection scheme is defined for each area.

From the engineering point of view, this research provides an effective design tool for coastal protection projects. It also can provide an assessment on the effectiveness of the existing coastal protection projects.

ACKNOWLEDGMENTS

First and foremost, unlimited thanks to GOD.

Thanks to all my family members for their support and prayer.

I would like to thank my supervisor, Dr. Tsanis for his constant support and encouragement. At all stages of the thesis, he has shown continuous interest and he has worked tirelessly to help solve all problems of technical and non-technical nature encountered in the course of this work. His honesty, integrity and work ethics have been a great source of motivation at all times. For all of this, I thank him greatly.

Thanks are also due to the members of the supervisory committee, Dr. John Vlachopoulos (Department of Chemical Engineering) and Dr. James Smith (School of Geography and Geology) for keeping track of the work progress. Their contributions are very much appreciated.

The author would like also to thank Dr. Mootaz Khaled and Dr. Mohamed Dabees for their indirect assistance with this work.

Special thanks to the Department of Civil Engineering, McMaster University.

To my wife Reham

TABLE OF CONTENTS

LIST OF FIGURES

LIST OF TABLES

LIST OF SYMBOLS

ψ_S^{cr} : the critical Shields parameter.
α : empirical constant.
α_c : calibration constant.
Π : a coefficient which defines the direction of the sediment transport.
γ : empirical constant.
τ : the combined wave-current shear stress.
Ψ : the complex wave velocity potential.
ε : the eddy viscosity.
ρ : the fluid density.
ϕ : the mean geographic latitude at the area.
ψ : the modified complex wave velocity potential.
ν : the molecular water viscosity 10^{-6} m^2/s.
E : the residual error.
λ : the ripple length.
θ : the wave angle measured counterclockwise from x-direction.
ω : the wave frequency.
η : water surface elevation measured from the still water level.
ψ_S : Shields parameter.
θ_0 : the incident offshore wave angle.
θ_b : the angle of wave incidence at the boundary measured anticlockwise from x_1-axis.
τ_{bx} and τ_{by} : the bed shear stresses in the x and y directions, respectively.
κ_c : a dimensionless constant used to calculate the critical shear stress.
τ_c : the current shear stress.
τ_{cr} : the critical shear stress.
κ_d : a coefficient which controls the degree of change in the cross-shore transport rate around the null-point.
γ_d : the wave breaking coefficient in deep water.
α_f : the filtration parameter.
ψ_g : the given modified complex wave velocity potential.
β_k : a scalar which requires that that p_{k-1} and p_k must be conjugate.
δ_L : the thickness of the oscillatory boundary layer.
Ψ_m : mobility number.
ε_q : a positive empirical constant.
η_r : the ripple height.
ε_r : the relative error of approximation.
δ_{rms} : the root mean square error.
γ_s : the wave breaking coefficient in shallow water.
ρ_s : the sediment particle density.

Δt : time step.

Δt_m : the morphological time step.

ϕ_{wc} : angle between the current and wave directions measured anticlockwise from the wave vector.

τ_{wm} : the maximum bottom shear stress due to wave oscillatory motion.

α_x and α_y : empirical smoothing parameters in x and y directions, respectively.

Δx and Δy : the grid sizes in x and y directions, respectively.

$\bar{k}(x)$: is some average of $k(x,y)$ over the y-direction.

$\psi_S^{2.5}$: Shields parameter with respect to conventional roughness of $2.5D$.

A : the amplitude function.

a : the wave amplitude.

A_{bm} : the amplitude of water particle excursions along the bed.

A_c : a dimensionless coefficient.

Accuracy = $\Delta h/h$: the ratio between the change in water depth at a certain point at the end of the morphological time step to the original water depth.

a_i, b_i, c_i : expansion coefficients ($i = 0$ to n).

A_w : a dimensionless coefficient.

b : the ratio between the root-mean-square wave height and the maximum wave height.

C : the Chezy coefficient.

c : the wave celerity.

C_f : dimensionless bed friction coefficient.

c_g : the wave group velocity.

C_r : the Coriolis parameter.

C_x and B_x : linear source term coefficients for the x-momentum equation.

C_y and B_y : linear source term coefficients for the y-momentum equation.

D : median grain size diameter.

E : the wave energy per unit area.

E_r : the roller energy per unit area.

F_d : an empirical direction function.

f_w : the wave friction coefficient.

g : the gravitational acceleration.

h : The water depth.

H : local wave height.

h : the water depth.

H_{rms} : the root-mean-square wave height.

H_s : the significant wave height.

i : the square root of -1.

k : the wave number.

k_c : the modified wave number.

k_n : the moveable bed roughness.

l : cosine the wave propagation angle with x_1-direction.

L : the local wave length.

l_a : the approximated cosine of wave incidence angle at the boundary.
l_h : the exact value of the cosine of the wave angle, obtained from Helmholtz equation.
l_{SL} : the distance measured from the shoreline to the point of interest.
m : sine the wave propagation angle with x_1-direction.
M_{Wx} and M_{Wy} : water discharges which represent the onshore mass flux caused by waves (Stokes drift) and rollers.
n : the wave index.
N : a constant used to determine the eddy viscosity.
Pe_Δ : grid Peclet number.
p_k : the conjugate vector to the previous vectors.
Q_b : the probability that at a specific point in the filed, the wave height reaches is maximum value.
q_{cx} and q_{cy} : the sediment transport loads due to mean current in x and y direction, respectively.
q_{wx} and q_{wy} : the sediment transport loads due to waves in x and y direction, respectively.
q_x and q_y : the total volumetric sediment transport rates in x and y directions, respectively.
R_b : the absolute values of the rate of bed level change.
R : the reflection coefficient of a boundary.
R_{ij} : the stresses due to rollers in breaking waves.
s : the density of the sediment relative to that of the fluid.
S : the wave phase function.
S_{ij} : the radiation stress tensor.
t : the time.
t : the time.
T : the wave period.
u and v : the depth averaged velocity components in x and y directions, respectively.
u_* : the combined wave-current shear velocity.
u_{*c} : the current shear velocity.
u_{*cr} : the critical shear velocity.
u_{bm} : the maximum bottom orbital velocity.
u_c : the depth averaged current velocity.
W : the sum of the dissipation functions.
x : the distance along the wave propagation direction.
x_1 : axis direction normal to the boundary and directed outside the computational domain.
x_2 : axis along the boundary.
x_b : the offshore distance measured from the breaking point.
X_B : the width of the surfzone.
z_b : the change in local bottom elevation.

Chapter 1: Introduction

1.1. General

Coastal zones are very active zones of human developments and recreation. The increasing development of coastal areas causes serious erosion and flooding problems. It is known that almost two thirds of the world's population resides within 200 km of the coast. Therefore, continuous engineering activities are needed to protect the coastal areas. Figure (1.1) shows a picture taken for the city of Ras El-Bar along the Mediterranean coast of Egypt in 1990, where the severe erosion of the shore put the coastal properties in danger. Another example of severe erosion is the city of Rosetta along the same coast. Figure (1.2) and Figure (1.3) show Rosetta's lighthouse at 1973 and 1980, respectively. The first picture in Figure (1.3) shows the lighthouse totally detached from the shore. The second picture shows how harsh the sea has attacked the beach so that the lighthouse does not seem to appear in the horizon in only 7 years. Figure (1.4) show two examples of the coastal protection measures; a system of groins is shown in Figure (1.4a) and a system of detached breakwaters is shown in Figure (1.4b).

In order to design the best coastal protection measure for a particular area, comprehensive coastal process modeling is required. Several categories of numerical models of beach evolution have been developed. The simplest type of these models is the shoreline models, which are based on the one-line theory to simulate shoreline changes in the long term. Models based on multiple line theories are used to simulate the whole coastal area, but still they have to rely on empirical relationships for estimating the

sediment transport rates. The most sophisticated type of coastal morphology models is the 3D models, which are mainly used for short term predictions of the coastal morphology due to a particular storm. The following two sections briefly describe the coastal processes that should be modeled by the successful coastal morphology model.

1.1.1. Coastal currents

Various currents exist in the nearshore region, such as ocean currents, tidal currents, and wind and wave currents. Ocean currents are almost constant throughout the year. Tidal currents are oscillatory and not uniform, but of large scale both in time and space. Wave-induced currents generated directly by the action of swell and wind waves are concentrated within or near the surfzone (Horikawa, 1988). This study will focus on the wave-induced currents because it has the dominant effect on the nearshore dynamics.

The wave-driven currents can be classified into alongshore currents and cross-shore currents. The alongshore currents are mainly caused by obliquely incident waves. The process of wave breaking causes the wave setup over the surfzone, which is proportional to the wave height at the breaking point. Since both waves and bathymetry are not uniform along the coast, the water surface at the shoreline is not uniform as well. Due to the inclination in the water surface at the shoreline, longshore currents are generated, which move masses of water towards sections of lower water surfaces, i.e. wave setups. At these sections, the longshore currents meet to form narrow channels of rip currents directed offshore. Outside the surfzone, the rip currents velocities become small due to the increased water depth. In addition, due to the wave set-down outside the surfzone at these locations are smaller than neighboring sections, which in turn generates

weak along shore currents that move masses of water away from this rip channel. This area is called the rip head.

The coastal currents play an important role in the sediment transport process in coastal areas, where they are responsible for the horizontal displacement of the sediment materials that have been brought up into suspension due to the wave action. Without the coastal currents, net sediments movement would be solely owing to gravity.

1.1.2. Beach profiles

In winter the mean wave conditions are more intense than in the summer. Therefore, sediment materials are transported offshore leaving a gentler beach profile than the summer profile. As a result, one or more offshore bars may form, which protect the beach from heavy wave attack because the waves break further offshore. The offshore bars also prevent severe sediment losses as they provide a mechanism for the temporary storage of the eroded sediments. In summer, the mean wave height decreases and sediments are transported onshore and the beach slope becomes steeper. A build up of sands on the shore forms what is called a berm and the offshore bars disappear. Figure (1.5) illustrates a typical seasonal beach profile changes.

1.2. Motivation

From the above discussion, it can be concluded that waves are the main deriving force in the surfzone. They directly control the currents in this zone. In addition, waves act as a stirring up factor for the bed sediments, which are then carried by the currents. It's also waves that define the shape of the beach profile. Therefore, efficient modeling of

waves in the surfzone would be considered a strong foundation for a reliable coastal morphology model.

A number of assumed empirical relationships and deterministic numerical models have become important tools for investigating coastal processes and for coastal engineering design (Thieler et al., 2000). Many of the assumptions used in these models are not valid in the context of modern oceanographic and geologic principles. The need is evident for a new integrated coastal processes model that can accurately simulate the nearshore coastal processes.

Among the types of beach evolution models, the 3D coastal morphology models are considered the best for accurately predicting morphological changes over the short term. However, over the long-term, these models are considered impractical due to the huge operational time required. Practical application of these types of models in the long term is a real motive for this study.

1.3. Objectives of the Study

This study aims to develop an efficient and integrated coastal processes model, which facilitates the following main objectives:

1. Provide accurate predictions for the wave heights and directions in the nearshore zone and around coastal structures,

2. Modeling of wave-induced currents as well as the wave setup and set-down in the surfzone,

3. Quantitative modeling of the morphological changes in the nearshore zone due to both short term and long term, and

4. Provide a tool for assessing the impact of existing coastal structures as well as designing future projects.

1.4. Scope of the Study

In order to achieve the objectives of the study, an integrated coastal engineering model (ICEM) is developed. The ICEM simultaneously models the waves, currents and sediment transport rates in the nearshore zone. Therefore, three main modules are developed. The first is the wave transformation module, which includes wave refraction, diffraction, shoaling, breaking, energy dissipation and reflection from beaches or structures. The nonlinear effects on wave heights in shallow depths are included as well. New boundary equations are developed for this model, which can handle very wide range of incidence wave angles. The second module is the coastal circulation module which can model the two dimensional currents in the surfzone and its capabilities include both the wind and wave forcing, Coriolis effect, bed friction, convective and cross momentum and momentum dispersion. The last module is a shear-stress-based sediment transport and morphological module, which calculates the sediment transport rates and bathymetric changes in the area.

Both the wave transformation and the coastal circulation modules are verified separately through various model tests. The ICEM is calibrated and verified with case studies, which demonstrate its practical capabilities as an integrated modeling system and

design tool. The ICEM is then used to study the structural impacts on the nearshore zone in different field areas.

1.5. Thesis Structure

This thesis is divided into seven chapters in addition to the introduction and conclusions. Chapter 2 provides a general review of the available beach changes models. A detailed review of the existing wave transformation models is included also in this chapter. Chapters 3 and 4 include the description of the wave transformation models. Two wave models are developed in these chapters; elliptic water wave transformation model and parabolic water wave transformation model. A new set of parabolic approximations for the original elliptic wave equation is presented in chapter 3. Both the parabolic and the elliptic water wave transformation models are verified using various experimental data. In Chapter 5, both the hydrodynamic and the sediment transport models are presented. The hydrodynamic model is verified through two experiments, which indirectly verifies the wave model as well. In Chapter 6 the sensitivity and grid dependency of the various modules are examined. In chapter 7, an Integrated Coastal Engineering Model developed by grouping the wave, hydrodynamic and sediment transport models is presented. The integrated model is applied to several cases. At the end of this chapter, a field case study is used where the integrated model is applied, calibrated and verified. Chapter 8 studies the structural impacts of different coastal structures. In this chapter, two field areas are used to demonstrate the practical capabilities of the model. Non-structural measures are

reviewed at the end of this chapter for completeness. Finally, the conclusions and the recommendations are presented in Chapter 9.

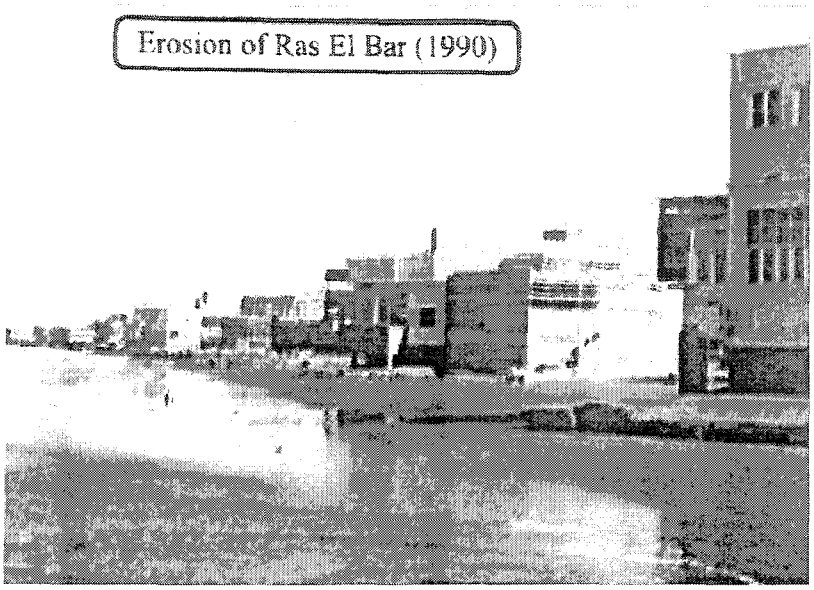

Figure (1.1): Erosion at Ras El-Bar, Egypt.

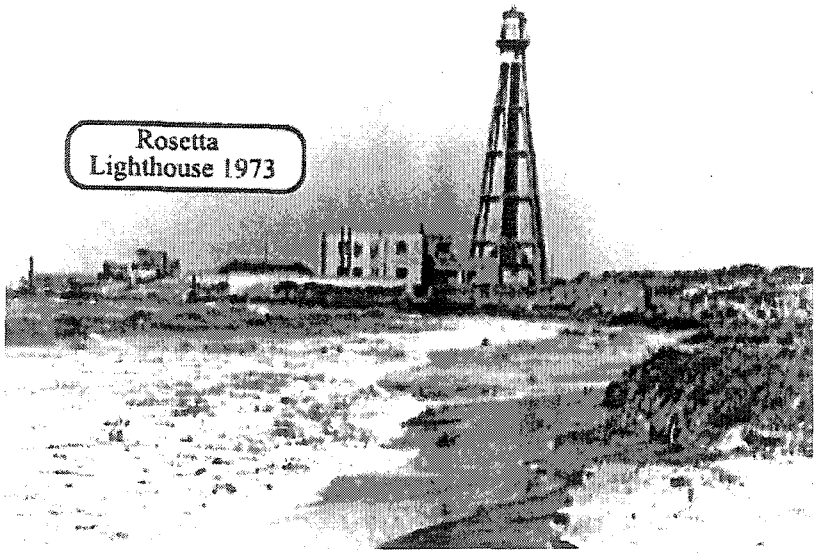

Figure (1.2): Rosetta lighthouse (1973).

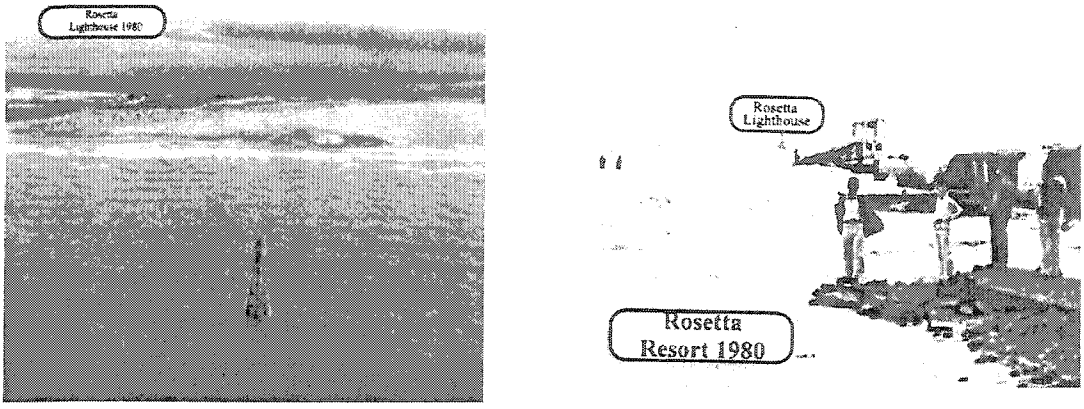

Figure (1.3): Erosion at Rosetta, Egypt.

a) Beach protected by a system of groins (Westhampton beach, New York, 1972)

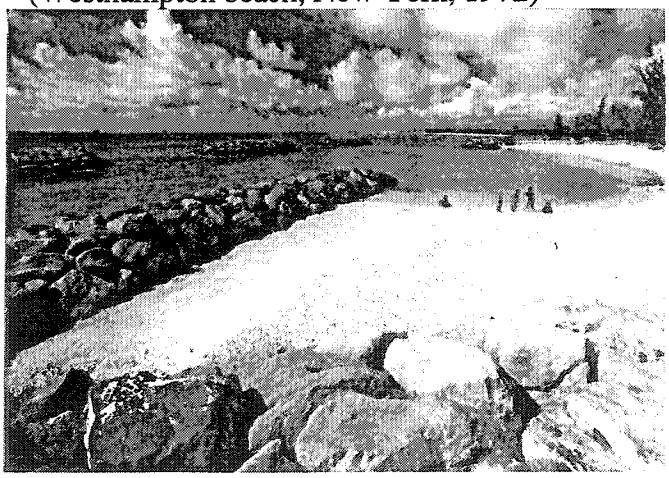

b) Beach protected by a system of detached breakwaters and a revetment (Sand Island, Ohaio)

Figure (1.4): Coastal protection works

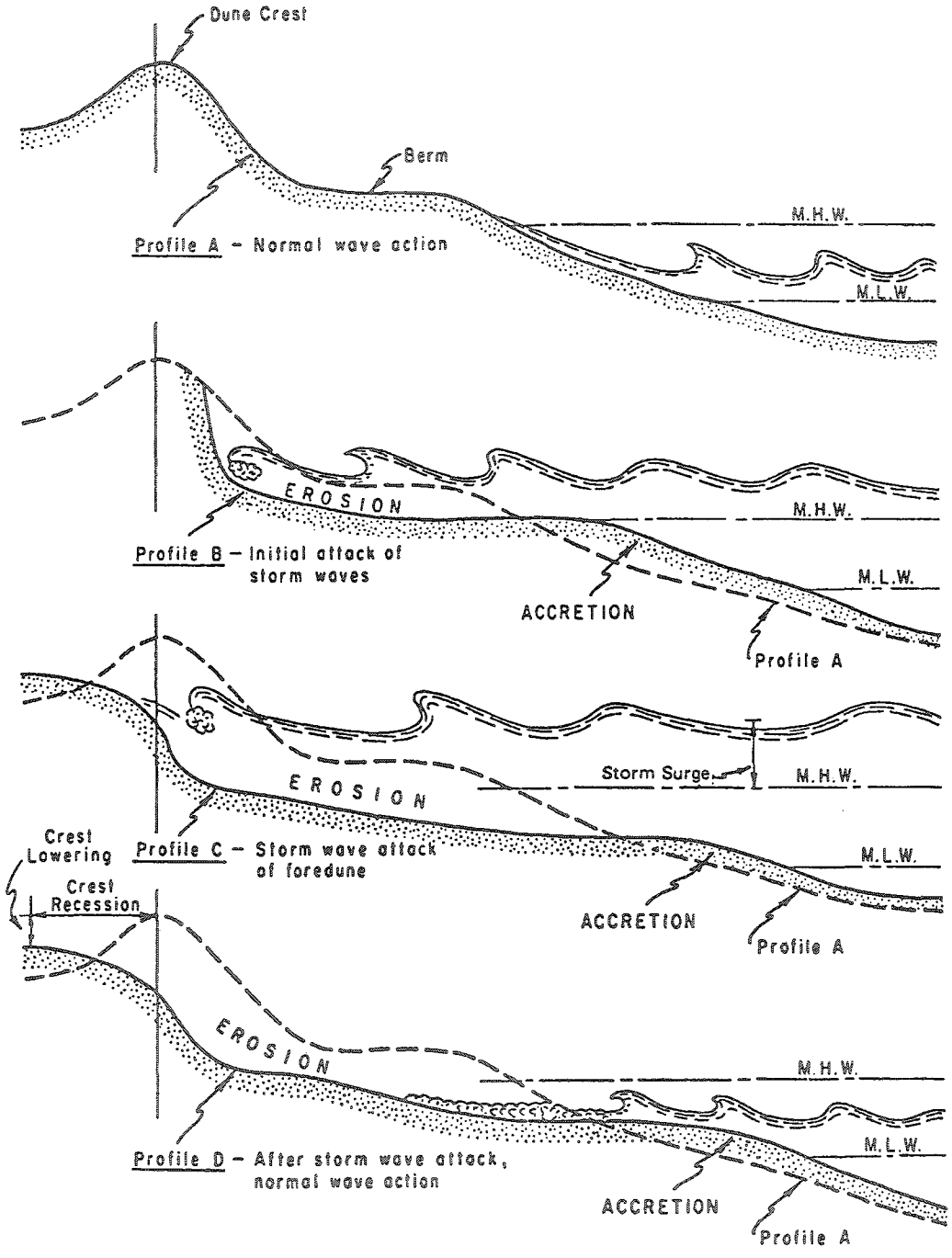

Figure (1.5): Seasonal beach profiles.

Chapter 2: Literature Review

This chapter provides background information about the available types of beach evolution models and discusses the available literature in the wave transformation and morphological models.

2.1. Prediction Methods for Beach Evolution

In the past, the prediction of beach evolution was mainly conducted by relying on coastal experience obtained in similar cases and on results of physical model tests (Horikawa, 1988). In recent years, however, numerical models have gradually appeared and applied for this purpose. The simplest types of these models are the ones that employ empirical methods based on observed trends of evolution of the objective beach. These models have the merits of simplicity and reliability. However, it is impossible to make a quantitative prediction of beach evolution based on them. On the other hand, physical model tests involve scaling problems, where similitude laws for movable bed tests have not yet been established. In addition, these tests usually require expensive facilities, labor and time.

The recent development of numerical models has been accelerated by the requirement for higher accuracy in the prediction of beach evolution due to increasing human activities on the coast. Numerical models of beach evolution can be classified according to the method of modelling into two general groups; shoreline or "line" models

and three-dimensional models (Horikawa, 1988). In shoreline models, beach evolution is represented by the change of the shoreline, which is estimated from the longshore sediment transport rate. The most typical line models are one-line (shoreline) models, but two-line and multi-line models have also been used to simulate the movements of selected contours. On the other hand, three-dimensional models predict the bottom topography from the spatial distribution of the sediment transport rates. This distribution is obtained from the nearshore wave and current field computed for the objective area. These types of models require much fewer idealizations than do the line models (Horikawa, 1988).

These two types of models have their respective advantages and disadvantages. The line models require relatively short computation time, but they cannot be used to predict local changes in the bottom topography. On the other hand, the 3D beach evolution models can be used to predict the details of the beach evolution and therefore have wider applicability. These types of models, however, require relatively long computation time. In addition, the relatively new 3D models have had limited application and verification and their use in predicting long-term beach evolution is questionable (Horikawa, 1988). Figure (2.1) shows the application ranges of beach evolution predictive models in terms of both time and spatial scales. The macro-scale models referred to in the figure denote empirical methods based on experience and data from similar beaches.

2.2. Contour Line Models

2.2.1. One-line models

The first mathematical model of shoreline change was introduced in 1956 by Pelnard-Considère's one-line theory. The primary assumption of this theory is that the beach profile moves parallel to itself out to a limiting depth of closure where there is no significant sediment movement. The one-line theory also assumes small angles of wave incidence and shoreline change, which limits its applicability. In addition, the cross-shore sediment transport is ignored in this theory on the assumption that the beach profile change due to this transport on the long-term cancels out. Pelnard-Considère applied his theory to a simplified case of shoreline change near a long impermeable groin. Several studies followed Pelnard-Considère's one-line theory and developed a large number of analytical solutions for various idealized cases of shoreline evolution. An extensive review of the basic assumptions and history of the one-line theory is discussed in Le Mèhautè and Soldate (1977). A number of numerical models were developed after the framework established by Pelnard-Considère (1956). Early numerical shoreline models require different treatment for different cases. The advances in computer technology enabled the development of generalized shoreline change models. Examples of such models are GENESIS developed by Hanson and Kraus (1989), LITPACK developed by the Danish Hydraulic Institute and ONELINE developed by Dabees and Kamphuis (1998). Leont'yev (1997) developed a model based on the one-line theory to predict the short-term shoreline changes due to cross-shore structure.

2.2.2. Multiple-lines models

Bakker (1968) extended Pelnard-Considère one-line theory and developed a two-contour-line mathematical model to determine shoreline evolution near groins and the performance of groin fields. To model the cross-shore sediment transport, Bakker divided the profile into two contour lines. The sediment movement in this direction was related to the actual slope deviation from the equilibrium slope. Perlin and Dean (1983) extended the two-line model of Bakker to a muli-line model restricted to depths that increase monotonically with distance offshore. Larsen et. al. (1990) presented a schematized 3-D model by coupling the shoreline change model GENESIS with the profile change model SBEACH (Larson and Kraus, 1989). Uda et. al. (1996) developed a contour line change model for coasts with steep slopes. Their model still uses the fundamental assumption of small incident wave angles. Uda et. al. (1998) used this model to simulate beach evolution behind breakwaters and to model the development of a river mouth delta. Dabees and Kamphuis (2000) developed a contour line model NLINE, which allows the local profile formation of bars and berms.

2.3. Three-Dimensional Beach Evolution Models

The three-dimensional beach evolution models predict the beach evolution on the basis of wave and current conditions calculated in advance over the area of interest. There have been early attempts to develop this kind of models (e.g. Wang et. al., 1975; Watanabe, 1982; and Yamagichi and Nishioka, 1984). In these attempts, quantitative verification of the models was not available. In addition, some of the computation

methods for the waves, nearshore currents, and sediment transport rates are not adequate. Watanabe et. al. (1986) developed a three-dimensional predictive model for short-term beach evolution. Their model overcomes many of the weaknesses found in the previous literature like the inadequacy of wave and current modelling. The total model consists of three sub-models for calculating waves, nearshore currents and sediment transport and beach change. A useful class of three-dimensional models is the Quasi-3D models, which couple a two-dimensional vertical model that calculates velocity profiles with a two dimensional horizontal model to determine the nearshore circulation, sediment transport and corresponding bottom changes (Briand and Kamphuis, 1990; Roelvink et. al. 1994). This type of model is used for short-time predictions (1 storm to 1 year). Watanabe et. al. (1986)'s model is more conventional class, which utilizes depth averaged near shore currents to calculate sediment transport and beach changes. Several models have been developed after Watanabe et. al. (1986)'s model like MIKE 21 developed by the Danish Hydraulic Institute, 3D-SHORE (Shimizu et. al., 1996), TELEMAC (Pèchon and Teisson, 1996), and Leont'yev (1999). The method used to calculate waves, currents and sediment transport distinguish one model from another.

The following sections review the existing wave transformation, circulation and sediment transport models.

2.4. Wave Transformation Models

In the early developed three-dimensional beach evolution models, the nearshore wave field was computed using either the wave energy equation (Wang et. al., 1975;

Watanabe, 1982) or the wave ray method (Yamagichi and Nishioka, 1984). These methods are, however, not applicable to the computation of the wave field under general conditions of complicated bottom topography and structure geometry, for which wave deformation due to combined refraction, diffraction, reflection and breaking exist (Horikawa, 1988).

Mathematical models have been proposed for combined refraction and diffraction of simple harmonic linear waves. The numerical method proposed by Ito and Tanimoto (1971, 1972) for harbour wave analysis, and refined by Tanimoto and Kobune (1975), allows easy specification of boundary conditions, but requires modifications to describe wave shoaling. The elliptic mild slope equation derived by Berkhoff (1972, 1976) requires no wave corrections for shoaling, but the treatment of boundary conditions (non-reflective boundary conditions and partial reflective boundary) is generally difficult.

Although the mild slope equation was derived based on the assumption of mild bottom slope, Booij (1981) showed that this equation is satisfactory even for bottom slope of the order of unity, which widely validates the equation for both the application in the field and in the lab. The first finite element water wave transformation model based on the mild slope equation was developed by Berkhoff (1972).

Ebersole et. al. (1986) solved the mild elliptic slope equation over a finite-difference grid (RCPWAVE model). They utilized a marching scheme to solve the forward scattered waves only and assumed that the diffractive effects in the direction of wave propagation are much less than those perpendicular to the direction of wave advance. Although, this model is very fast and reliable, it cannot model wave reflections.

In addition, the principal direction of wave propagation has to be known in prior. Panchang et. al. (1988) developed a finite difference method for solving the elliptic mild slope equation in large domains using marching scheme. Like Ebersole et. al. (1986), the principal wave direction has to be known in prior, and waves are not allowed to deviate much from this direction. However, this model overcomes the other limitation in that it allows backscattering and propagation of waves opposite to their primary direction.

Panchang et. al. (1991) used the central finite difference scheme to directly solve the elliptic mild slope equation. They solved the system matrix using both the conventional and preconditioned conjugate gradient method. Although the agreement between the analytical and experimental results was generally good, their method can only be applicable to very small wave angles. Li and Anastasiou (1992) solved the equation using muti-grid technique in order to enhance the convergence. Li et. al. (1993) used the multigrid method to solve the elliptic mild-slope equation for irregular wave propagation. Following the successful results of Panchang et. al. (1991)'s model, which was based on the conjugate gradient method, Li (1994a) developed a generalized conjugate gradient algorithm to solve the mild slope equation. Unlike Panchang et al.'s conventional conjugate gradient algorithm, this algorithm does not need preconditioning to enhance the convergence. Despite its numerical advantages, however, this model can only simulate small wave angles. As mentioned before, the problem with all the elliptic water wave transformation models is the treatment of the lateral boundaries. All the models mentioned above used a boundary condition that is correct for right angle incident

waves with respect to the boundary. This treatment results in considerable unwanted reflections when the angle of incidence becomes relatively large.

Behrendt (1985) developed a series of high order boundary conditions following the approach given by Engquist and Majda (1977). He used the finite element method for his model. Maa et. al. (1998) developed a model (RDE), which employs thrifty Gauss Elimination method to solve the resulting system matrix. This method basically replaces the huge memory requirement with a large hard disk space requirement. He used second order parabolic approximation of the elliptic equation to represent the absorbing boundaries. Kirby (1989) compared between the different available parabolic boundary conditions for the elliptic water wave transformation models.

Rather than approximating the actual boundary conditions, the approximation can be done to the bathymetry of the sea region outside the computational domain, where it is assumed constant. In this case the scattered waves at the lateral boundary can be described by a Bessel-Fourier series. Within the finite element framework, this information is naturally incorporated through the use of a "superelement". Finite-element models of this type have been developed by Houston (1981), Tsay and Liu (1983), Kostene et. al. (1986), and Chen and Houston (1987).

Despite the success of the finite element models in treating the open boundaries, they can be cumbersome to construct and apply. Grid-generation is considered a major task and can take several weeks. Therefore, finite-difference elliptic models are sometimes preferred due to their simplicity and ease of construction and application (Xu and Panchang, 1993). However, inadequate treatment of the open boundary conditions is

a challenge. Xu and Panchang (1993) developed a finite difference model, which uses an optimisation criterion to relate the solutions inside and outside the computational domain. Their model is verified to absorb the wave energy at the lateral boundaries quite efficiently. However, the computational method described by the authors cannot be applied to very large wave problems. Therefore, the treatment of absorbing boundaries for large wave problems remains a challenge.

Another form of the mild slope equation for purely harmonic case is the hyperbolic form. This time-dependent form of the wave equation was proposed by Copeland (1985) and is solved by finite difference by Madsen and Larsen (1987). This method is employed by MIKE 21 module. The computing technique used in this model requires that all boundaries be totally reflective (Maa et. al., 2000). Therefore, incident waves have to be introduced from the interior and sponge layers must be installed on the passing-through boundaries, where the wave energy can be totally or partially dissipated (Larsen and Dancy, 1983).

Due to the difficulty of the boundary treatment in the models based on the mild slope equation, many studies have been made on the parabolic equation method. This method essentially gives an approximate solution of the mild slope equation. Li (1994b) developed an evolution equation based on the mild slope equation using perturbation methods. He solved the resulting parabolic equation marching in time using ADI method. At the steady state, the solution converges to the original mild slope equation. Although this method has a lot of numerical advantages, it employs the conventional radiation condition at the boundaries and therefore does not allow for large wave incidence angles

at the boundaries. The first parabolic model, in space, was derived by Radder (1979). He assumed that the derivatives of the wave potential in the x-direction (principal direction of wave propagation) are very small. His approximation is considered the lowest-order parabolic approximation of the elliptic equation which corresponds to [1/0] Padé approximation or the lowest order binomial expansion. Booij (1981) developed a higher order parabolic model, which permits waves angles up to 56.5°. Booij's model corresponds to the [1/1] Padé approximation. Kirby (1986a) provided a [2/2] Padé approximation for the elliptic equation. He also utilized a minimax approach to find the best approximation for wave propagating at large angles from the x-direction. Both models can give reasonable results for large wave angles up to 70°. Dalrymple and Kirby (1988) developed a wide-angle model based on the Fourier transform method for a bathymetry consisting of parallel contours. Their analysis shows that the wave field can be decomposed into an angular spectrum; that is the superposition of many synchronous wave trains propagating at different angles to the x-axis varying from 0° to ±90°. Dalrymple et. al. (1989) extended this model to the irregular bathymetry situation. Although there is no longer an angle limitation for this model, the formulas are quite complicated, and the CPU time required is more than that for other parabolic models (Li, 1997). Li (1997) developed a nonlinear parabolic approximation for the Helmholtz equation. His model does not have angle limitation for forward wave propagation. He used the upwind scheme in order to solve the approximate nonlinear equation using a marching technique. Li's (1997) model can give reasonable results even for large angles

of up to 70°. For the case of small wave angles, Kirby's (1986a) minimax model gives more accurate results due to upwind scheme used in Li's (1997) model.

The mild-slope equation was developed using the linear wave theory, which is valid for relatively large depths. To account for effects of non-linearity on the wave propagation characteristics, a simple adjustment of the phase and group velocities gives often enough accuracy for practical purposes (Dingemans, 1997). Several adjustments of the linear wave equation have been proposed by Walker (1974, 1976) and Hedges (1976). Hedges' (1976) form of accounting for effects of non-linearity has been used successfully in applications with the parabolic wave model CREDIZ (Dingemans, 1983, Dingemans et al., 1984, and Dingemans and Radder, 1986). Kirby and Dalrymple (1986) proposed a method which effectively gives an approximation for both shallow and deep water.

2.5. Nearshore Circulation Models

Putnam et al. (1949) first proposed a formula for calculating the mean longshore current velocity on the basis of momentum conservation. Other early approaches were made by Inman and Quinn (1951), Nagai (1954), Galvin and Eagleson (1965), Eagleson (1965), and Sato and Tanaka (1966). In early 1960's, Longuet-Higgins and Stewart (1960, 1961, 1962, 1964) introduced the concept of radiation stress in order to analyze the modulation of waves in the presence of a current or long waves. The radiation stress is defined as the excess momentum flux induced by the wave motion. It has been widely applied to predict water wave phenomenon, such as wave set-up and set-down, and surf beat, and to analyze the nearshore current system (Horikawa, 1988).

The depth-integrated conservation equations have been used widely to simulate the nearshore circulation assuming that the nearshore current field varies slowly in space and in time on a scale that is large compared with a typical wavelength or wave period of sea or swell waves. A number of early numerical approaches or techniques have been proposed to solve the depth-integrated conservation equation system or similar systems (Noda, 1974; Birkermeier and Dalrymple, 1975; Liu and Mei, 1976; Ebersole and Dalrymple, 1980; Nishimura, 1982; Nishimura et al., 1985). These approaches can be classified into two groups; unsteady and steady flow analyses. In unsteady flow analysis, time-derivative terms are regarded as residual error terms that vanish at steady state. Steady flow analysis is a more direct approach to an equilibrium flow pattern, in which the time-derivative terms in the governing equations are set at zero throughout the computation. Examples of these methods are the simple relaxation method, Hardy-Cross method, ADI method, and the full implicit method.

Development and applications of horizontal two-dimensional finite-difference numerical models to simulate nearshore circulation in open coasts have been done intensively over the last two decades (Leendertse, 1970; Butler, 1978; Wanstrath, 1978; Sheng, 1983; Chu and Yeh, 1985; Schuepfer et al., 1988; Vemulakonda et al., 1988). The main advantage of using the finite-difference scheme is its simplicity and ease to maintain (Maa, 1990). Various techniques have been developed to improve the stability and resolution. For example, a semi-implicit scheme developed by Leendertse (1970), a fully-implicit scheme by Butler (1978), and an economical fully-implicit scheme, the Double Sweep method, by Abbott (1980). The traditional fully-implicit scheme can use a large

time step to solve the governing equations, but it still requires considerable computer memory space and also consumes considerable computer time because it needs to solve a large matrix equation many times. The Double Sweep Method avoids solving the big matrix equation and saves both the memory space and computing time.

Variable grid size system has been used with finite-difference scheme to increase the resolution at areas of interest and also to cover a sufficicently large area without significantly increasing the computing cost (Sheng, 1983; Vemulakonda et al., 1988). Recently, the curvilinear coordinate system has been used with the finite-difference method. This scheme serves the same function as the variable grid size and provides more flexible representation of complex shorelines (Wanstrath, 1978; Sheng, 1987). However, the curvilinear coordinate system is not easy to understand and a complex transformation of the governing equations is needed. Maa (1990) developed a numerical finite-difference method that employs both the economic implicit scheme and variable grid size. Park and Borthwick (2001) developed a quad-tree grid numerical model. In their model, grid adaptation is achieved through seeding points distributed according to flow criteria.

Numerical models which use the finite-element technique have also been developed and applied to many locations (Ariathurai, 1974; Wang and Connor, 1975; Chen, 1978; Athow et al., 1987; Granat, 1987). The main advantage of using the finite-element method is to better approximate complex bathymetry and land boundaries. However, this kind of model requires using an artificially high eddy viscosity and small time increment to obtain a stable calculation of detailed current information at small embayments (Maa, 1990). To overcome this drawback, Westerink et al. (1985) developed

a finite-element model that operates in the frequency domain. This approach solves all the problems, but the program codes are extremely complicated.

By considering the vertical non-uniformity of the radiation stresses, de Vriend and Stive (1987), Svendsen and Lorenz (1989), Svendsen and Putrevu (1994), Sanchez-Arcilla et al. (1992), Briand and Kamphuis (1993) and van Dongeren et al. (1994) developed quasi-3D models. Shi et al. (2003) developed a curvilinear version of van Dongeren's et al. (1994) model (SHORECIRC).

Although quasi-3D models can give a three dimensional picture of the velocities in the surfzone, they are dependent on proper specification of the bottom boundary layer dynamics, a subject that still requires further research (Park and Borthwick, 2001). Nizam (1992) proposed a more advanced 3D approach for wave-current interaction by combining a 2D propagation model for the wave field with a σ- transformed 3D current circulation model. However, his 2D wave propagation scheme ignores diffraction and reflection to avoid numerical instability.

Three-dimensional circulation models can be used to study the dynamics in the nearshore zone. Practically, however, the two-dimensional depth-integrated models are preferable given the spatial and temporal scales of the typical coastal domains. Abbott et al. (1985) collected the experimental evidence which suggests that the circulations generated in numerical models of free-surface flows that are two-dimensional in plan may be physically realistic. In addition, Jamart and Ozer (1987) concluded that the two-dimensional models can yield results identical to those of the three-dimensional models.

2.6. Sediment Transport Rate in Coastal Areas

In order to quantitatively evaluate bottom change caused by waves and currents, the sediment transport rate must be evaluated. If the mechanism of sediment movement were, in principle, completely known, the rate of sediment transport could be calculated by tracing the movement of individual sediment particles (Horikawa, 1988). However, governing equations of sediment movement based on fundamental physics have not been established owing to the enormous complexity of the phenomenon. Therefore, formulas for sediment transport rate have been developed based on a macroscopic approach to oscillatory and steady fluid motion.

Most calculation procedures for coastal sediment transport have been developed by adopting and modifying the results for sediment transport in rivers (Horikawa, 1988). In a river, the driving force of the sediment movement is the flow itself. In the nearshore region, however, the driving forces are not only currents but waves as well. Transporting mechanisms such as wave breaking, onshore or offshore currents in the vicinity of sea bottom and oscillatory fluid motion in the swash zone are characteristics of the coastal region. A precise evaluation of these fluid motions is essential to obtain reliable formulas for the sediment transport rate.

Einstein (1942) carefully observed the motion of sand particles under unidirectional flow and found that a specific sand particle entrained or picked up by the flow remained in motion for a certain distance defined stochastically, stopped to reside on the bottom for a certain period, and then repeated the above process. Based on this observation he concluded that the pick up rate of sand particles is closely related to the

time period during which the lift force acting on the particle is greater than its immersed weight. He introduced a well-known formula for calculating sediment transport under unidirectional flow, based on stochastic concepts. However, although the pick-up rate of a solid particle as introduced by Einstein (1942) is a factor contributing to the sediment motion, in actuality the transport of a collection of particles is complex, and many additional hypotheses must be introduced to describe the phenomena. Because of this problem, the stochastic approach has rarely been applied to estimate nearshore sediment transport rates. Following Einstein's (1942) hypothesis, Nielsen et al. (1978) estimated the amount of sand lifted up from the crest of ripples to form suspended sand clouds. Yamashita et al. (1983) estimated the number of sand particles which initiated rolling motion by the effect of fluid motion and then formulated the bed load transport rate by taking the product of the number of these particles and their advection speed as calculated by Hino et al. (1982).

In a different approach, Bagnold (1963) and other researchers suggested that the sediment transport rate is closely related to the fluid energy, or power, generated by the fluid motion in the vicinity of the bed. Hence, this model is called "power model". In the power model, it is assumed that the number of sediment particles in motion is related to the bottom shear stress and that the particles move at a certain speed according to the current. This model is conceptually simpler than the stochastic approach described above, and most of the sediment transport formulas developed so far have been based on the power model.

The stochastic and power approaches mainly apply to the bed load transport rate. Concerning the suspended particle load, if suspended particles are assumed to move at the same speed as the fluid, the sediment transport rate can be evaluated from the vertical distribution of the sediment concentration, which is obtained from the solution of the diffusion equation. In order to obtain the solution of the sediment diffusion equation, the diffusion coefficient and the sediment concentration at a certain reference level must be specified. A number of investigations have been carried out in the field and laboratory to study the suspended sediment distributions. Reasonable results have also been obtained in theoretical treatments (e.g. Rouse, 1937; Hino, 1963; Horikawa and Watanabe, 1970). Komar (1978) investigated the relative importance of suspended load and bed load transports. Traditionally, the suspended load is expected to be dominant under certain circumstances, such as sediment transport in the vicinity of the wave breaking point. Kraus and Dean (1987) made numerous simultaneous measurements of the vertical distribution of the longshore transport rate flux at several points across the surfzone. They found that the suspended load was dominant throughout the surfzone under 0.5~1.5 m breaking wave heights on an average grain size beach (0.22mm).

Several formulas have been developed to quantify the sediment transport rate based on either the power model or the stochastic model. These formulas can be classified according to the direction of sediment movement into three categories; cross-shore sediment transport formulas, longshore sediment transport formulas, and formulas for sediment transport under the coexistence of waves and currents.

2.6.1. Cross-shore sediment transport rate

Based on the experimental results of Watanabe et al. (1980), Watanabe (1982) presented an on-offshore sediment transport formula. Although, his formula describes the full range of the data, it is still based on experimental data. Kajima et al. (1982) and Shimizu et al. (1985) carried out experiments for a wide range of wave values of the Shields parameter by using a prototype wave flume. In particular, Shimizu et al. obtained Shields parameter to values up to 2.5. Shimizu et al. (1985) showed that Watanabe's (1982) formula fits the data well. Bowen (1980) and Bailard (1981, 1984) theoretically investigated the relationship between the cross-shore transport rate and fluid velocity. They determined an equilibrium beach profile shape by setting the time-averaged transport rate to zero. Mimura et al. (1986) carried out two dimensional wave flume experiments by generating irregular waves and investigated the wave irregularities on beach profile change with the aim of determining the representative wave height of irregular waves. Their results showed that the representative wave height depends on the mode of sediment movement and the location of interest. It was concluded, however, that the efficiency of irregular waves to generate sediment transport is lower than that of a regular wave.

The cross-shore sediment transport rate strongly depends on the mechanism (mode) of sediment movement (Horikawa, 1988). However, most studies on the cross-shore transport rate have mainly been concerned with the sediment transport rate on rippled beds. Sunamura (1980) showed that the asymmetric ripple shape is an important

factor controlling the net transport rate. Sunamura (1984) introduced a formula for the cross-shore transport rate within the nearshore zone including the swash zone.

2.6.2. Longshore sediment transport rate

Longshore transport is among the most important nearshore processes that control the beach morphology and determine in large part weather shores erode, accrete, or remain stable. The main cause of the longshore sediment transport is the obliquely breaking waves to the coast and the longshore current they generate. Therefore, the direction of the longshore sediment transport is the same as the longshore current, so that only the absolute value of the transport rate is required.

The term "potential" sediment transport rate is used, because calculations of the quantity imply that sediment is available in sufficient quantity for transport, and that obstructions do not slow or stop transport of sediment alongshore (U.S. Army, 1998). The following summarizes the several methods used to predict the potential longshore sediment transport rate.

2.6.2.1. Energy flux method

This method assumes that the potential longshore sediment transport rate, dependent on an available quantity of littoral material, is most commonly correlated with the so-called longshore component of wave energy flux or power. Savage (1962) summarized the available data from field and laboratory studies and developed an equation which was latter adopted by the U.S. Army Corps of Engineers in 1966, which became known as the "CERC formula" (U.S. Army 1998). Based on Komar and Inman's (1970) transport relationship and other available field data, the CERC formula for littoral

and sand transport was updated from its 1966 version. Since 1966, several studies have been done to adjust the CERC formula. Bailard (1981, 1984) developed an energy-based model, which presents the CERC formulas empirical constant K as a function of the breaker angle and the ratio of the orbital velocity magnitude and the sediment fall speed, also based on the root-mean-squared wave height at breaking. Bailard calibrated the model using eight field and two laboratory data sets. Komar (1988), after re-examining the available field data, suggested that the previous relationships resulted from two data sets with K values based on erroneous or questionable field data. Revising these K values, Komar (1988) concluded that existing data suggests little dependence of the empirical K coefficient on sediment grain sizes, at least for the range of sediments in the data set. Komar stressed that K should depend on sediment grain size, and the absence of such a trend in his analysis must result from the imperfect quality of the data. del Valle, Medina, and Losada (1993) have presented an empirically based relationship for the K parameter, adding sediment transport data representing a range in median sediment grain size (0.40mm to 1.5mm) from the Adra River Delta, Spain to the available database as modified by Komar (1988). Results of their analysis reinforce a decreasing trend in the empirical coefficient K with sediment grain size, even with the corrections to the database as suggested by Komar (1988). From laboratory data, a relationship between K and the surf similarity parameter, beach slope divided by the square root of the wave steepness at the breaking point, has also been observed (Kamphuis and Readshaw 1978). These data suggest that the value of K increases with increasing value of surf similarity parameter.

A promising empirical relationship, based empirically upon laboratory results, is that developed by Kamphuis (1991), which correlates well with laboratory and field data sets. However, for application to field studies, the use of a physically based relationship based solely on field data, such as the CERC formula, is preferred. Wang et al. (1998) found that Kamphuis' (1991) formula predicted consistently lower longshore transport rates than those predicted by the broadly used CERC formula. However, the lower predictions by Kamphuis' (1991) formula matched the measured values closer than the CERC formula predictions for low-wave conditions. On the other hand, Miller (1998, 1999) concluded that CERC formula is better than Kamphuis' (1991) for storm conditions.

White and Grandon (1993) used sand tracer data from Santa Barbara and Torrey Pines, California, and profile and dredging records from Santa Barbara, California, to compare 20 longshore transport models. They concluded that CERC equation performed as well or better than the other models. Of the six models including the effect of grain size that White and Grandon evaluated, they concluded that Bailard's (1984) relationship performed the best. However, the data set used for comparison only represented grain sizes in the range 0.15 to 0.25mm, and therefore was not particularly suited for testing the dependence of longshore sediment transport relationships on grain size outside this limit range. Schoonees and Theron (1995) evaluated the determination of the empirical K using numerous existing field data obtained mainly from sediment tracer and structural blocking and concluded that significant uncertainties in K could be induced by the scatter of existing wave data.

Several studies have been done on the effect of the breakwaters or shelters on the longshore sediment transport rate (Ozasa and Brampton, 1980; Hanson and Kraus, 1989). The wave heights are essentially reduced in areas sheltered by breakwaters due to wave diffraction, hence, a longshore current towards the breakwater is induced by the force resulting from the longshore gradient in breaker height. Dabees and Kamphuis (1998) modified the original Kamphuis' (1991) to include the transport by wave height gradient.

2.6.2.2. Longshore current method

Early workers such as Grant (1943) stressed that sand transport in the nearshore results from the combined effects of waves and currents. The waves induce sand in motion and the longshore currents produce a net sand advection (U.S. Army 1998). Walton (1980, 1982) proposed a longshore sediment transport calculation method using the breaking-wave-driven longshore current model of Longuet-Higgins (1970). From practical standpoint, it is often easier and more accurate to measure the longshore current than it is to determine the breaker angle needed in the CERC formulation. Formulations for the current distribution across non-planar, concave-up beach profiles are presented by Komar (1977), McDougal and Hudspeth (1983, 1989) and by Bodge (1988).

2.6.3. Sediment transport rate under coexistence of waves and currents

All the formulas developed to calculate the sediment transport rate under coexistence of waves and currents are based on the bottom shear stress. That is to say, these formulas were introduced on the basis of the power model.

Bijker (1971) developed a transport formula for a combination of current and waves by modifying the transport formula for currents through the introduction of a modified bottom shear stress to include the effect of wave stirring up.

Watanabe (1982), Watanabe et al. (1984) and Shimizu et al. (1983) treated the sediment transport due to currents and waves separately. Therefore, it is rather easy to incorporate with the results of previous studies on the cross-shore as well as the longshore sediment transport rates, and also it is possible to take into account the effects of cross-shore and longshore sediment transport on the beach evolution separately (Horikawa, 1988). Although the bottom configuration change appearing around coastal structures is a complex phenomenon, it appears that such change can be evaluated using these formulas.

Madsen (1993) developed a procedure for calculating the sediment transport rates outside the surfzone based on the solution of the combined wave-current boundary layer. Although this approach is the most sophisticated approach out there, its application to the surfzone is questionable due to the induced turbulence from wave breakers and rollers (U.S. Army, 1998). Leont'yev (1999) used the energetic-based formula of Bailard (1981) to calculate the sediment transport rates over a two dimensional grid covering the surfzone. He modified the formula to account for the wave breaking (Leont'yev, 1997).

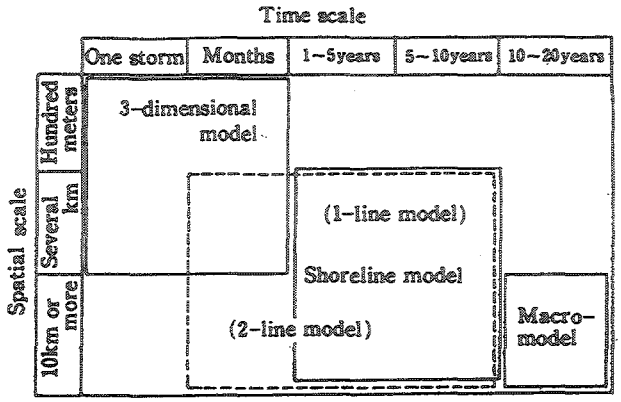

Figure (2.1): Application ranges of beach evolution predictive models (Horikawa, 1988)

Chapter 3: Elliptic Wave Model Development

3.1. General

As a train of regular waves moves towards the shore from deep water, it encounters several important transformations. As the water depths decrease towards the shore, both the wave phase celerity and the wave length decrease at the same time (Sorensen, 1993). If the wave energy was constant as the wave train propagates to shallow water, the continuous decrease in wave length should cause the wave height to continuously increase. This process is called the shoaling effect. Accordingly, the wave steepness increases as the wave train propagates towards the shore until it reaches its limit where waves break and lose height and energy. In addition, if the water depth varies along the wave crest, the portion of the wave in shallower water will have a lower celerity. This will cause the wave crest to reorient as the wave propagates forward and consequently to change its alignment towards the alignment of the bottom contours. It will also cause the wave crest length to increase or decrease, resulting in a respective decrease or increase in wave energy density and height. This process is called the wave refraction. If a portion of the wave crest is intercepted by a structure, energy will flow laterally along the un-intercepted portion of the wave and spread into the lee of the structure. This energy redistribution is called the wave diffraction. Wave diffraction will occur anytime the wave height is not constant along the crest of a wave and the energy flows from points of higher to lower wave height or energy density. When a wave encounters a partial or complete barrier a certain portion of the wave energy is reflected.

The focus of this chapter will be on the development of an elliptic water wave transformation model that may be employed to evaluate wave refraction, diffraction, shoaling and reflection. This is done for long-crested monochromatic waves, which may represent a selected design wave height, period and direction.

3.2. Linear Wave Theory

The linear or small amplitude wave theory was first developed by Airy (1845). This wave theory is extensively used in practice for a variety of reasons. It is much easier to apply than the more complex finite amplitude theories that are available, while still yielding useful results for many applications (Sorensen, 1993). And this theory is most useful as a building block for dealing with more complex phenomena such as reflecting waves, wave refraction and diffraction, and wave spectra.

It is important, however, to have a clear picture of the limitations of this theory. The derivation assumes that the wave amplitude is small relative to the wave length and the water depth. Consequently, for high waves at sea or for waves propagating in shallow nearshore areas where these assumptions do not strictly hold, the small amplitude wave theory is of more limited accuracy. However, experiments have shown that the small amplitude theory yields surprisingly realistic results for conditions that markedly deviate from the small amplitude assumption.

According the linear wave theory, the wave surface profile can be given by:

$$\eta = \frac{H}{2}\cos(kx - \omega t) \tag{3.1}$$

where, η is the water surface elevation measured from the still water level, H is the local wave height, x is the distance along the wave propagation direction, t is the time, k is the wave number, and ω is the wave frequency. The wave number and wave frequency are defined as;

$$k = \frac{2\pi}{L} \tag{3.2}$$

where L is the local wave length, and;

$$\omega = \frac{2\pi}{T} \tag{3.3}$$

where T is the wave period, respectively.

The relation between the wave number k and the wave frequency ω is established from the linear wave theory through the dispersion relation as follows:

$$\omega^2 = gk \tanh(kh) \tag{3.4}$$

where g is the gravitational acceleration and h is the water depth.

The wave group velocity c_g is defined according to the linear wave theory as follows:

$$c_g = nc = \frac{c}{2}(1 + \frac{2kh}{\sinh 2kh}) \tag{3.5}$$

where n is the wave index and c is the wave celerity, which is given by:

$$c = \frac{L}{T} = \frac{gT}{2\pi} \tanh \frac{2\pi h}{L} \tag{3.6}$$

3.3. Elliptic Water Wave Transformation Model

For an analytical solution of a combined refraction-diffraction problem, the solution of the three-dimensional Laplace equation with appropriate surface, bottom, and lateral boundary conditions is needed. A significant step towards the solution of such problem is achieved by Berkhoff (1972) through the development of the mild slope equation. This is a two-dimensional elliptic partial differential equation that describes the complete transformation of small amplitude waves including refraction, diffraction and reflection. The following sections describe the development of a new finite-difference water wave transformation model based on this equation with the implementation of new boundary equations.

3.3.1. Model equations

Several forms for the elliptic mild slope equation are derived (see Dingemans, 1997 for details). In this study, the time-independent form is adapted, which is an elliptic partial differential equation for the complex velocity potential Ψ as follows:

$$\nabla \cdot \left(cc_g \nabla \Psi\right) + k^2 cc_g \Psi = 0 \tag{3.7}$$

where the complex velocity potential is defined as:

$$\Psi = \frac{igHT}{4\pi} e^{iS} \tag{3.8}$$

where i is the square root of -1, S is the wave phase function, which can be given by (Dingemans, 1997):

$$S = \tan^{-1}\left[\frac{\mathrm{Im}(i\Psi)}{\mathrm{Re}(i\Psi)}\right] \tag{3.9}$$

With the Transformation,

$$\psi = \sqrt{cc_g}\,\Psi\,, \tag{3.10}$$

the mild-slope equation (3.7) can be written in the form of a Helmholtz equation with the modified wave number k_c:

$$\nabla^2\psi + k_c^2\psi = 0 \tag{3.11}$$

where the modified wave number k_c is given by:

$$k_c^2 = k^2 - \frac{\nabla^2 (cc_g)^{1/2}}{(cc_g)^{1/2}} \tag{3.12}$$

where k, c_g, and c can be calculated using the linear wave theory through Equations (3.4), (3.5) and (3.6), respectively.

Equation (3.11) is used as the governing equation for the elliptic model and is discretized over a uniform rectangular grid as follows:

$$\psi_E + \psi_W + \psi_N + \psi_S + [(k_c \Delta x)^2 - 4]\psi_P = 0 \tag{3.13}$$

where ψ_P, ψ_N, ψ_S, ψ_E and ψ_W are the values of the modified complex velocity potential at the grid point, north, south, east and west points, respectively, with the spatial grid sizes in both directions are equal (i.e. $\Delta x = \Delta y$). The grid size should not exceed one tenth of local wave length in order to ensure stability of the scheme (Dingemans, 1997).

3.3.2. Energy dissipation

In order to account for the wave energy dissipation in the mild slope equation, another term should be added to the modified wave number in Equation (3.12), as follows (Dingemans, 1997):

$$k_c^2 = k^2 - \frac{\nabla^2 (cc_g)^{1/2}}{(cc_g)^{1/2}} + i\omega \frac{W}{cc_g} \tag{3.14}$$

where, W is the sum of the dissipation functions due to factors like wave breaking, which has units of [T^{-1}].

The dissipation due to wave breaking can be given by (Kirby and Dalrymple, 1994):

$$W = \frac{\alpha c_g (1 - (\gamma h / H)^2)}{h} \tag{3.15}$$

where, α and γ are empirical constants determined by Dally et al. (1985) to be equal to 0.017 and 0.4, respectively.

For the case of random waves, the model developed by Battjes and Janssen (1978) is adopted. It assumes that the root-mean-square wave height H_{rms} is the characteristic wave height of the field. The wave breaking dissipation function is given by:

$$W = \frac{\alpha_c}{\pi} \omega Q_b \frac{1}{b^2} \tag{3.16}$$

where α_c is a calibration constant of the order of unity, Q_b is the probability that at a specific point in the field, the wave height reaches its maximum value H_m, which is given by:

$$Q_b = \exp[-(1 - Q_b)/b^2] \tag{3.17}$$

and b is ratio between the root-mean-square wave height and the maximum wave height (H_{rms}/H_m). The maximum wave height is obtained according to Miche's criterion (Beltrami et al., 2001):

$$H_m = \frac{2\pi\gamma_d}{k}\tanh\left(\frac{\gamma_s}{2\pi\gamma_d}kh\right) \tag{3.18}$$

where γ_s and γ_d are the wave breaking coefficients in shallow and deep water which have values around 0.7 and 0.14, respectively.

3.3.3. Boundary conditions

This section reviews the available boundary conditions for Equation (3.13) and describes the development of a new parabolic-type boundary condition for the problem.

3.3.3.1. Review of existing boundary conditions

The main problem accompanied with computational models of the mild slope equation is the treatment of the absorbing boundaries. Many researchers have studied the boundary conditions for the elliptic mild slope equation. For outgoing waves, the following radiation boundary condition, for a boundary perpendicular to x_1-axis, is perfectly absorbing.

$$\frac{\partial \Psi}{\partial x_1} = ik\cos\theta_b\,\Psi = ikl\Psi \tag{3.19}$$

where, Ψ is the complex velocity potential, k is the local wave number, θ_b is the angle of wave incidence at the boundary measured anticlockwise from x_1-axis. However, the wave angle at the boundary is not known in priori. Therefore, approximate outgoing boundary conditions were utilized in elliptic models on the assumption that all outgoing waves exit the domain in a direction perpendicular to the boundary ($l = 1$), like the models developed by Panchang et al. (1991), Li (1994a) and Li (1994b). This assumption is not always true and can lead to spurious reflections as pointed out by Kirby (1989). To alleviate this

approximation of normal incidence, Kirby (1986a and 1989) proposed the parabolic approximations which can accommodate waves exiting through larger angles.

Rather than approximation of the actual boundary conditions, the sea region outside the computational domain can be represented by a constant depth. In this case, it is possible to exactly describe the properties of the scattered waves outside the computational domain (Xu and Panchang, 1993), and the Dirichilet to Neumann (DtN) operators can be used to represent the boundary conditions. The non-local DtN methods, however, have the disadvantage of being cumbersome and still have the assumption of constant depth along the boundary.

The following section reviews the existing parabolic approximation for the elliptic mild slope equation.

3.3.3.2. Parabolic approximation of the wave equation

Equation (3.11) can be rewritten as (Dingemans, 1997):

$$\frac{\partial^2 \psi}{\partial x_1^2} = -k_c^2 \left(1 + \frac{1}{k_c^2} \frac{\partial^2}{\partial x_2^2} \right) \psi \tag{3.20}$$

Equations (3.11) and (3.20) permit the propagation of waves in all directions. The propagation of waves in the positive x_1-direction can be described by means of pseudo-differential operators as (Dingemans, 1997):

$$\frac{\partial \psi}{\partial x_1} = ik_c \left(1 + \frac{1}{k_c} \frac{\partial}{\partial x_2} \right)^{1/2} \psi \tag{3.21}$$

The general solution of Equation (3.11) is:

$$\psi = Ae^{iS} \qquad \text{where} \qquad S = \vec{k}_c \cdot \vec{x} \tag{3.22}$$

Substituting Equation (3.22) into Equation (3.21) yields:

$$k_{c1} = k_c\left(1-\left(\frac{k_{c2}}{k_c}\right)^2\right)^{1/2} \quad \text{or} \quad l = (1-m^2)^{1/2} = (1+z)^{1/2} \tag{3.23}$$

where $l = k_{c1}/k_c$ or cosine the wave propagation angle with x_1-direction, and $m = k_{c2}/k_c$ or sine the wave propagation angle with x_1-direction. From now on, the subscript "c" will be dropped for convenience.

The operator correspondence is used, where:

$$il \sim \frac{1}{k}\frac{\partial}{\partial x_1} \quad \text{and} \quad im \sim \frac{1}{k}\frac{\partial}{\partial x_2} \tag{3.24}$$

With these relations the correspondence between Equation (3.21) and Equation (3.23) is established. Approximation to the square root in Equation (3.23) is equivalent to approximation to the pseudo-differential operator in Equation (3.21), after substituting Equation (3.24). Several approximations have been attempted for the relative wave number l. Taylor series expansion has been used around $m = 0$. This approach, however, results in high order derivatives, which is inconvenient when it comes to application.

The $[p/q]$ Padé expansion of a function $l(z)$ which has a series expansion $l(z) = \sum_{i=0}^{p+q} c_i z^i$ is defined as (Dingemans, 1997):

$$[p/q] \quad l_a(z) = \frac{a_0 + a_1 z + a_2 z^2 + \ldots\ldots + a_p z^p}{b_0 + b_1 z + b_2 z^2 + \ldots\ldots + b_q z^q} \tag{3.25}$$

where $l_a(z)$ is the approximated function of the relative wave number l.

The coefficients of the expansion can be determined by comparing the coefficient of the Taylor expansion of $[p/q]$ $l_a(z)$ around $z = 0$ with the coefficients c_i of the expansion of the function $l(z)$ (Dingemans, 1997).

One advantage of Padé approximation over the Taylor series is that it gives, for the same order of approximation, lower order derivatives than the Taylor series does. For example, the Padé approximant [2/1] can be shown to be equivalent to Taylor series of the third order (Dingemans, 1997) after expressing the high order derivative in Taylor series by lower-order derivatives. Padé approximant [2/1] contains only fourth order values of m, which corresponds to fourth order derivative of ψ, while Taylor expansion contains sixth order values of m, which corresponds to sixth order derivative of ψ. Therefore, it can be shown that Padé approximant [2/2] is better than [3/1] than [4/0], and so on.

Kirby (1986a), proposed a minimax approximation for the square root according to:

$$l_a = \frac{p_0 + p_1 z}{1 + q_1 z} \tag{3.26}$$

where l_a is the approximated l. He derived values for the coefficients p_0, p_1 and q_1 according to the required range of the incidence angle. This approximation gives good results for wider range of angles.

Dingemans (1997) mentioned that the following approximation was considered:

$$l_a = \frac{1 - m^2}{1 - \alpha m^2} \tag{3.27}$$

The coefficient α is determined from a minimization of the root mean square error δ_{rms} of approximation:

$$\delta_{rms} = \frac{\int_0^{m_{max}} (l - l_a)^2 \, dm}{\int_0^{m_{max}} l^2 \, dm} \tag{3.28}$$

where m_{max} is the maximum expected value for m. The advantage of this approach over Padé approximation [1/1] is that it is correct for the limiting cases. However, for small angles, Padé approximation gives better results (Dingemans, 1997).

According to Givoli (1992), Halpern and Trefethen (1988) considered several other approximations to the square root in Equation (3.23) including Chebyshev, Chebyshev-Padé, Newman, L^2 and L^∞ approximations. They compared the various approximations in several numerical experiments. One observation from these experiments is that Padé approximants are by far the best at nearly normal incidence (l = 1), and by far the worst at nearly tangent incidence.

3.3.3.3. Generalized Padé approximation

All the existing approximations were derived so that the principal wave propagation direction is the x_1-direction (i.e. $z = m = 0$), and according to the order of accuracy, the range of applicability is set. A general set of [p/q] Padé approximations for the square root in Equation (3.23) is derived for a general wave propagation angle θ_b with the x_1-direction (Saied and Tsanis, 2004a). The coefficients of Equation (3.25) is determined by comparing the coefficient of the Taylor expansion of [p/q] $l_a(z)$ around $z = d = -\sin^2\theta_b$ with the coefficients c_i of the expansion of the function $l(z)$ around $z = d$.

Using this procedure, the following set of generalized Padé approximants are derived (Saied and Tsanis, 2004a):

[2/2] $$l_a = \frac{\sqrt{1+d}\,(16+12d+d^2+20z+10zd+5z^2)}{16+20d+5d^2+12z+10zd+z^2} \tag{3.29}$$

[2/1] $$l_a = \frac{1}{4}\frac{(8+8d+d^2+8z+6zd+z^2)}{\sqrt{1+d}\,(2+d+z)} \tag{3.30}$$

[1/2] $$l_a = -4\frac{(1+d)^{3/2}(6+d+5z)}{-24-40d-15d^2-8z-10zd+z^2} \tag{3.31}$$

[1/1] $$l_a = \frac{\sqrt{1+d}\,(4+d+3z)}{4+3d+z} \tag{3.32}$$

[1/0] $$l_a = \frac{2+d+z}{2\sqrt{1+d}} \tag{3.33}$$

[0/0] $$l_a = \sqrt{1+d} \tag{3.34}$$

where $d = -sin^2\theta_b$, θ_b is the prescribed primary wave angle at the boundary, $z = -sin^2\theta$ and θ is the wave angle at the boundary, which is unknown in priori. Equations (3.29) to (3.34) are exact when $\theta = \theta_b$. The conventional Padé approximants can be derived from Equations (3.29) to (3.34) by setting $\theta_b = 0°$.

Figure (3.1) compares between different approximated l with $\theta_b = 45°$ and the exact from Equation (3.23) for different values of m (sine the wave angle with x_1-direction). The exact solution represents a circle. Figure (3.2) compares between the conventional Padé approximations ($\theta_b = 0°$) and the corresponding generalized approximations for $\theta_b = 75°$. It can be shown that the conventional approximation fails to approximate the square root at 75°.

Table (3.1) summarizes the relative error of approximation for a range of wave angles between 60° to 80° using the conventional Padé [1/1] approximation and the corresponding generalized approximation for θ_b = 70°. The relative error of approximation is calculated as follows:

$$\varepsilon_r = \frac{|l_a - l_h|}{l_h} \times 100 \tag{3.35}$$

where l_h is the exact value of the cosine of the wave angle, obtained from Helmholtz equation (Equation (3.23)). It can be shown that for this range of large wave angles the error resulting from Equation (3.32) does not exceed 7%, while the conventional approach fails to approximate the square root.

Table (3.1): Comparison between the generalized and the conventional Padé [1/1] approximations

Wave angle			Conv. Padé [1/1]		New Padé [1/1]	
θ	$m = \sin\theta$	l_h	l_a	Error %	l_a	Error %
60	0.86603	0.5	0.53846	7.69231	0.49344	1.31223
65	0.90631	0.42262	0.48317	14.3286	0.42163	0.23395
70	0.93969	0.34202	0.43341	26.721	0.34202	0
75	0.96593	0.25882	0.39158	51.2938	0.2602	0.53247
80	0.98481	0.17365	0.35987	107.241	0.18617	7.21298

Substituting Equation (3.24) into Equations (3.29)-(3.34), the approximate differential operators for Helmholtz Equation can be found as follows (Saied and Tsanis, 2004a):

[2/2]
$$(1+\frac{5}{4}d+\frac{5}{16}d^2)\psi_x = ik\sqrt{1+d}(1+\frac{3}{4}d+\frac{d^2}{16})\psi + \frac{i\sqrt{1+d}(\frac{5}{4}+\frac{5}{8}d)}{k}\psi_{yy} - \frac{(\frac{3}{4}+\frac{5}{8}d)}{k^2}\psi_{xyy} + \frac{5i\sqrt{1+d}}{16k^3}\psi_{(4y)} - \frac{1}{16k^4}\psi_{x(4y)} \quad (3.36)$$

[2/1]
$$(1+\frac{d}{2})\psi_x = \frac{ki}{\sqrt{1+d}}(1+d+\frac{d^2}{8})\psi + \frac{i(1+\frac{3}{4}d)}{\sqrt{1+d}k}\psi_{yy} - \frac{1}{2k^2}\psi_{xyy} + \frac{i}{8\sqrt{1+d}k^3}\psi_{yyyy} \quad (3.37)$$

[1/2]
$$(1+\frac{5}{3}d+\frac{5}{8}d^2)\psi_x = ik(1+d)^{3/2}(1+\frac{d}{6})\psi + \frac{5i}{6k}(1+d)^{3/2}\psi_{yy} - \frac{(1+\frac{4}{5}d)}{3k^2}\psi_{xyy} + \frac{1}{24k^4}\psi_{x(4y)} \quad (3.38)$$

[1/1]
$$(1+\frac{3}{4}d)\psi_x = ki\sqrt{1+d}(1+\frac{d}{4})\psi + \frac{3i\sqrt{1+d}}{4k}\psi_{yy} - \frac{1}{4k^2}\psi_{xyy} \quad (3.39)$$

[1/0]
$$\sqrt{1+d}\psi_x = ik(1+\frac{d}{2})\psi + \frac{i}{2k}\psi_{yy} \quad (3.40)$$

[0/0]
$$\psi_x = ki\sqrt{1+d}\psi \quad (3.41)$$

Kirby (1986a) compared between the results of minimax approximation with θ_b = 0 and minimax approximation with general angle θ_b. He concluded that generalization of the centre wave angle does not give significantly better approximations, as the minimax approximation with θ_b = 0 over larger range of wave angles usually gives satisfactory results.

Unlike minimax approximation, conventional Padé approximation does not work well for large wave angles (i.e. more than 60°). However, the generalized Padé approximation yields good results for large wave angles, as shown in Table (3.1).

Figure (3.3) compares between the error in calculating l using minimax approximation and the Padé approximation for the square root in Equation (3.23). Two minimax approximations are shown, the first is for θ_b = 0° with 70° wave angle range, and the second is for θ_b = 45° with 30° wave angle range. Two Padé [1/1] approximations are shown as well, the first is for θ_b = 45° and the second is for θ_b = 70°. It can be shown that at $\theta = \theta_b$, the Padé approximation relative error is effectively zero and increases rapidly with the deviation from the centre angle. The minimax approximation, however, is consistent over a wider range of wave angles but it does not guarantee lowest relative error at $\theta = \theta_b$. Also, it can be shown that the generalized minimax approximation does not give significant improvement over the conventional one (θ_b = 0).

Therefore, the generalized Padé approximations can be used as boundary conditions for the elliptic water wave models. They can be used to remove reflections from the elliptic solution by continuously updating the boundary equations for the wave angle θ_b calculated from the previous iteration until convergence is reached, since they are exact at $\theta = \theta_b$.

In addition, Equations (3.36) - (3.41) are easy to use in programming because the centre angle can be set and changed flexibly through the parameter d.

Another advantage of Equations (3.36) - (3.41) is that they are well suited for application as a parabolic model solving marching in space and updating the values of d

using an approximate value from the nearest known cell. In this chapter, however, these equations are only used as absorbing boundaries for the elliptic mild slope equation in the case of large angle of incidence.

Table (3.2) shows the range of applicability of the generalized [1/1] and [2/1] Padé approximations for different values of θ_b. These ranges were calculated so that error in calculating l does not exceed 3%. It can be shown that the [1/1] Padé approximation with $\theta_b = 50°$ provides fairly large range of application. However, for $\theta_b > 60°$, the range of application is very small. Therefore, it is not recommended to set $\theta_b > 60°$ for the first iteration unless the wave angle is known. In addition, it is shown from Table (3.2) that the generalized [2/1] approximation with $\theta_b = 50°$ is only 6% better than the generalized [1/1] approximation, which is not significant giving the complicated formulation of the [2/1] formulation.

Table (3.2): Range of application for the generalized Padé [1/1] approximations ($\varepsilon_r < 3\%$)

Centre angle θ_b	Padé [1/1]		Padé [2/1]	
	Angle range	Range length	Angle range	Range length
0	-50° ~ 50°	100°	-61° ~ 61°	122°
10	-54° ~ 54°	108°	-61° ~ 61°	122°
20	-55° ~ 55°	110°	-63° ~ 63°	126°
30	-59° ~ 59°	118°	-65° ~ 65°	130°
40	-63° ~ 63°	126°	-68° ~ 68°	136°
50	-67° ~ 67°	135°	-72° ~ 72°	144°
60	±(32° ~ 72°)	80°	-76° ~ 76°	152°
70	±(55° ~ 77°)	44°	±(45° ~ 80°)	70°
75	±(65° ~ 81°)	32°	±(58° ~ 82°)	48°

The boundary conditions are set using the generalized Padé [1/1] approximation (Equation (3.39)) for the non-reflecting boundaries, conditioned with that the angle θ_b does not exceed 75°, where the x_1-axis is considered the direction normal to the boundary. A symmetric boundary condition is used when the incident wave angle at the boundary is more than 85°:

$$\frac{\partial \psi}{\partial x_1} = 0 \tag{3.42}$$

For the offshore given boundary, the following boundary condition is used:

$$\frac{\partial \psi}{\partial x_1} = ik_c \cos\theta_0 (2\psi_g - \psi) \tag{3.43}$$

where ψ_g is the given complex velocity potential, which is computed from Equations (3.10) & (3.8) and θ_0 is the given wave angle at the offshore boundary.

Partial reflections can be included by multiplying the right hand side of the boundary Equation (Equations (3.36) - (3.41)) by the coefficient γ, where:

$$\gamma = \frac{1-R}{1+R} \tag{3.44}$$

where R is the reflection coefficient.

The angles at the non-reflecting boundaries are estimated for the first iteration by the simple Snell's Law as follows:

$$k_0 \sin(\theta_0 - \alpha) = k \sin(\theta_b - \alpha) \tag{3.45}$$

where, θ_0 is the incident wave angle measured anticlockwise from the x_1-direction, θ_b is the approximated wave angle at the boundary, and α is the angle that the contour lines make with x_1-axis at the boundary location.

3.3.4. Solution method

The system of equations (3.13), (3.39), (3.42) and (3.43) is solved iteratively using the conjugate gradient method. Panchang et al. (1991) applied the conjugate gradient algorithm to solve a similar system using the simple radiation boundary condition assuming normal wave incidence at the boundaries. In order to enhance the convergence, preconditioning of the coefficient matrix is necessary. Li (1994a) proposed a generalized conjugate gradient algorithm based on minimizing the function:

$$f(x) = \frac{1}{2}\left|A_{i\times j}x_{j\times 1} - b_{i\times 1}\right|^2 \tag{3.46}$$

where $A_{i\times j}$ is the system matrix which contains coefficients according to Equation (3.13), $x_{j\times 1}$ is the unknown vector that contains the desired grid-point values of the modified wave potential, and $b_{i\times 1}$ is a vector that contains information from Equation (3.43). His algorithm does not need preconditioning of the coefficient matrix and converges very fast. Like Panchang et al. (1991), he assumed normal wave incidence at the absorbing boundaries.

A slightly different algorithm has been used after multiplying the coefficient matrix A by its conjugate transpose A^* so that a symmetric positive definite matrix is obtained and convergence is guaranteed (Nocedal and Wright, 1999). The algorithm can be summarized as follows:

$$
\begin{aligned}
& r_0 = A^*(Ax_0 - b) \\
& p_0 = -r_0 \\
\text{while} \quad & Ax - b \neq 0 \\
& u_k = A^* A p_k \\
& \alpha_k = \frac{r_k^T A^* A r_k}{u_k^T u_k} \\
& x_{k+1} = x_k + \alpha_k p_k \\
& r_{k+1} = r_k + \alpha_k u_k \\
& \beta_{k+1} = \frac{r_{k+1}^T A^* A r_{k+1}}{r_k^T A^* A r_k} \\
& p_{k+1} = -r_{k+1} + \beta_{k+1} p_k \\
& k = k+1 \\
& \text{end while}
\end{aligned}
\tag{3.47}
$$

where, p_k is the conjugate vector to the previous vectors (p_0, p_1, ... p_{k-1}), β_k is a scalar which requires that that p_{k-1} and p_k must be conjugate with respect to A, and the superscript "T" stands for the transpose of a complex vector, which contains transposed conjugate elements of the original vector. A FORTRAN 77 code has been developed to perform the above algorithm using sparse matrix techniques, where only the non-zero elements are stored.

3.3.5. Numerical results and discussion

The experimental data obtained by Berkhoff (1982) are used to test the model performance. The experimental bathymetry consists of an elliptic shoal situating on a plane sloping beach of 1:50 slope. Figure (3.4) shows the bottom contours of the computational domain along with the labelled transects 1-8 for which experimental data are available. The wave height was 0.0464 m and the wave period was 1 second. A gravel beach was installed to absorb the wave energy at the downstream end. The present model

is applied using $\Delta x = \Delta y = 0.1$m and the grid has 250 × 200 points, which covers a domain of 25m × 20m. The residual error is calculated each 100 iterations from:

$$E = \frac{\sum\left|(\nabla^2\psi + k_c^2\psi\right|^2}{\sum\left|\psi\right|^2} \tag{3.48}$$

The reflection coefficient R is set to 0.0 at the downstream boundary. It takes the model 2300 iterations for the linear solution without boundary refinements to reduce the residual error E to the order of 10^{-7} as shown in Figure (3.5). The wave height pattern is presented in Figure (3.6). Solution refinement can be done using the proposed boundary equation (Equation (3.39)).

Because of the iterative nature of the present model, the refinement can include non-linear effects. The approach proposed by Kirby and Dalrymple (1986) is used to calculate the wave numbers using the following relation instead of Equation (3.4):

$$\omega^2 = gk[1 + (ka)^2 F_1 \tanh^5(kh)]\tanh[kh + (ka)F_2]$$

where

$$F_1 = \frac{\cosh(4kh) + 8 - 2\tanh^2(kh)}{8\sinh^4(kh)} \quad \text{and} \quad F_2 = \left(\frac{kh}{\sinh(kh)}\right)^4 \tag{3.49}$$

and $a = H/2$ is the wave amplitude.

Convergence is reached after 5 iterations for the nonlinear model requiring successively fewer iterations in each round, which makes the total number of iterations 6600 to reach the nonlinear solution. Panchang et al. (1991) solved the same problem assuming normal incidence at the boundaries (l = 1) and reached convergence after 5 iterations as well. Therefore, the proposed boundary equations do not require extra

iterations to converge to the non-linear solution, although being two orders higher than the boundaries implemented by Panchang et. al. (1991).

The wave height pattern for the nonlinear model is shown in Figure (3.7). The data, linear and nonlinear solutions are compared in Figure (3.8a-h). The linear model results are comparable with the experimental data for relatively deep waters. The nonlinear model, however, compares very well with the experimental data for both deep and shallow waters.

Considering the experimental data to be error-free, the root mean square error *rmse* can be calculated for each transect from:

$$rmse = \left[\frac{1}{n} \sum_{i=1}^{n} (y_i - x_i)^2 \right]^{1/2} \tag{3.50}$$

where y_i and x_i are the measured and calculated normalized wave heights, respectively, and n is the number of experimental data points in the section. Table (3.3) shows the root mean square difference between the experimental data and the model solution for both the linear and nonlinear cases. It is clear that for the case of the linear model, the error increases significantly for transects 5, 6, 7 and 8 due to the shallow water depths. On the other hand, the nonlinear model results are consistent over all transects, which proves that the nonlinear model performs well in both shallow and deep water depths.

Table (3.3): Root mean square error for the linear and nonlinear model results

Transect #	1	2	3	4	5	6	7	8
Linear Model	0.0715	0.1382	0.1363	0.1641	0.2520	0.2076	0.2226	0.1503
Nonlinear Model	0.0761	0.0931	0.0961	0.0996	0.0976	0.1054	0.0946	0.0946

The effect of different parabolic boundary conditions on the internal solution is studied by getting the lateral boundaries closer to the domain of interest. Therefore, the computational domain is reduced to 25m × 10m. The generalized [1/1] Padé approximation, the minimax approximation for angle range of 80° and the conventional [1/1] Padé approximation are compared in Figure (3.9a, b and c), respectively. In the first two cases, the effect of the lateral boundaries on the internal solution is very little, as shown in Figure (3.9a and b), respectively. However, using the conventional [1/1] Padé approximation as boundary conditions greatly affects the internal solution, as shown in Figure (3.9c).

Figure (3.10a-c) shows the model results in the three cases for transect 5, respectively. The root mean square errors are calculated using Equation (3.50) and are shown in Figure (3.10). It can be shown that using the generalized [1/1] Padé approximation as boundary equation (Figure (3.10a) gives better results and less root mean square error than the minimax approximation (Figure (3.10b). On the other hand, using the conventional [1/1] Padé approximation as boundary conditions greatly affects the internal solution, as shown in Figure (3.10c), where the root mean square error is 0.2701.

In order to test the significance of the proposed boundary conditions, the circular shoal problem proposed by Kirby (1986a) and Dalrymple et al. (1989) is adopted. Owing to the axisymmetry of the circular shoal, the wave focusing pattern behind the shoal should be independent of the incident wave angle if the model is correct (Dalrymple et

al.,1989). The water depth used here is the same adopted by Dalrymple et al. (1989), which is:

$$h = \begin{cases} h_0 & r > R \\ h_0 + \alpha - \beta\left[1 - (0.2X')^2 - (0.2Y')^2\right]^{1/2} & r < R \end{cases} \tag{3.51}$$

where h_0 = 0.336 m, α = 0.12, β = 0.2, and R = 4 m is the radius of the shoal, $r = (X'^2 + Y'^2)^{1/2}$ and (X', Y') = coordinates with the origin at the crest of the shoal. The wave period is 1 s. Three computational domains are used for the analysis based on the location of the circular shoal as shown in Figure (3.11a-c). The circular shoal is located at (6 m, 10 m) for the case of normal incidence (i.e. $\theta_0 = 0°$) and at (6 m, 6 m) otherwise.

Three runs have been done using the present model for wave angles θ_0 = 0°, 45°, and 70°. The wave height patterns behind the shoal for the three cases as well as the patterns obtained by conventional [1/1] Padé approximation for θ_0 = 0° and 45°, and the minimax approximation (80° angle range) are shown in Figure (3.12a-f). For the case of conventional Padé [1/1] approximation with θ_0 = 45° (Figure (3.12c)), the symmetry is well preserved due to the fact that reflections from the East and North boundaries are exactly the same. The internal solution, however, is affected by these reflections, which can be noticed from Figure (3.12c). For the case of θ_0 = 70°, the conventional [1/1] Padé approximation boundary equations fail to preserve the symmetry as shown in Figure (3.12e).

The results of the proposed boundary equations are shown in Figure (3.12b and d). It can be shown that the symmetry is well preserved for the two runs and the results do not change much with the inclination angle.

Comparing Figure (3.12d, e and f), it can be concluded that the generalized [1/1] Padé approximation is the best parabolic boundary equation.

In order to test the internal solution, two transects, which are 10 and 15 m behind the shoal crest, are plotted in Figure (3.13a and b), respectively, for the case of $\theta = 70°$. The dots represent the solution for the zero inclination angle case, which is considered as a reference for comparison. At the axis of symmetry behind the shoal, the agreement between the reference case results and the results obtained by applying the proposed boundary equations is very good. Some differences, however, are detected off centre. On the other hand, reflections from the boundaries are noticeable for the case of the conventional Padé approximation. These reflections affect the internal solution as shown in Figure (3.13a and b), especially near the East boundary (Distance > 10m) at which the wave angle is large with respect to the boundary. The minimax approximation results in reflections from the East boundary as well, and the internal solution at the axis of symmetry is slightly affected, as shown in Figure (3.13a and b).

A practical application of the wave model is examined for the case of wave field around an offshore breakwater. According to Horikawa (1988), Watanabe and Maruyama (1986) measured the wave field around a single offshore breakwater in the laboratory. In the experiment, a detached breakwater made of a steel plate 2.67 m long was placed at a water depth of 6.0cm and parallel to the shoreline on a plane beach of mortar with slope of 1:50. The breakwater was designed to almost perfectly reflect the incident waves. The waves were incident normal to the breakwater and the contour lines, and the deepwater wave height and period were 2.0 cm and 1.2 s. The length of the breakwater is almost

three times the local wavelength. The wave field is theoretically expected to be symmetric about the centreline, and was observed as nearly symmetric in the physical model. Therefore, the model was applied to half of the domain. The grid spacing was 5 cm. The wave energy dissipation due to breaking is included through the application of Equation (3.15). Iterations are required because Equation (3.15) contains the wave height, which is initially unknown. The accelerated iterative method proposed by Beltrami et al. (2001) is used, where the dissipation function at iteration n is calculated from:

$$W_n^a = \frac{W_n - W_{n-1}^a}{2} \tag{3.52}$$

where W_n^a and W_{n-1}^a are the dissipation functions used by the model for iterations n and n-1, respectively, and W_n is the dissipation function calculated from Equation (3.15). The adjustment that Equation (3.52) imposes accelerates the convergence because the dissipation function is an increasing function of the wave height. Accordingly, the value W_n is always greater than the true value because it is based on the wave heights at the previous iteration which are larger than the true values. Therefore, Equation (3.52) gives better estimate for the dissipation function.

Figure (3.14) shows the normalized wave height pattern around the breakwater. Figure (3.15) and Figure (3.16) show the model results and the measurements. The agreement is generally good. The model can handle the reflections from the structures and can include dissipation effects.

3.4. Summary

A new elliptic water wave transformation model has been developed in this chapter. The finite-difference method is used to discretize the governing equation over a two-dimensional grid and the generalized conjugate gradient method is used to solve the resulting system matrix. A set of generalized Padé approximants has been developed and used as a boundary condition for the elliptic model. The new boundary condition based on [1/1] generalized Padé approximation is proven to be better than all the existing rational approximations. In addition the boundary equations are easy to implement and can be used in practice where they allow the application of the elliptic wave model without having to rotate grids to reduce the wave angle at the boundaries. The elliptic wave model is verified through several experimental tests and showed the efficiency of the new boundary conditions. The elliptic model, however, is very demanding in terms of computation time, which makes it difficult to apply in practice. Therefore, the next chapter will tackle some additional techniques used to enhance the computation time of the wave model through approximation to the elliptic equation.

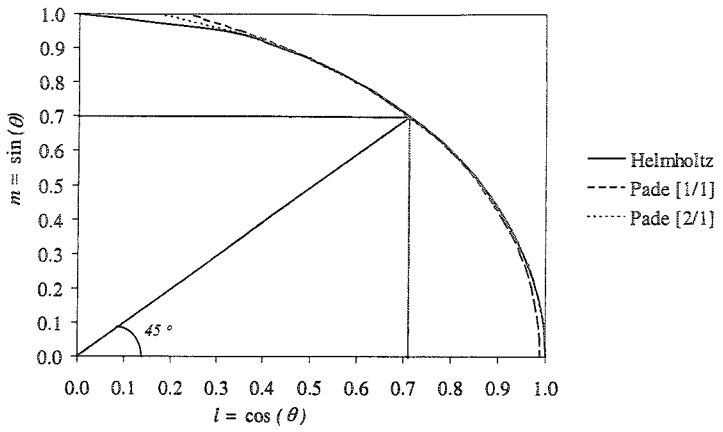

Figure (3.1): Comparison between different Padé approximations ($\theta_b = 45°$)

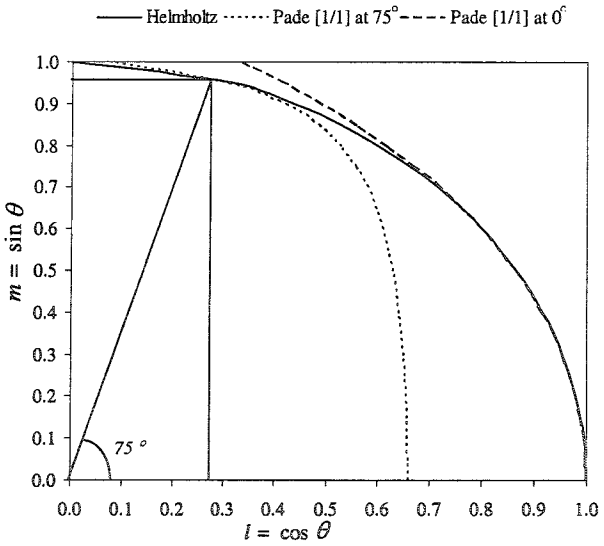

Figure (3.2) : Comparison between conventional [1/1] Padé approximation ($\theta_b = 0°$) and generalized [1/1] Padé approximation ($\theta_b = 75°$)

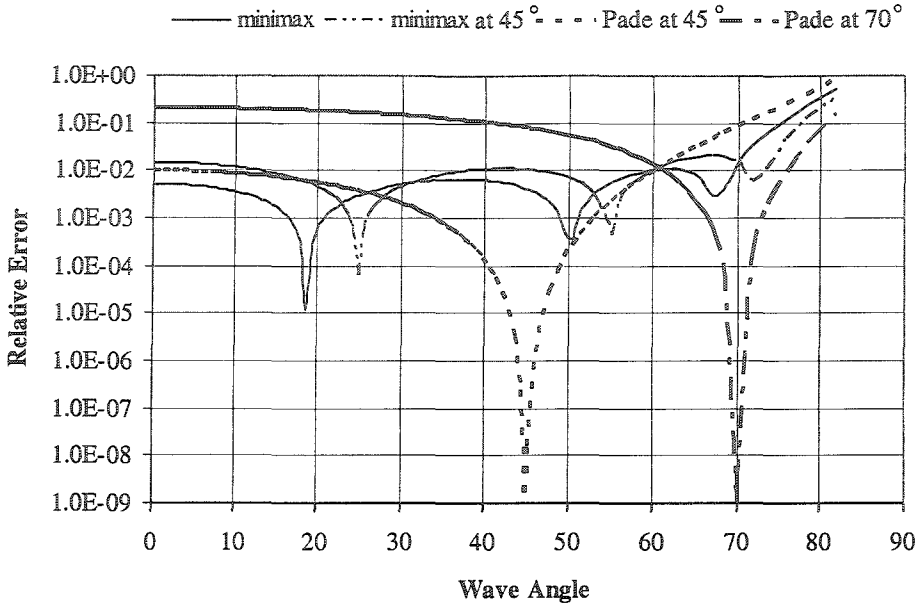

Figure (3.3) : Comparison between minimax approximations and Padé approximations

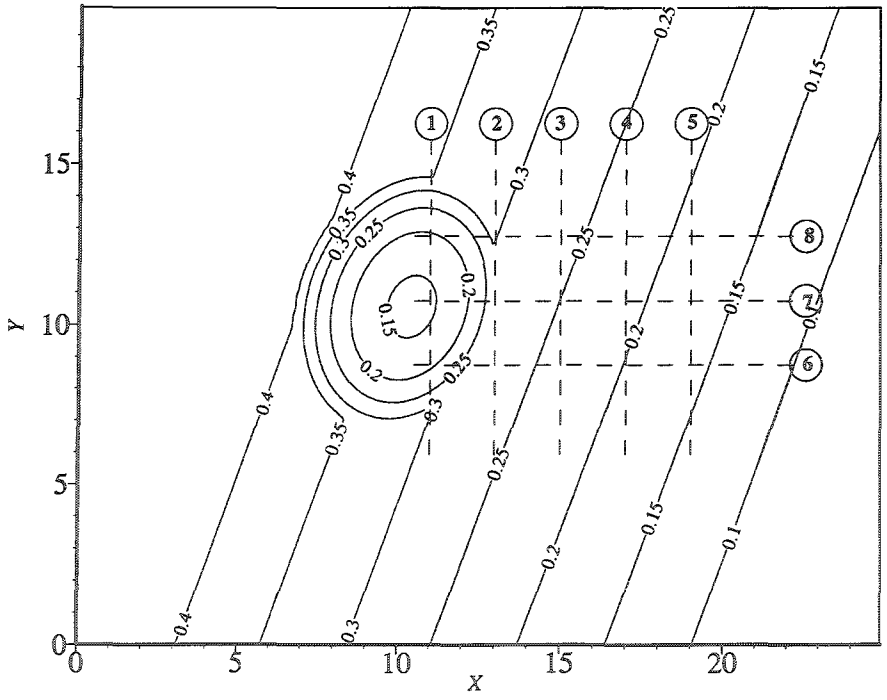

Figure (3.4): Elliptical shoal bathymetry

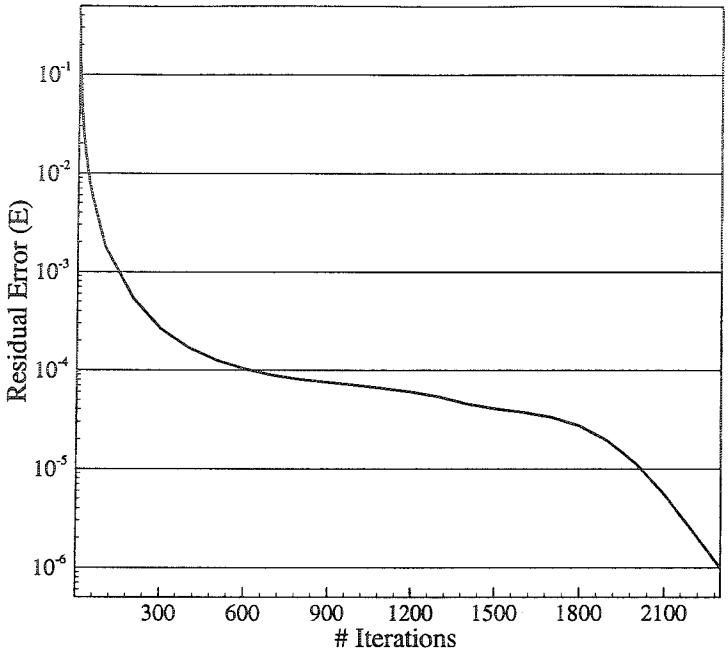

Figure (3.5): Elliptical model convergence

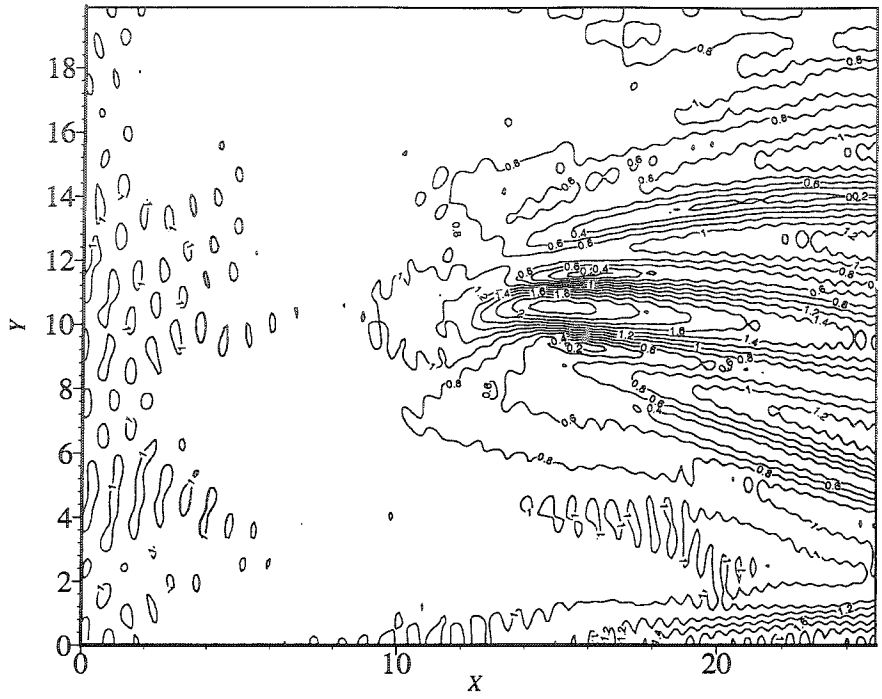

Figure (3.6): Linear wave height pattern behind the elliptical shoal

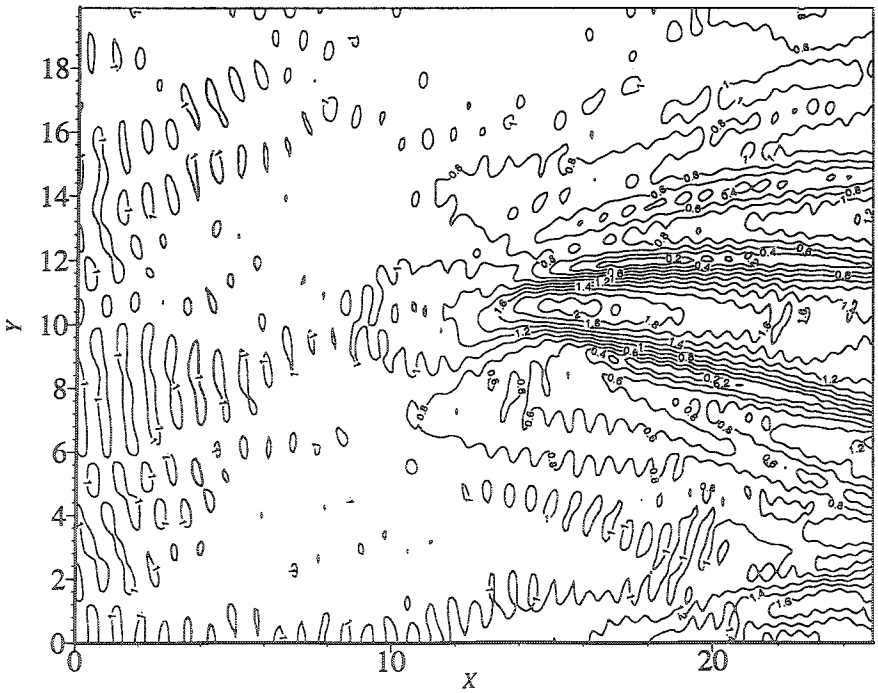

Figure (3.7) : Non-linear wave height pattern behind the elliptical shoal

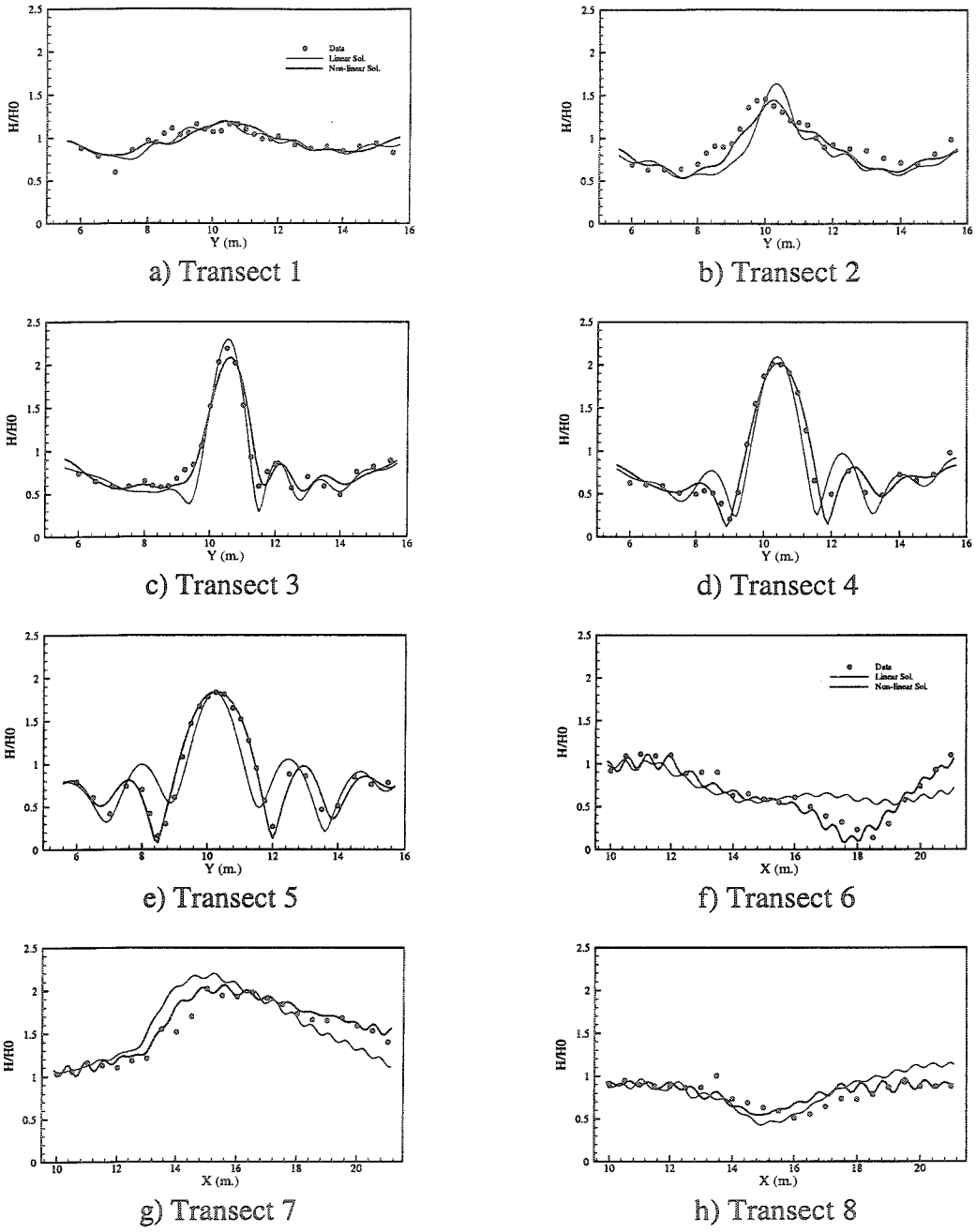

Figure (3.8) : Comparison between elliptical shoal data, linear and non-linear solution

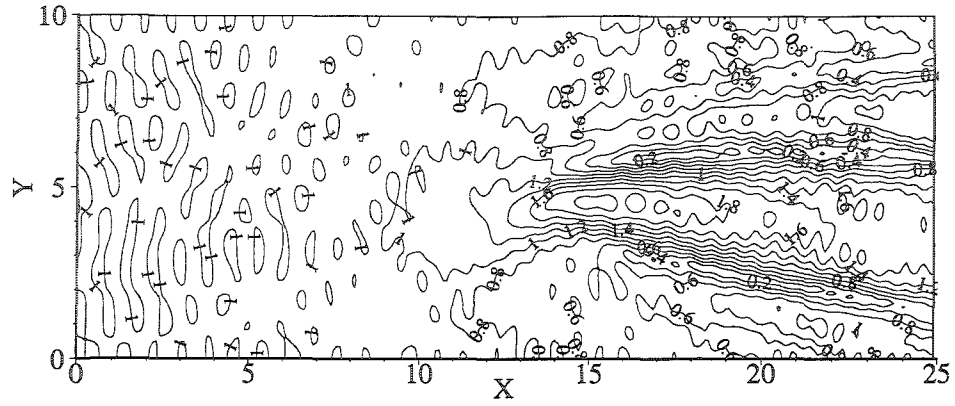

a) Generalized Padé approximation

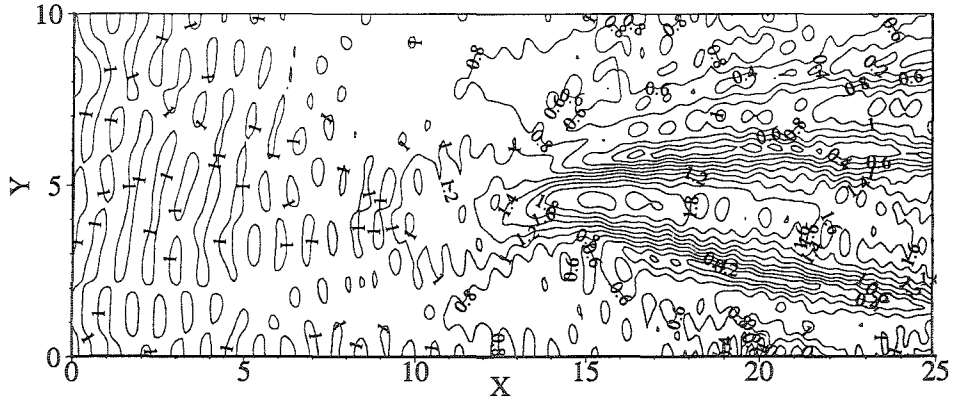

b) Minimax approximation

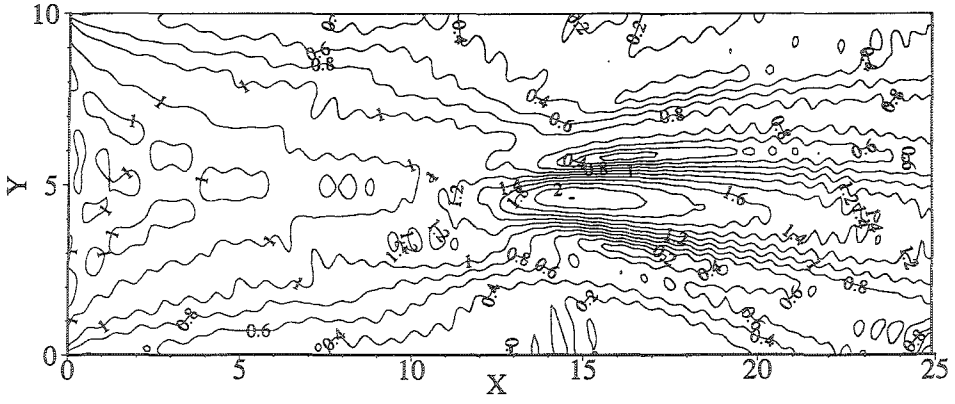

c) Conventional Padé approximation

Figure (3.9) : Comparison between the effects of boundary equations on the internal solution

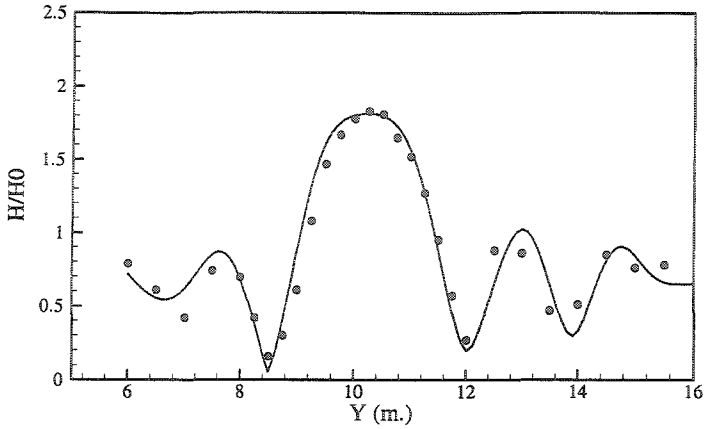

a) Generalized Padé approximation (*rmse* = 0.1276)

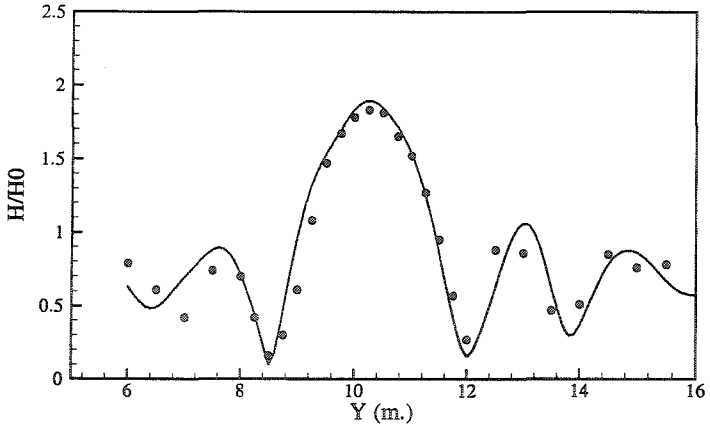

b) Minimax approximation (*rmse* = 0.1472)

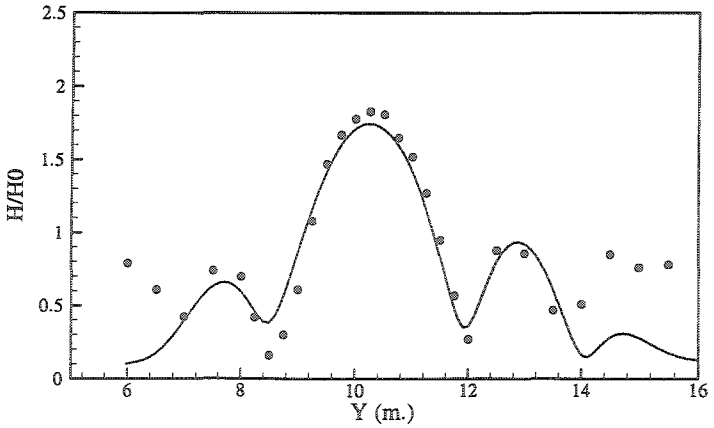

c) Conventional Padé approximation (*rmse* = 0.2701)

Figure (3.10) : Transect 5 data and internal solution for different boundary equations

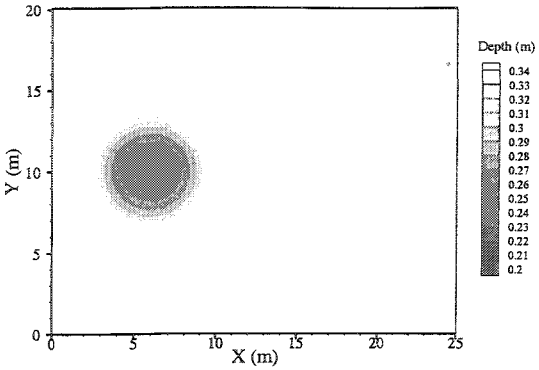

a) $\alpha = 0.12$, $\beta = 0.2$ and $\theta_0 = 0°$

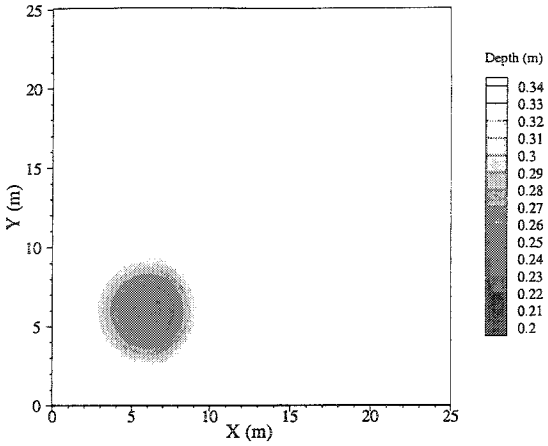

b) $\alpha = 0.12$, $\beta = 0.2$ and $\theta_0 = 45°$

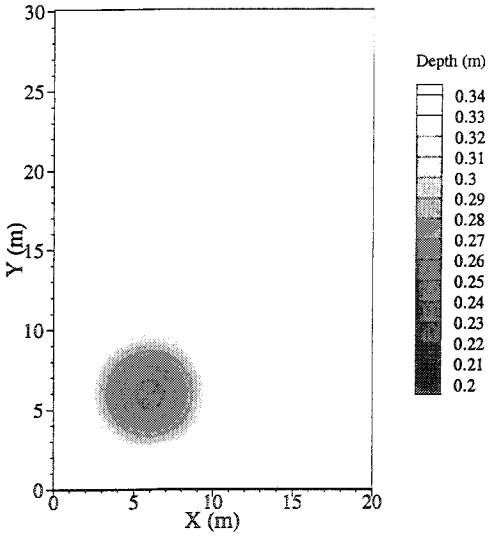

c) $\alpha = 0.12$, $\beta = 0.2$ and $\theta_0 = 70°$

Figure (3.11): Circular shoal computational domains

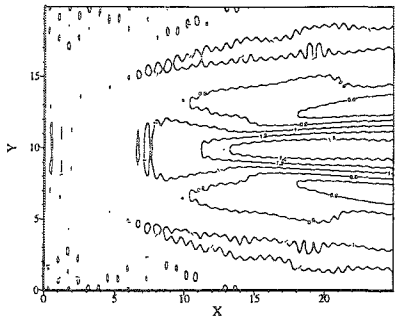

a) Reference Case (Wave angle = 0°)

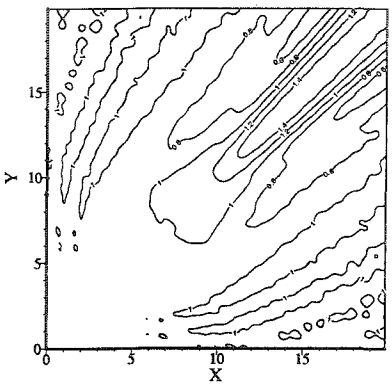

b) Wave angle = 45°
Using Padé approx. $\theta_b=45°$

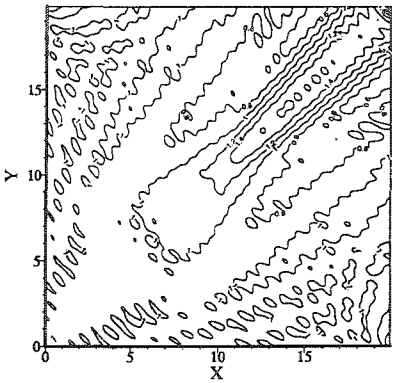

c) Wave angle = 45°
Using Padé approx. $\theta_b=0°$

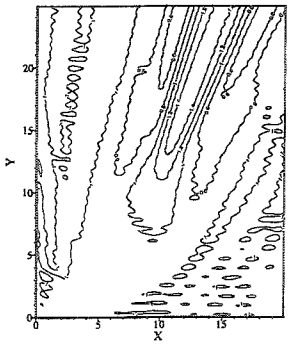

d) Wave angle = 70°
Using Padé approx. $\theta_b=70°$

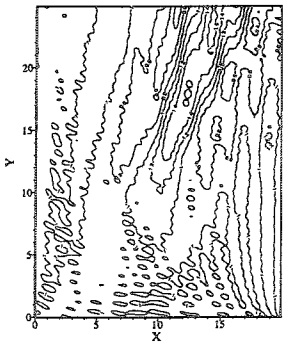

e) Wave angle = 70°
Using Padé approx. $\theta_b=0°$

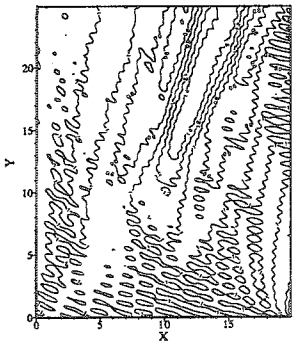

f) Wave angle = 70°
Using minimax approx.

Figure (3.12) : Wave height pattern behind a circular shoal

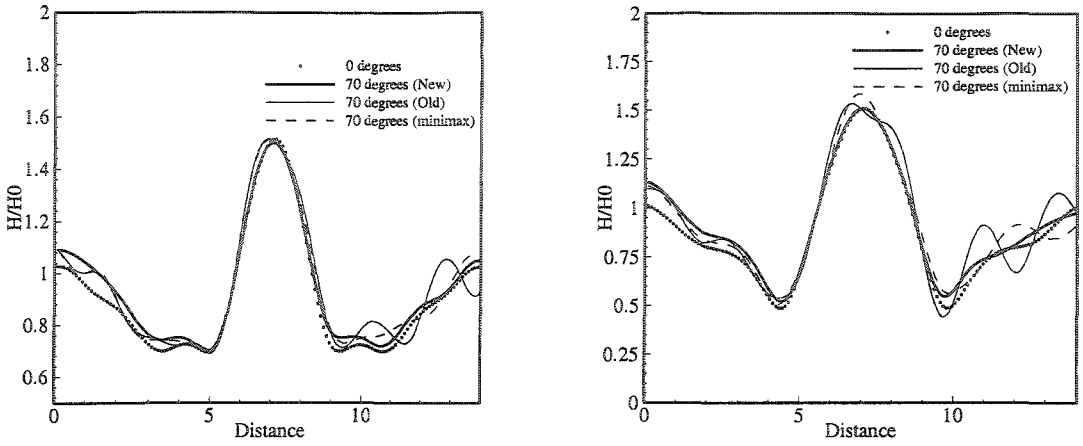

a) Section at 10 m b) Section at 15 m

Figure (3.13) : Cross section behind the circular shoal after 10 meters and 15 meters from the center of the shoal

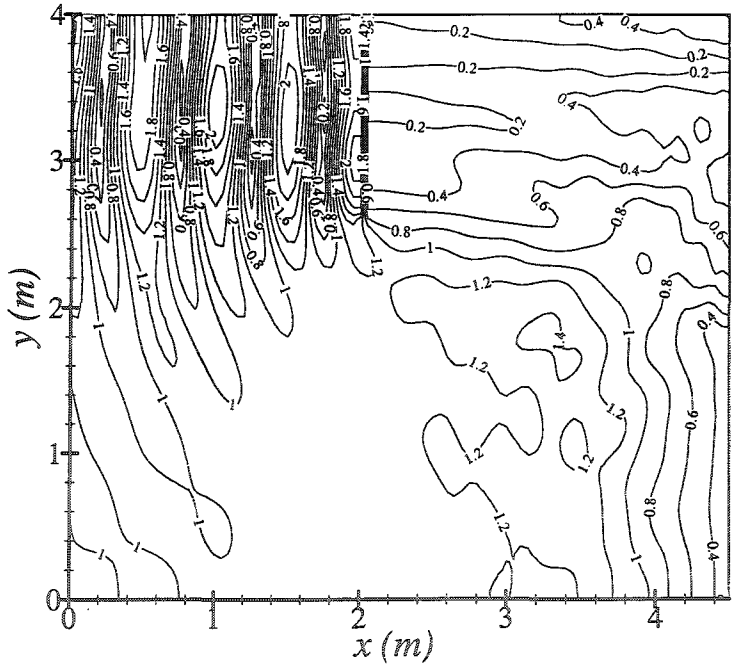

Figure (3.14) : Wave height pattern for an offshore breakwater

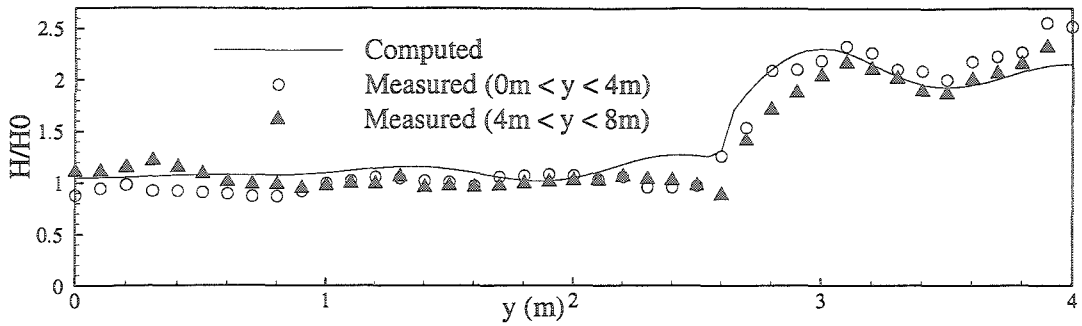

a) Cross section at x = 2.0m (front side)

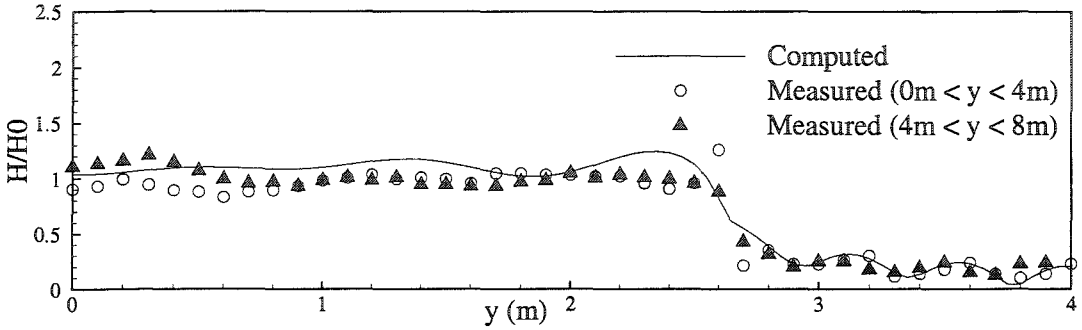

b) Cross section at x = 2.0m (rear side)

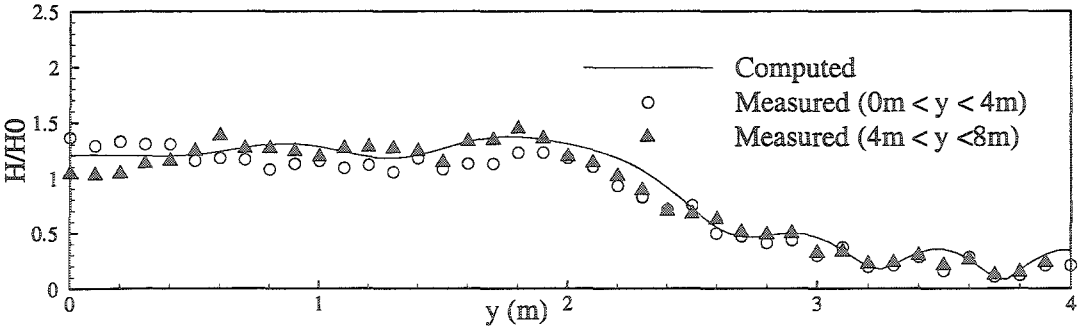

c) Cross section at x = 3.0m

Figure (3.15) : Alongshore distribution of wave heights

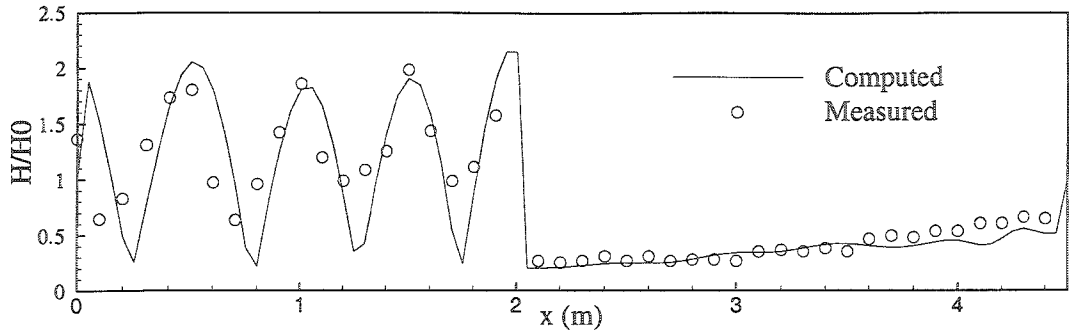

a) Long. section at y = 4.0m

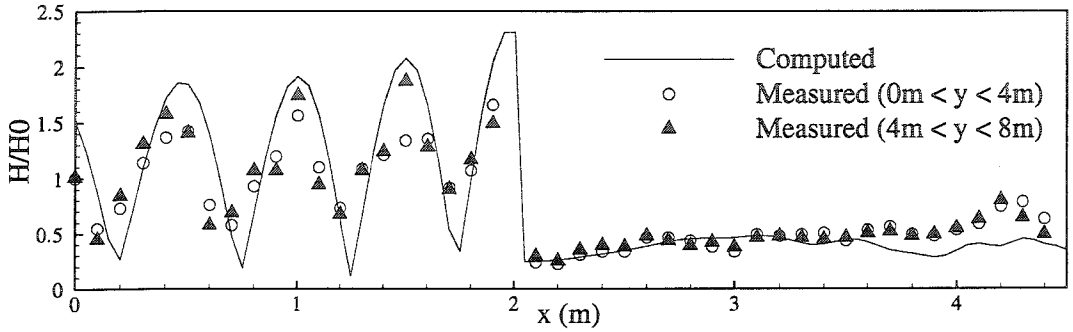

b) Long. section at y = 3.0m

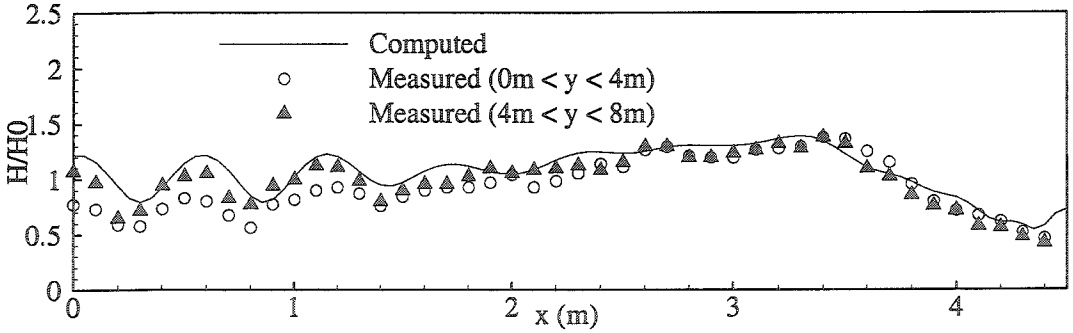

c) Long. section at y = 2.0m

Figure (3.16) : Cross-shore distribution of wave heights

Chapter 4: Practical Wave Models

In this chapter two new wave models are presented. The first is a parabolic model, which can simulate combined wave refraction and diffraction. The second model is an integrated model that groups the parabolic model and the elliptic model which was developed in the last chapter.

4.1. Parabolic Model Development

4.1.1. Parabolic models: brief review

The mild slope equation, being elliptic, is computationally demanding. Therefore, parabolic approximations are very useful in cases where wave reflections are not important. Several parabolic models have been proposed. The mild slope equation used to derive the parabolic equation is of the form of Helmholtz equation (Li, 1997):

$$\nabla^2\psi + k_c^2\psi = 0 \tag{4.1}$$

Assuming that the water depth is constant, Equation (4.1) can be written as:

$$A_{xx} + 2ikA_x + A_{yy} = 0 \tag{4.2}$$

where A is the amplitude function, which is given by:

$$\psi = A\exp(i\,k\,x) \tag{4.3}$$

assuming that x is the predominant direction of wave propagation.

Radder (1979) assumed that the derivatives of the wave potential in the x-direction are very small, which leads to:

$$2ikA_x + A_{yy} = 0 \tag{4.4}$$

Equation (4.4) is considered the lowest-order parabolic approximation of the Helmholtz equation which corresponds to [1/0] Padé approximation or the lowest order binomial expansion.

A possible plane wave solution can be given by:

$$A = a\exp ik\left[(l-1)x + my\right] \tag{4.5}$$

where l = cos θ, m = sin θ, a is the wave amplitude and θ is the wave angle measured counterclockwise from x-direction. Substituting Equation (4.5) into Equation (4.2), the relationship between l and m can be established as follows:

$$l_h = \sqrt{1-m^2} \tag{4.6}$$

where l_h is the exact cosine the wave angle according to Helmholtz equation. Equation (4.6) represents a circle. However, substituting Equation (4.5) into Equation (4.4) leads to the following first order parabolic approximation:

$$l_a = 1-\frac{1}{2}m^2 \tag{4.7}$$

where, l_a is the approximated cosine of the wave angle. Equation (4.7) corresponds to the first order binomial expansion for the square root in Equation (4.6). Radder's simple parabolic model (Equation (4.7) or Equation (4.4)) can accurately predict the propagation of plane waves with angles up to 43° without creating more than 5% error in l, where the error in l is defined as $(l_h\text{-}l_a)/l_h \times 100$ (Li, 1997).

Other parabolic approximations are obtained by approximating the square root in Equation (4.6). Booij (1981) developed a higher order parabolic model, which permits

waves angles up to 56.5°. For constant water depth, this parabolic model can be written as:

$$2ikA_x + A_{yy} + iA_{xyy}/2k = 0 \tag{4.8}$$

Substituting Equation (4.5) into Equation (4.8), it can be found that Booij's model is based on [1/1] Padé approximation of l.

Kirby (1986a) provided a [2/2] Padé approximation of l which leads to the following parabolic equation:

$$2ikA_x + A_{yy} - 3A_{xyy}/2ik - A_{xyyyy}/8ik^3 + A_{yyyy}/2k^2 = 0 \tag{4.9}$$

which is accurate up to 68°.

Kirby (1986a) utilized a minimax approach to approximate the square root in Equation (4.6). For constant water depth, his parabolic model reads:

$$2ikA_x + 2(b_1 - a_1)A_{yy} - 2ib_1A_{xyy}/k + 2k(a_0 - 1)A = 0 \tag{4.10}$$

where the values a_0, a_1, and b_1 are found by requiring that the error in l be minimized over a given range of wave angles. The approximated l can be found as follows:

$$l_a = \frac{a_0 + a_1m^2}{1 + b_1m^2} \tag{4.11}$$

The results of this equation at large wave angles are approximately as accurate as Equation (4.9).

Parabolic models based on the transformation given by Equation (4.5) have the following stability criteria (Dingemans, 1997):

$$\Delta x \le L/3 \qquad \text{and} \qquad \Delta y \le L/10 \tag{4.12}$$

where L is the local wave length.

Dalrymple and Kirby (1988) developed a wide-angle model based on the Fourier transform method for a bathymetry consisting of parallel contours. Their analysis shows that the wave field can be decomposed into an angular spectrum; that is the superposition of many synchronous wave trains propagating at different angles to the x-axis varying from 0° to ±90°. Dalrymple et al. (1989) extended this model to the irregular bathymetry situation. Although there is no longer an angle limitation for this model, the formulas are quite complicated, and the CPU time required is more than that for other parabolic models (Li, 1997).

Li (1997) developed a nonlinear parabolic approximation for the Helmholtz equation. His model does not have angle limitation for forward wave propagation. However, Kirby's (1986a) model gives better results for small angles. In addition, Li's (1997) model cannot be applied to angles greater than 70° because of the upwinding scheme used to ensure the stability of the numerical scheme.

In the following section a new parabolic model is developed based on the generalized Padé approximation, which was developed in the previous chapter. The new model is tested for complex bathymetry using the experiment reported by Berkhoff (1982). The case of circular shoal over flat bottom reported by Kirby (1986a) is chosen to test the new model for large wave angles. The new parabolic model results are compared with Li's (1997) model and Kirby's (1986a) model, which are considered the best parabolic models before the development of the current model.

4.1.2. Generalized Padé approximation-based parabolic model

4.1.2.1. Theory

Kirby (1986a) developed a parabolic model for weakly nonlinear waves on slowly varying depth based on the approximation given by Equation (4.11). The values of the coefficients a_0, a_1, and b_1 are evaluated by the minimax approach which minimizes the maximum error in l over a given range of wave angles. He solved for the forward-scattered waves only, which has a possible plane wave solution on the form:

$$\psi^+ = A\exp\left(i\int\bar{k}(x)\,dx\right) \tag{4.13}$$

where $\bar{k}(x)$ is some average of $k(x,y)$ over the y-direction and where the wave phase is assumed to accumulate principally in the x-direction.

The approach proposed by Kirby and Dalrymple (1986) to account for nonlinear effects for shallow water depths is used. As mentioned in the previous chapter, the modified dispersion equation is given by:

$$\omega^2 = gk[1+(ka)^2 F_1 \tanh^5(kh)]\tanh[kh+(ka)F_2] \tag{4.14}$$

Incorporating Equation (4.14) into the parabolic model based on Equation (4.11) leads to:

$$\begin{aligned} &c_g A_x + i(\bar{k}-a_0 k)c_g A + \tfrac{1}{2}(c_g)_x A + \frac{i}{\omega}(a_1 - b_1\frac{\bar{k}}{k})(cc_g A_y)_y \\ &-\frac{b_1}{\omega k}(cc_g A_y)_{yx} + \frac{b_1}{\omega}\left(\frac{k_x}{k^2}+\frac{(c_g)_x}{2kc_g}\right)(cc_g A_y)_y + \\ &\frac{i\omega}{2}\left[\left(1+DF_1(ka)^2\right)\frac{\tanh(kh+F_2 ka)}{\tanh(kh)}-1\right]A+\frac{W}{2}A=0 \end{aligned} \tag{4.15}$$

where the subscripts represent derivatives and W is the dissipation function, which is defined in the previous chapter.

A set of generalized Padé approximations for the square root in Equation (4.6) centered at a certain wave angle $\theta = \theta_b$ has been developed in the last chapter. The error in calculating l with this method is effectively zero at $\theta = \theta_b$. The model based on the generalized [1/1] Padé approximation has the same form as Equation (4.15). However, the coefficients a_0, a_1, and b_1 in Equation (4.11) can be given as functions of the wave angles as follows (Saied and Tsanis, 2004b):

$$a_0 = \frac{\cos\theta_b(4-\sin^2\theta_b)}{4-3\sin^2\theta_b}$$
$$a_1 = \frac{-3\cos\theta_b}{4-3\sin^2\theta_b} \qquad (4.16)$$
$$b_1 = \frac{-1}{4-3\sin^2\theta_b}$$

For $\theta_b = 55°$, the error in calculating l using Equation (4.16) does not exceed 5% for wave angles up to 70°. Therefore, a rational approximation based on Equations (4.11) and (4.16) with $\theta_b = 55°$ can be comparable to the [2/2] conventional Padé approximation or the minimax approximation, which are accurate for angles up to 68° based on the 5% error criteria. The main advantage of Equation (4.16) over the minimax approximation, however, is that it is more accurate whenever the wave angle θ is known or can be estimated approximately.

The angle θ_b is estimated from the previously-calculated upstream grid points as follows:

$$m = \mathrm{Im}\left(\frac{\partial A/\partial y}{k\,A}\right)$$
$$l = \left[\mathrm{Im}\left(\frac{\partial A/\partial x}{A}\right) + \bar{k}\right]/k \qquad (4.17)$$
$$\theta_b = \tan^{-1}(m/l)$$

4.1.2.2. Boundary conditions

One of the main advantages of the parabolic model is that it does not need either offshore or onshore boundary conditions due to the marching scheme implemented in the solution. At the offshore end of the numerical domain, the offshore wave conditions are set as the initial conditions. The lateral boundary conditions can either be an absorbing or generating boundary. A perfectly absorbing boundary condition is given by:

$$\frac{\partial A}{\partial y} = iAk\sin\theta \qquad (4.18)$$

where θ is the wave angle at the boundary measured counterclockwise from the x-axis. Similarly, the generating boundary condition is given by:

$$\frac{\partial A}{\partial y} = ik\sin\theta(2A_g - A) \qquad (4.19)$$

where, A_g is the generating wave potential at the boundary. Estimation of the wave angle θ at the boundary and the generating wave potential A_g is discussed in the following section.

4.1.2.3. Numerical discretization

A new parabolic model is developed based on Equations (4.15) and (4.16) in which a marching scheme is implemented based on Crank-Nicolson scheme (given by

Kirby, 1986a). The scheme is extended to include higher-order derivatives by writing the term $(cc_g A_y)_{yx}$ as:

$$\begin{aligned}\left(cc_g A_y\right)_{yx}\Big|_{\substack{x=(i+\frac{1}{2})\Delta x \\ y=j\Delta y}} &= [(cc_{g\,j+1}^{i+1} + cc_{g\,j}^{i+1})(A_{j+1}^{i+1} - A_j^{i+1}) \\ &- (cc_{g\,j}^{i+1} + cc_{g\,j-1}^{i+1})(A_j^{i+1} - A_{j-1}^{i+1})]/2\Delta y^2\Delta x \\ &- [(cc_{g\,j+1}^{i} + cc_{g\,j}^{i})(A_{j+1}^{i} - A_j^{i}) \\ &- (cc_{g\,j}^{i} + cc_{g\,j-1}^{i})(A_j^{i} - A_{j-1}^{i})]/2\Delta y^2\Delta x\end{aligned} \tag{4.20}$$

For the south boundary (i.e. $j = \frac{3}{2}$), Equation (4.18) is discretized as follows:

$$\frac{A_{(i,2)} - A_{(i,1)}}{\Delta y} = ik\sin\theta_b\left(\frac{A_{(i,2)} + A_{(i,1)}}{2}\right) \tag{4.21}$$

For the north boundary (i.e. $j = j_{\max} - \frac{1}{2}$), Equation (4.18) is discretized as follows:

$$\frac{A_{(i,j\max)} - A_{(i,j\max-1)}}{\Delta y} = ik\sin\theta_b\left(\frac{A_{(i,j\max)} + A_{(i,j\max-1)}}{2}\right) \tag{4.22}$$

where θ_b is the estimated wave angle at the boundary and k is the wave number at the mid-point between the two discrete points that appear in the equation, which is given by:

$$k = \frac{k_{(i,j)} + k_{(i,j+1)}}{2} \tag{4.23}$$

for the two discrete points *(i,j)* and *(i,j+1)*.

Similarly, the lateral generating boundary condition is given by Equation (4.19) is discretized according to:

$$\frac{A_{(i,2)} - A_{(i,1)}}{\Delta y} = ik\sin\theta_b\left(2A_{g(i)} - \frac{A_{(i,2)} + A_{(i,1)}}{2}\right) \tag{4.24}$$

for the south boundary and:

$$\frac{A_{(i,j\max)} - A_{(i,j\max-1)}}{\Delta y} = ik\sin\theta_b \left(A_{g(i)} - \frac{A_{(i,j\max)} + A_{(i,j\max-1)}}{2} \right) \tag{4.25}$$

for the north boundary.

At the islands or shorelines, where the water depth is negative, the wave height is zero. Therefore, the wave potential is set to zero:

$$A_{(i,j)} = 0.0 \qquad \text{for points of negative water depth} \tag{4.26}$$

The discretization of Equation (4.15) and its boundary conditions (Equations (4.18) and (4.19)) using the Crank-Nicolson implicit scheme results in a tridiagonal matrix formulation for each column *i*. The next section describes the solution procedure.

4.1.2.4. Solution method

Figure (4.1) shows a flow-chart for the parabolic model. Before the model starts the spatially marching scheme, it calculates the linear wave characteristics over the whole computational domain. The wave number $\bar{k}(x)$ is then calculated for each column by:

$$\bar{k}_{(i)} = \sum_{j=1}^{j_{\max}} k_{(i,j)} \cos\theta_0 / j_{\max} \tag{4.27}$$

Then the offshore wave conditions (wave height H_0 and angle θ_0) are imposed along the first two offshore columns (i.e. i =1 and 2) as an initial condition according to:

$$\begin{aligned} A_{(1,1)} &= H_0 / 2. \\ A_{(i,j+1)} &= A_{(i,j)} \exp[ik\Delta y \sin\theta_0] \\ A_{(i+1,j)} &= A_{(i,j)} \exp\left[i\Delta x \left(k\cos\theta_0 - \frac{\bar{k}_{(i+1)} + \bar{k}_{(i)}}{2} \right) \right] \end{aligned} \tag{4.28}$$

where the wave number k is the wave number at the mid-point between the two discrete points that appear in the equation.

The generating lateral boundary is identified according to the offshore wave angle θ_0 where the south boundary is considered a generating boundary if θ_0 is positive and vice versa. The values of A_g along the generating boundary are determined beforehand according to:

$$A_{g(1)} = \frac{A_{(1,j)} + A_{(1,j+1)}}{2}$$
$$A_{g(i)} = A_{g(i-1)} \exp\left[i\Delta x \left(k\cos\theta_0 - \frac{\bar{k}_{(i)} + \bar{k}_{(i-1)}}{2} \right) \right] \qquad (4.29)$$

where $j = 1$ if the south boundary is considered or $j = j_{max} - 1$ if the north boundary is considered.

After the initialization of the parameters through Equations (4.27), (4.28) and (4.29), the spatially marching scheme starts. Due to the nonlinearity of Equation (4.15), iterations are required. In this model iterations are done in two ways. The first is called the "internal iterations" which is done along each column before proceeding to the next as shown in Figure (4.1). The wave angles θ_b are calculated inside each internal loop for the first exterior loop only as shown in Figure (4.1). The angle θ_b is required at $(i-\frac{1}{2})\Delta x$, where i is the column at which the wave potential A is calculated. However, for the first internal iteration, the angle θ_b is calculated at $(i-\frac{3}{2})\Delta x$ because the wave potential at i would not be known. Generally, the wave angles for interior points (i.e. $j_{max} > j > 1$) are

calculated between two columns *i1* and *i2* and at the row *j* from Equation (4.17) as follows:

$$
\begin{aligned}
m_{i1} &= \mathrm{Im}\left[\frac{A_{(i1,j+1)} - A_{(i1,j)}}{A_{(i1,j+1)} + A_{(i1,j)}} + \frac{A_{(i1,j)} - A_{(i1,j-1)}}{A_{(i1,j)} + A_{(i1,j-1)}}\right]/(k\Delta y) \\
m_{i2} &= \mathrm{Im}\left[\frac{A_{(i2,j+1)} - A_{(i2,j)}}{A_{(i2,j+1)} + A_{(i2,j)}} + \frac{A_{(i2,j)} - A_{(i2,j-1)}}{A_{(i2,j)} + A_{(i2,j-1)}}\right]/(k\Delta y) \\
m &= (m_{i1} + m_{i2})/2 \\
l &= 2\,\mathrm{Im}\left[\frac{A_{(i2,j)} - A_{(i2-1,j)}}{A_{(i2,j)} + A_{(i2-1,j)}}\right]/(k\Delta x) + \frac{\bar{k}_{(i2)} + \bar{k}_{(i2-1)}}{2k} \\
\theta_b &= \tan^{-1}(m/l)
\end{aligned}
\tag{4.30}
$$

The internal angles θ_b are estimated from Equation (4.30) by substituting *i1* = *i2* = *i-1* for the first iteration and *i1* = *i-1* and *i2* = *i* otherwise.

The wave angle θ_b at the south and north boundaries are calculated at the column *i2* (i.e. at the column *i2* = *i-1* for the first internal iteration or at *i2* = *i* otherwise). For the south boundary (i.e. $j = \frac{3}{2}$ or $y = \Delta y/2$), the wave angle is estimated from the following equation after substituting $j = 1$:

$$
\begin{aligned}
m &= 2\,\mathrm{Im}\left[\frac{A_{(i2,j+1)} - A_{(i2,j)}}{A_{(i2,j+1)} + A_{(i2,j)}}\right]/(k\Delta y) \\
l_1 &= 2\,\mathrm{Im}\left[\frac{A_{(i2,j)} - A_{(i2-1,j)}}{A_{(i2,j)} + A_{(i2-1,j)}}\right]/(k\Delta x) \\
l_2 &= 2\,\mathrm{Im}\left[\frac{A_{(i2,j+1)} - A_{(i2-1,j+1)}}{A_{(i2,j+1)} + A_{(i2-1,j+1)}}\right]/(k\Delta x) \\
l &= (l_1 + l_2)/2 + \frac{\bar{k}_{(i2)} + \bar{k}_{(i2-1)}}{2k} \\
\theta_b &= \tan^{-1}(m/l)
\end{aligned}
\tag{4.31}
$$

For the north boundary (i.e. $j = j_{\max} - \frac{1}{2}$), the wave angle is estimated from the following equation after substituting $j = j_{max}$:

$$
\begin{aligned}
m &= 2\,\mathrm{Im}\left[\frac{A_{(i2,j)} - A_{(i2,j-1)}}{A_{(i2,j)} + A_{(i2,j-1)}}\right] / (k\Delta y) \\
l_1 &= 2\,\mathrm{Im}\left[\frac{A_{(i2,j)} - A_{(i2-1,j)}}{A_{(i2,j)} + A_{(i2-1,j)}}\right] / (k\Delta x) \\
l_2 &= 2\,\mathrm{Im}\left[\frac{A_{(i2,j-1)} - A_{(i2-1,j-1)}}{A_{(i2,j-1)} + A_{(i2-1,j-1)}}\right] / (k\Delta x) \\
l &= (l_1 + l_2)/2 + \frac{\bar{k}_{(i2)} + \bar{k}_{(i2-1)}}{2k} \\
\theta_b &= \tan^{-1}(m/l)
\end{aligned}
\tag{4.32}
$$

Based on the estimation of the wave angles and the given potential, the coefficients of the tridiagonal matrix for the i^{th} column is calculated. The matrix is then solved to obtain values of the wave potential along the i^{th} column. The calculated results are then filtered to remove the noise according to (Kirby, 1986b):

$$A_{(i,j)} = \alpha_f A_{(i,j)} + (1 - 2\alpha_f) A_{(i,j)} + \alpha_f A_{(i,j)} \tag{4.33}$$

where α_f is the filtration parameter = 0.1 ~ 0.3 (Kirby, 1986b).

The wave amplitudes *a(i,j)* are then calculated from:

$$a_{(i,j)} = \frac{\mathrm{Re}[A_{(i,j)}]}{\cos(S_{(i,j)})} \tag{4.34}$$

where *S(i,j)* is the wave phase angle, which is given by:

$$S_{(i,j)} = \tan^{-1} \frac{\mathrm{Im}[A_{(i,j)}]}{\mathrm{Re}[A_{(i,j)}]} \tag{4.35}$$

The wave phase function calculated from Equation (4.35) is corrected for quadrant using the signs of both the real and imaginary parts of the wave potential. The wave dissipation function W is calculated along the i^{th} column according to the most recent wave amplitudes. The accelerated iteration method (Beltrami et al., 2001) described in the previous chapter is used. Internal iterations continue along the i^{th} column, where the coefficients of the tridiagonal matrix, the dissipation function and the wave angles are updated at the end of each iteration as shown in Figure (4.1). After the internal iterations are done along the i^{th} column, the generating wave potential is updated for the next column (i.e. $i = i+1$) according to:

$$A_{g(i)} = \frac{A_{(i,j)} + A_{(i,j+1)}}{2}$$
$$A_{g(i+1)} = A_{g(i)} \exp\left[i\Delta x \left(k\cos\theta_b - \frac{\bar{k}_{(i)} + \bar{k}_{(i+1)}}{2} \right) \right] \tag{4.36}$$

where θ_b is the wave angle at the boundary calculated from Equation (4.31) or (4.32). The model then proceeds to the next column and continues until it reaches the last column ($i = i_{max}$).

The outer iterations deal with the whole computational domain. After the values of the wave potential A for the whole numerical domain are obtained, the wave angles for the internal points are calculated exactly at $(i-\frac{1}{2})\Delta x$ from Equation (4.30) with $i1 = i\text{-}1$ and $i2 = i$. At the boundaries, the wave angles are calculated at $i\Delta x$. For the south boundary, the following equation is used with $j = 1$:

$$m = 2\,\mathrm{Im}\left[\frac{A_{(i,j+1)} - A_{(i,j)}}{A_{(i,j+1)} + A_{(i,j)}} \right] / (k\Delta y) \tag{4.37}$$

$$l_1 = \mathrm{Im}\left[\frac{A_{(i,j)} - A_{(i-1,j)}}{A_{(i,j)} + A_{(i-1,j)}} + \frac{A_{(i,j+1)} - A_{(i-1,j+1)}}{A_{(i,j+1)} + A_{(i-1,j+1)}}\right] / (k\Delta x)$$

$$l_2 = \mathrm{Im}\left[\frac{A_{(i+1,j)} - A_{(i,j)}}{A_{(i+1,j)} + A_{(i,j)}} + \frac{A_{(i+1,j+1)} - A_{(i,j+1)}}{A_{(i+1,j+1)} + A_{(i,j+1)}}\right] / (k\Delta x)$$

$$l = (l_1 + l_2)/2 + \frac{\bar{k}_{(i)}}{k}$$

$$\theta_b = \tan^{-1}(m/l)$$

For the north boundary, the following equation is used with $j = j_{max}$:

$$m = 2\,\mathrm{Im}\left[\frac{A_{(i,j)} - A_{(i,j-1)}}{A_{(i,j)} + A_{(i,j-1)}}\right] / (k\Delta y)$$

$$l_1 = \mathrm{Im}\left[\frac{A_{(i,j)} - A_{(i-1,j)}}{A_{(i,j)} + A_{(i-1,j)}} + \frac{A_{(i,j-1)} - A_{(i-1,j-1)}}{A_{(i,j-1)} + A_{(i-1,j-1)}}\right] / (k\Delta x)$$

$$l_2 = \mathrm{Im}\left[\frac{A_{(i+1,j)} - A_{(i,j)}}{A_{(i+1,j)} + A_{(i,j)}} + \frac{A_{(i+1,j-1)} - A_{(i,j-1)}}{A_{(i+1,j-1)} + A_{(i,j-1)}}\right] / (k\Delta x) \qquad (4.38)$$

$$l = (l_1 + l_2)/2 + \frac{\bar{k}_{(i)}}{k}$$

$$\theta_b = \tan^{-1}(m/l)$$

At the end of each outer iteration, the generating wave potential A_g is calculated along the generating boundaries from:

$$A_{g(i)} = \frac{A_{(i,j)} + A_{(i,j+1)}}{2} \quad \text{for } i = 3 \text{ to } i_{max} \qquad (4.39)$$

where $j = 1$ for the south boundary or $j = j_{max} - 1$ for the north boundary.

The model allows the user to choose either method of iteration or both. If the linear solution is required, the number of both the inner and outer iterations is set to 1.

4.1.2.5. Numerical results and discussion

In order to test the new parabolic model for cases of complex bathymetry, the case reported by Berkhoff (1982) is considered. The experimental bathymetry consists of an elliptic shoal situating on a plane sloping beach of 1:50 slope. Figure (4.2) shows the bottom contours of the computational domain along with the labelled transects 1-8 for which experimental data are available. The incident wave height is 0.0464 m and the wave period is 1 s. For a computational domain of 25 m × 20 m, the grid size is $\Delta x = \Delta y =$ 0.25 m, which corresponds to 101 × 81 grid points. Five internal iterations for each column are required for convergence of Equation (4.15). Figure (4.3) shows the wave height pattern behind the elliptic shoal using the new parabolic model.

Comparison between the numerical results from the parabolic model and the experimental data along the eight transects are shown in Figure (4.4a-h). Considering the experimental data to be error-free, the root mean square error for the parabolic model results can be calculated using Equation (3.50). Table (4.1) shows the root mean square differences between the experimental data and the model results for the eight transects. Overall, it can be concluded that the model can simulate the wave pattern for complicated bathymetry very well.

Table (4.1): Root mean square error for the parabolic model results

Transect #	1	2	3	4	5	6	7	8
Parabolic Model	0.0712	0.0941	0.1133	0.0987	0.0997	0.0850	0.0781	0.0971

In order to test the capability of the new parabolic model for wide wave angles, the circular shoal problem used to test the nonlinear parabolic model, which was developed by Li (1997), is adopted. Owing to the axisymmetry of the circular shoal, the wave focusing pattern behind the shoal should be independent of the incident wave angle if the model is correct (Dalrymple et. al., 1989). The water depth used is the same adopted by Dalrymple et al. (1989), which is:

$$h = \begin{cases} h_0 & r > R \\ h_0 + \alpha - \beta\left[1 - (0.2X')^2 - (0.2Y')^2\right]^{1/2} & r < R \end{cases} \tag{4.40}$$

where $h_0 = 0.336$ m, $\alpha = 0.12$ and 0.18, $\beta = 0.2$ and 0.3, $R = 4$ m is the radius of the shoal, $r = (X'^2 + Y'^2)^{1/2}$ and (X', Y') = coordinates with the origin at the crest of the shoal. The wave period is 1 s. Six computational domains are used for the analysis based on the location of the circular shoal and the values of the parameters α and β as shown in Figure (4.5a-f). The circular shoal is located at (6 m, 10 m), (6 m, 6 m) and (6 m, 6 m) for the cases of incident wave angles of 0°, 45° and 70°, respectively.

Figure (4.6) shows the wave height patterns behind the circular shoal using the new parabolic model for different incident wave angles. In Figure (4.6a-c), the parameters α and β are chosen as 0.12 and 0.2, respectively. Figure (4.6b) and Figure (4.6c), which correspond to wave angles 45° and 70°, respectively are compared with Figure (4.6a), which corresponds to the case of normal wave incidence. It can be shown that the overall agreements between the two cases and the case of normal incidence are good. The wave heights along the wave focusing crest are correct without any angle distortion. The symmetry, however, is distorted for the case of $\theta_0 = 70°$.

In order to increase the shoal height, the values of 0.18 and 0.3 were assigned to the parameters α and β, respectively. For the case of θ_0 = 45° (Figure (4.6e)), the wave heights along the wave focusing crest are correct without any angle distortion. The case of θ_0 = 70° (Figure (4.6f)), however, reports significant change of the wave heights along the wave focusing crest from the case of normal incidence but still without angle distortion. The symmetry is distorted for both cases especially for the case of θ_0 = 70°.

In order to compare Kirby's (1986a) model with the present model for wide wave angles, the same cases described above are resolved using Kirby's (1986a) model. Figure (4.7) shows the results of Kirby's model. For θ_0 = 45°, the coefficients a_0, a_1 and b_1 in Equation (4.11) are set to 0.999465861, -0.822482968 and -0.335107575, respectively, which corresponds to range of applicability up to 50°. For θ_0 = 70°, the range of applicability has to be increased to 80°, which corresponds to values of 0.985273164, -0.925464479 and -0.550974375 for the coefficients a_0, a_1 and b_1 respectively. Figure (4.7) shows very similar results to the present model in cases of θ_0 = 45° (Figure (4.7a and c)). For the case of wide wave angle (θ_0 = 70°), significant shift towards the downstream of the wave pattern behind the shoal is evident in Figure (4.7b and d)).

Figure (4.8a-b) shows the longitudinal sections along the wave focusing crests for the current model and Kirby's (1986a) model. It can be shown that both models perform well for the two cases of θ_0 = 45°. However, the present model is better as Kirby's (1986a) model underestimates the wave heights behind the shoal crest.

For the cases of θ_0 = 70°, Kirby's (1986a) model significantly underestimates the wave heights behind the shoal due to the shift in the wave pattern, which confirms that

the present model performs better for wide angles as well. In addition, the new model is much more user friendly than Kirby's (1986a) model because the coefficients a_0, a_1 and b_1 are calculated internally through Equation (4.16) unlike Kirby's (1986a) model where the user has to specify a certain range of applicability for wave angles.

The results of Li's (1997) model for the same cases were inspected as well. Due to the upwind scheme used in his model, Li (1997) reported that Kirby's (1986a) model is better for small wave angles, which implicitly implies that the present model is better as well because it is better than Kirby's (1986a) model. For the case of $\theta_0 = 70°$ and small bottom variations (i.e. $\alpha = 0.12$ and $\beta = 0.2$), Li (1997) reported slight shift of the wave pattern behind the shoal crest. Being less than the shift reported by Kirby's (1986a) model, Li concluded that his model is better than Kirby's (1986a) model for this case. The present model, however, is better than both models for this case as shown in Figure (4.6c) and Figure (4.8a). For the large bottom variation case (i.e. $\alpha = 0.18$ and $\beta = 0.3$) with $\theta_0 = 70°$, after inspecting Li's (1997) model results, it can be shown that in addition to the shift of the wave pattern towards the downstream, the wave pattern immediately behind the shoal crest is shifted in the x-direction (the direction at which the line by line solution is performed). This may be explained by the upwind scheme implemented in this model. However, Li's (1997) model results for this particular case are smoother and its symmetry is less distorted than the results of the present model.

Based on the preceding discussion, Table (4.2) illustrates the favourable parabolic model for respective wave angle and bottom variation combinations. Overall, the proposed model is considered the best model.

Table (4.2): Favourable parabolic model for respective wave angle and bottom variation combinations.

	Small wave angles (≤ 45°)	Large wave angles (> 45°)
Small bottom variations	Present model	Present model
Large bottom variations	Present model	Li's (1997) model

4.2. Parabolic/Elliptic Integrated Wave Model

Although the parabolic model developed in the last section is fast and stable, it cannot model wave reflection in front of coastal structures. In this section, an integrated wave transformation model is developed which employs an iterative elliptic model using the parabolic model's solution as an initial solution. This method is proven to significantly reduce the total number of iterations required by the elliptic model, and accordingly the computation time. In cases where nonlinear effects are important, the elliptic model can be applied only once after the nonlinear parabolic solution is obtained.

4.2.1. Application of the integrated model

The integrated model is first applied to the elliptic shoal case in order to determine the improvement in the total number of iterations required by the elliptic model. The same grid described in section 4.1.2.5 is used for the parabolic model. For the elliptic model, a finer grid is used to ensure that the grid size does not exceed one tenth of the local wave length. Therefore, a fine grid of $\Delta x = \Delta y = 0.25/3 = 0.083$ m is constructed by the integrated model using linear interpolation. The elliptic model needs a single iteration to yield the nonlinear solution with 1200 internal iterations to reduce the error E to the order of 10^{-7}. As shown in the previous chapter, it takes the elliptic model a total of 6600 iterations to reach convergence for the nonlinear case, of which 2300

iterations for the first sweep (linear solution). This indicates about 80% saving in the total number of iterations and consequently huge saving in the simulation time since the time required by the parabolic model is relatively ignored.

Comparison between the numerical results of the parabolic and the integrated models with the experimental data along the eight transect of Figure (4.2) are shown in Figure (4.10a-h). The root mean square differences between the integrated model results and the experimental data for the eight transects are shown in Table (4.3). Overall, the agreement between the experimental data and the integrated model results is very good. Comparison between the parabolic model and the integrated model results show that the integrated model is slightly better because it yields smaller root mean square error for most sections. However, the parabolic model can be used efficiently in cases of complex bathymetry where wave reflection is insignificant. Generally, it can be concluded that both the integrated and the parabolic models can simulate the wave pattern behind complicated bathymetry like the elliptic shoal case.

Table (4.3): Root mean square error for the integrated model results

Transect #	1	2	3	4	5	6	7	8
Integrated Model	0.0645	0.0826	0.1097	0.0915	0.0867	0.0994	0.1261	0.0822

In order to test the significance of the initial condition for cases of large wave angles and large bottom variation, the case of the circular shoal given by Equation (4.40) is adopted. The parameters α, β and R were assigned values of 0.18, 0.3, and 4.0 respectively, in order to develop a circular shoal with large bottom variation. The wave

focusing behind the shoal is expected to be intensified as shown in Figure (4.6d-f). The incident wave angle is set as large as 70°. Only the linear solution is sought in this case for the sake of comparison. The parabolic solution is shown in Figure (4.6f). The integrated model constructs a fine grid of $\Delta x = \Delta y = 0.05$ m before the elliptic solver begins in order to satisfy the stability criteria. It requires 3400 iterations for the elliptic solver to get the residual error E within the order of 10^{-7} as shown in Figure (4.11). In order to test the significance of the initial condition for the elliptic solver, the number of outer iterations for the parabolic model is set to zero, so that the elliptic solver starts with initial solution according to the offshore wave characteristics. Using the same grid, the elliptic solver requires 14,300 iterations to get the residual error E within the same order (10^{-7}). This suggests that in this case the integrated model application improves the convergence by about 76% apart from the quality of the solution. Figure (4.12) compares between the wave height patterns for the two cases of initial solution. It can be shown from Figure (4.12b) that in addition to the slow convergence for the case of the conventional initial solution, the wave focusing behind the circular shoal does not seem to form, which suggest the need for additional iteration by reducing the accuracy one order of magnitude (i.e. 10^{-8}). On the other hand, if the parabolic solution is used, the wave focusing behind the shoal does not have to be formed rather than being corrected. Therefore, it needs less number of iterations to reduce the residual error to a certain accuracy. In addition, the choice of the accuracy can be done more freely by the user as realistic wave patterns are expected regardless of the chosen accuracy, as shown in Figure

(4.12a). The sensitivity of the solution to the chosen accuracy will be discussed in more details in chapter 6.

4.3. Summary

A new parabolic water wave transformation model has been developed in this chapter. The model is based on the generalized [1/1] Padé approximation which was developed in the previous chapter. The model is proven to be better than all the existing parabolic models. The model can simulate wave patterns for complicated bathymetry. In addition, the numerical test case of the circular shoal confirms that the new parabolic model can simulate the wave pattern behind the shoal for very large angles up to 70°. The new model is fast, stable and user friendly. However, due to the marching scheme implemented, it cannot model wave reflection, where the full elliptic model has to be used. In this chapter, a practical technique was developed to reduce the computation time of the iterative elliptic solver. An integrated parabolic/elliptic water wave transformation model has been developed. The parabolic model results are used as an initial solution for the elliptic iterative solver, which reduces the total number of iterations required, especially, in cases where nonlinear effects are considered. In addition, this technique allows the user to choose the accuracy of the elliptic solver more freely because the elliptic solver basically modifies the parabolic solution rather than establishing the wave pattern from scratch.

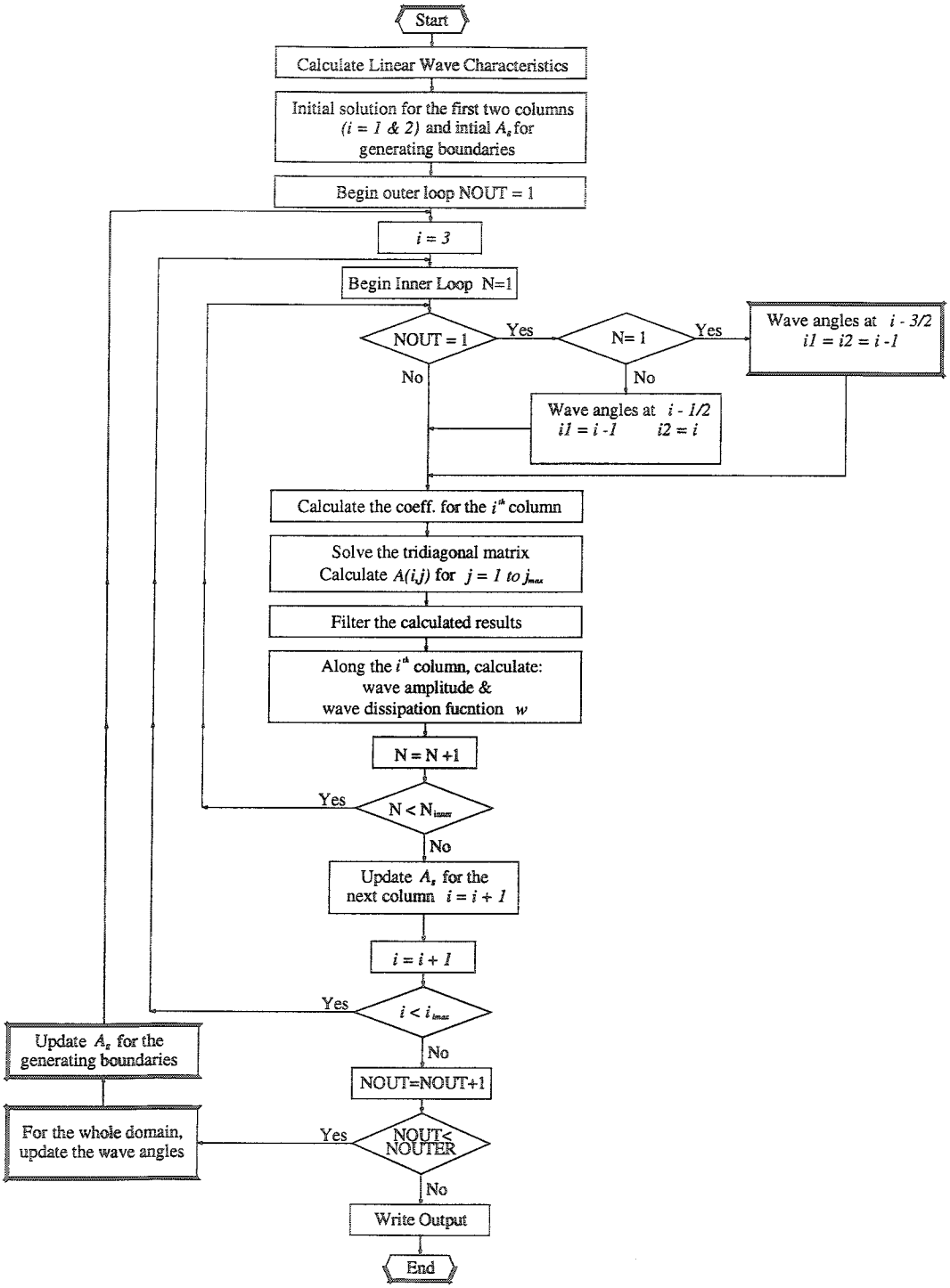

Figure (4.1): Flow-chart of the parabolic model

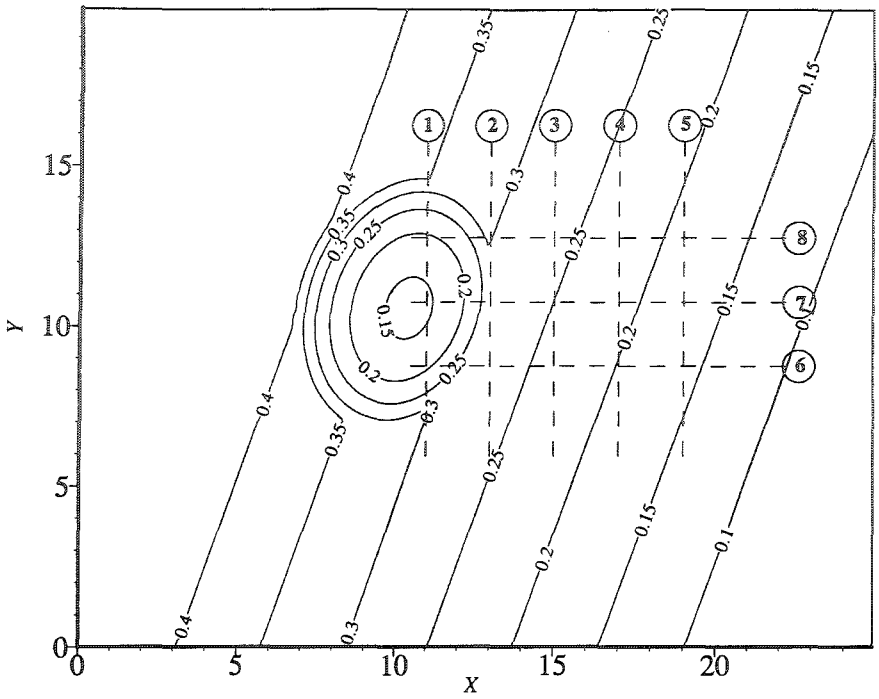

Figure (4.2): Elliptic shoal bathymetry

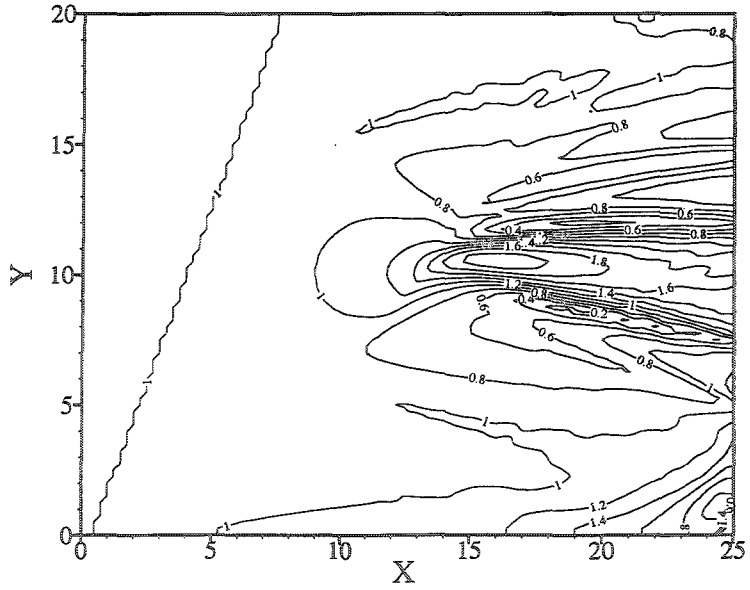

Figure (4.3): Wave height pattern behind the elliptic shoal (new parabolic model)

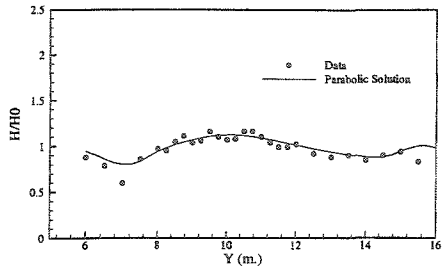

a) Transect 1

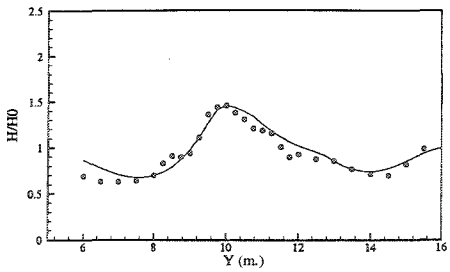

b) Transect 2

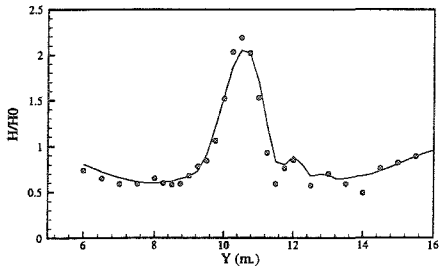

c) Transect 3

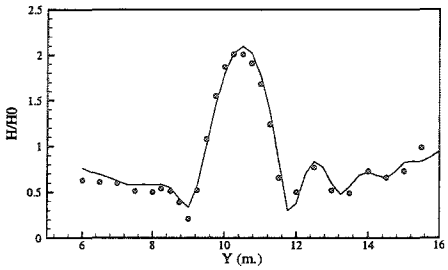

d) Transect 4

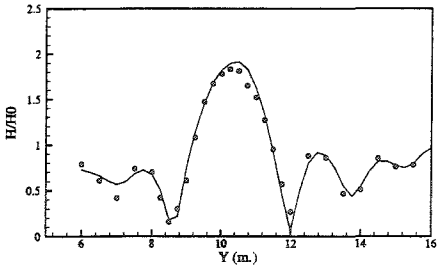

e) Transect 5

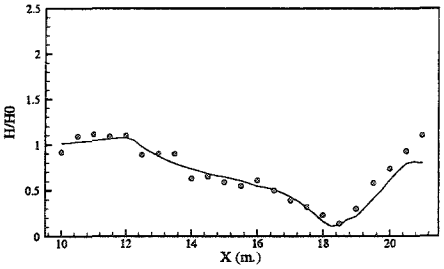

f) Transect 6

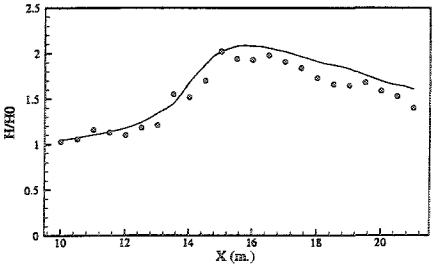

g) Transect 7

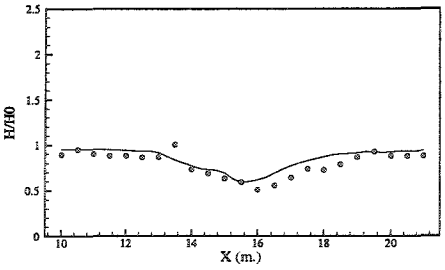

h) Transect 8

Figure (4.4): Comparison between experimental and computational results for the elliptic shoal case

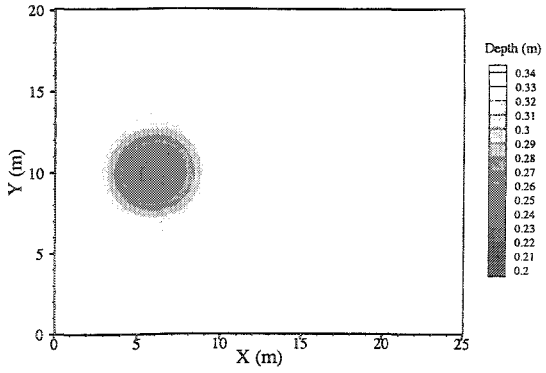

a) $\alpha = 0.12$, $\beta = 0.2$ and $\theta_0 = 0°$

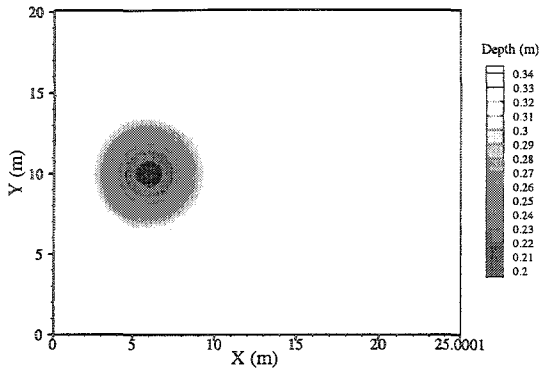

b) $\alpha = 0.18$, $\beta = 0.3$ and $\theta_0 = 0°$

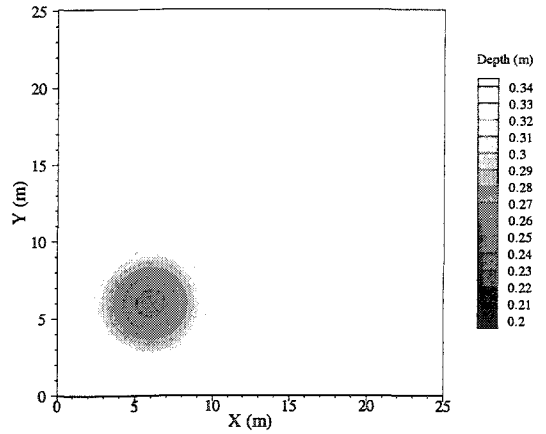

c) $\alpha = 0.12$, $\beta = 0.2$ and $\theta_0 = 45°$

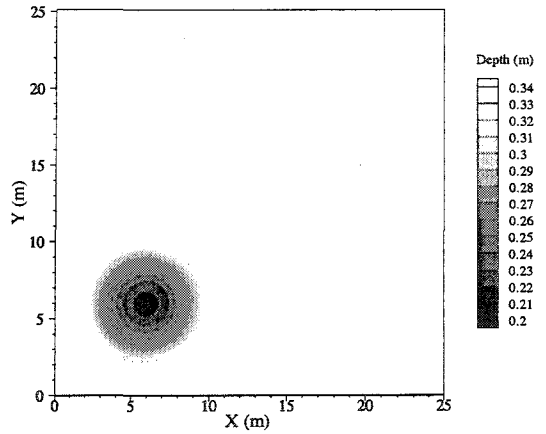

d) $\alpha = 0.18$, $\beta = 0.3$ and $\theta_0 = 45°$

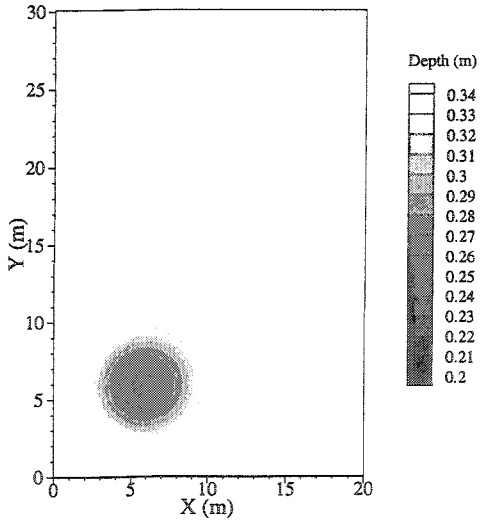

e) $\alpha = 0.12$, $\beta = 0.2$ and $\theta_0 = 70°$

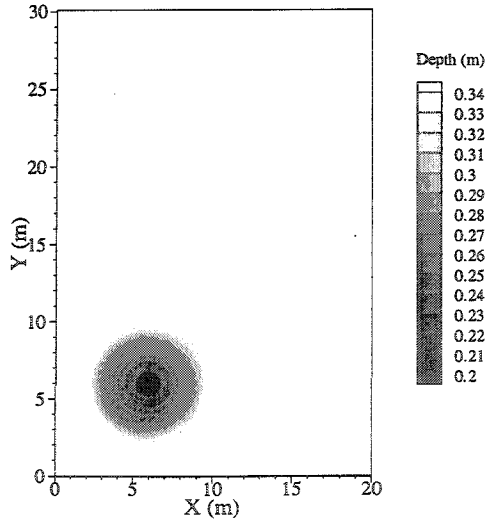

f) $\alpha = 0.18$, $\beta = 0.3$ and $\theta_0 = 70°$

Figure (4.5): Computational domains for the circular shoal case

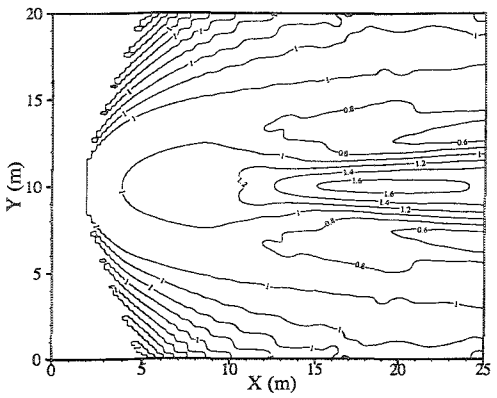

a) $\alpha = 0.12$, $\beta = 0.2$ and $\theta_0 = 0°$

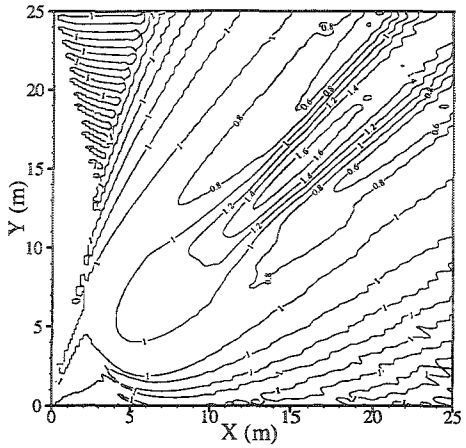

b) $\alpha = 0.12$, $\beta = 0.2$ and $\theta_0 = 45°$

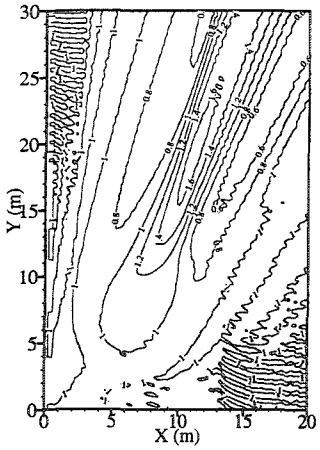

c) $\alpha = 0.12$, $\beta = 0.2$ and $\theta_0 = 70°$

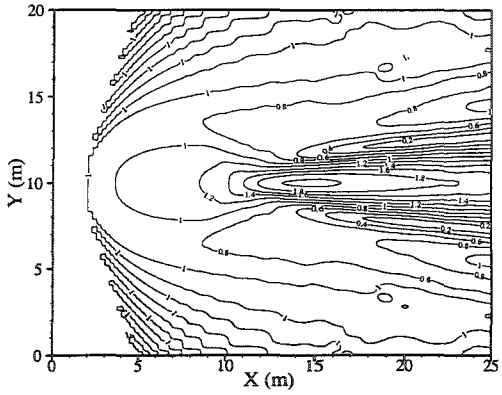

d) $\alpha = 0.18$, $\beta = 0.3$ and $\theta_0 = 0°$

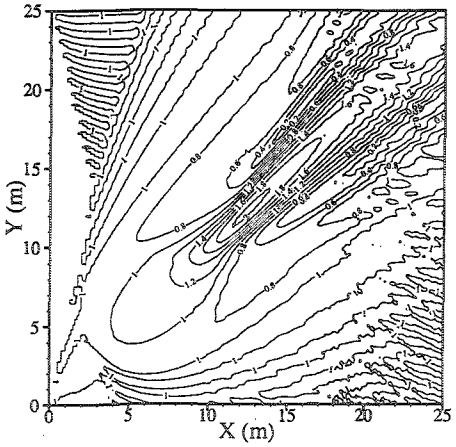

e) $\alpha = 0.18$, $\beta = 0.3$ and $\theta_0 = 45°$

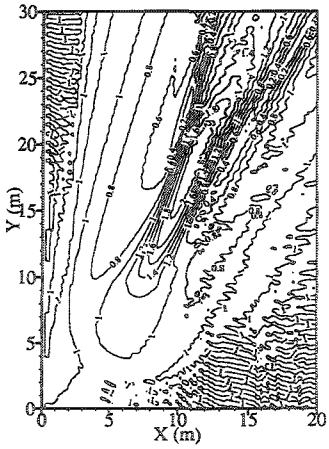

f) $\alpha = 0.18$, $\beta = 0.3$ and $\theta_0 = 70°$

Figure (4.6): Wave height patterns behind the circular shoal using the new parabolic model

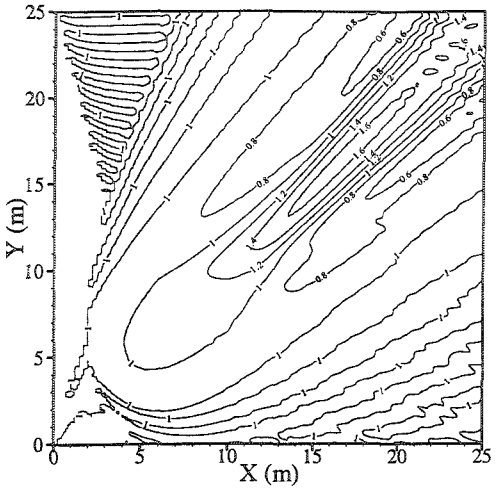

a) $\alpha = 0.12$, $\beta = 0.2$ and $\theta_0 = 45°$

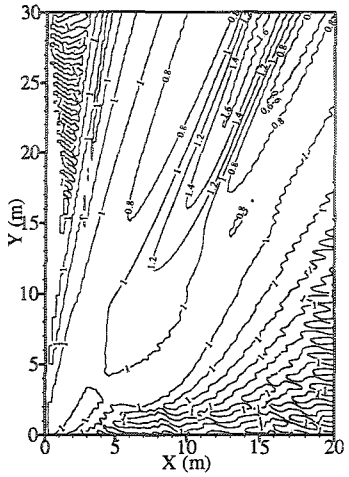

b) $\alpha = 0.12$, $\beta = 0.2$ and $\theta_0 = 70°$

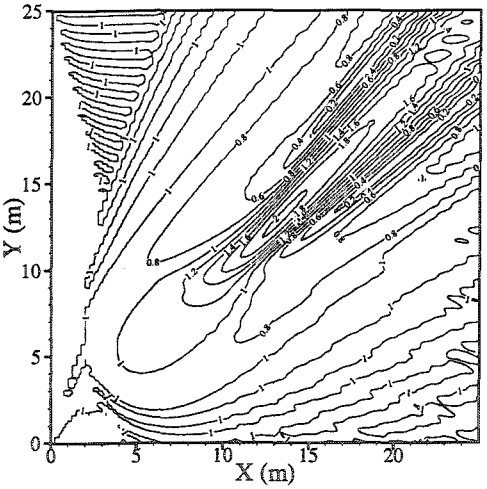

c) $\alpha = 0.18$, $\beta = 0.3$ and $\theta_0 = 45°$

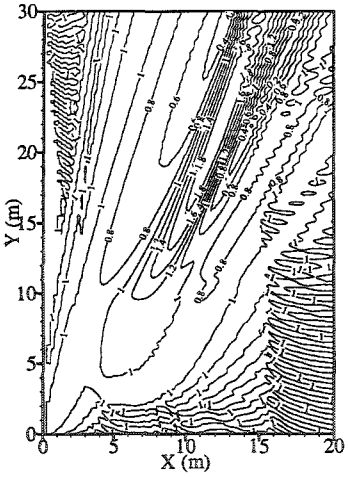

d) $\alpha = 0.18$, $\beta = 0.3$ and $\theta_0 = 70°$

Figure (4.7): Wave height patterns behind the circular shoal using Kirby's (1986a) model with angle ranges 50° (for a and c) and 80° (for b and d)

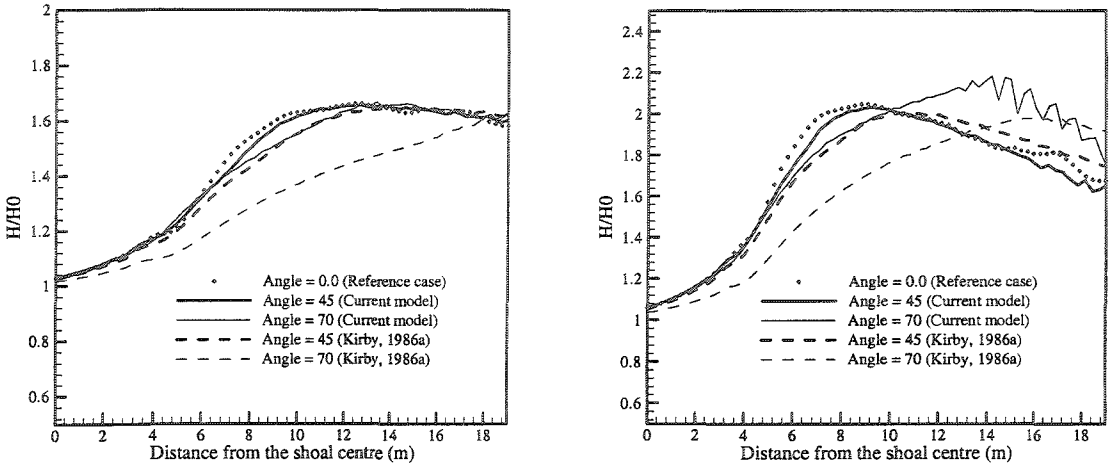

a) $\alpha = 0.12$ and $\beta = 0.2$ b) $\alpha = 0.18$ and $\beta = 0.3$

Figure (4.8): Longitudinal sections along the centre of the shoal (in the direction of wave propagation)

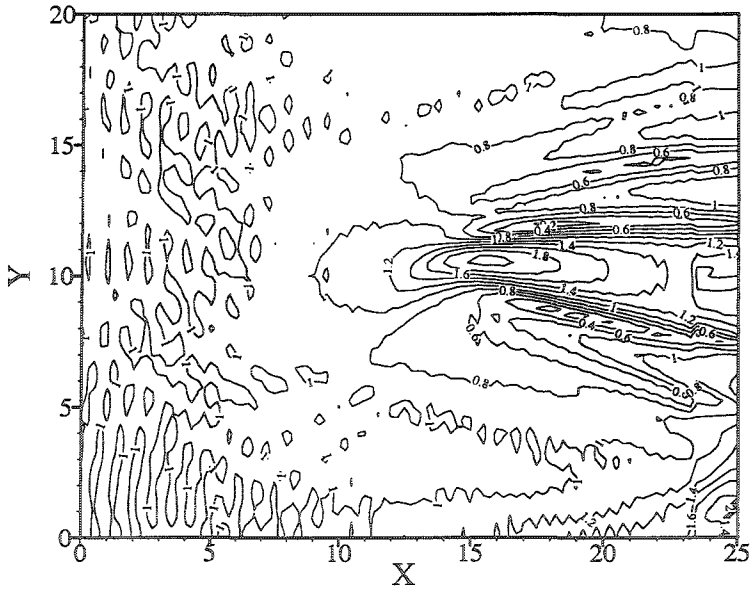

Figure (4.9): Wave height pattern behind the elliptic shoal (using the integrated model)

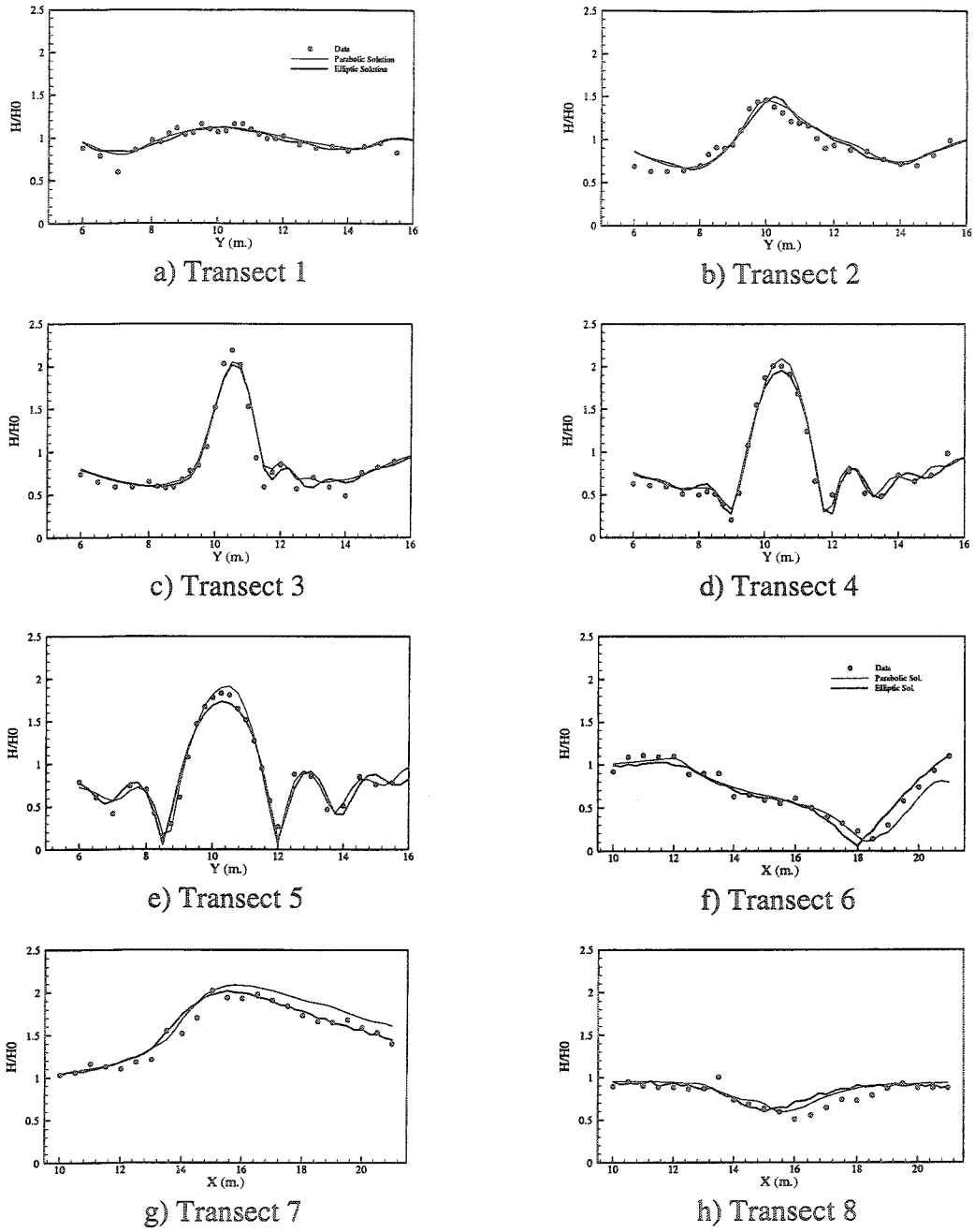

a) Transect 1

b) Transect 2

c) Transect 3

d) Transect 4

e) Transect 5

f) Transect 6

g) Transect 7

h) Transect 8

Figure (4.10): Comparison between experimental and computational results for the elliptic shoal case (parabolic and integrated models)

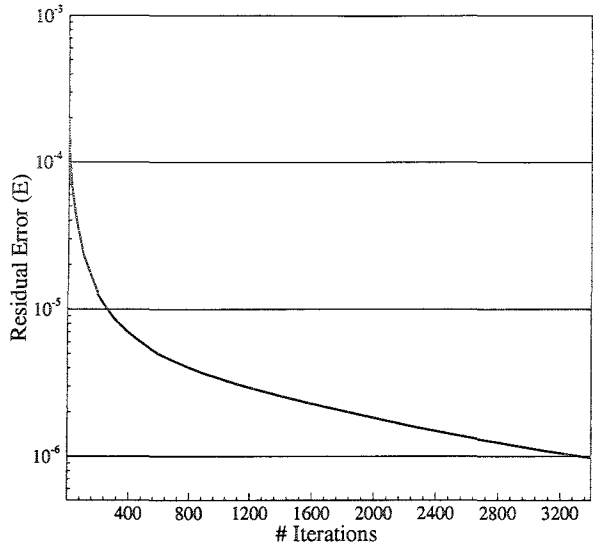

Figure (4.11): Convergence of the elliptic solver inside the integrated model for the case of circular shoal ($\alpha = 0.18$, $\beta = 0.3$ and $\theta_0 = 70°$)

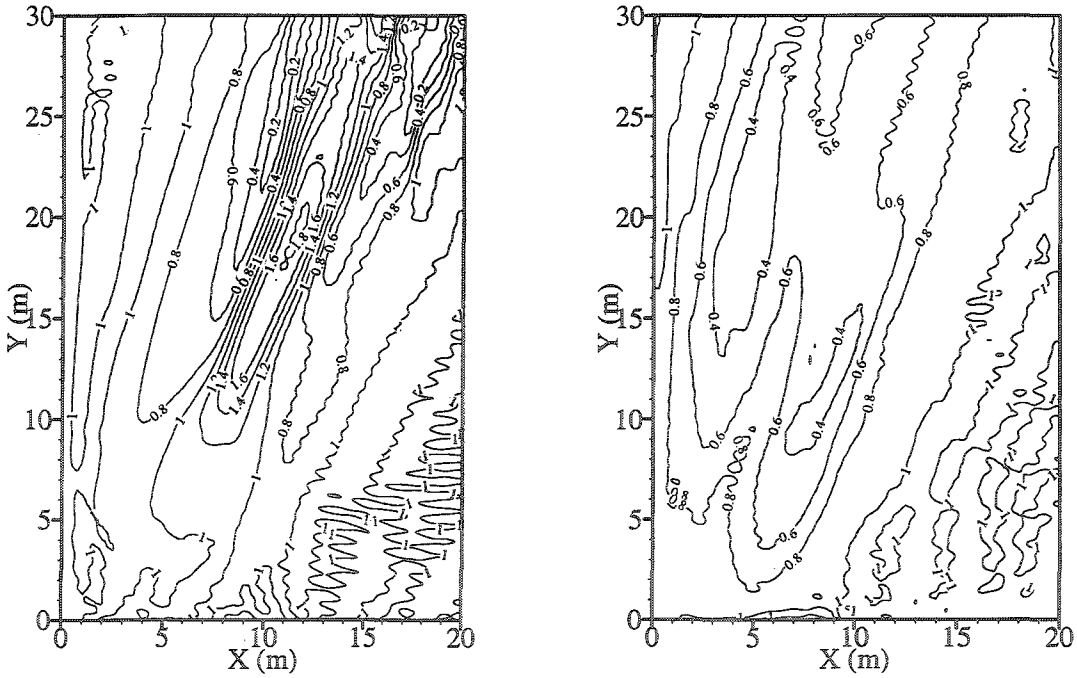

a) with parabolic initial solution
number of iterations = 3400

b) without parabolic initial solution
number of iterations = 14300

Figure (4.12): Comparison between the elliptic solutions for the for the case of circular shoal ($\alpha = 0.18$, $\beta = 0.3$ and $\theta_0 = 70°$)

Chapter 5: Hydrodynamic and Sediment Transport Models Development

Three-dimensional models in coastal areas are not quite practical, because in these areas it is required to solve a relatively large domain for the wave-driven currents on a relatively fine mesh and over a long period of time. In addition, the vertical current structure is very complicated in the surf-zone and needs a very fine vertical mesh to reach reasonable results. Abbott et al. (1985) collected the experimental evidence which suggests that the circulations generated in numerical models of free-surface flows that are two-dimensional in plan may be realistic physically. In addition, Jamart and Ozer (1987) concluded that the two-dimensional models can yield results identical to those of the three-dimensional models. In this chapter a two-dimensional depth-integrated hydrodynamic model is developed and applied for coastal areas.

A two-dimensional sediment transport rate model is developed based on the wave and current information over the computational domain. The model calculates for each discrete point in the domain the bottom shear stress, which is considered the main driving force of sediment motion. Based on the sediment transport rates, the morphological changes can be calculated using the sediment budget equation.

The next sections describe the development and application of the hydrodynamic, the sediment transport rate and the morphology models.

5.1. Hydrodynamic Model Development

5.1.1. Model equations

The hydrodynamic model proposed in this study is intended to predict the wave-driven currents. In coastal areas, the hydrodynamic circulation reaches the steady state in relatively small time compared to the duration of a particular storm. Therefore, the steady state solution is more important than the transient solution. The choice of a transient model rather than a steady state model in this study was based on two reasons. The first is that the transient term can be viewed as a residual error term, which vanishes at the steady state. The second reason is to confirm that the model reaches the steady state in relatively short period of time for coastal domains.

The governing equations are the depth averaged Navier-Stokes equations, which read:

$$\frac{\partial \eta}{\partial t} + \frac{\partial (h+\eta)u}{\partial x} + \frac{\partial (h+\eta)v}{\partial y} = 0 \tag{5.1}$$

$$\frac{\partial u}{\partial t} + u\frac{\partial u}{\partial x} + v\frac{\partial u}{\partial y} = -g\frac{\partial \eta}{\partial x} + \varepsilon\left(\frac{\partial^2 u}{\partial x^2} + \frac{\partial^2 u}{\partial y^2}\right) + C_x u + B_x \tag{5.2}$$

$$\frac{\partial v}{\partial t} + u\frac{\partial v}{\partial x} + v\frac{\partial v}{\partial y} = -g\frac{\partial \eta}{\partial y} + \varepsilon\left(\frac{\partial^2 v}{\partial x^2} + \frac{\partial^2 v}{\partial y^2}\right) + C_y u + B_y \tag{5.3}$$

where η is the water surface elevation, h is the water depth, u and v are the depth averaged velocity components, ε is the eddy viscosity, C_x and B_x define a linear source term for the x-momentum equation, and C_y and B_y define a linear source term for the y-momentum equation. The source term can include the radiation stresses, Coriolis forces,

bed friction, etc. The eddy viscosity ε is given by Horikawa (1988) after Longuet-Higgins (1970) as follows:

$$\varepsilon = N l_{SL} \sqrt{g(h+\eta)} \tag{5.4}$$

where, N is a constant whose value is deduced to be smaller than 0.016 and l_{SL} is the distance measured from the shoreline to the point of interest. Other form for the eddy viscosity term is given by Leont' yev (1999) based on available surfzone mixing data (Bowen and Inman, 1974) as follows:

$$\varepsilon = 0.006\left(\frac{gH_{0rms}T}{\nu}\right)^{1/4} H_{0rms}\sqrt{gH_{0rms}} \tag{5.5}$$

where, H_{0rms} is the offshore root mean squared wave height and $\nu = 10^{-6}$ m^2/s is the kinematic viscosity of water. The longshore current profiles modeled with this relationship are in satisfactory agreement with the observed ones both in laboratory (Badiei and Kamphuis, 1995) and in the sea during a storm (Kuriyama, 1994).

The bed friction term can be given by Leont' yev (1999) after, Le Blond and Tang (1974) as follows:

$$\tau_{bx} = \frac{2}{\pi} C_f \rho u_{bm}\left[(1+\cos^2\theta)u + v\sin\theta\cos\theta\right] \tag{5.6}$$

$$\tau_{by} = \frac{2}{\pi} C_f \rho u_{bm}\left[(1+\sin^2\theta)v + u\sin\theta\cos\theta\right] \tag{5.7}$$

where, τ_{bx} and τ_{by} are the bed shear stresses in the x and y directions, respectively, C_f is dimensionless bed friction coefficient, which is usually of the order of 0.01, θ is the wave angle, and u_{bm} is the maximum bottom orbital velocity, which can be obtained from the linear wave theory as follows:

$$u_{bm} = \frac{\omega H}{2\sinh(kh)} \tag{5.8}$$

where k is the wave number and ω is the wave angular frequency.

Equations (5.6) and (5.7) contribute to the source terms in Equations (5.2) and (5.3) as follows:

$$\begin{aligned} C_x &= [\frac{-2}{\pi} C_f u_{bm} / h_w](1+\cos^2\theta) \\ B_x &= [\frac{-2}{\pi} C_f u_{bm} / h_w]v^* \sin\theta\cos\theta \\ C_y &= [\frac{-2}{\pi} C_f u_{bm} / h_s](1+\sin^2\theta) \\ B_x &= [\frac{-2}{\pi} C_f u_{bm} / h_s]u^* \sin\theta\cos\theta \end{aligned} \tag{5.9}$$

where, h_w and h_s are the water depths at the points where the x- and y- components of the velocity are calculated, respectively, and u^* and v^* are the x- and y- components of the velocity at the points where the y- and x- velocity components are calculated, respectively.

The forcing due to waves can be obtained from (Leont'yev, 1999):

$$\begin{aligned} F_x &= \frac{\partial}{\partial x}(S_{xx} + R_{xx}) + \frac{\partial}{\partial y}(S_{xy} + R_{xy}) \\ F_y &= \frac{\partial}{\partial y}(S_{yy} + R_{yy}) + \frac{\partial}{\partial x}(S_{yx} + R_{yx}) \end{aligned} \tag{5.10}$$

where, S_{ij} is the radiation stress tensor, and R_{ij} are the stresses due to rollers in breaking waves (Dally and Osiecki, 1994). The radiation stresses are given by:

$$S_{xx} = \frac{E}{2}[2n(1+\cos^2\theta)-1] - \frac{\rho M_{Wx}^2}{h}$$
$$S_{yy} = \frac{E}{2}[2n(1+\sin^2\theta)-1] - \frac{\rho M_{Wy}^2}{h} \qquad (5.11)$$
$$S_{xy} = S_{yx} = \frac{E}{2} n \sin 2\theta - \frac{\rho M_{Wx} M_{Wy}}{h}$$

where $E = \rho g H^2/8$ is the wave energy per unit area, $n = c_g/c$ is the wave index, and M_{Wx} and M_{Wy} are water discharges which represent the onshore mass flux caused by waves (Stokes drift) and rollers:

$$(M_{Wx}, M_{Wy}) = (E + E_r)(\cos\theta, \sin\theta)/(\rho c) \qquad (5.12)$$

where, E_r is the roller energy per unit area:

$$E_r = 4\beta_r \frac{c}{gT}\left(\frac{H}{\gamma_s h}\right)E \qquad (5.13)$$

where, $\beta_r \approx 0.9$, c is the wave celerity and γ_s is the breaking constant in shallow water.

The stresses due to rollers are given by:

$$R_{xx} = 2E_r \cos^2\theta$$
$$R_{yy} = 2E_r \sin^2\theta \qquad (5.14)$$
$$R_{xy} = R_{yx} = E_r \sin 2\theta$$

The forcing due to the waves given by Equation (5.10) and the Coriolis forces contributes to the source term in Equations (5.2) and (5.3) as follows:

$$B_x = \frac{-1}{h_w \rho} F_x + C_r v^*$$
$$B_y = \frac{-1}{h_s \rho} F_y - C_r u^* \qquad (5.15)$$

where $C_r = 2\pi\sin\phi/(24\times3600)$ is the Coriolis parameter, ϕ is the mean geographic latitude at the area and the x and y-axis directions are from North to South and from West to East, respectively.

5.1.2. Boundary conditions

A no-flow boundary condition is imposed on the boundaries along islands, shorelines and breakwaters. At the lateral open boundaries, uniform flow is assumed:

$$\frac{\partial u}{\partial y} = 0.0 \ , \ \frac{\partial v}{\partial y} = 0.0 \tag{5.16}$$

In order for Equation (5.16) to be correct, the domain has to be extended laterally so that uniform conditions are satisfied. At the offshore boundary, a no-flow boundary condition is applied.

5.1.3. Numerical scheme

The coastal domains considered in this analysis are usually relatively large domains. This makes the direct solution of Equations (5.1)-(5.3) cumbersome due to the large system matrix. Therefore, the ADI (Alternating Directional Implicit) scheme was chosen to discretize the governing equations. The discretization was done so that the boundary conditions can be implemented easily. Therefore, the continuity and momentum equations are solved uncoupled in order to be able to implement Equation (5.16) as a lateral boundary condition. The uncoupling of the equations leads to a discretization, which is conditionally stable according to:

$$\Delta t \le \frac{2\min(\Delta x, \Delta y)}{\sqrt{2gh_{\max}}} \tag{5.17}$$

where Δt is the time step and Δx and Δy are the grid sizes in the x and y directions, respectively.

An ADI discretization which solves the continuity and the momentum equations simultaneously is usually unconditionally stable. However, it looses its accuracy for Courant numbers higher than 4 (Shen, 1991). In addition, Equation (5.16) cannot be implemented as a lateral boundary condition unless the matrix is solved by a method other than the double sweep method, which looses the advantage of the ADI scheme. The current scheme, although conditionally stable, can work with Courant numbers up to two, without any loss of accuracy as will be shown in the sensitivity analysis (Chapter 6).

The time step is split into two fractional steps. In the first fractional step, the equations are solved sweeping in x-direction. In the second fractional step the equations are solved sweeping in y-direction. For the first fractional time step, Equation (5.1) is discretized as follows:

$$\frac{\eta^n - \eta^o}{\Delta t/2} + \frac{u_e^o(h_e + \eta_e^n) - u_w^o(h_w + \eta_w^n)}{\Delta x} + \frac{v_n^o(h_n + \eta_n^o) - v_s^o(h_s + \eta_s^o)}{\Delta y} = 0 \qquad (5.18)$$

where the superscripts n represent the values at the current time step, while the superscripts o represent the known values from the old time step. The subscripts e, w, s and n represent the values at the East, West, South and North faces of the control volume as shown in Figure (5.1). The values at the faces can be linearly interpolated as follows:

$$\eta_e = \frac{\eta_E + \eta_P}{2},\ \eta_w = \frac{\eta_W + \eta_P}{2},\ \eta_n = \frac{\eta_N + \eta_P}{2} \text{ and } \eta_s = \frac{\eta_S + \eta_P}{2} \qquad (5.19)$$

where the subscripts E, W, S and N represent the values at the discrete points as shown in Figure (5.1).

Equations (5.18) and (5.19) can be written in the form of linear discrete equations as follows:

$$
\begin{aligned}
&a_P\eta_P^n = a_W\eta_W^n + a_E\eta_E^n + b \\
&a_P = \frac{2}{\Delta t} + \frac{u_e^o - u_w^o}{2\Delta x} \\
&a_E = -\frac{u_e^o}{2\Delta x} \qquad\qquad a_W = \frac{u_w^o}{2\Delta x} \\
&b = \frac{2}{\Delta t}\eta_P^o - \frac{u_e^o h_e - u_w^o h_w}{\Delta x} - \frac{v_n^o h_n - v_s^o h_s}{\Delta y} - \frac{v_n^o(\eta_N^o + \eta_P^o) - v_s^o(\eta_S^o + \eta_P^o)}{2\Delta y}
\end{aligned}
\tag{5.20}
$$

Similarly, for the second fractional time step, the linear discrete equations which describe Equation (5.1) can be written as follows:

$$
\begin{aligned}
&a_P\eta_P^n = a_S\eta_S^n + a_N\eta_N^n + b \\
&a_P = \frac{2}{\Delta t} + \frac{v_n^o - v_s^o}{2\Delta y} \\
&a_N = -\frac{v_n^o}{2\Delta y} \qquad\qquad a_S = \frac{v_s^o}{2\Delta y} \\
&b = \frac{2}{\Delta t}\eta_P^o - \frac{v_n^o h_n - v_s^o h_s}{\Delta y} - \frac{u_e^o h_e - u_w^o h_w}{\Delta x} - \frac{u_e^o(\eta_E^o + \eta_P^o) - u_w^o(\eta_W^o + \eta_P^o)}{2\Delta x}
\end{aligned}
\tag{5.21}
$$

For the first fractional time step, Equation (5.2) is discretized as follows:

$$
\begin{aligned}
\frac{u_w^n - u_w}{\Delta t/2} + u_w\frac{u_P^n - u_W^n}{\Delta x} + v^*\frac{u_n - u_s}{2\Delta y} = -g\frac{\eta_P^n - \eta_W^n}{\Delta x} + \varepsilon\frac{u_e^n - 2u_w^n + u_f^n}{\Delta x^2} \\
+ \varepsilon\frac{u_n - 2u_w + u_s}{\Delta y^2} + C_x u_w^n + B_x
\end{aligned}
\tag{5.22}
$$

where, the superscripts o, which indicate the old values, have been removed for convenience, $v^* = (v_s + v_w + v_n + v_{nw})/4$, and u_w, u_e, u_f, u_n, u_s, v_s, v_w, v_n and v_{nw} are defined in Figure (5.2).

The derivative in the second term in Equation (5.22) (the advective term) is defined in terms of the values of the velocities at the discrete points. However, the velocities are defined at the control volume faces. Therefore, an approximation of the values of velocities at the discrete points in terms of the velocities at the faces is proposed as follows:

$$u_P = u_w\left(\frac{\alpha+1}{2}\right)+u_e\left(\frac{1-\alpha}{2}\right) \qquad \text{and} \qquad u_W = u_f\left(\frac{\alpha+1}{2}\right)+u_w\left(\frac{1-\alpha}{2}\right) \tag{5.23}$$

where the value of α at the faces of the control volumes is given as a function of the grid Peclet number Pe_Δ. Peclet number is the ratio between the advection and the diffusion which can be defined as follows:

$$Pe_\Delta = \frac{u\Delta x}{\varepsilon} \tag{5.24}$$

where, u is the local velocity and Δx is the grid spacing. Solving the one dimensional advection-diffusion problem results in the following expression for α:

$$\alpha = 1-\frac{2\left(\exp(Pe_\Delta)-1\right)}{\left(\exp(Pe_\Delta)-1\right)} \tag{5.25}$$

If the problem is advection dominated (i.e. $Pe_\Delta \rightarrow \infty$), the value of α tends to unity, which leads to the upwinding difference scheme, as defined by Equation (5.23). On the other hand, if the problem is diffusion dominated (i.e. $Pe_\Delta \rightarrow 0$), α tends to be zero, which leads to the central differencing scheme. The calculation of the exponent in Equation (5.25), however, is computationally expensive. Therefore, the following approximation is used instead of Equation (5.25):

$$\alpha = \frac{(Pe_\Delta)^2}{5 + (Pe_\Delta)^2} \tag{5.26}$$

which has the same limiting characteristics as Equation (5.25).

Equations (5.22) and (5.23) can be written in the following linear form:

$$\begin{aligned} a_P u_w^n &= a_E u_e^n + a_W u_f^n + b \\ a_P &= \frac{2}{\Delta t} + \frac{2\varepsilon}{\Delta x^2} - C_x + \frac{u_w \alpha}{\Delta x} \\ a_E &= \frac{\varepsilon}{\Delta x^2} - \frac{u_w(1-\alpha)}{2\Delta x} \\ a_W &= \frac{\varepsilon}{\Delta x^2} + \frac{u_w(1+\alpha)}{2\Delta x} \\ b &= \frac{2}{\Delta t} u_w - v^* \frac{u_n - u_s}{2\Delta y} - g\frac{\eta_P^n - \eta_W^n}{\Delta x} + \varepsilon \frac{u_n - 2u_w + u_s}{\Delta y^2} + B_x \end{aligned} \tag{5.27}$$

where α is given by Equation (5.26) and Pe_Δ is given by Equation (5.24) with $u = u_w$.

Similarly, for the second fractional time step, the linear discrete equations which describe Equation (5.2) can be written as follows:

$$\begin{aligned} a_P u_w^n &= a_N u_n^n + a_S u_s^n + b \\ a_P &= \frac{2}{\Delta t} + \frac{2\varepsilon}{\Delta y^2} - C_x + \frac{v^* \alpha}{\Delta y} \\ a_N &= \frac{\varepsilon}{\Delta y^2} - \frac{v^*(1-\alpha)}{2\Delta y} \\ a_S &= \frac{\varepsilon}{\Delta y^2} + \frac{v^*(1+\alpha)}{2\Delta y} \\ b &= \frac{2}{\Delta t} u_w - u_w \frac{u_e - u_f}{2\Delta x} - g\frac{\eta_P^n - \eta_W^n}{\Delta x} + \varepsilon \frac{u_e - 2u_w + u_f}{\Delta x^2} + B_x \end{aligned} \tag{5.28}$$

where α is given by Equation (5.26) and Pe_Δ is given by:

$$Pe_\Delta = \frac{v^* \Delta y}{\varepsilon} \tag{5.29}$$

Using the same procedure, the linear discrete equations which describe Equation (5.3) for the first fractional time step can be written as follows:

$$
\begin{aligned}
a_P v_s^n &= a_E v_e^n + a_W v_w^n + b \\
a_P &= \frac{2}{\Delta t} + \frac{2\varepsilon}{\Delta x^2} - C_y + \frac{u^* \alpha}{\Delta x} \\
a_E &= \frac{\varepsilon}{\Delta x^2} - \frac{u^*(1-\alpha)}{2\Delta x} \\
a_W &= \frac{\varepsilon}{\Delta x^2} + \frac{u^*(1+\alpha)}{2\Delta x} \\
b &= \frac{2}{\Delta t} v_s - v_s \frac{v_n - v_f}{2\Delta y} - g \frac{\eta_P^n - \eta_S^n}{\Delta y} + \varepsilon \frac{v_n - 2v_s + v_f}{\Delta y^2} + B_y
\end{aligned}
\tag{5.30}
$$

where α is given by Equation (5.26) and Pe_Δ is given by:

$$
Pe_\Delta = \frac{u^* \Delta x}{\varepsilon} \tag{5.31}
$$

and $u^* = (u_w + u_e + u_s + u_{se})/4$.

Similarly, for the second fractional time step Equation (5.3) can be described by the following linear equations:

$$
\begin{aligned}
a_P v_s^n &= a_N v_n^n + a_S v_f^n + b \\
a_P &= \frac{2}{\Delta t} + \frac{2\varepsilon}{\Delta y^2} - C_y + \frac{v_s \alpha}{\Delta y} \\
a_N &= \frac{\varepsilon}{\Delta y^2} - \frac{v_s(1-\alpha)}{2\Delta y} \\
a_W &= \frac{\varepsilon}{\Delta y^2} + \frac{v_s(1+\alpha)}{2\Delta y} \\
b &= \frac{2}{\Delta t} v_s - u^* \frac{v_e - v_w}{2\Delta x} - g \frac{\eta_P^n - \eta_S^n}{\Delta y} + \varepsilon \frac{v_e - 2v_s + v_w}{\Delta x^2} + B_y
\end{aligned}
\tag{5.32}
$$

where α is given by Equation (5.26) and Pe_Δ is given by:

$$Pe_{\Delta} = \frac{v_s \Delta y}{\varepsilon} \tag{5.33}$$

Equations (5.20), (5.21), (5.27), (5.28), (5.30) and (5.32) are solved using the tridiagonal matrix algorithm.

After the computation of the velocity components on the faces of the control volumes their mean values referring to the mesh center are calculated by linear interpolation. After each 100 time steps, the total kinetic energy divided by the fluid density in the flow domain is computed from the sum:

$$E_{kin}^{n} = \sum \left(u^2 + v^2\right) \Delta x \Delta y h / 2 \tag{5.34}$$

The steady state is reached when the ratio $\left|E_{kin}^{n+1} - E_{kin}^{n}\right| / E_{kin}^{n+1}$ becomes less than a chosen convergence value (of the order of 10^{-3}).

5.1.4. Model application

Nishimura et al. (1985) observed the circulation behind an offshore breakwater and measured the depth averaged velocities in the laboratory. The experiment consists of a uniform bottom slope 1:50. A detached breakwater was installed parallel to the shoreline at a depth of 6 cm. The breakwater length was about 2.7 m, corresponding to three local wavelengths. The beach and the breakwater were exposed to perpendicularly incident waves of 2.0 cm in height and 1.2 s in period (Horikawa, 1988). Under these conditions, as is well known, a pair of symmetric circulation cells is generated behind the breakwater. Figure (5.3) shows the computational domain and the depth bathymetry used in the study this case.

The integrated wave model developed in the last chapter is used to simulate the wave pattern behind the breakwater. The parabolic model uses a relatively coarse grid of Δx = 0.5 m and Δy = 0.18 m. Both nonlinearity and wave energy dissipation due to breaking were considered. For the dissipation model, Equation (3.16) was used with γ_s = 0.83. Figure (5.4) shows the wave height pattern simulated by the parabolic model, which is considered as an initial solution for the elliptic solver. The elliptic model develops a finer grid in order to satisfy the stability criteria. In the direction of wave propagation (i.e. the x-direction), the grid size is 10 times smaller than the grid size used by the parabolic model (i.e. Δx = 0.05 m). In the alongshore direction, the grid size was chosen to be 4 times smaller than the parabolic grid size (i.e. Δy = 0.045 m). It takes the model only 3600 iterations to reduce the error to the order of 10^{-9} as shown in Figure (5.6). Figure (5.5) shows the final wave pattern used by the hydrodynamic model. A coarser grid is constructed for the hydrodynamic model, in which the resultant wave data and radiation stresses at four neighboring points were averaged (i.e. Δy = 0.2 m and Δy = 0.18 m). It was assumed that C_f = 0.01 and N = 0.01. Figure (5.7) shows the computed nearshore field behind the detached breakwater, where the length of each arrow represents the value of the depth averaged velocity. For comparison, the corresponding flow pattern obtained through the physical model experiment is shown in Figure (5.8). The circulation patterns in these two figures show good agreement in overall shapes, scales and locations. The computed elevation of the mean water level for this case is shown in Figure (5.9). A slight wave setdown occurs outside the surfzone, whereas the wave setup is larger near the shoreline, particularly in the upstream side.

Nishimura et al. (1985) used the same 1:50 beach physical model but with a 1.5 m long jetty situated perpendicular to the shoreline. Waves are obliquely incident at 60° to the shoreline, which induce a longshore current that moves around the jetty. The incident wave height was 1.8 cm and the period was 1.2 s. Figure (5.10) shows the computational domain and the depth contours used to represent this case. The calculated current field is shown in Figure (5.11). The current field in the corresponding physical model experiment is plotted in Figure (5.12). The sets of parallel arrows in the figure denote longshore components of local velocities measured by using small propeller-type current meters (Horikawa, 1988). Overall agreement between the numerical and physical results is good. Figure (5.13) illustrates the computed elevation of the mean water level around the jetty. Wave setup appears on the upstream side of the jetty due to the damming effect of the jetty. In the two cases discussed above, the model reached the steady state in relatively small period of time (of the order of 3 minutes), during which no significant bathymetric changes are expected. Figure (5.14) shows the total kinetic energy of the flow.

5.1.5. Model limitations

In general, wave-induced currents are not uniform in the vertical direction; the upper and lower layers can even flow in opposite directions under certain circumstances (Horikawa, 1988). Therefore, the proposed model cannot model the boundary layer drift and the undertow, which exist near the shoreline.

Near the shore boundary, where the swashing motion of the fluid is complicated, the basic equations themselves are questionable (Horikawa, 1988).

5.2. Sediment Transport Model

Several mathematical models can describe the sediment transport due to the combined wave-current outside the surfzone. However, inside the surfzone, the sediment transport process is very complicated due to wave breaking and induced turbulence. Even the most sophisticated models cannot simulate the sediment movement in this zone. Therefore, a simple empirical model is expected to yield comparable results with other sophisticated models after suitable calibration. The model described in this section calculates the total sediment transport loads by superposing the separate transport loads due to waves and currents.

5.2.1. Total sediment transport due to a mean current

According to Horikawa (1988), Watanabe et al. (1986) developed a formula of the rate of transport due to mean current, which reads:

$$\begin{aligned} q_{cx} &= Q_c u \qquad\qquad q_{cy} = Q_c v \\ Q_c &= A_c(\tau - \tau_{cr})/\rho g = A_c(u_*^2 - u_{*cr}^2)/g \end{aligned} \tag{5.35}$$

where q_{cx} and q_{cy} are the transport loads in x and y direction, respectively, u and v are the mean flow velocities in x and y directions, respectively, τ_{cr} and u_{*cr} are the critical shear stress and shear velocity, respectively, τ and u_* are the combined wave-current shear stress and shear velocity, respectively and A_c is a dimensionless coefficient (of the order 0.1~1).

According to van der Velden (1989), the approach of Bijker is used to calculate the combined wave-current shear stress and the combined wave-current shear velocity as:

$$\tau = \tau_c \left\{ 1 + \frac{1}{2} \left(\xi \frac{u_{bm}}{u_c} \right)^2 \right\} \tag{5.36}$$

and

$$u_*^2 = u_{*c}^2 \left\{ 1 + \frac{1}{2} \left(\xi \frac{u_{bm}}{u_c} \right)^2 \right\} \tag{5.37}$$

where τ_c and u_{*c} are the current shear stress and current shear velocity, respectively, u_c is the current velocity (i.e. $u_c = \sqrt{u^2 + v^2}$) and ξ is given by:

$$\xi = C \sqrt{\frac{f_w}{2g}} \tag{5.38}$$

where C is the Chezy coefficient and f_w is the wave friction coefficient.

The Chezy coefficient can be given by (van der Velden, 1989):

$$C = 18 \log_{10} \left(\frac{12h}{k_n} \right) \tag{5.39}$$

where k_n is the moveable bed roughness.

The current critical shear velocity u_{*c} can be given in terms of Chezy's coefficient as follows:

$$u_{*c} = u_c \frac{\sqrt{g}}{C} \tag{5.40}$$

In oscillatory flows, the maximum bottom shear stress τ_{wm} is expressed in the form of a wave friction factor f_w as follows:

$$\tau_{wm} = \frac{1}{2} f_w \rho u_{bm}^2 \tag{5.41}$$

where ρ is the fluid density. Several mathematical formulas have been proposed for the wave friction coefficient. Usually, Nielsen's (1992) formula for wave friction coefficient yields comparable sediment transport rates. He adjusted the coefficients in Swart's (1974) formula as follows:

$$f_w = \exp\left[5.5\left(\frac{A_{bm}}{k_n}\right)^{-0.2} - 6.3\right] \tag{5.42}$$

where $A_{bm} = u_{bm} / \omega$ is the amplitude of water particle excursions along the bed.

The movable bed roughness which appears in Equations (5.39) and (5.42) is defined as the equivalent diameter of static spherical sand particles that produces the same bottom roughness to the flow. Nielsen (1992) suggested that the movable bed roughness for flat sand beds under oscillatory sheet-flow may be expressed as:

$$k_n = 170\sqrt{\psi_S^{2.5} - 0.05}\, D \tag{5.43}$$

where D is the mean grain size and $\psi_S^{2.5}$ is the Shields parameter with respect to conventional roughness of $2.5D$. Generally, the Shields parameter ψ_S for pure wave motion is defined by:

$$\psi_S = \frac{\tau_{wm}}{(s-1)\rho g D} \tag{5.44}$$

where $s = \rho_s / \rho$ is the density of the sediment relative to that of the fluid. Combining Equations (5.41) and (5.44), $\psi_S^{2.5}$ can be given by:

$$\psi_S^{2.5} = \frac{\frac{1}{2} f_{2.5}\, \rho u_{bm}^2}{\rho(s-1)gD} \tag{5.45}$$

where $f_{2.5}$ is the wave friction coefficient with respect to conventional roughness of $2.5D$, which is given by:

$$f_{2.5} = \exp\left[5.5\left(\frac{A_{bm}}{2.5D}\right)^{-0.2} - 6.3\right] \tag{5.46}$$

In order to account for the roughness contribution from the moving sand over ripples, Nielsen (1992) added a term to Equation (5.43) as follows:

$$k_n = 8\eta_r^2 / \lambda + 170\sqrt{\psi_S^{2.5} - 0.05}\, D \tag{5.47}$$

where λ is the ripple length and η_r is the ripple height. According to Leont'yev (1999), Kaczmarek et al. (1994) showed that the magnitude of k_n under regular wave conditions is about twice as that for random waves with the same significant height, which suggests:

$$k_n = 4\eta_r^2 / \lambda + 85\sqrt{\psi_S^{2.5} - 0.05}\, D \tag{5.48}$$

The geometry of the vortex ripples are calculated as a function of the mobility number Ψ_m, which is defined as:

$$\Psi_m = \frac{u_{bm}^2}{(s-1)gD} \tag{5.49}$$

Based on field data, Nielsen (1992) suggested the following formula for the ripple length λ:

$$\frac{\lambda}{A_{bm}} = \exp\left(\frac{693 - 0.37\ln^8 \Psi_m}{1000 + 0.75\ln^7 \Psi_m}\right) \tag{5.50}$$

and the ripple height η_r is calculated as follows:

$$\frac{\eta_r}{A_{bm}} = 21\Psi_m^{-1.85} \tag{5.51}$$

The mobility number and the wave bottom excursion amplitude in Equations (5.50) and (5.51) are calculated based on the significant wave height H_s, which is related to the root mean square wave height H_{rms} through:

$$H_s = \sqrt{2}\, H_{rms} \tag{5.52}$$

5.2.2. Total sediment transport due to waves

According to Horikawa (1988), Watanabe et al. (1984) developed the following formula for the sediment transport load due to wave motion:

$$\begin{aligned} q_{wx} &= F_d Q_w u_{bm} \cos\theta \qquad\qquad q_{wy} = F_d Q_w u_{bm} \sin\theta \\ Q_w &= A_w(\tau - \tau_{cr})/\rho g = A_w(u_*^2 - u_{*cr}^2)/g \end{aligned} \tag{5.53}$$

where q_{wx} and q_{wy} are the transport loads in x and y direction, respectively, A_w is a dimensionless coefficient (of the order 0.1~1) and F_d is a direction function which defines the direction of the sediment transport load and smoothes the discontinuity at the null-point (where the net transport is zero) (Horikawa, 1988). The direction function F_d is defined as:

$$F_d = \tanh\left(\kappa_d \frac{\Pi_c - \Pi}{\Pi_c}\right) \tag{5.54}$$

where κ_d is a coefficient which controls the degree of change in the cross-shore transport rate around the null-point, which has value of the order of unity, and Π defines the direction of the sediment transport as follows:

$$\Pi = \frac{u_{bm}^2}{sgD}\frac{h}{L_0} \begin{cases} < \Pi_c & \text{onshore transport} \\ > \Pi_c & \text{offshore transport} \end{cases} \tag{5.55}$$

in which Π_c is a critical value of Π at the null-point, which is expected to be of the order of unity. However, it has to be determined empirically through trial computations (Horikawa, 1988).

5.2.3. Critical shear stress

The critical condition for sediment movement is given in terms of the critical Shields parameter ψ_S^{cr} defined in Equation (5.44). The following common values of ψ_{cr} are used (Horikawa, 1988):

$$\psi_S^{cr} = \begin{cases} 0.11 & \text{for fine sands; } D/\delta_L < 1/6.5 \\ 0.06 & \text{for coarse sands; } D/\delta_L > 1/4 \end{cases} \tag{5.56}$$

where δ_L represents the thickness of the oscillatory boundary layer, which is given by:

$$\delta_L = \sqrt{\frac{\nu T}{\pi}} \tag{5.57}$$

Linear interpolation is applied to determine ψ_S^{cr} for the range $1/6.5 < D/\delta_L < 1/4$ as follows:

$$\psi_S^{cr} = -\frac{13}{25}\left(\frac{D}{\delta_L} - \frac{1}{4}\right) + 0.06 \tag{5.58}$$

It is known that sediment transport rates generally take larger values in the surfzone than in the offshore zone, which may be attributed to the presence of intensive turbulence generated by wave breaking (Horikawa, 1988). In order to incorporate this effect, the values of the critical shear velocity are specified as follows:

$$u_{*cr}^2 = \begin{cases} 0.0 & \text{in the surfzone} \\ (s-1)gD\psi_S^{cr}\tanh^2(\kappa_c x_b / X_B) & \text{outside the surfzone} \end{cases} \quad (5.59)$$

where X_B is the width of the surfzone, x_b is the offshore distance measured from the breaking point and the value of the dimensionless constant κ_c is expected to be of the order of unity.

5.3. Coastal Morphology Model

Using the model described in sections 5.2, a spatial distribution of sediment transport rates is estimated from local wave and current conditions. The change in local bottom elevation z_b is calculated by solving the conservation equation of sediment mass, which reads:

$$\frac{\partial z_b}{\partial t} + \frac{\partial q_x}{\partial x} + \frac{\partial q_y}{\partial y} = 0.0 \quad (5.60)$$

where q_x and q_y are the total volumetric sediment transport rates in x and y directions, respectively and t is the time.

The formulas for sediment transport rates described in section 5.2 do not take into account the bottom slope. Therefore, even if a jagged profile were to grow in the course of calculation with Equation (5.60), such that the local slope exceeded the repose angle of the sediment, the unphysical slope could not be reduced (Horikawa, 1988). Although the wave-current field varies with beach transformation, the change of the flow field alone cannot be expected to completely suppress the creation of bottom jags. In reality, if the local slope becomes steep, sediment grains tend to move downward owing to the force of

gravity. In order to incorporate this effect, the following equation is used to calculate the change of bottom elevation (Horikawa, 1988):

$$\frac{\partial z_b}{\partial t} = -\frac{\partial}{\partial x}\left(q_x - \varepsilon_q |q_x| \frac{\partial z_b}{\partial x} \right) - \frac{\partial}{\partial y}\left(q_y - \varepsilon_q |q_y| \frac{\partial z_b}{\partial y} \right) \tag{5.61}$$

where ε_q is a positive constant determined empirically.

Equation (5.61) corresponds to the use of the following modified sediment transport rates:

$$q_x' = q_x - \varepsilon_q |q_x| \frac{\partial z_b}{\partial x} \qquad q_y' = q_y - \varepsilon_q |q_y| \frac{\partial z_b}{\partial y} \tag{5.62}$$

Equation (5.61) is solved numerically using finite difference method. A staggered mesh is employed in which the bottom elevation change z_b is calculated at the nodes and the transport loads are calculated at the faces using linear interpolation. The finite difference for the first term on the right hand side of Equation (5.61) is given by:

$$-\frac{1}{\Delta x}\left((q_{xi+1,j} - q_{xi,j}) - \varepsilon_q \left\{ |q_{xi+1,j}| \frac{z_{bi+1,j} - z_{bi,j}}{\Delta x} - |q_{xi,j}| \frac{z_{bi,j} - z_{bi-1,j}}{\Delta x} \right\} \right) \tag{5.63}$$

in which the sediment transport loads are defined at the old time step.

The time derivative on the left hand side of Equation (5.61) is discretized using the modified Lax scheme as follows:

$$\frac{1}{\Delta t}\left(z_{bi,j}^n - \left\{ \begin{array}{r} \frac{\alpha_x}{4}(z_{bi+1,j} + z_{bi-1,j}) + \frac{\alpha_y}{4}(z_{bi,j+1} + z_{bi,j-1}) \\ + (1 - \alpha_x/2 - \alpha_y/2) z_{bi,j} \end{array} \right\} \right) \tag{5.64}$$

where $z_{bi,j}^n$ is the value of the bottom elevation change at the new time step and α_x and α_y are empirical smoothing parameters in x and y directions, respectively.

For the explicit solution scheme described by Equation (5.63), the following stability condition for the time step must be enforced (Horikawa, 1988):

$$\Delta t \le \min\left\{\frac{1}{2}\frac{\Delta x^2}{\varepsilon_q |q_x|_{\max}}, \frac{1}{2}\frac{\Delta y^2}{\varepsilon_q |q_y|_{\max}}\right\} \tag{5.65}$$

where $|q_x|_{\max}$ and $|q_y|_{\max}$ are the maximum values of $|q_x|$ and $|q_y|$, respectively.

The updated morphology is calculated at the end of the simulation time from:

$$h^n = h^o - z_b \tag{5.66}$$

where h^n and h^o are the new and old water depths, respectively.

5.3.1. Test cases

Several tests are performed to examine the capabilities of the coastal morphology model. The equilibrium beach profile concept is used to generate the initial beaches according to the median grain size D as follows:

$$h(x) = Ax^{2/3} \tag{5.67}$$

where $h(x)$ is the water depth at distance x offshore and $A = 0.07\text{m}^{1/3}$ for a silty sand of median grain size $D = 0.1$mm (Herbich, 1991). Figure (5.15) shows the bathymetry of a typical equilibrium silty sand beach, which is used for the analysis.

The first test is for a system of offshore breakwaters subjected to constant wave conditions. The system consists of 5 detached breakwaters of 200 meters length and 200 meters spacing. The breakwaters are located 240 meters from the shoreline as shown in Figure (5.16) and Figure (5.17). First the parabolic wave model is run to simulate the wave heights and angles behind the system of detached breakwaters. A perpendicular

wave of 2.0 m significant height and 9.0 s period is used. The hydrodynamic model is then applied to simulate the currents induced behind the breakwaters. Figure (5.16) shows the realistic circulation developed behind the breakwaters. The coastal morphology model is then applied given both the wave and current information over a period of 60 days. Figure (5.17) shows the beach deformation after 60 days of the model application, where salients are realistically formed behind the breakwaters. It is shown from Figure (5.16) that the source if sediments that build up the salients is from the vicinity of the breakwaters, which explains the erosion that happens between the breakwaters as shown in Figure (5.17).

The second case is intended to test the coastal morphology's model behaviour for the case of groined beach. The same silty sand beach used in the previous case is adopted. A constant wave climate of 1.5 meters significant height and 9 s period is assumed. Large offshore wave angle (θ_0 = 45°) is used in order to derive significant amount of littoral drift so that the groins effect is signified. The system is composed of four groins of 240 m length and spaced at 1000 m, which corresponds to 4 times the groin length. Figure (5.18) shows the wave-induced currents around the groin system. Accordingly, the coastal morphological changes are calculated over a period of 90 days. Figure (5.19) shows the beach morphological changes due to the groin system where the initial beach contours are shown in grey scale, while the beach contours after 90 days of wave application are shown as lines. Again, the general behaviour of the coastal morphology model is realistic, where sediments build up on the up-drift faces of the groins and erosion occurs on the down-drift faces.

5.4. Summary

In this chapter a coastal hydrodynamics model has been developed. The conventional time-dependent depth-integrated Navier Stokes equations are discretized over a two dimensional staggered grid using the ADI method. The wave-driven currents are considered through the radiation stress terms. The effects of the surface rollers and Stokes drift are considered in the formulation of the radiation stress. The model results are compared very well with the results from two experimental cases.

The second part of this chapter was directed to the development of a sediment transport model and a coastal morphology model. The sediment transport model is based on the bed shear stress in which the sediment loads due to waves and currents are evaluated separately. The effect of the induced turbulence in the surfzone is considered in the model by considering no threshold for sediment movement in the breaking zone. A coastal morphology model is then developed based on the sediment budget equation, which is solved explicitly over a two dimensional grid. The coastal morphology model showed realistic results for two different test cases.

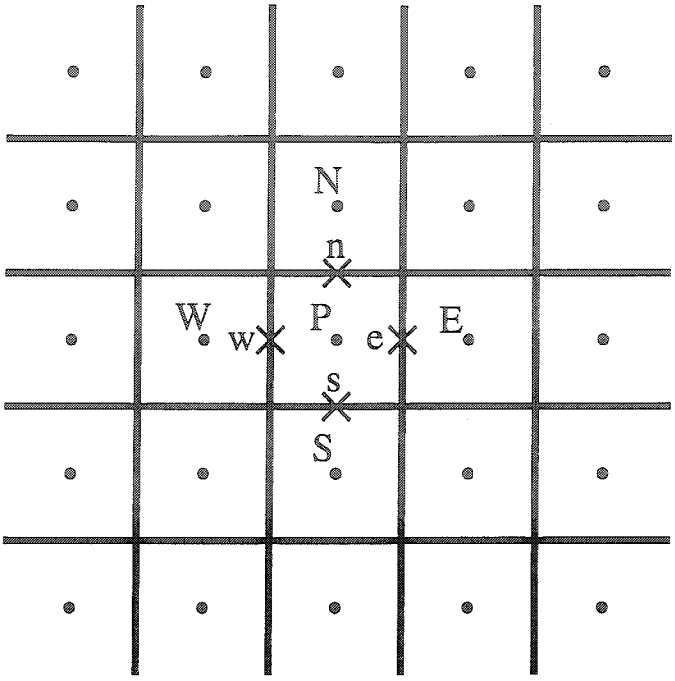

Figure (5.1): Definition of grid points

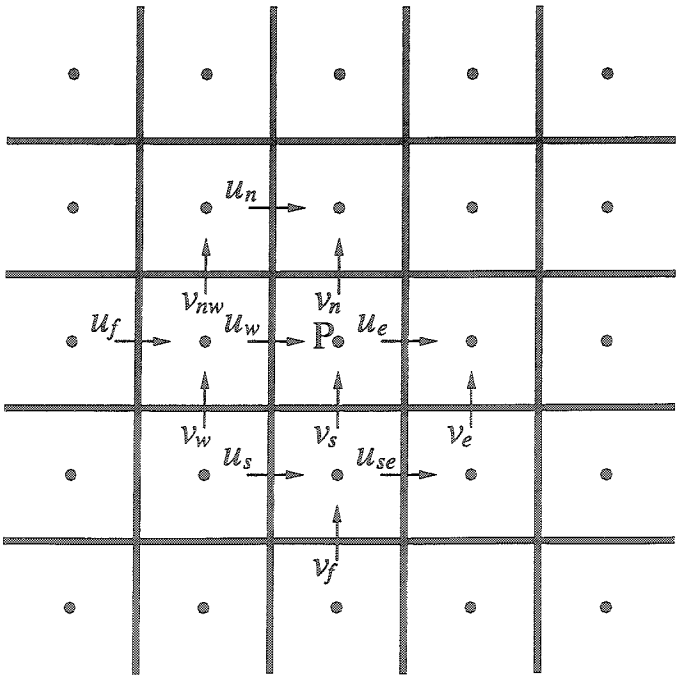

Figure (5.2): Definition of velocity components

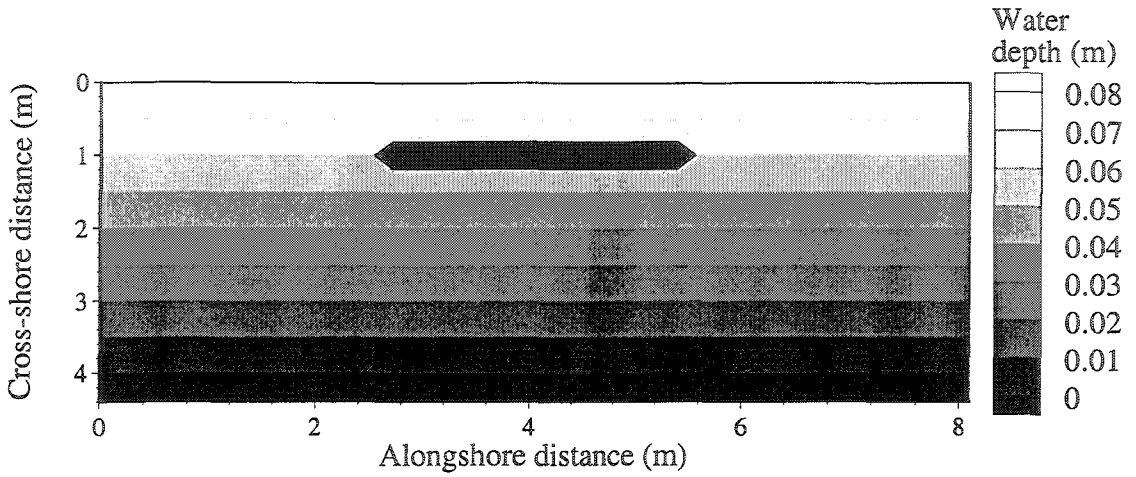

Figure (5.3): Computational domain (case of an offshore breakwater).

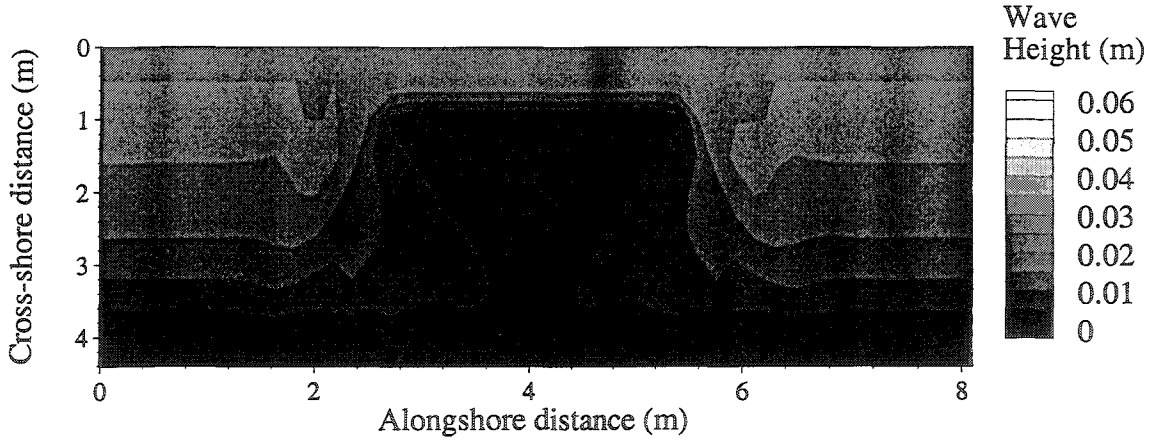

Figure (5.4): Wave height pattern using the parabolic model.

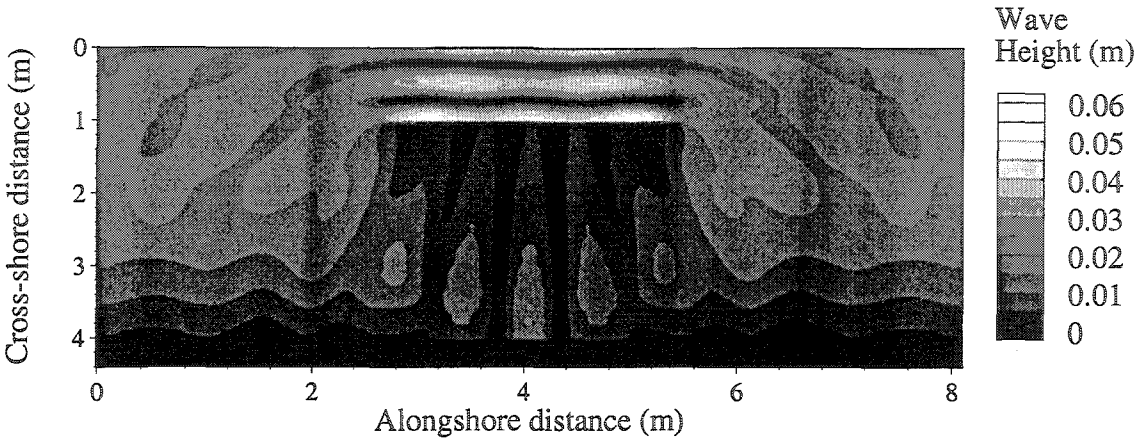

Figure (5.5): Wave height pattern using the elliptic model.

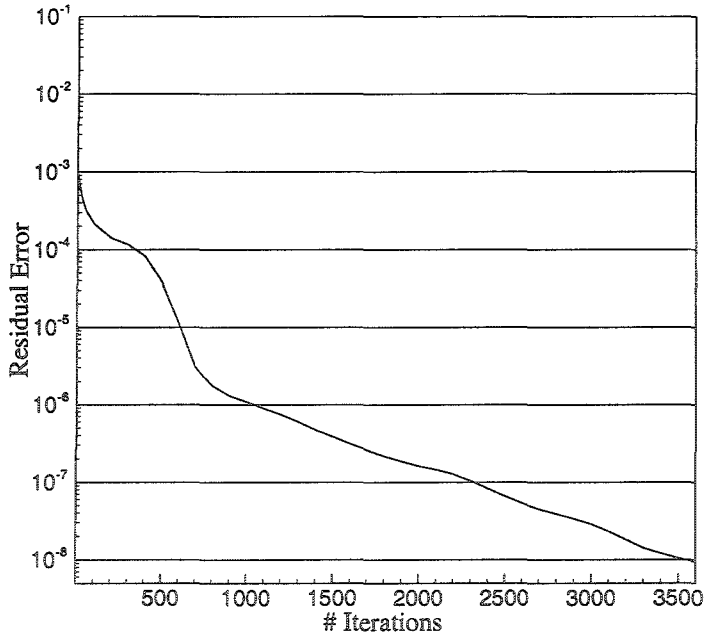

Figure (5.6): Convergence of the elliptic solver.

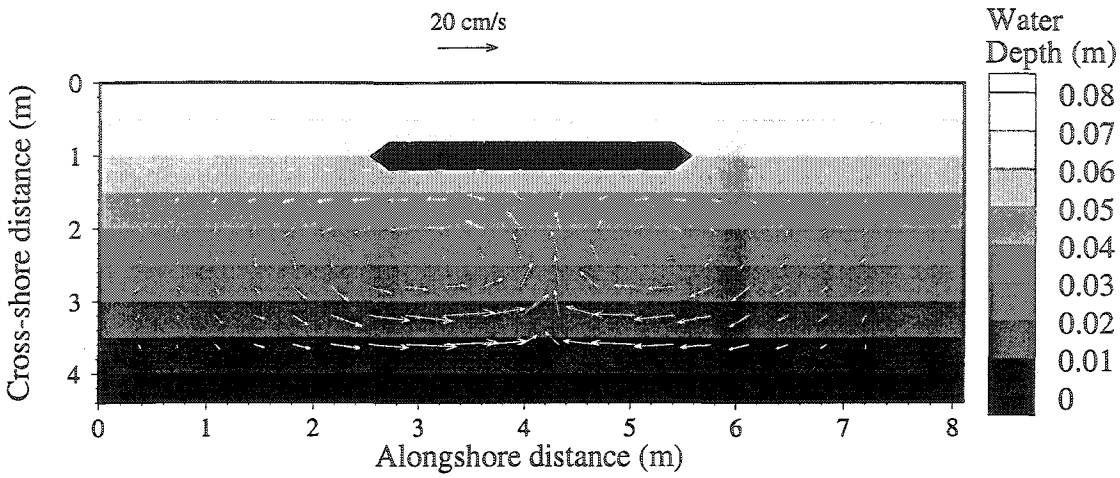

Figure (5.7): Computed circulation behind a detached breakwater.

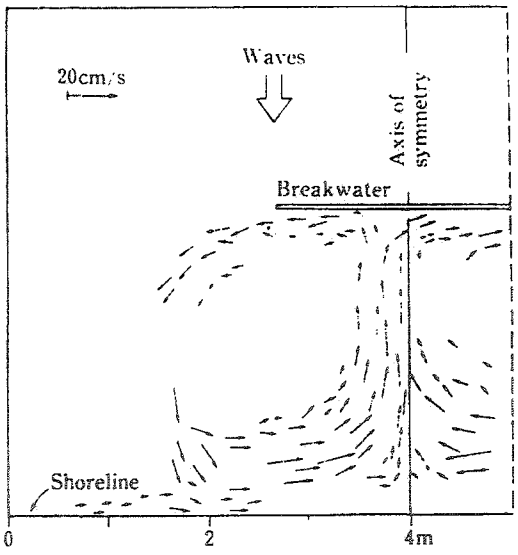

Figure (5.8): Observed circulation behind a detached breakwater (Nishimura et al., 1985) scanned from Horikawa (1988 pp 289)

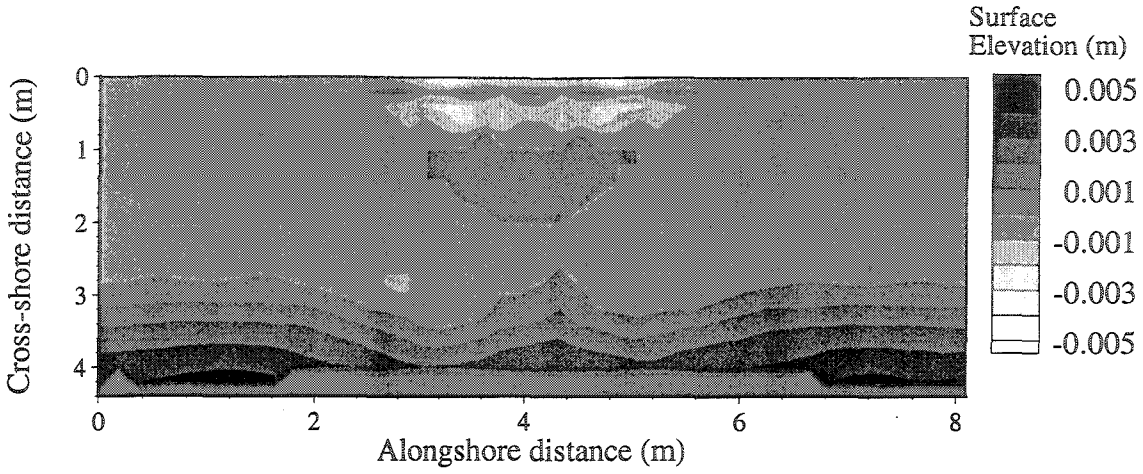

Figure (5.9): Computed elevation of mean water level behind a detached breakwater.

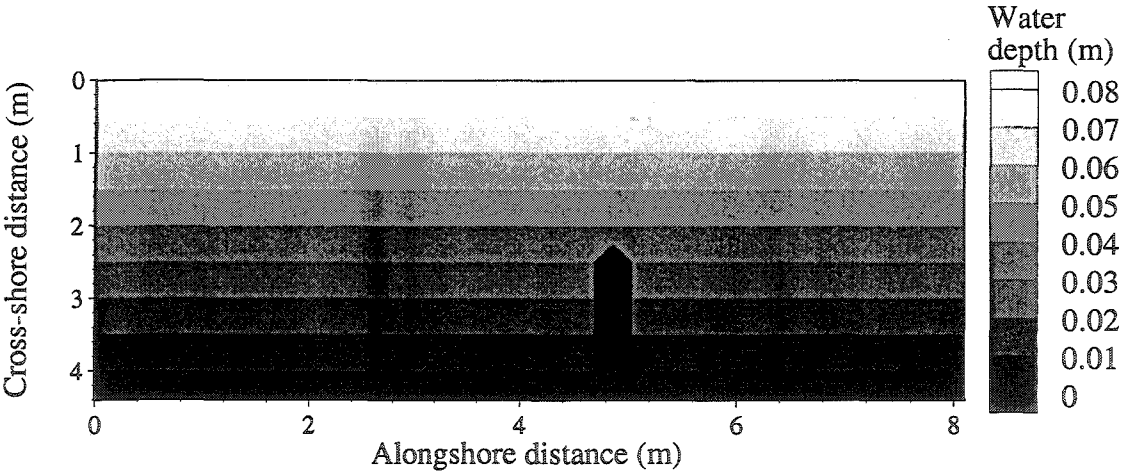

Figure (5.10): Computational Domain (case of the jetty).

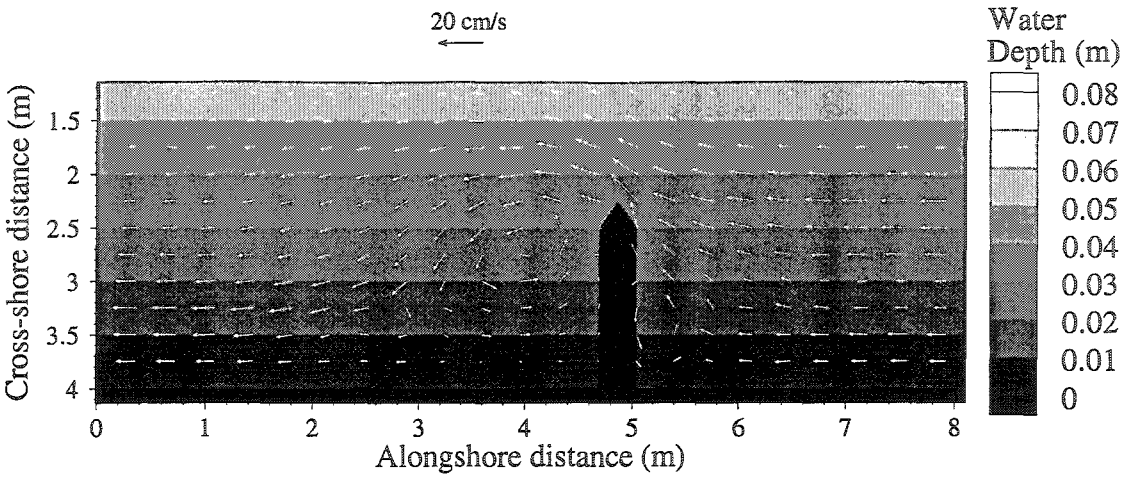

Figure (5.11): Computed longshore current around a jetty.

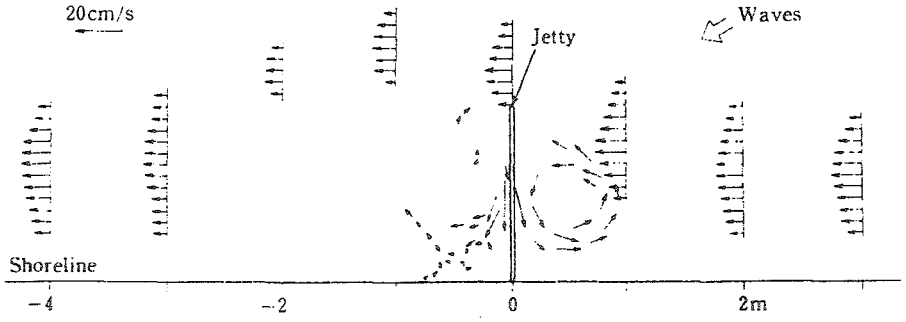

Figure (5.12): Observed longshore current around a jetty (Nishimura et al., 1985) scanned from Horikawa (1988).

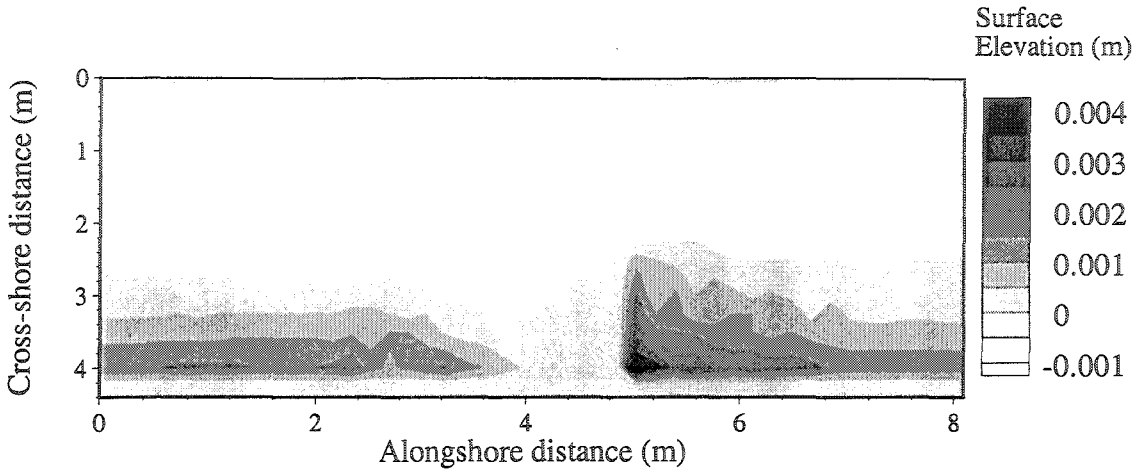

Figure (5.13): Computed elevation of mean water level around a jetty.

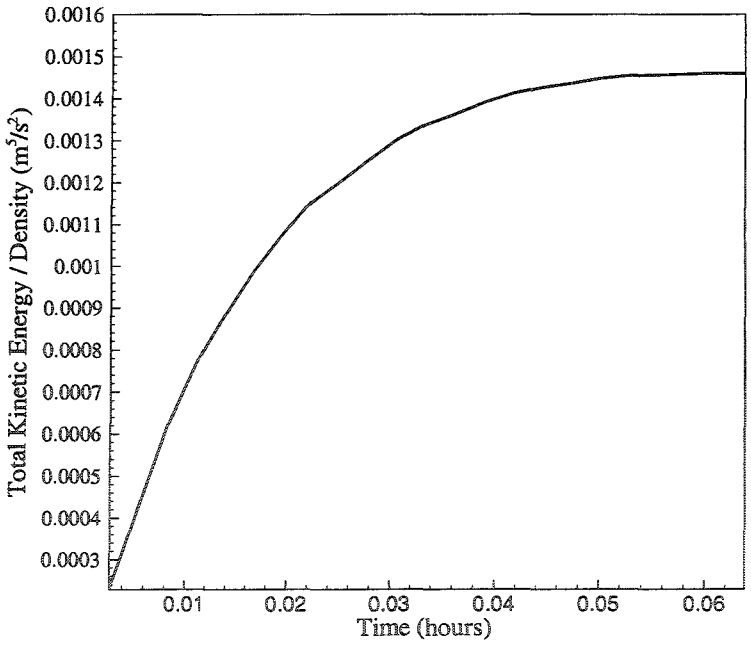

Figure (5.14): Total kinetic energy evolution.

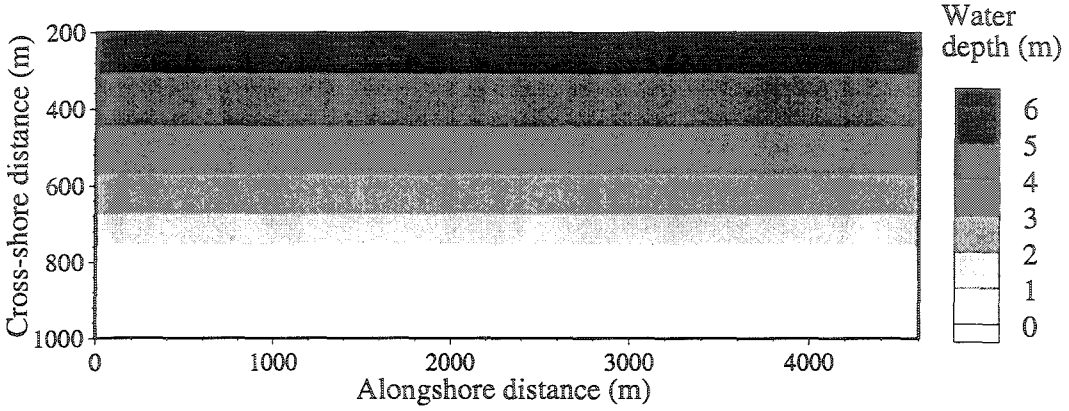

Figure (5.15): Typical silty sand beach (numerical domain).

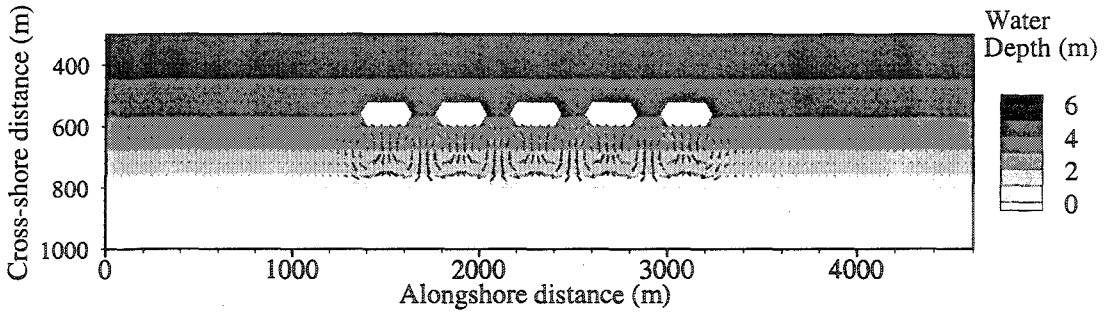

Figure (5.16): Circulation behind the detached breakwater system.

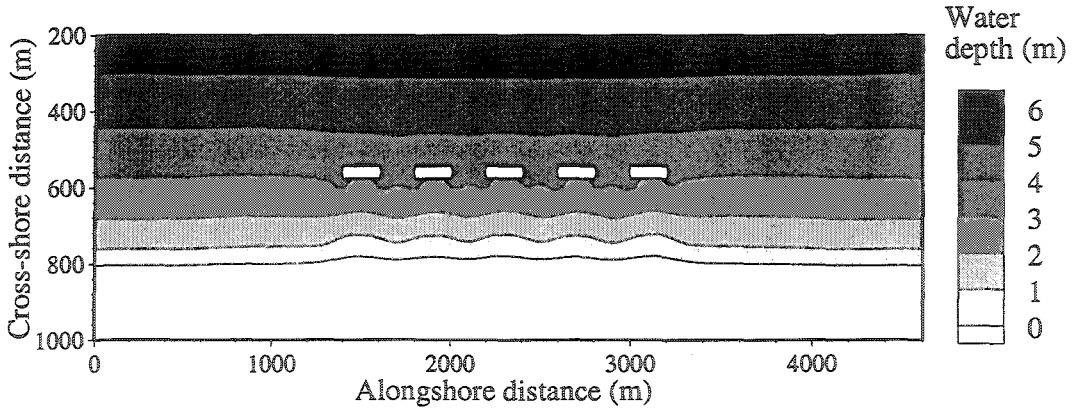

Figure (5.17): Morphological changes due to detached breakwater system.

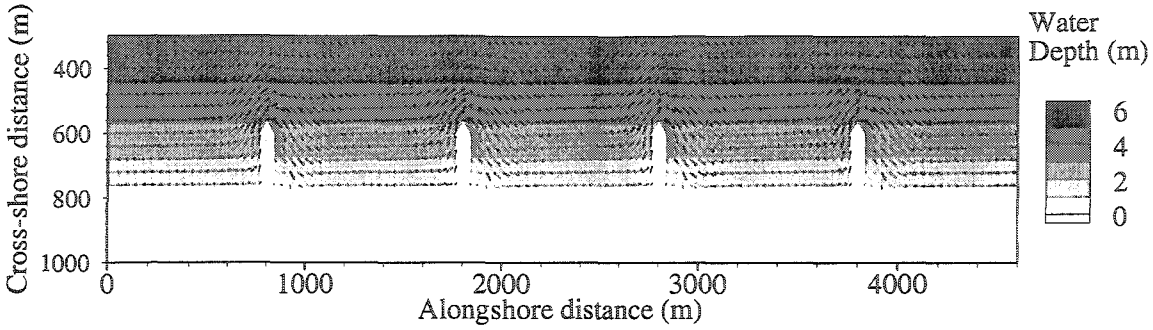

Figure (5.18): Circulation around a system of groins.

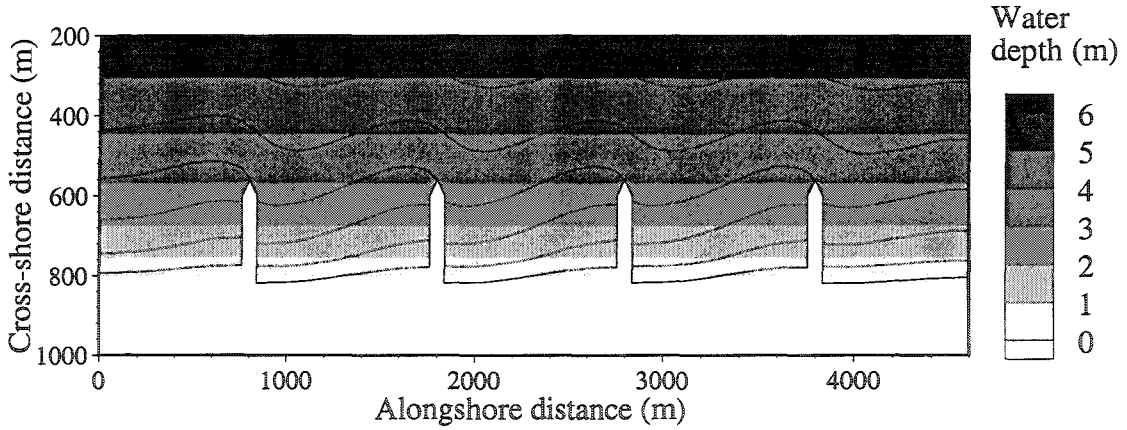

Figure (5.19): Morphological changes due to a system of groins.

Chapter 6: Sensitivity Analysis

The effects of the various model parameter values on the wave, hydrodynamics and sediment transport modeling results are studied. The following sections (a) describes the coastal domains used in the analysis, (b) performs sensitivity analysis for the wave model, (c) performs sensitivity analysis for the hydrodynamic model and (d) performs sensitivity analysis for the sediment transport model.

6.1. Coastal Domains

The analysis is done using typical coastal domains, where the soil may be as fine as silty sand or as coarse as fine gravel. The Equilibrium beach profile concept is used to generate various types of beaches according to the median grain size D. The equilibrium beach profile proposed by Bruun (1954) is used, which reads:

$$h(x) = Ax^{2/3} \tag{6.1}$$

where $h(x)$ is the water depth at distance x offshore and A is a dimensional scale parameter (Herbich, 1991). The parameter A is found using Figure (6.1), given by Herbich (1991) after Moore (1982). Using Equation (4.1) and Figure (6.1), three beaches were proposed for this study. The first is a silty sand beach with median grain size 0.1 mm and $A = 0.07\ m^{1/3}$. The second is a sandy beach with median grain size 0.35 mm and $A = 0.2\ m^{1/3}$. The last one is a gravel beach with median grain size 3 mm and $A = 0.4\ m^{1/3}$.

A flat bed domain was also needed in the analysis of the diffraction patterns behind coastal structures making the total number of domains used four. The first three

domains extend 1000 meters alongshore and 500 meters cross-shore. Table (6.1) gives a short description for the four domains used in the analysis.

Table (6.1): The coastal domains

Domain	Onshore Slope	Offshore slope (at 400 m)	Average Depth (over 400m)	D (mm)	A ($m^{1/3}$)
Domain#1	1:60	1:170	2.0	0.13	0.07
Domain#2	1:20	1:50	4.0	0.5	0.156
Domain#3	1:20	1:50	4.0	1.0	0.2
Domain#4	Zero	Zero	2.0		

6.2. Wave Model Sensitivity Analysis

The integrated parabolic/elliptic wave model is used in this section since it can be applied as a parabolic model or as an elliptic model without using the parabolic solution as an initial solution. The wave model includes a number of important parameters. In this section, the following effects will be studied:

1. Effect of γ on the position of the breaker line,

2. Effect of α on the modeled breaking waves,

3. Solution dependency on the grid size,

4. Capability of the parabolic model to model the diffraction patterns, and

5. Effect of wave approach angles on the wave model and the model's capability to simulate different wave angles.

Table (6.2), describes the runs performed by the parabolic wave model and the elliptic wave model.

Table (6.2): Wave model sensitivity analysis runs.

Run#	Main parameters			Model used	Domain	Hz. grid (m)		Input	Effects studied
	H_0	T	θ_0			Δx	Δy		
PW1	1.0	6.0	0.0	Parabolic	Domain#1 with offshore breakwater of length = $3L_0$	10	10	γ= 0.9	Effect of γ on the position of the breaker line.
PW2								γ= 0.8	
PW3								γ= 0.7	
PW4								γ= 0.6	
PW5	1.5	6.0	0.0	Parabolic	Domain#2 with offshore breakwater of length = $3L_0$	10	10	γ= 0.9	Effect of γ on the position of the breaker line.
PW6								γ= 0.8	
PW7								γ= 0.7	
PW8								γ= 0.6	
PW9	2.5	6.0	0.0	Parabolic	Domain#3 with offshore breakwater of length = $3L_0$	10	10	γ= 0.9	Effect of γ on the position of the breaker line.
PW10								γ= 0.8	
PW11								γ= 0.7	
PW12								γ= 0.6	
PW13	1.0	6.0	0.0	Parabolic	Domain#1 with offshore breakwater	10	10	α=0.7	Effect of α on modeled breaking waves (γ= 0.9)
PW14								α=1.0	
PW15								α=1.3	
PW16	0.5	6.0	0.0	Parabolic	Domain#1 with offshore breakwater of length = $3L_0$	10	10	γ= 0.6 α=1.0	Effect of offshore wave height.
PW17	1.0	6.0	0.0						
PW18	1.5	6.0	0.0						
PW19	2.0	6.0	0.0						
PW20	1.0	4.0	0.0	Parabolic	Domain#1 with offshore breakwater of length = $3L_0$	10	10	γ= 0.6 α=1.0	Effect of wave period.
PW21	1.0	5.0	0.0						
PW22	1.0	6.0	0.0						
PW23	1.0	7.0	0.0						
EW1	0.2	5.66	0.0	Elliptic	Domain#4	5	5	Accuracy 10^{-6}	Effect of accuracy on the elliptic solution.
EW2								Accuracy 10^{-5}	
EW3								Accuracy 10^{-4}	
EW4								Accuracy 10^{-3}	
EW5	0.2	5.66	0.0	Parabolic /Elliptic	Domain#4	5	5	Accuracy 10^{-6}	Effect of accuracy on the elliptic solution.
EW6								Accuracy 10^{-5}	
EW7								Accuracy 10^{-4}	
EW8								Accuracy 10^{-3}	
EW9	0.2	5.66	0.0	Parabolic /Elliptic	Domain#4	5	5		Elliptic model grid dependency
EW10						2.5	2.5		
EW11						1.67	1.67		

PW24	0.2	5.66	0.0	Parabolic	Domain#4	20	10		Parabolic model grid dependency
PW25						20	5		
PW26						10	5		
PW27						5	5		
EW12	0.2	5.66	20	Parabolic /Elliptic	Domain#4	2.5	2.5		Model capabilities for wide angles.
EW13			30						
EW14			50						
EW15			60						

6.2.1. Effect of breaking coefficient on the position of the breaker line

The breaker line position is very important in wave modeling, because it defines the width of the surfzone at which most of the sediment transport takes place. Therefore, it is important to study the sensitivity of the breaking coefficient γ on the position of the breaker line.

The runs PW1 to PW12 are used in this analysis, where the values of the breaking coefficient γ range from 0.9 to 0.6 for the three domains (i.e. the three soil types). Elliptic refinement of the parabolic solution is done for completeness. The target accuracy was set at 10^{-10}. The position of the breaker line is determined by the offshore distance at which the normalized wave height H/H_0 equals 0.9.

6.2.1.1. Silty sand beach

The runs PW1 to PW4 use Domain#1, which is a silty sand beach. Figure (6.2a-d) shows the contours of the normalized wave heights for the four runs, from which the position of the breakerline can be determined.

6.2.1.2. Sandy beach

The same analysis done in the last section for the silty sand beach is repeated here using runs PW5 to PW8 for the sandy beach (Domain#2). In this case the offshore root

mean square wave height is set to 1.5 meters in order to observe the breaking criteria on the steep sandy beach slope. Figure (6.3a-d) shows the contours of the normalized wave heights for the four runs, from which the position of the breakerline can be determined.

6.2.1.3. Gravel beach

The same is done for the gravel beach (Domain#3) with the runs PW9 to PW12. The offshore root mean square wave height was set to 2.0 m. Figure (6.4a-d) shows the contours of the normalized wave heights for the four runs, from which the position of the breakerline can be determined.

6.2.1.4. Discussion

The runs PW1 to PW12 are used to investigate the sensitivity of the wave model to the breaking coefficient γ. Only the parabolic wave model was investigated, because the elliptic refinements do not affect the position of the breakers but only the diffraction pattern behind the breakwater. It can be shown from Table (6.3) that the breaker line moves onshore by increasing the value of the breaking coefficient. A power equation can fit the data very well as shown in Figure (6.5). The equations that best fit the data are as follows:

$$X_B = 150.73\ \gamma^{-1.5634} \qquad \text{Silty sand beach} \qquad (6.2)$$

$$X_B = 104.14\ \gamma^{-1.2273} \qquad \text{Sandy beach} \qquad (6.3)$$

$$X_B = 105.3\ \gamma^{-1.6552} \qquad \text{Gravel beach} \qquad (6.4)$$

where, X_B is the distance from the shoreline to the breaker line.

It can be seen from Figure (6.5) that the wave model is very sensitive to the coefficient of breaking γ. Therefore, the choice of the coefficient of breaking γ should be made carefully.

Table (6.3): Effect of breaking coefficient on the position of the breakwater

γ	Position of the breaker line		
	Silty sand beach (H_0=1.0)	Sandy beach (H_0=1.5m)	Gravel beach (H_0=2.0)
0.9	180	115	125
0.8	205	145	153
0.7	275	157	190
0.6	330	195	245

6.2.2. Effect of the dissipation calibration constant

The wave energy dissipation due to wave breaking is governed by the following Equation:

$$f_b = \frac{\alpha}{\pi} \omega Q_b \frac{1}{b^2} \tag{6.5}$$

where, α is a calibration constant (standard value is 1.0), Q_b is the probability that at a specific point in the field, the wave height reaches its maximum value, ω is the angular wave frequency, and b is the ratio between the actual wave height and the maximum wave height (Beltrami, G.M. et al., 2001, after Battjes and Janssen, 1978).

Three runs were used to study the effect of changing the constant α on the wave model results. The reference for comparison was based on run PW14, which is essentially the same as run PW1 using Domain#1 and a value of unity for α. The value of α is set to 0.7 for PW13 and 1.3 for PW15. Figure (6.6a-c) shows the normalized wave height contours for the three runs. The larger value of α, the larger energy dissipation, and

consequently, the farther the breaker line from the shoreline. The constant α, however, does not affect the wave pattern behind the offshore breakwater because the wave heights are too small and no breaking occurs in the lee side of the structure.

6.2.3. Effect of offshore wave height

The effect of changing the offshore wave height on the transformed wave is studied by changing the offshore wave height in the range from 0.5 m to 2.0 m for Domain#1. Runs PW16 to PW19 are used for this purpose. Figure (6.7a-d) shows the normalized wave heights for the four runs. Figure (6.7) shows that the model is very sensitive to the offshore wave height. For the first two runs, no breaking occurs offshore the breakwater; therefore, the diffraction pattern behind the breakwater remains unchanged. However, diffraction pattern behind the breakwater starts to change if the offshore wave height exceeds 1.5 m due to the breaking of wave offshore the breakwater, as shown in Figure (6.7-c and d). The absolute breaking wave heights are very similar for the four runs as shown in Figure (6.8). For the last two runs, where breaking occurs before the breakwater, the diffracted wave heights behind the breakwater are quite similar as shown in Figure (6.8c, and d). Therefore, the following can be concluded:

1. The normalized diffraction pattern behind the breakwater does not change by changing the offshore incident wave height as long as the breakwater is located offshore the breaker line,

2. The absolute diffraction pattern behind the breakwater does not change by changing the offshore incident wave height, if the breakerline is located offshore the breakwater,

3. The absolute breaking wave heights do not change by changing the incident wave height, and

4. The model is insensitive to the incident wave height. However, the position of structures with respect to the breaker line is very important.

6.2.4. Effect of wave period

The effect of changing the wave period on the transformed wave is studied in this section. This is done using runs PW20 to PW23 through which the wave period is changed in the range from 4.0 seconds to 7.0 seconds. The wave period directly affects the wave length. Therefore, the ratio between the breakwater length and the wavelength changes by changing the wave period. Due to this reason, the diffraction pattern behind the breakwater changes significantly from one run to another, as shown in Figure (6.9a-d).

Figure (6.9) shows also that the position of the breaker line changes significantly by the change in the wave period. The breakerline moves offshore as the wave period decreases, or the steepness of the wave increases. Table (6.4) shows how the position of the breakerline X_B changes with the wave period T. The position X_B is defined as the distance from the shoreline to the point at which the wave height is 90% of the incident wave height.

A power equation can best fit the data as shown in Figure (6.10). For this particular case the equation is as follows:

$$X_B = 1592.8T^{-1.956} \tag{6.6}$$

Using Equation (6.6), it can be shown that a change of +5% and -5% of the wave period can cause a change in the position of the breakerline of -5.5% and +6.5%, respectively. This change is acceptable. However, a change of +20% and -20% of the wave period can cause a change in the position of the breakerline of -20% and +30%, respectively, which is not acceptable.

Table (6.4): Breakerline position

T (s.)	X_B (m)
4.0	313
5.0	225
6.0	180
7.0	162

6.2.5. Effect of initial solution and target accuracy on the elliptic model

In order to study the effect of the target accuracy, which should be set by the user, 8 runs are performed on domain#4. The first four runs (EW1 to EW4) use the offshore wave conditions as an initial condition for the elliptic solver;

$$H = H_0 \qquad \theta = \theta_0 \tag{6.7}$$

The other four runs (EW5 to EW8) use the parabolic solution as an initial solution for the elliptic model.

Figure (6.11a-d) shows the normalized wave height patterns for the first grope of runs. It can be shown that the solution changes significantly by changing the accuracy. It needs 1100 iterations to bring the error down to the order of 10^{-07}. It is shown from Figure (6.11a-d) that significant loss of the solution quality occurs if the accuracy is set less than 10^{-4}.

On the other hand, Figure (6.12a-d) shows the normalized wave height contours for the other group of runs. It can be shown that even for accuracy as low as 10^{-3}, the elliptic solution is acceptable. Figure (6.12c and d), which correspond to accuracies 10^{-5} and 10^{-4}, respectively, look very much the same. Figure (6.12-a) is effectively the same except for some kinks due to the round off errors. It takes the model only 500 iterations to bring the error down to the order of 10^{-6}, and 300 iterations to bring the error down to the order of 10^{-5}. It can be concluded that using the parabolic approximation as an initial condition for the elliptic model is an effective tool to enhancing the solution quality and reducing the total number of iterations required to reach an acceptable solution.

6.2.6. Grid dependency analysis

For the purpose of studying the grid dependency of the wave models, a flat bed domain was chosen (Domain#4), and the incident wave length was set to 50.0 meters, which corresponds to 5.66 seconds wave period. A 140 meters length breakwater was set in the middle of the domain. First, the elliptic model is studied through runs EW9 to EW11 through which the grid sizes are 5 m, 2.5 m and 1.67 m, respectively. It should be noted that the grid size should be less or equal to one tenth of the wave length. Therefore, the 5 meters grid size was adopted for run EW9 as the upper limit. Figure (6.13a-c) shows the normalized wave heights after the three runs EW9, EW10, and EW11, respectively. In order to achieve a symmetric solution for runs EW10 and EW11 (Figure (6.13b and c)), the target accuracy has to be reduced to 10^{-7} and 10^{-9}, respectively. In addition, the smaller the grid size considered, the larger the matrix to be solved. Therefore, it requires a total of 2000 relatively slower iterations (due to the bigger matrix) for the grid of 2.5

meters size, and 11,000 relatively slower iterations for the grid of size 1.67 meters. On the other hand, only 500 iterations are required to reach the solution for a grid of 5.0 meters size (Figure (6.13a)). Comparing Figure (6.13a-c), it can be shown that solution is very much the same, except for smoother contours for the finer grids. Therefore, it can be concluded that the elliptic model is grid-independent, and the best grid size is the largest possible one, which corresponds to one tenth of the wave length.

The parabolic model grid dependency is studied using runs PW24 to PW27. The constraints for the grid sizes are as follows:

$$\Delta x \le L/3 \qquad \text{and} \qquad \Delta y \le L/10 \tag{6.8}$$

where, L is the local wave length. Table (6.2) shows the input parameters for the four runs. Figure (6.14a-d) shows the output of the four runs. Keeping in mind that the reflections in front of the breakwater cannot be modeled, Figure (6.14b) seems to represent the closest solution to the elliptic solution, which corresponds to upper limits of Equation (6.8). It is useful to note that even for larger grid size in y-direction, the solution is still acceptable, as shown in Figure (6.14a), which corresponds to $\Delta y = L/5$. On the other hand, refining the grid in x-direction does not improve the solution as shown in Figure (6.14c and d). On the contrary, more noise appear in the breakwater lee side. Therefore, artificial smoothing has to be introduced in case of fine grids. In conclusion, the best grid sizes for the parabolic model is the upper limit of Equation (6.8).

6.2.7. Model capabilities for wide angles

In order to test both the elliptic and parabolic wave models for wide angles, domain #4 is used for the runs, and the wave angle is set at 20°, 30°, 50° and 60°. Figure

(6.15a-d) compares between the elliptic and the parabolic solutions for small wave angles (20° and 30°). It can be concluded that the parabolic model can acceptably simulate the diffraction pattern behind the offshore breakwater for small wave angles.

Figure (6.16a-d) compares between the elliptic and the parabolic solutions for wide wave angles (50° and 60°). The parabolic model solutions are similar to the elliptic wave model in areas around the breakwater. However, significant changes are reported away from the breakwater. Therefore, the initial parabolic solution is not expected to improve convergence of the elliptic solver for the case of large wave angle with respect to coastal structures. In all cases, the elliptic model simulations are realistic.

6.3. Hydrodynamics Model Sensitivity Analysis

The hydrodynamic model's sensitivity is tested for the following parameters:

1. Bed friction coefficient C_f,
2. Eddy diffusivity ε,
3. Time step Δt, and
4. Grid sizes (Δx and Δy).

Table (6.5), describes the runs made by the hydrodynamic model. Domain #1 is used for all the runs. The simulation time for all the runs was one hour, which ensures that the model reaches the steady state.

Table (6.5): Sensitivity analysis runs for the hydrodynamic model

Run#	Wave Run #	Hz. grid (m)		Δt (s)	Main parameters		Effects studied
		Δx	Δy		C_f	ε (m^2/s)	
H1	PW1	10	10	2.2	0.01	1.646	Grid dependency.
H2		20	20				
H3		30	30				
H4		40	40				
H5		50	50				
H6	PW1	20	20	0.2	0.01	1.646	Effect of the time step on the solution.
H7				0.5			
H8				1.0			
H9				2.0			
H10				3.0			
H11				3.6			
H12				4.4			
H1	PW1	10	10	2.2	0.01	1.646	Effect of the bottom friction coefficient on the solution.
H13					0.009		
H14					0.008		
H15					0.011		
H16					0.012		
H1	PW1	10	10	2.2	0.01	1.646	Effect of eddy diffusivity on the solution.
H17						-10%	
H18						-20%	
H19						+10%	
H20						+20%	

6.3.1. Grid dependency analysis

In order to study the hydrodynamic model's grid dependency, the runs H1 to H5 have been used. The same coastal domain is solved with different grid sizes and the kinetic energy at the steady state is calculated for each run. Table (6.5) shows the input parameters used for the study. It should be kept in mind that as the grid gets coarser the geometrical representation of the problem changes. Table (6.6) shows the results of the five runs. It can be shown that the kinetic energy and maximum velocities for the first

three runs are the same. As the grid gets coarser, the domain's and coastal structure's geometric representation change and significant changes in the results start to appear. For example, the 180 m long offshore breakwater, which is adopted in wave analysis, cannot be represented by grids of 40 m or 50 m size.

Table (6.6): Grid dependency for the hydrodynamic model.

Run #	Grid size $\Delta x \times \Delta y$	K.E./ρ (m^5/s^2)	u_{max} (m/s)	v_{max} (m/s)	η_{max} (cm)	η_{min} (cm)
H1	10×10	7064	0.4195	0.4269	12.77	-2.8
H2	20×20	7404	0.4172	0.4163	10.83	-2.9
H3	30×30	7232	0.4040	0.4391	9.69	-3.4
H4	40×40	6773	0.3310	0.4078	9.34	-2.6
H5	50×50	8114	0.5060	0.3953	8.60	-2.0

6.3.2. Time step dependency analysis

In order to study the time step dependence, the time step was changed in the range from 0.2 to 4.4 seconds, as shown in Table (6.5). The results show that the model is independent of the time step as shown in Figure (6.17), where the total kinetic energy of the flow does not depend on the time step.

6.3.3. Effect of the bed friction coefficient

In order to study the effect of the bed friction coefficient on the hydrodynamic model, the runs H13 to H16 have been used and compared with the reference run H1. The combined wave current friction coefficient C_f is changed by ±10% and ±20%. Table (6.7) summarizes the outputs. It can be shown that the model is very sensitive for the bed friction coefficient as 10% and 20% decrease in the friction coefficient results in 18% and 40% increase in the total kinetic energy, respectively. On the other hand, overestimating

the bed friction coefficient by 10% and 20%, leads to a decrease in the total kinetic energy by 14% and 25%, respectively. The water surface elevations are not sensitive to the bed friction coefficient as shown in Table (6.7).

Table (6.7): Effect of changing the coefficient of friction on the model results.

Run #	C_f	K.E./ρ (m^5/s^2)	u_{max} (m/s)	v_{max} (m/s)	η_{max} (cm)	η_{min} (cm)
H1	0.01	7064	0.4195	0.4269	12.77	-2.8
H13	0.01-10%=0.009	8319	0.4610	0.4518	12.77	-2.8
H14	0.01-20%=0.008	9896	0.5074	0.4790	12.77	-2.9
H15	0.01+10%=0.011	6057	0.3830	0.4047	12.77	-2.7
H16	0.01+20%=0.012	5243	0.3512	0.3836	12.77	-2.7

6.3.4. Effect of the eddy diffusivity

In order to study the effect of the eddy diffusivity on the hydrodynamic model, the runs H17 to H20 have been used and compared with the reference run H1. The eddy diffusivity is changed by ±10% and ±20%. In this study, the eddy diffusivity is calculated by the empirical formula proposed by Leont'yev (1999) because it sets a constant value for the eddy diffusivity throughout the whole computational domain. Therefore, the effect of changing the eddy diffusivity by a certain value can be studied. Table (6.8) summarizes the outputs. It can be shown that underestimating the eddy diffusivity by 10% and 20% leads to increase in the total kinetic energy by 5% and 10%, respectively. On the other hand, a 10% and 20% overestimation of the eddy diffusivity lead to 4% and 8% of decrease in the total kinetic energy, respectively. The water surface elevations do not change with the change of the eddy diffusivity. Therefore, the hydrodynamic model is less sensitive to the eddy diffusivity than the bed friction coefficient.

Table (6.8): Effect of changing the eddy diffusivity on the model results.

Run #	ε (m^2/s)	K.E./ρ (m^5/s^2)	u_{max} (m/s)	v_{max} (m/s)	η_{max} (cm)	η_{min} (cm)
H1	1.646	7064	0.4195	0.4269	12.77	-2.8
H17	1.646-10%=1.481	7396	0.4314	0.4308	12.78	-2.8
H18	1.646-20%=1.317	7763	0.4437	0.4347	12.78	-2.8
H19	1.646+10%=1.811	6761	0.4081	0.4229	12.76	-2.8
H20	1.646+20%=1.975	6482	0.3972	0.4188	12.76	-2.8

6.4. Sediment Transport Model Sensitivity Analysis

The sensitivity of the parameters involved in the sediment transport model is tested in this section. The model parameters can generally be classified into six groups, which define the water column, the sediment properties, the current, the wave, the geometry and the calibration parameters. As shown in Table (6.9), the water column and the sediment properties are defined by the water depth h and the median grain size D, respectively. The current is described by its depth averaged speed u_c which has an angle ϕ_{wc} measured anticlockwise from the wave propagation direction. The maximum orbital velocity at the top of the bottom boundary layer u_{bm} and the wave period T are used to describe the waves. The geometric parameters that are involved in the model are the width of the surfzone X_B and the offshore distance x_b measured from the breaking point. Finally, three calibration parameters are discussed here; κ_d and Π_c which are used to calibrate the direction function for the transport due to waves, and κ_c which is used in the smoothing function for the critical shear stress between the surfzone and the deep zone. Both A_c and A_w are not included in the analysis because they affect the transport loads linearly. Therefore, they have been assigned a fixed value of 0.5 throughout the analysis. The effect of each one of the previous parameters is separately studied in the following

sections. Table (6.9) describes the runs used in the analysis. All the parameters are tested by changing the parameter of interest over a certain range and fixing all other parameters as shown in Table (6.9). The current transport loads QCX and QCY, wave transport loads QWX and QWY and the total loads QSTX and QSTY are calculated for all the runs.

Table (6.9): Sensitivity analysis runs for the sediment transport model.

	Parameter	Lower limit	Upper limit	Fixed value
Water column	h (m)	0.1	10.0	2.5
Sediment	D (mm)	0.05	7.5	0.2
Current	u_c (m/s)	0.0	3.0	0.2
	ϕ_{wc}	$-\pi$	π	0.0
Wave	u_{bm} (m/s)	0.0	1.0	0.35
	T (s)	4.0	10.0	7.0
Geometry	X_B (m)	30.0	70.0	50.0
	x_b (m)	-50.0	300.0	100.0
Calibration	κ_d	0.0	20.0	1.0
	Π_c	0.1	2.0	1.0
	κ_c	0.0	2.0	1.0

6.4.1. Effect of water depth

The effect of the water depth on the transport loads is studied by changing the depth from as shallow as 10 cm to as deep as 10.0 m. Figure (6.18) shows the relation between the water depth and the transport loads. Generally, it can be concluded that the transport loads decrease with the increase of the water depth. The model is more sensitive to the water depth in shallow depths than in large depths as shown in Figure (6.18). The model realistically estimates negative (offshore) transport loads due to waves for relatively large water depths, which can be explained by the increase in wave height as the water depth increases giving that the maximum bottom orbital velocity u_{bm} is fixed at 0.35 m/s.

6.4.2. Effect of grain size

The effect of the grain size on the transport loads is studied by changing the median grain size from 0.05 mm to 7.5 mm as shown in Table (6.9). As shown in Figure (6.19), initially the sediment transport loads increase rapidly with the increase of the grain size. This phenomenon is explained by the initial increase of the ripple size due to the decrease in the mobility number Ψ_m, which in turn causes an increased wave friction coefficient and consequently increased sediment loads. At a certain point (D = 0.8 mm), the decrease in the mobility number is not transformed into increase of the vortex ripples size. Therefore, the sediment transport rates starts to decrease gradually owing to the direct effect of the decreased mobility on the transport loads. At a certain point (D = 6.15 mm), where the mobility of the flow is so low that the bottom shear stress is less than the critical shear stress, sediment transport stops. As discussed in the last chapter, the grain size is a major factor in determining the critical shear stress, the bottom shear stress, the bottom roughness, the shape of the vortex ripples and the transport loads. This explains the changing trend of the sediment loads with the grain size as shown in Figure (6.19). Therefore, it is concluded that model is very sensitive to grain size.

6.4.3. Effect of the average current speed

The effect of the current speed on the transport loads is studied by changing the current speed in the range from 0.0 m/s to 3 m/s. As shown in Figure (6.20), the current transport load increases rapidly with the increase of the current speed due to the direct relation between the current speed and the transport load due to the current. The wave

transport load increases indirectly and slowly, however, due to the increased combined wave-current shear stress as shown in Figure (6.20).

6.4.4. Effect of current direction

The current direction is given relative to the wave direction by the inclination angle ϕ_{wc}, which is measured anticlockwise from the wave direction. Figure (6.21) shows the relation between the current inclination angle and the transport loads. The transport in x-direction (wave direction) is maximized when the current coincides with the wave direction, as shown in Figure (6.21a). The transport due to waves is not related to the current direction. Therefore, it remains unchanged as shown in Figure (6.21a and b). Both the total and current transport loads, however, decrease rapidly with the deviation of the current from the wave direction. As the inclination angle changes, the transport in the y-direction fluctuates around the zero in a sinusoidal fashion as shown in Figure (6.21b).

6.4.5. Effect of the maximum bottom orbital velocity

The effect of the maximum bottom orbital velocity on the transport loads is studied by changing its values in the range from 0.0 to 1.0 m/s, as shown in Figure (6.22). Although the transport due to current seems to be an increasing function of the bottom orbital velocity, this is not necessarily the case. Initially, no transport load exists due to the threshold of sediment movement. Then the sediment load due to the current increases rapidly due to the increase in the bottom orbital velocity which is accompanied with a rapidly increasing ripple size (i.e increasing roughness and transport load). When the bottom orbital velocity reaches a certain value (u_{bm} = 0.18 m/s), the increased mobility results in the decrease of the size of the vortex ripple size, which in turn causes the

reduction of the bottom roughness and consequently the reduction of the transport loads. At a certain point, the direct effect of increased transport loads due to increased mobility dominates the indirect effect of reduced transport loads due to reduced bottom roughness (caused by the increased mobility), as shown in Figure (6.22). The direction of the current transport loads is always the same as the current direction. The direction of the wave transport loads, however, is changing. Large waves with large bottom orbital velocities result in offshore (negative) transport and vice versa, as shown in Figure (6.22). The transport due to waves reverses its direction at a null point (u_{bm} = 0.4 m/s) at which the transport is effectively zero. As shown in Figure (6.22), there is no discontinuity at the null point due to the application of the smoothing direction function F_d. It is shown from Figure (6.22), that the wave transport load is very sensitive to large value of the bottom orbital velocity, unlike the current transport load.

6.4.6. Effect of the wave period

The effect of the wave period on the transport loads is studied by changing its value in the range from 4.0 to 10.0 s. Figure (6.23) shows the relation between the wave period and the transport loads for a constant direction function (i.e. F_d = 1), which is realistically a decreasing function for both the current and wave transport loads (i.e. steeper waves derive more sediments into motion). The model is more sensitive to short waves (smaller wave period) than long waves, as shown in Figure (6.23). The wave transport, however, changes its direction from offshore transport for short wave to onshore transport for long waves, as shown in Figure (6.24). Due to the smoothing direction function, the wave transport load is not always a decreasing function with the

wave period. It is, however, realistically a decreasing function for the offshore transport until the stable point (at T = 6.4 s) where no transport occurs and turns to an increasing function for longer waves (i.e. swells of $T > 6.4$ s), which cause onshore transport.

6.4.7. Effect of the surfzone width

The effect of the surfzone width on the sediment transport rates for a point outside the surfzone is studied by changing the width of the surfzone from 30.0 m to 70.0 m. Figure (6.25) shows that the transport loads slightly increase with the increase of the surfzone width. The surfzone width affects the calculation of the critical shear stress, where the ratio between the offshore distance x_b and the surfzone width X_B is used to smooth the critical shear stress from zero inside the surfzone to its regular values offshore. It is therefore worth mentioning that the width of the surfzone does not affect the sediment transport rates for a point inside the surfzone due to the fact that the critical shear stress is assumed zero in this zone.

6.4.8. Effect of the offshore distance

The effect of the offshore distance in shown in Figure (6.26), where its value varies from -50.0 m inside the surfzone to 300.0 m outside the surfzone. As mentioned in the previous section, the transport loads inside the surfzone (i.e. $x_b < 0$) are not affected by the offshore distance x_b due to the fact that the critical shear stress is zero. Outside the surfzone, the transport loads starts to decrease rapidly until it reaches a stable value. The transport loads inside the surfzone are enhanced due to the increased turbulence due to wave breaking.

6.4.9. Effect of the calibration parameter κ_d

The calibration parameter κ_d is used as a scaling parameter in the direction smoothing function F_d. Therefore, it does not affect the transport due to the current as shown in Figure (6.27). The smaller the value of κ_d the smoother the transport loads around the null point. Therefore, for a point 100.0 m offshore the breaker line, the wave transport load is not affected for $\kappa_d > 10$. Smoothing effects, however, are significant for values of $\kappa_d < 10$, as shown in Figure (6.27). In other words, it is to say that the larger the value of κ_d the smaller the smoothing zone around the null point.

6.4.10. Effect of the calibration parameter Π_c

The dimensionless calibration parameter Π_c is used to identify the null point at which the wave transport changes its direction. Therefore, the transport due to current does not affect by changing this parameter, as shown in Figure (6.28). It is shown in Figure (6.28) that the offshore wave transport load is very sensitive to this parameter. The onshore wave transport rate, however, is less sensitive to this parameter. The importance of this parameter lies in the identification of the direction of the wave transport.

6.4.11. Effect of the calibration parameter κ_c

The calibration parameter κ_c is used as a scaling parameter in the calculation of the critical shear stress. Large values of κ_c correspond to large critical shear stress and consequently smaller transport rates, as shown in Figure (6.29). In the surfzone, both the values of the critical shear stress and κ_c is effectively zero. Like κ_d, the smaller the value

of κ_c the smoother the transition between zero critical shear stress at the surfzone and its regular values offshore, which is translated into smoother sediment transport rates.

6.5. Summary

In this chapter the sensitivity of the wave, hydrodynamic and sediment transport models have been studied. The equilibrium beach profile concept has been used to develop numerical domains for the analysis. It was found that the wave model is very sensitive to the breaking coefficient. The offshore wave height does not affect the breaking wave pattern in the surfzone. However, the diffraction pattern due to coastal structures may be affected by the change in the offshore wave height if the structures extend beyond the surfzone. On the other hand, the wave model is sensitive to the wave period. The elliptic model is proved to be highly dependent on the initial solution. Therefore, the combined parabolic/elliptic model is a very useful tool to reduce the total number of iterations and improve the solution quality. The best grid size for the wave models, parabolic and elliptic, is the largest possible grid size according to the stability criteria. The elliptic wave model is proved to be capable of modeling large wave angles. However, the parabolic wave model results for the case of large wave angles with coastal structures yields unreliable results. Therefore, using the parabolic solution as an initial solution for the elliptic wave models, for these cases, is not expected to improve the elliptic solver's converge. However, the parabolic model can still be used to simulate diffraction patterns behind coastal structures for small wave angles.

The hydrodynamic model is proved to be grid independent as long as the grid can geometrically represent the beach and the structures. The model is time-step independent as well. The hydrodynamic model is not quite sensitive to the bed friction coefficient and is less sensitive to the eddy diffusivity.

The sediment transport model sensitivity analysis evolved the effect of the parameters used in the model. The analysis is a very useful tool for the model calibration, where the behavior of the model was described under the change of the calibration parameters. The model is found to be most sensitive to grain size, current average velocity and bottom orbital velocity. The non-dimensional calibration parameter Π_c has the greatest effect on the wave transport load.

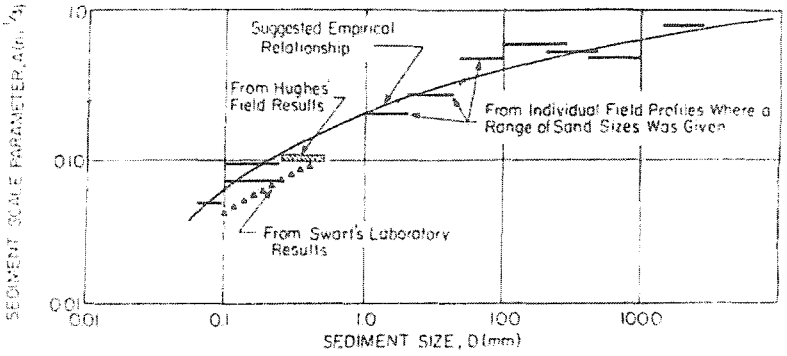

Figure (6.1): Beach profile scale factor *A* versus sediment diameter

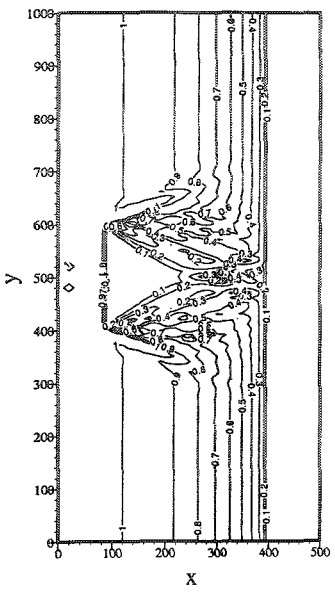

a) $\gamma = 0.9$

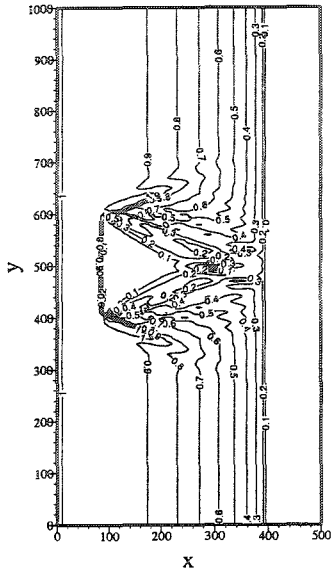

b) $\gamma = 0.8$

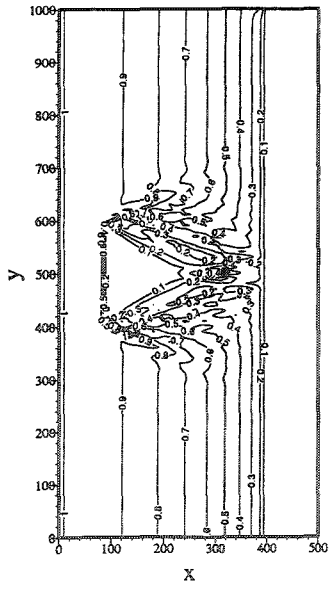

c) $\gamma = 0.7$

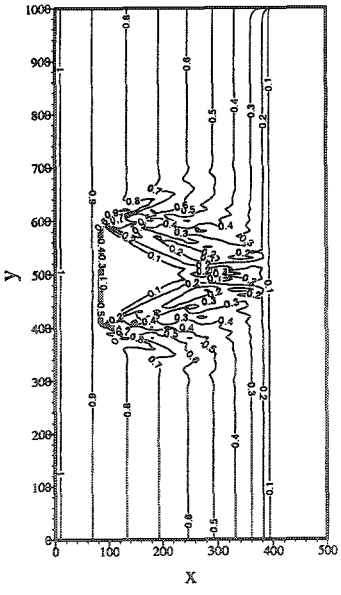

d) $\gamma = 0.6$

Figure (6.2): Effect of breaking coefficient on the position of the breakwater for silty sand beach

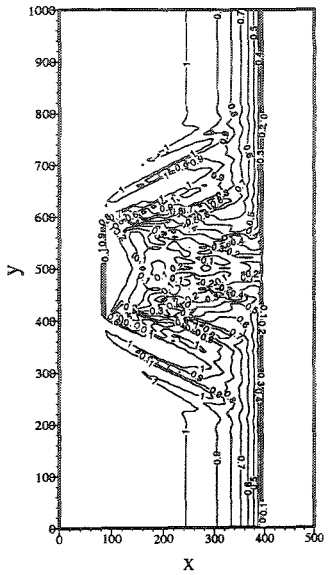

a) $\gamma = 0.9$

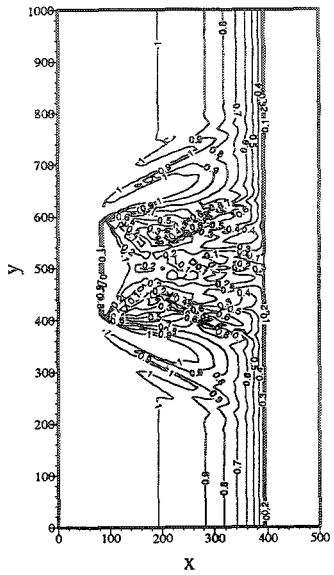

b) $\gamma = 0.8$

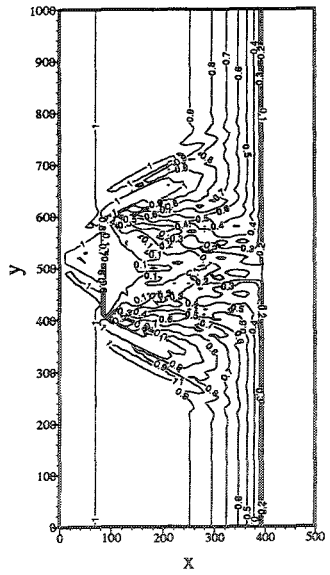

c) $\gamma = 0.7$

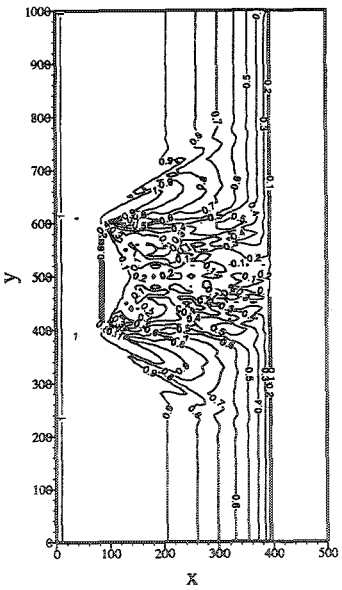

d) $\gamma = 0.6$

Figure (6.3): Effect of breaking coefficient on the position of the breakwater for sandy beach

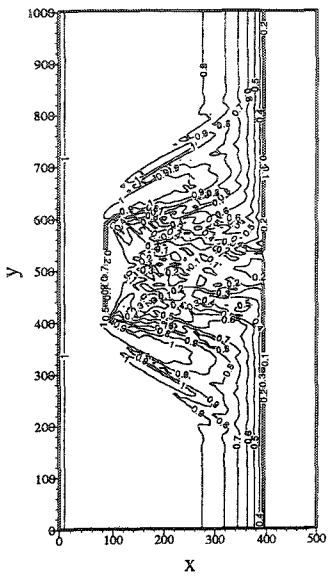

a) $\gamma = 0.9$

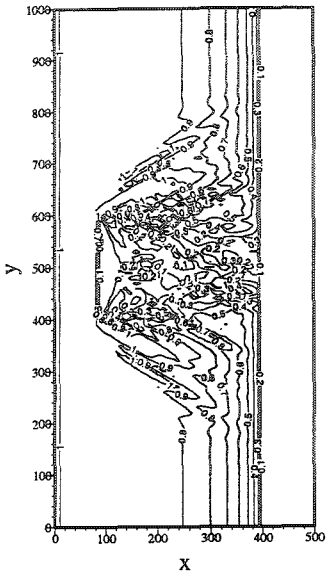

b) $\gamma = 0.8$

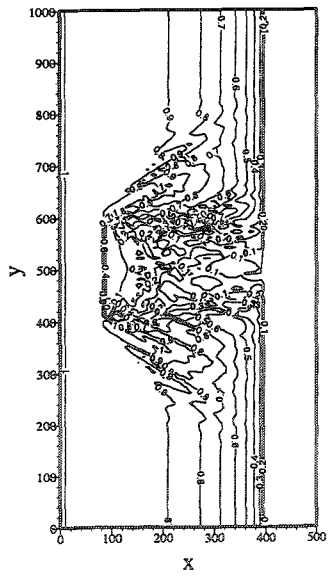

c) $\gamma = 0.7$

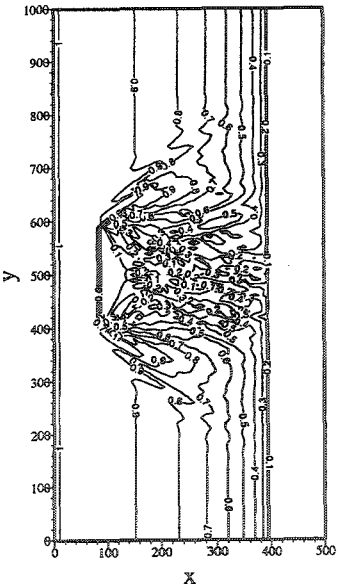

d) $\gamma = 0.6$

Figure (6.4): Effect of breaking coefficient on the position of the breakwater for a gravel beach

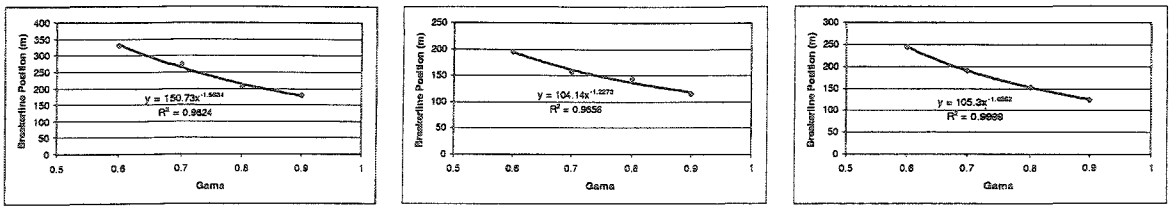

a) Silty sand beach b) Sandy beach c) Gravel beach

Figure (6.5): Relation between the breaker line position and the breaking coefficient.

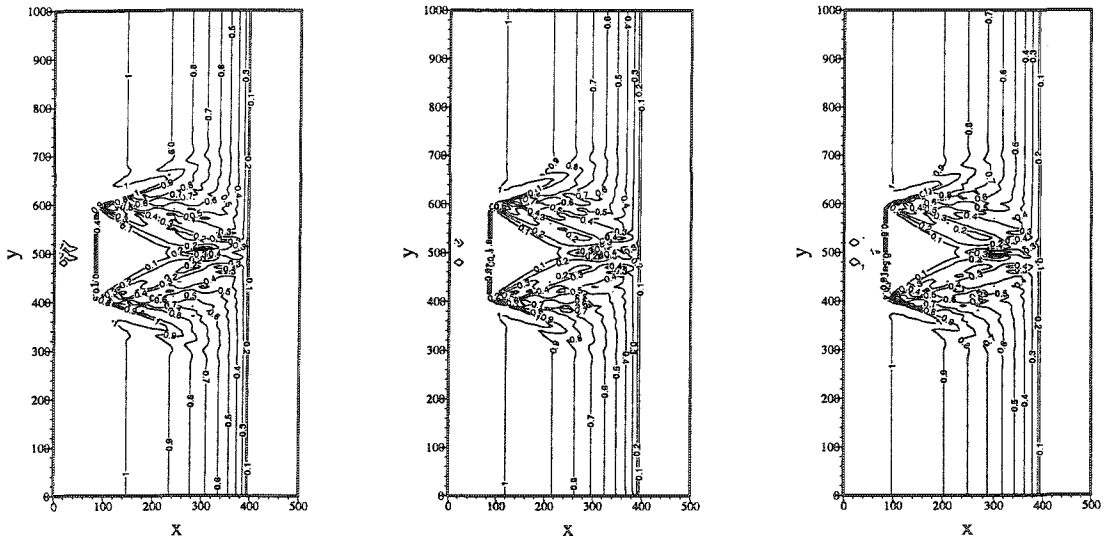

a) $\alpha = 0.7$ b) $\alpha = 1.0$ c) $\alpha = 1.3$

Figure (6.6): Effect of the calibration constant on the transformed wave.

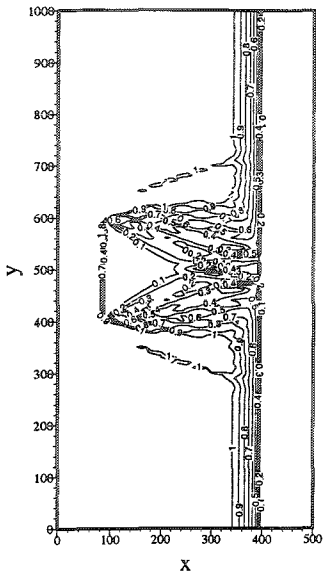

a) $H_0 = 0.5m$

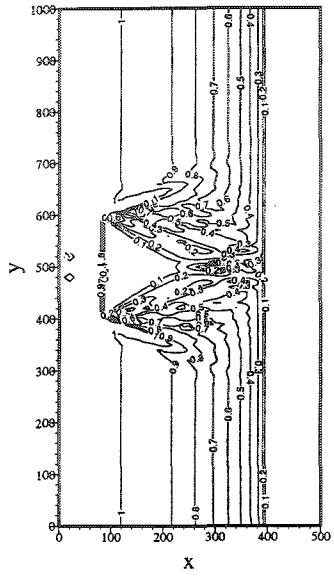

b) $H_0 = 1.0m$

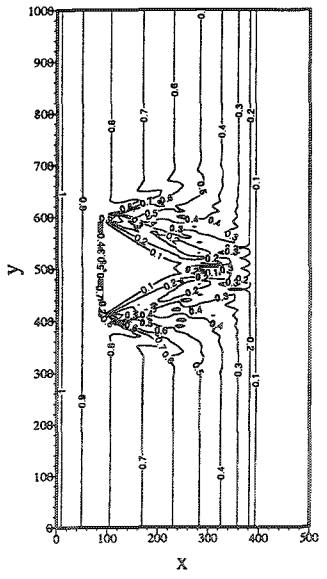

c) $H_0 = 1.5m$

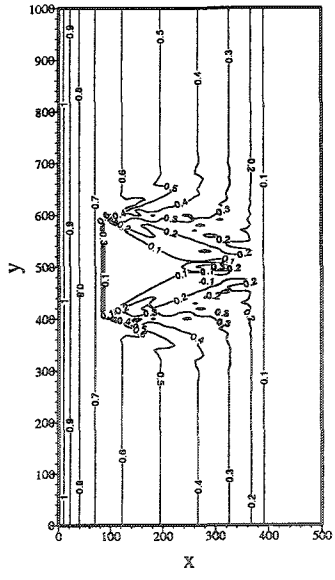

d) $H_0 = 2.0m$

Figure (6.7): Effect of offshore wave height (normalized wave height contours).

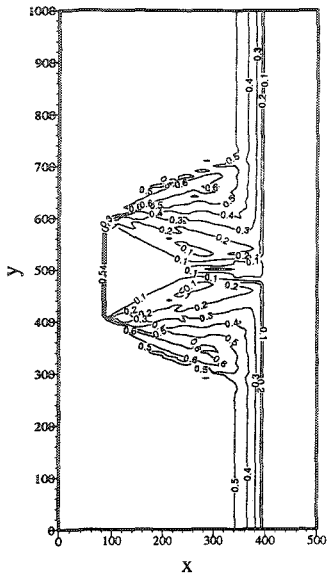

a) $H_0 = 0.5m$

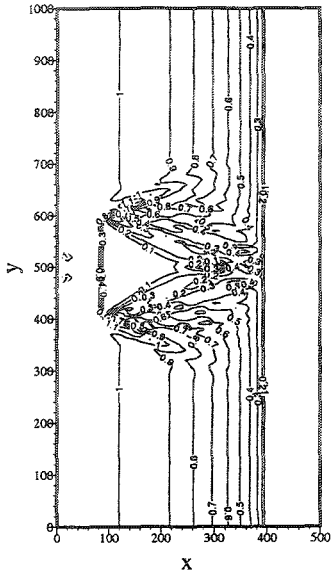

b) $H_0 = 1.0m$

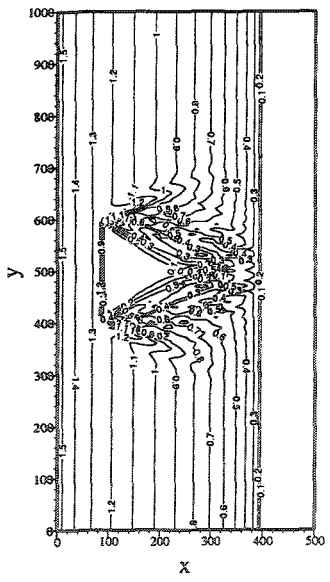

c) $H_0 = 1.5m$

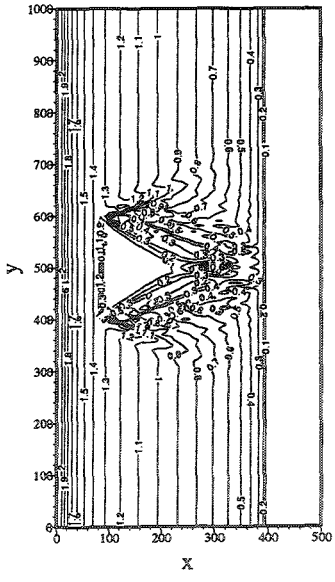

d) $H_0 = 2.0m$

Figure (6.8): Effect of offshore wave height (absolute wave height contours).

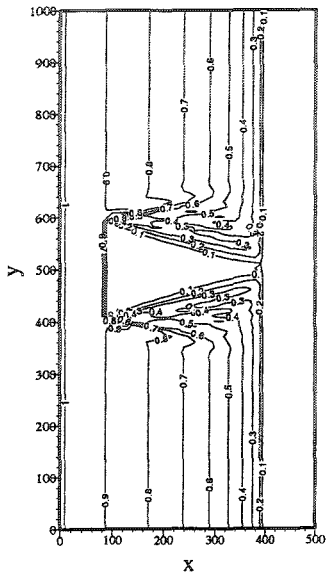

a) T = 4.0 s

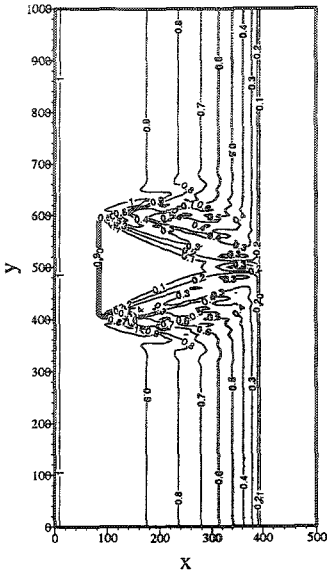

b) T = 5.0 s

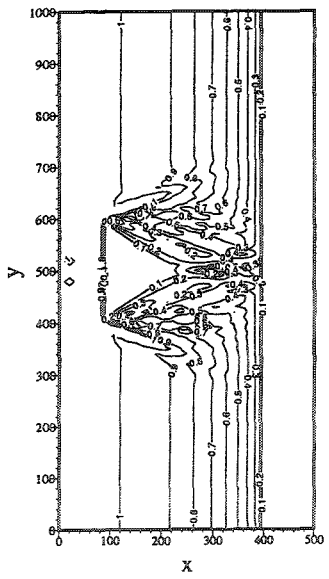

c) T = 6.0 s

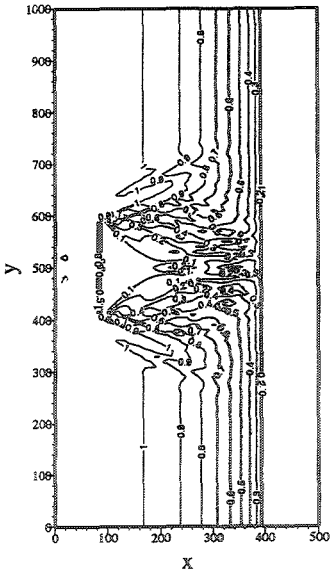

d) T = 7.0 s

Figure (6.9): Effect of wave period.

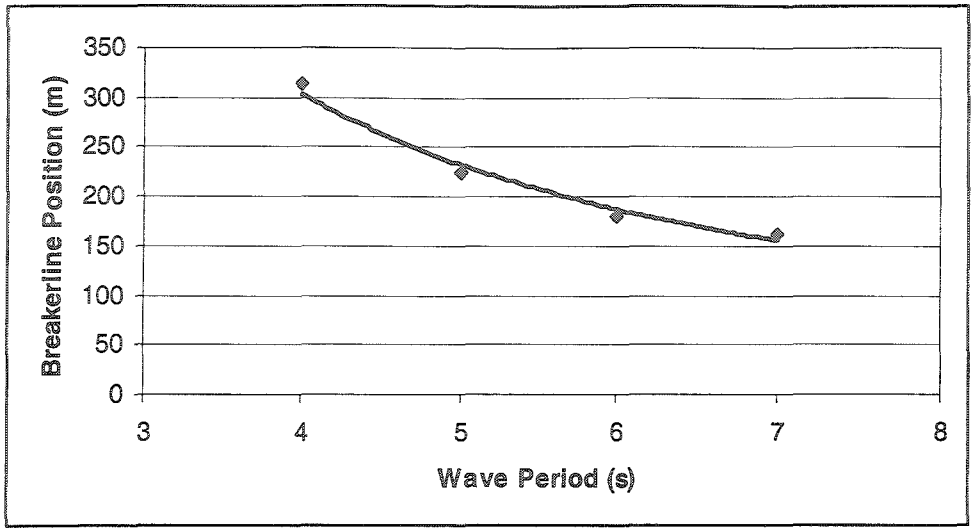

Figure (6.10): Relation between the wave period and the position of the breakerline.

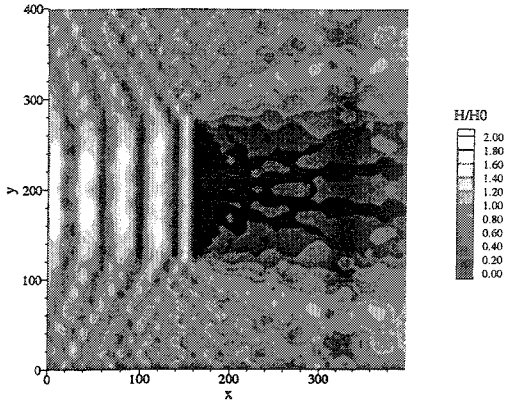

a) Accuracy = 10^{-6}

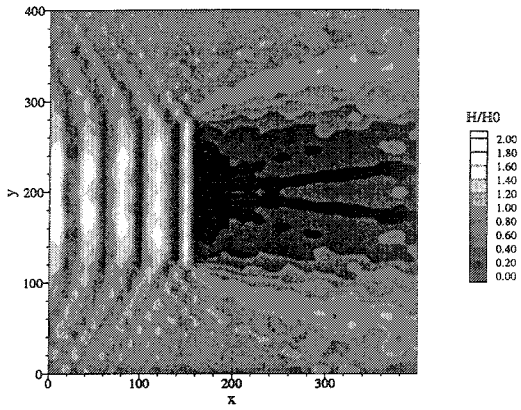

b) Accuracy = 10^{-5}

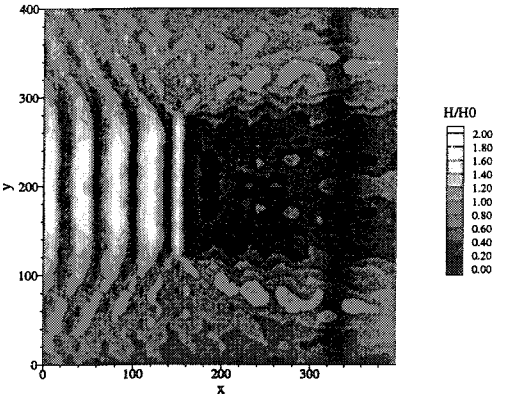

c) Accuracy = 10^{-4}

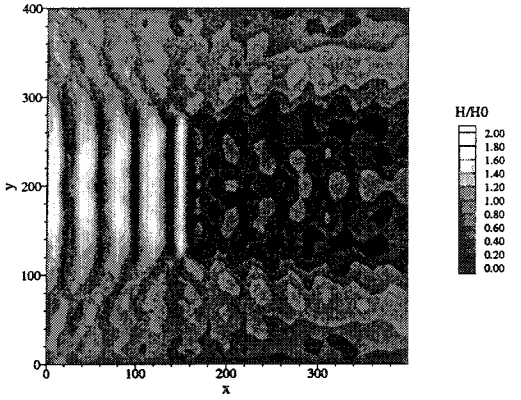

d) Accuracy = 10^{-3}

Figure (6.11): Normalized wave height contours (Deep water conditions are set as initial condition).

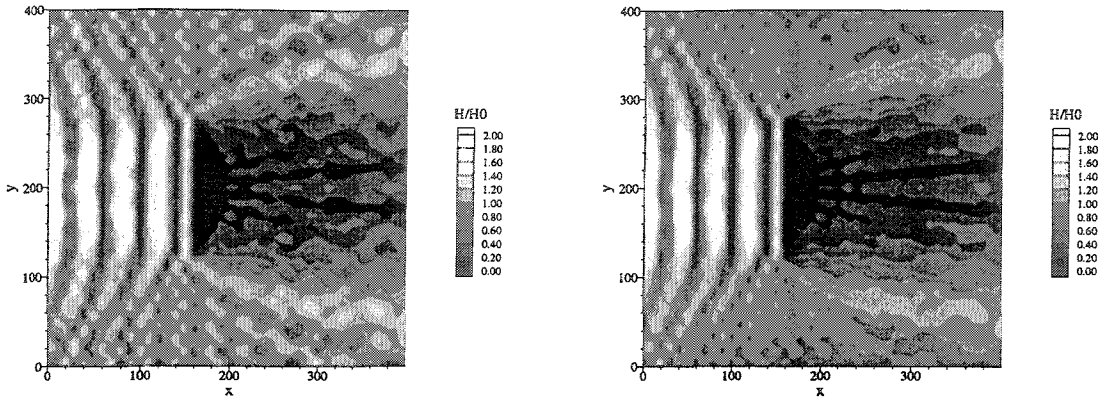

a) Accuracy = 10^{-6} b) Accuracy = 10^{-5}

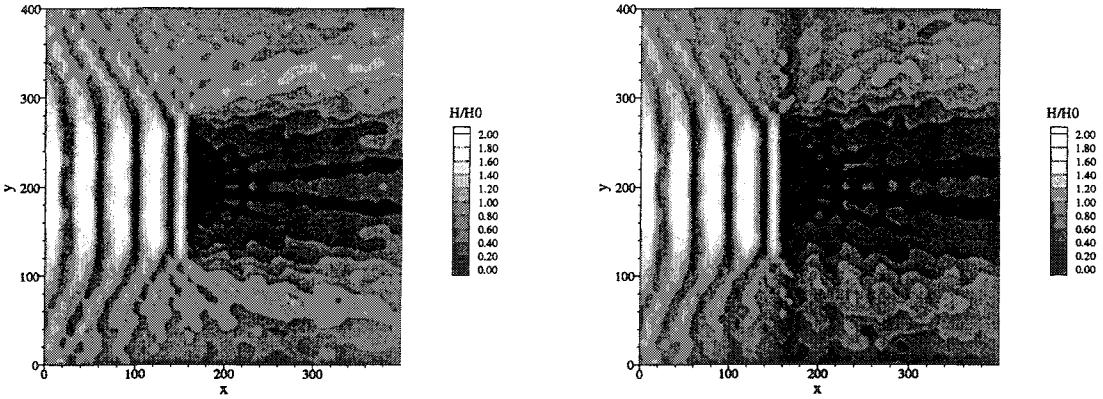

c) Accuracy = 10^{-4} d) Accuracy = 10^{-3}

Figure (6.12): Normalized wave height contours (Parabolic solution is used as initial condition).

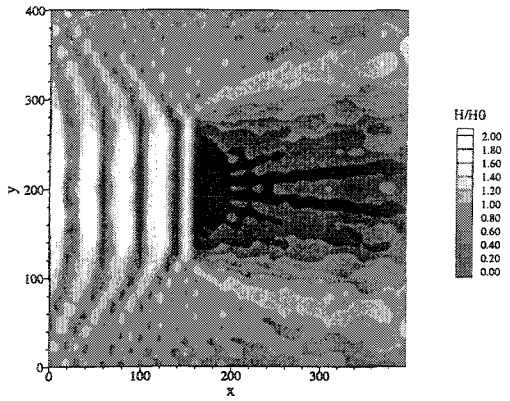

a) $\Delta x = \Delta y = 2.5$m, Accuracy = 10^{-5}

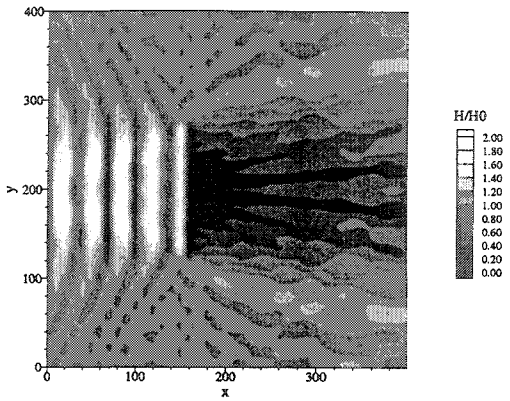

b) $\Delta x = \Delta y = 2.5$m, Accuracy = 10^{-7}

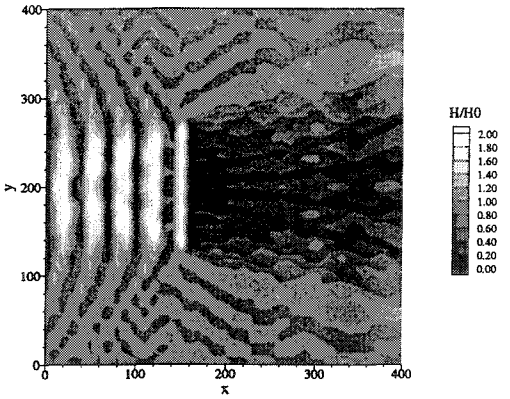

c) $\Delta x = \Delta y = 0.167$m, Accuracy = 10^{-9}

Figure (6.13): Normalized wave height contours (elliptic model with different grid size and accuracy).

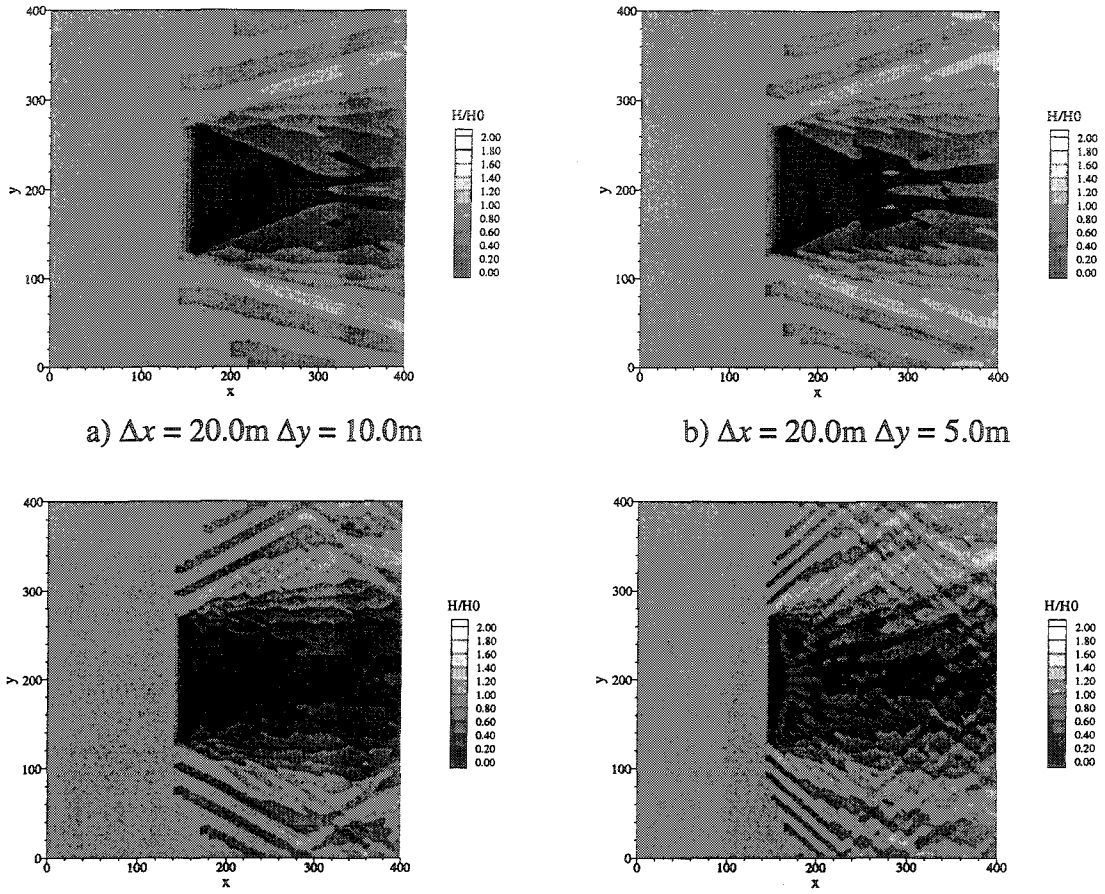

a) $\Delta x = 20.0\text{m}$ $\Delta y = 10.0\text{m}$

b) $\Delta x = 20.0\text{m}$ $\Delta y = 5.0\text{m}$

c) $\Delta x = 10.0\text{m}$ $\Delta y = 5.0\text{m}$

d) $\Delta x = 5.0\text{m}$ $\Delta y = 5.0\text{m}$

Figure (6.14): Normalized wave height contours (parabolic model with different grid size and accuracy).

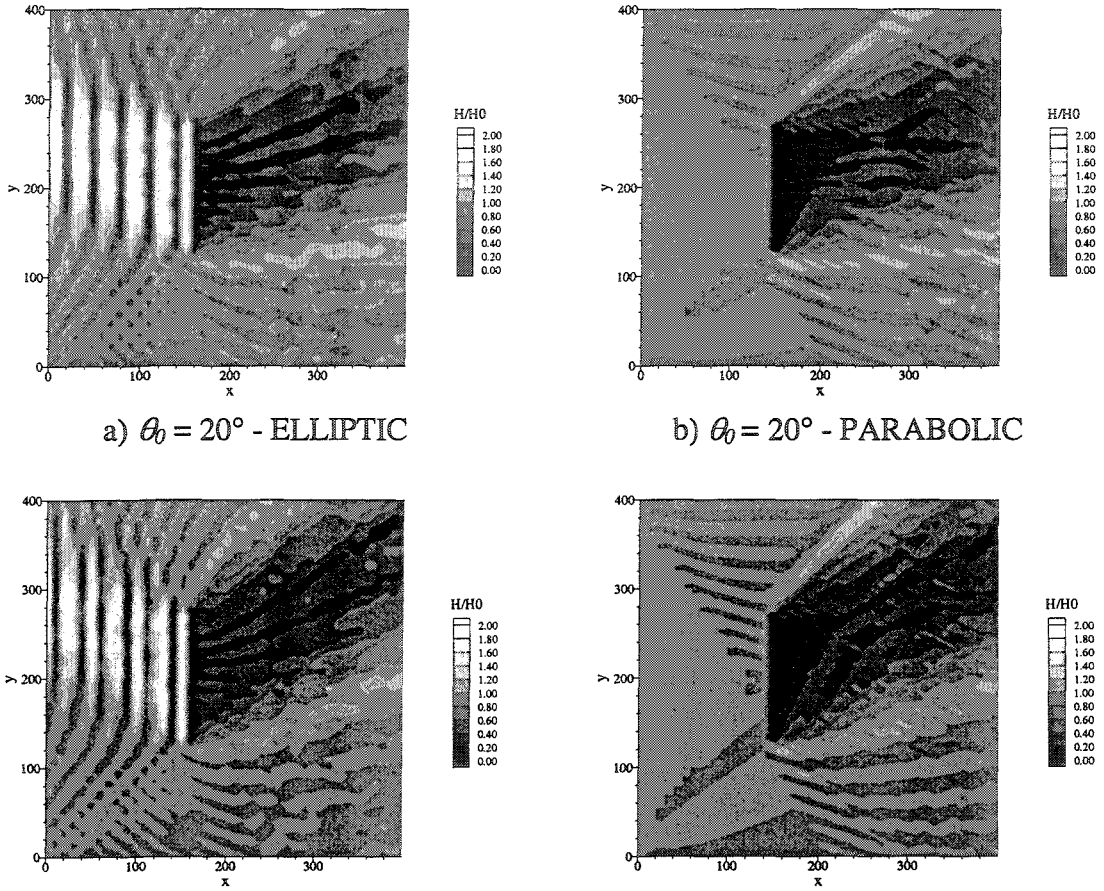

a) $\theta_0 = 20°$ - ELLIPTIC

b) $\theta_0 = 20°$ - PARABOLIC

c) $\theta_0 = 30°$ - ELLIPTIC

d) $\theta_0 = 30°$ - PARABOLIC

Figure (6.15): Comparison between the elliptic and the parabolic solutions for small wave angles.

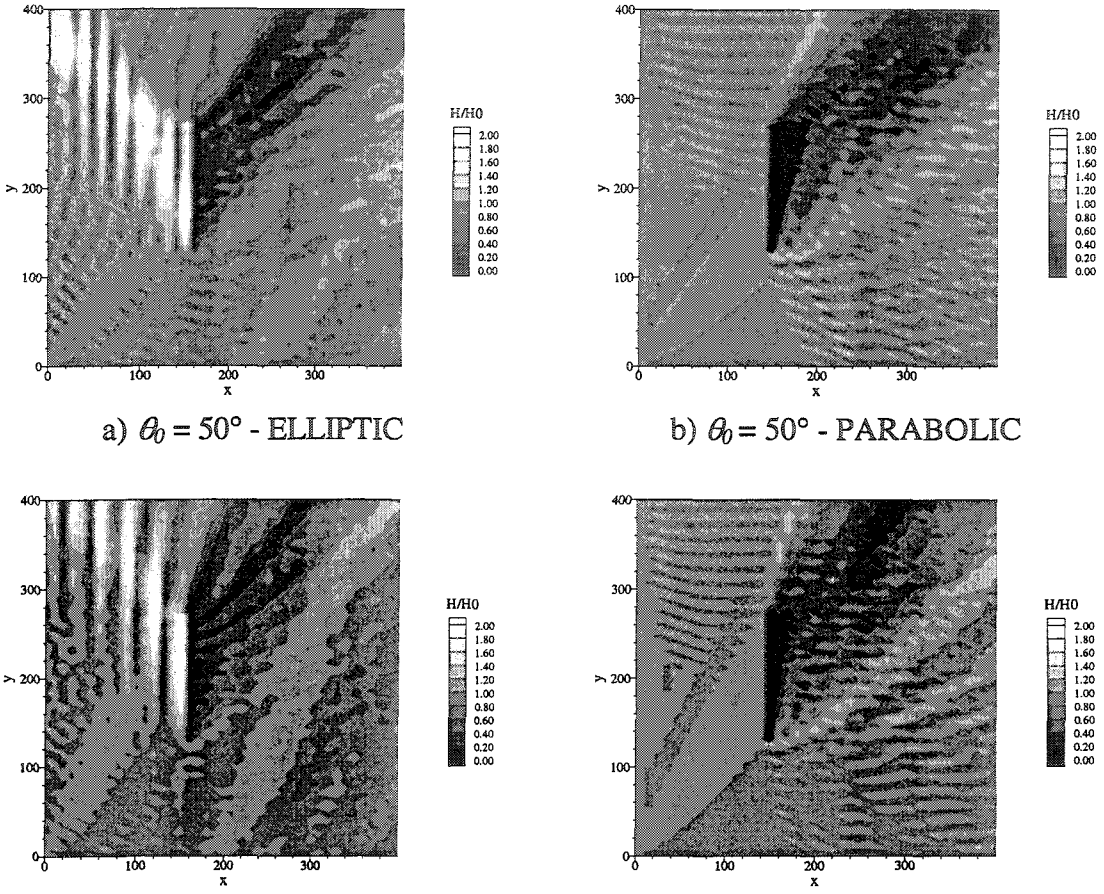

a) $\theta_0 = 50°$ - ELLIPTIC

b) $\theta_0 = 50°$ - PARABOLIC

c) $\theta_0 = 60°$ - ELLIPTIC

d) $\theta_0 = 60°$ - PARABOLIC

Figure (6.16): Comparison between the elliptic and the parabolic solutions for large wave angles.

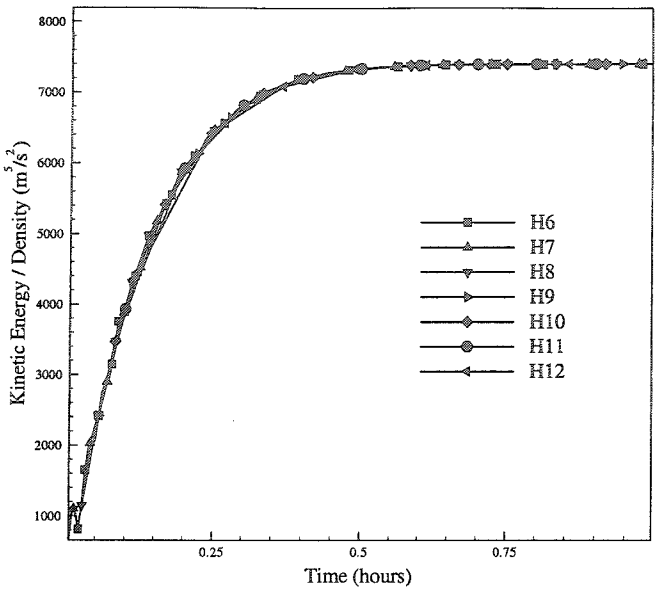

Figure (6.17): Effect of changing the time step on the total kinetic energy of the flow.

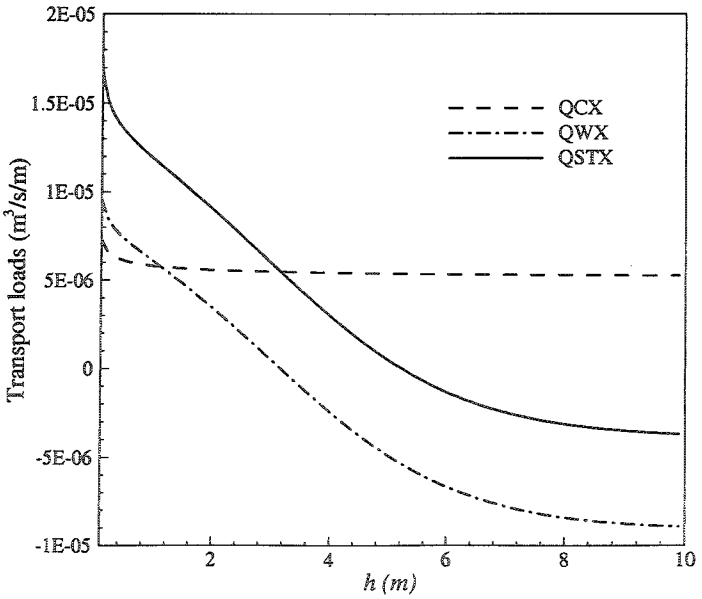

Figure (6.18): Effect of changing the water depth h on sediment transport rates.

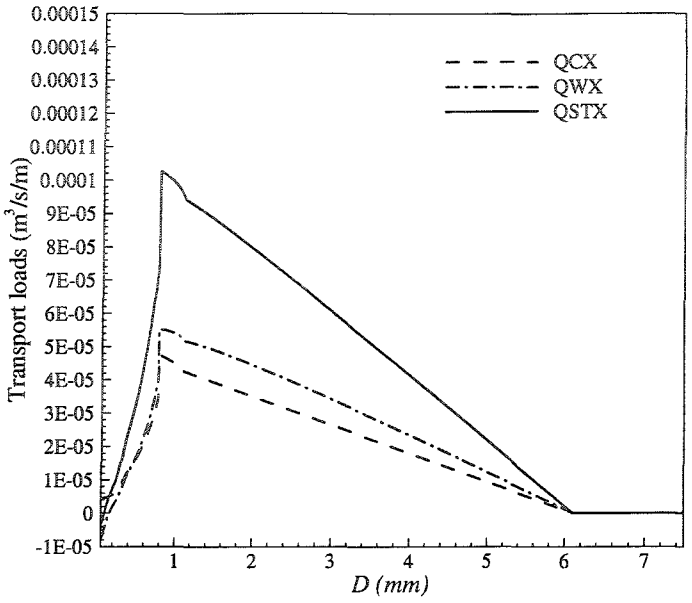

Figure (6.19): Effect of changing the grain size D on sediment transport rates.

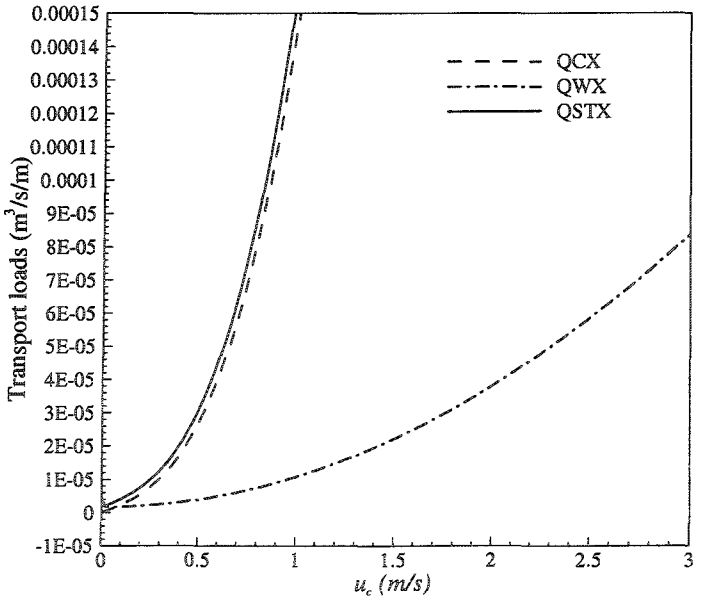

Figure (6.20): Effect of changing the average current speed u_c on sediment transport rates.

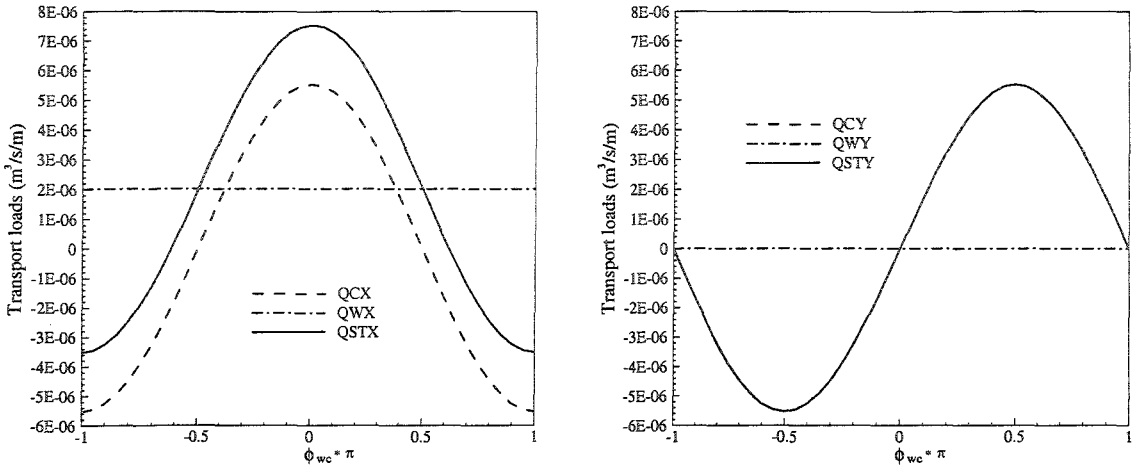

a) *X*-direction transport rates a) *Y*-direction transport rates

Figure (6.21): Effect of changing the current direction ϕ_{wc} on sediment transport rates.

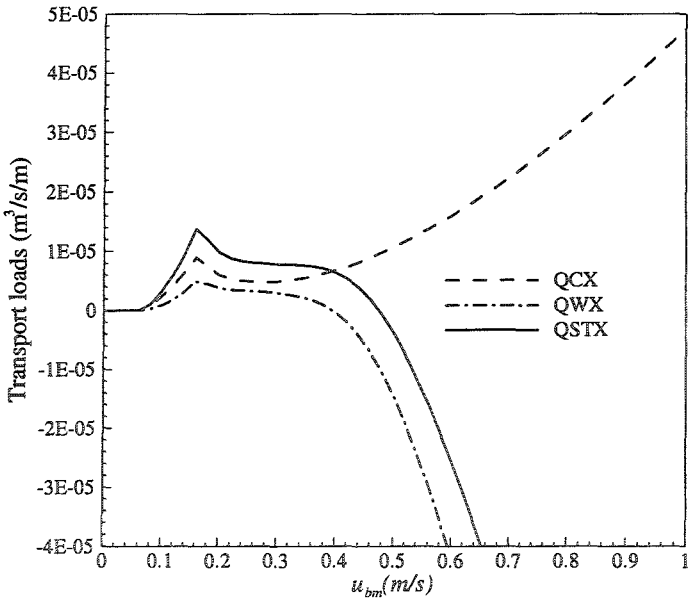

Figure (6.22): Effect of changing the maximum bottom orbital velocity u_{bm} on sediment transport rates.

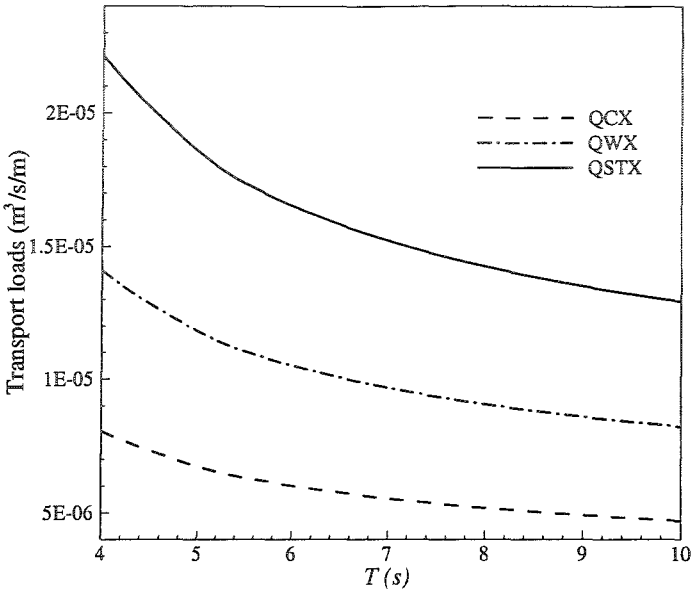

Figure (6.23): Effect of changing the wave period T on sediment transport rates ($F_d = 1$).

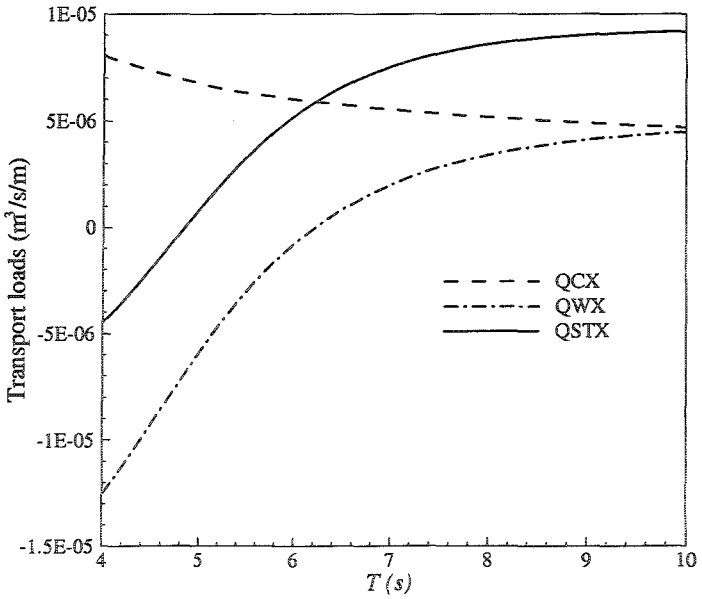

Figure (6.24): Effect of changing the wave period T on sediment transport rates.

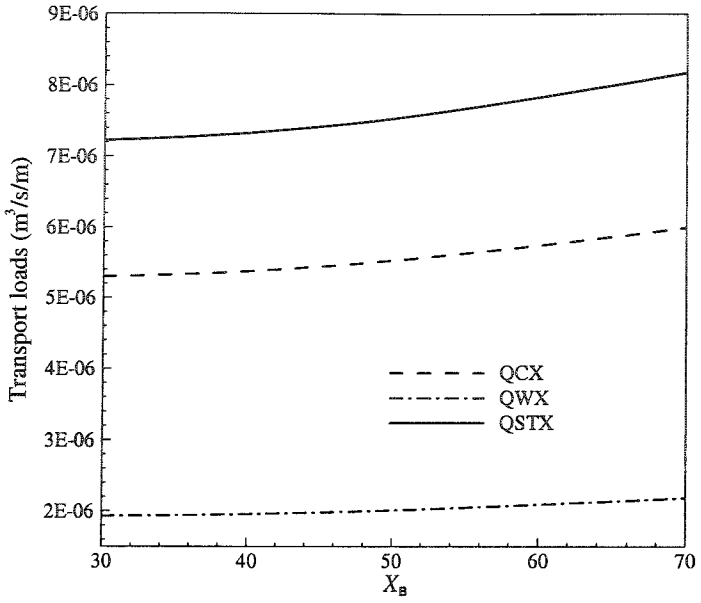

Figure (6.25): Effect of changing the surfzone width X_B on sediment transport rates.

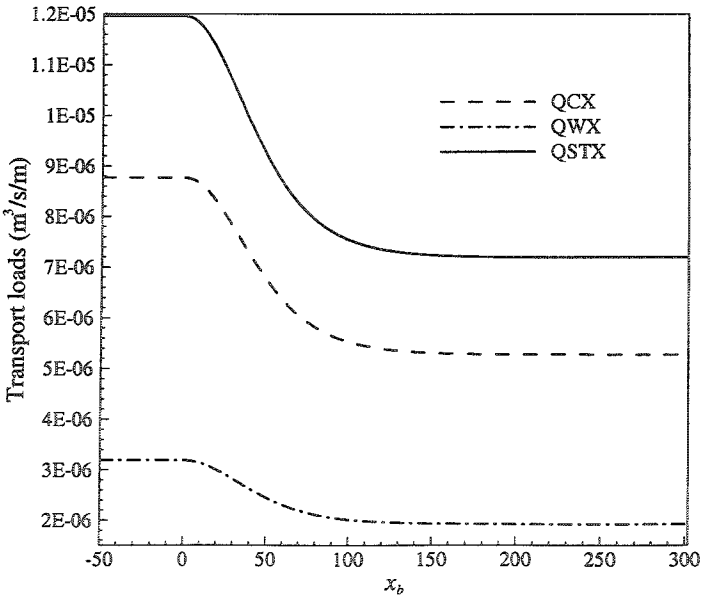

Figure (6.26): Effect of changing the offshore distance x_b on sediment transport rates.

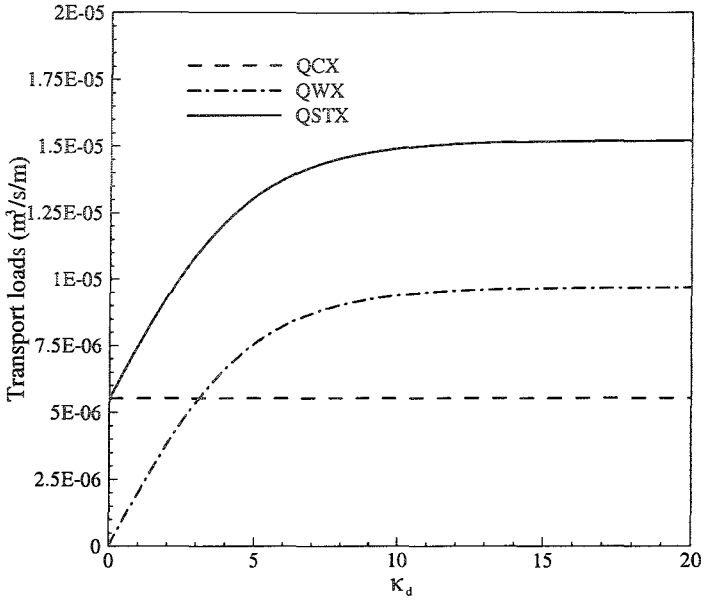

Figure (6.27): Effect of changing the calibration parameter κ_d on sediment transport rates.

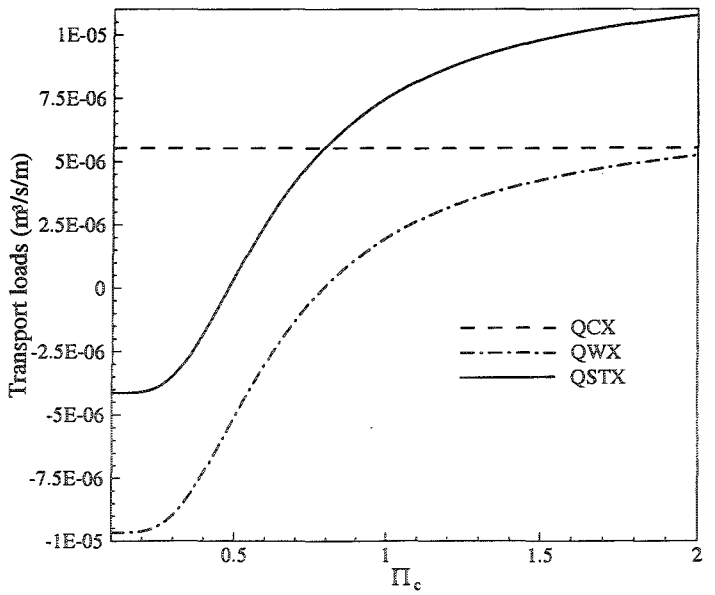

Figure (6.28): Effect of changing the calibration parameter Π_c on sediment transport rates.

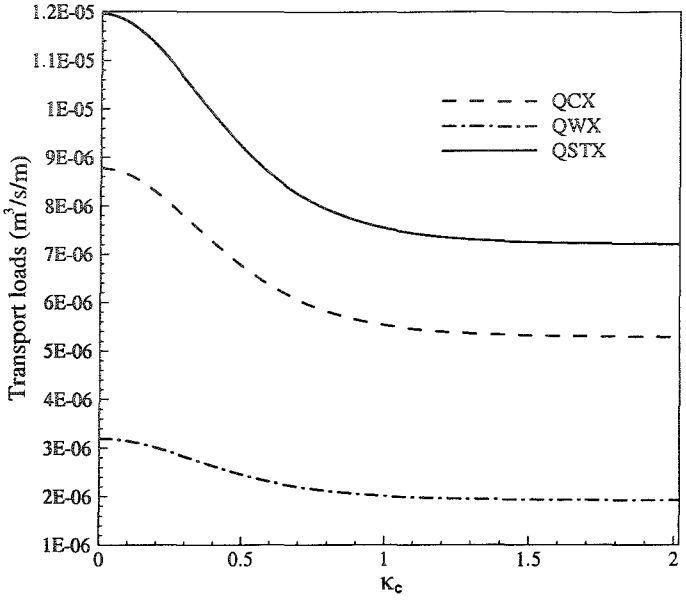

Figure (6.29): Effect of changing the calibration parameter κ_c on sediment transport rates.

Chapter 7: Integrated Coastal Engineering Model Development

In this chapter an Integrated Coastal Engineering Model (ICEM) is presented that models the simultaneous effects of waves, currents, and morphological changes on the sediment transport rates in coastal areas. A number of coastal protection cases, i.e. groins, breakwaters, etc., are used to test the functionality of the model and a case study is used for model verification.

7.1. ICEM Development

The coastal bathymetric changes are expected to cause significant changes in both the wave pattern and the hydrodynamics in the coastal zone. Therefore, the modeling of sediment transport in the coastal zone requires the simultaneous simulation of waves, currents and sediment transport. In this section all the models developed in the preceding chapters are integrated in order to form a morphological model which includes full feed-back from the continuously evolving bathymetry to the waves, the currents and the sediment transport. Therefore this model is called the Integrated Coastal Engineering Model (ICEM).

7.1.1. Model structure

Figure (7.1) shows the structure of the model. The model consists of three main modules as shown in the figure; the wave transformation module, the coastal circulation module and the sediment transport module. Different grid sizes are used for the wave, the hydrodynamics and the sediment transport models. Linear interpolation is used to

calculate the values of the different parameters over different grids. First, the wave transformation module transforms the offshore monochromatic representative wave over a two dimensional grid, which covers the whole coastal domain. With the wave information available over the two dimensional grid, the circulation model calculates the corresponding wave forcing and simulates the coastal currents marching in time until it reaches the steady state. Finally, both wave and current information are passed to the sediment transport and morphological module, which calculates the sediment fluxes over a staggered two dimensional grid and then calculates the morphological changes, imposing the necessary boundary conditions for the structures. The waves, currents and sediment transport rates are recalculated every so-called morphological time step Δt_m. The morphological time step is determined by the most rapid bathymetric evolution inside the model area and is automatically calculated by the model. Part of the ICEM FORTRAN code is listed in Appendix 1.

7.1.2. Wave transformation module

The integrated parabolic/elliptic wave transformation model described in chapter 4 is used, which is essentially a combination between two modules; parabolic and elliptic. The parabolic model is an efficient tool for the determination of wave fields in large coastal areas where backscattering is neglected. The elliptic refinements can be done for specific user-defined areas, where the backscattering is important.

7.1.3. Hydrodynamics module

The coastal hydrodynamics model is described in chapter 5. It solves the time-dependent two-dimensional depth-integrated Navier-Stokes equations. As mentioned in

chapter 5, the model can simulate currents driven by waves, Coriolis effect and wave rolling in the surfzone.

7.1.4. Sediment transport and morphological module

The sediment transport rates due to coexisting waves and currents are calculated using the empirical formulas developed by Watanabe et al. (1986), as discussed in chapter 5. The model behaviour and sensitivity are described in details in chapter 6. The morphological changes are calculated by imposing the sediment budget equation as described in chapter 5.

7.2. Model Input/Output

The ICEM is a user friendly package. The user has to fill out four self explanatory input files as shown in Appendix 2. The first is "input.dat", which contains the required information for the wave model. It contains also the locations of the emerged and submerged structures. This file defines also the grid sizes for all the models. The second file is "inputh.dat", which defines the necessary parameters for the hydrodynamics model like the time step, the mean geographic latitude, etc. Although the hydrodynamic model detects the steady state and stops the hydrodynamic run at the steady state, the simulation time can be defined by the user so that the model never goes beyond it. The third input file is "inputm.dat", which is for the morphological model. The last input file "wavespec.dat" defines the time series of the wave field. Each line contains the significant offshore wave height, direction, angle and the duration in days. The

bathymetry of the modelled region is stored in the file "depth.dat", which usually contains the initial bathymetry.

The output of the ICEM are summarised in the following forms; wave heights, wave vectors, current vectors, surface water elevation, sediment transport fluxes, morphological changes and bathymetry. The user can define both the temporal and spatial intervals at which output is printed. The model writes an output file for each one of the previous forms. For example, the wave heights are stored in the file "waves.dat", the currents are stored in the file "current.dat", and "bathym.dat" for the bathymetry, etc. These output files are written in a way that allows the software Tecplot (a professional drawing software) to read them. Tecplot macros have been developed for each file so that contour and vector plots as well as animations are produced automatically. Therefore, the FORTRAN code ICEM has been linked with a powerful graphics interface and is user friendly.

7.3. ICEM Sensitivity

In this section the sensitivity of the ICEM model is studied. The analysis considers the calibration parameters for the morphology model and the effect of the morphological time step. It should be mentioned that all the parameters studied in chapter 6 affect the behaviour of the integrated model. The analysis is done on a silty sand beach with an offshore breakwater of 180 m length. The incident wave has a significant wave height of 1.0 m and period of 6.0 seconds. The offshore breakwater is located 300 meters

from the shoreline and parallel to it, which makes its length about three times the local wave length. The simulation period for all the runs is 10 days.

7.3.1. Effect of the smoothing parameters

The smoothing parameters α_x and α_y used in Equation (5.64) to smooth the contours are studied. Table (7.1) summarises the runs used in the analysis. The first four runs study the effect of the equal smoothing parameters, where $\alpha_x = \alpha_y$ and their values are changed from 0.0 to 0.05. Figure (7.2) compares between the results, where the original beach is shown in grey scale and the deformed beach is shown as contour lines. It is shown that small values of the smoothing parameters result in sharp contour lines as shown in Figure (7.2a and b). On the other hand, large values of the smoothing parameters may result in a change of the shape of the salient as shown in Figure (7.2d) where the two peaks of the salient is merged into one. The best values of these parameters is of other order of 0.01, which ensures smooth contours while the general shape of the beach is preserved, as shown in Figure (7.2c). The last two runs study the effect of distorted smoothing, where $\alpha_x \neq \alpha_y$, as shown in Table (7.1). It is shown from Figure (7.3) that these parameters can be used to control the size and shape of the salient. As the parameter α_y increases, the salient's two peaks tend to merge into one peak as shown in Figure (7.3a). On the other hand, the shape of the deformed shoreline is sensitive to the parameter α_x as shown in Figure (7.3b). Generally, the smoothing parameters can be used in the model calibration to adjust the shape of the deformed beach.

Table (7.1): Runs used to study the effect of the smoothing parameters

Run	α_x	α_y	ε_q
1	0.0	0.0	10.0
2	0.001	0.001	10.0
3	0.01	0.01	10.0
4	0.05	0.05	10.0
5	0.01	0.02	10.0
6	0.02	0.01	10.0

7.3.2. Effect of the parameter ε_q

The sensitivity of the model to the parameter ε_q is studied by changing its value from 10.0 to 100.0. The parameter ε_q is used to account for the movement of sediment owing to gravity, which helps to suppress the bottom jags that may appear during the course of calculation. Table (7.2) summarises the runs used to study the effect of the parameter ε_q with the smoothing parameters. The first two runs tests the behaviour of the model using ε_q = 10.0 and 100.0, respectively without smoothing. Figure (7.4) compares between the results of the first two runs. It is shown that the model is sensitive to the parameter ε_q if no smoothing is included (i.e. $\alpha_x = \alpha_y = 0.0$). The bottom jags appearing in Figure (7.4a) is suppressed by the large value of ε_q as shown in Figure (7.4b). However, the shoreline is not sensitive to the parameter ε_q unlike the smoothing parameters. On the other hand, the effect of ε_q on the solution is studied in cases where smoothing is included. Figure (7.5) compares between the results of the last two runs, where the parameter ε_q is assigned the same values of 10.0 and 100.0, respectively. Although, the contour lines in Figure (7.5b), which corresponds to ε_q=100.0, are smoother, the model is shown to be not sensitive in cases where smoothing is included. Therefore, it is concluded

that smoothing the contour lines either artificially through the parameters α_x and α_y or through the parameter ε_q removes the bottom jags. However, the artificial contour smoothing through the parameters α_x and α_y is preferred because the shoreline is sensitive to the smoothing parameters just like any other depth contour line.

Table (7.2): Runs used to study the effect of ε_q

Run	α_x	α_y	ε_q
1	0.0	0.0	10.0
2	0.0	0.0	100.0
3	0.01	0.01	10.0
4	0.01	0.01	100.0

7.4. Model Tests

Several model tests are performed to examine the ICEM capabilities for modeling the morphological changes due to various coastal structures. The equilibrium beach profile concept is used to generate the initial beaches according to the median grain size D.

7.4.1. Emerged offshore detached breakwater system

The first test is for a system of offshore breakwaters subjected to constant wave condition. The same beach profile and location of structures for the case described in chapter 5 is used in order to signify the bathymetric effects on the wave and current fields. The case discussed in chapter 5 can be considered as a case of a single morphological time step equals the total simulation time (in this case 60 days). As the salients advance towards the breakwaters, it is expected that the circulation cells behind the breakwaters will get smaller and stronger. Therefore, the rate of change of salient's

geometry changes with time. In order to investigate the effect of the morphological time step on the solution, three trial runs have been done using Δt_m = 20, 10 and 5 days, which corresponds to 3, 6 and 12 morphological time steps, respectively. Figure (7.6) shows the circulation behind the breakwaters after 40 days for the three cases. It can be seen that significant changes of the hydrodynamics occur due to the bathymetric changes. The final bathymetry after 60 days for the three cases is compared in Figure (7.7). The case of 3 morphological time steps does not represent the dynamic impact of the bathymetric change on both waves and hydrodynamics, and therefore, the final results can only be considered as qualitative results. On the other hand, the maximum shoreline advance for the cases of 6 and 12 morphological time steps are 85 m and 95 m, respectively. Although the third case is theoretically more accurate, the salients shapes do not completely agree with practice due to the contour lines irregularities as shown in Figure (7.7c). The second case, however, agrees more with practice as shown in Figure (7.7b). In addition, the difference in the maximum shoreline advance between the second and third cases is only 10%, which can be accounted for during the calibration of the sediment transport model. Therefore, the best morphological time step which accounts for the dynamic effect of bathymetric changes and does not affect the quality of the solution is of the order of 10 days. It is worth mentioning in this stage that the hydrodynamic model needs about 20 minute to reach the steady state, which is ignored compared with the morphological time step (10 days). Therefore, the transient effects of the wave-induced hydrodynamics are not important in the context of sediment transport.

Although the morphological time step can be specified by the user, as done in the last test, it is recommended to let the model calculate its value automatically, where its value is identified according to the rate of bed level change. The faster the bed changes, the smaller the morphological time step is chosen and vice versa. After the model calculates the sediment transport fluxes, the absolute value of the rate of bed level change R_b is calculated for the whole domain using the sediment budget equation as:

$$R_b = \left| \frac{q_{xi,j} - q_{xi+1,j}}{\Delta x} + \frac{q_{yi,j} - q_{yi,j+1}}{\Delta y} \right| \tag{7.1}$$

The morphological time step is then calculated from:

$$\Delta t_m = \min\left[\frac{h}{R_b}\left(\frac{\Delta h}{h}\right) \right] = \min\left[\frac{h}{R_b} Accuracy \right] \tag{7.2}$$

where the $\Delta h/h$ is the ratio between the change in water depth at a certain point at the end of the morphological time step and the original water depth, which is defined by the user as the required accuracy. The smaller the value of the ratio $\Delta h/h$ (the higher accuracy), the smaller the morphological time step. The morphological time step is not allowed to extend beyond the duration of wave attack, where different wave transformation is needed and consequently hydrodynamic and sediment transport rates will change. In addition, the morphological time step is not allowed to exceed the 50 days limit. In this way, the model will overcome the incorrect input of excessively large values of the accuracy by the user.

In order to study the effect of the accuracy on the solution, the case of detached breakwater system is reanalysed using different values of the accuracy. Figure (7.8)

compares between the results of simulation after 60 days for three values of the accuracy. It is shown that the case of 10% accuracy gives comparable results to the case of 5% accuracy, while the simulation time is significantly smaller. Therefore, the recommended value of the accuracy is of the order of 10%. This physically means that the waves, currents and sediment transport rates have to be recalculated if the bathymetric change in any point within the calculation domain reaches 10%.

7.4.2. Emerged groin system

The second test is for the case of groined beach. The same beach configuration and wave climate described in chapter 5 is adopted here for the sake of comparison. Figure (7.9) compares between the model results for values of accuracy of 20%, 10% and 5%. It is evident that the shoreline position does not change from one case to another. The case of 5% accuracy, however, has an unstable shoreline and contour lines. Therefore, it is concluded that the high accuracy causes instability in the solution. Figure (7.10) shows the circulation around the groin system after 60 days, where the bathymetric impacts on the circulation around the groin system is evident.

7.4.3. Submerged offshore detached breakwater system

In addition to the ICEM's capabilities in modelling the morphological changes around emerged structures, the submerged structures can be modelled as well. The capabilities of the model to simulate morphological changes around this type of structures are tested in the present and the following sections. The submerged structures are defined in the file "input.dat" by their location and height above the bed. The same beach, wave climate and breakwater locations used in section 7.4.1 are adopted in this section for the

sake of comparison between the emerged and submerged systems. The submerged breakwater heights above the bottom are 2.5 m. The morphological time step is determined by 10% accuracy. The waves break at the breakwaters crests, which reduce the wave heights behind the submerged sills and circulation cells form behind the sills similar to those form behind the emerged breakwater. However, the currents at the top of the submerged cells intensify due to the reduced depth as shown in Figure (7.11). In addition, offshore circulation cells between the breakwaters and at both ends of the system form due to the sudden wave breaking over the crests of the structures and the large current topping the breakwaters. As a result of this circulation pattern, salients form behind the submerged breakwaters, while severe erosion around the submerged sills take place, as shown in Figure (7.12). In addition, the salients size is relatively smaller than that form due to the emerged breakwaters.

7.4.4. Submerged groin system

In this section a submerged groin system is tested. The same groin system configuration described in section 7.4.2 is adopted. The groins are 2.0 meters height above the seabed. The morphological time step is determined from Equation (7.2) using 10% accuracy. The circulations around the submerged and emerged groin systems are similar as shown in Figure (7.13) and Figure (7.10). However, due to the reduced depth over the submerged groins, the littoral current is intensified and the blocking length of the groins is reduced. Despite the change in hydrodynamics, the shoreline changes due to both submerged and emerged groin systems are similar as long as both systems are not saturated, as shown in Figure (7.14) and Figure (7.9), respectively. The submerged

system does not divert the littoral transport as much as the emerged system does as shown in Figure (7.13). Therefore, its impact on the offshore bathymetry is less than the emerged system as shown in Figure (7.14).

7.5. Ras El-Bar Case Study

The Nile Delta coast, on the Mediterranean Sea, was found through many centuries. The continuous discharge of large quantities of sediments from the Nile into the Mediterranean over thousands of years formed two peninsulas in the sea at the two main branches of the Nile, i.e. Rosetta and Damietta, as shown in Figure (7.15). In the course of time the supply of sediment by the Nile exceeded the losses due to wave and current action, resulting in a continuous advance of the shoreline towards the sea (Mobarek, 1972). This process continued until the erosive wave action and the continuous supply of sediment materials reach a stability condition. By the end of the 18^{th} century and the start of the 19^{th} century, several regulation projects along the River Nile have been constructed, which reduced the sediment supply from the Nile to Mediterranean and erosion from Rosetta and Damietta peninsulas was observed. After the construction of the High Dam in 1964, the sediments carried out to the Nile delta have been significantly reduced. Besides, after the completion of the Faraskour Dam, at the end of Damietta promontory, the supply of the River Nile water to the Mediterranean has been completely cut. Accordingly, the River Nile lost the stability with the Mediterranean and severe erosion was observed. Between 1908 and 1954, the Rosetta peninsula receded about 1.7 Km, whilst between 1902 and 1940, the Damietta peninsula receded about 1.8 Km. The

problem has not attracted the proper attention until it started to affect the national economy and the welfare of the people living on the coast. Erosion attacked the beach summer resorts, waves flooded villages on the coast, fisheries deteriorated and danger existed of severe salt water intrusion.

Ras El-Bar city is located west of Damietta Nile branch as shown in Figure (7.16). As part of the Nile delta, Ras El-Bar beach is mainly composed of silty sand with median diameter of 0.12 mm (Mobarek, 1972). Several coastal protection projects have been implemented to reduce or eliminate the erosion at Ras El-Bar. First, the west (terminal) jetty was constructed in 1941, which was intended to protect the River Nile exit. In 1970, three groins were constructed on the western side and the beach was artificially nourished with sediments dredged from the river mouth (Frihy et al, 1991). A dolos and riprap revetment was placed within the groin field (Dabees and Kamphuis, 1998). Erosion continued beyond the western groin and progressively diminishes to the west and is negligible along the western half of Ras El-Bar (Frihy et al, 1991). A system of detached breakwaters was constructed in 1991 west of the groin field (Dabees and Kamphuis, 1998). The breakwaters were placed 400 meters offshore such that the tombolo formation is prevented. Finally, in 1994, the beach was nourished with two hundred thousands cubic meters of sand.

7.5.1. Data analysis and model setup

The time series wave data over a complete representative year at Ras El-Bar is available from the Coastal Research Institute, Alexandria, 1996. The significant wave data is given each 6 hours. The wave gauge was located at the Eastern side of Damietta

promontory at 7-meters depth of water (Dabees and Kamphuis, 1998). Figure (7.17) shows the annual wave rose at Ras El-Bar. Over the year, only 240 days were considered, where the wave heights are larger than 0.75 meters. The monthly wave roses were analysed in order to come out with a design time series. It was assumed that over one month, short duration storms which have the same range of wave heights can be grouped into a single prolonged storm. First, the monthly wave data time series is divided into wave directional bands of 20°-width. Then, the time series within each band is clustered and the similar wave records (wave period T and wave height H) are grouped to form a prolonged record, which has an average wave period and wave height of the constituting records. The clustering is based on the Hierarchical technique (see Davis (1973) for details), which joins the most similar observations, then successively connects the next most similar observations to these. The Euclidian distance d_{ij} is used as a measure of the similarity between the variables at times i and j, which is given by:

$$d_{ij} = \sqrt{\frac{(H_i - H_j)^2 + (T_i - T_j)^2}{2}} \tag{7.3}$$

where H_i and H_j denote the wave heights measured at times i and j, respectively whereas T_i and T_j denote the wave periods measured at times i and j, respectively. The smaller the value of the Euclidian distance d_{ij}, the greater the similarity between the pair i and j.

The study was conducted in three main phases. The first phase is from 1986 to 1991 before the construction of the detached breakwaters. The second and third phases study the effect of the detached breakwaters from 1991 until 1993 and 1995, respectively.

The same coordinate system and modelled region used by Dabees and Kamphuis (1998) is adopted in this study. The modelled region covers 4 Km of beach and 1 Km offshore from an arbitrary baseline. Figure (7.18) shows a schematic diagram of the modelled region and the existing structures showing the initial contour map of November 1986.

Measured shorelines of 1986, 1993 and 1995 were digitized from Dabees and Kamphuis (1998), while the initial bathymetry was digitized from Herbich et al (1996).

7.5.2. Model calibration and verification

The model is calibrated and verified using the measured shorelines of 1993 and 1995, respectively. The morphological model parameters described in chapter 5 are adjusted beforehand, so that winter and summer profiles are formed appropriately. Using the average wave conditions (H_s = 1.0m and T_s = 7.5s), the parameters A_c and A_w are set approximately to reproduce the 1993 shoreline. The actual wave climate is then used over the period from November 30, 1986 to July 1, 1993, (phase 1 and 2) where the calculated shoreline is compared with the actual shoreline to fine tune the calibration parameters. The optimized values of the calibration parameters A_c, A_w, K_c, K_d and Π_c for Ras El-Bar area are 0.11, 0.15, 1.0, 0.2 and 2.0, respectively.

Figure (7.19) shows the measured and computed shoreline advance from 1986 to 1993 after calibration (Saied and Tsanis, 2004c). The error in the total shoreline advance is less than 5%. The root mean square difference, *rmse*, between the measured and the calculated shorelines at 1993 can be calculated from:

$$rmse = \left[\frac{1}{n} \sum_{i=1}^{n} (y_i - x_i)^2 \right]^{1/2} \tag{7.4}$$

where y_i and x_i are the measured and the calculated shoreline advance from 1986 to 1993, respectively, and n is the number of experimental data points. Using Equation (7.4), the root mean square difference between the measured and the calculated shorelines at 1993 is found to be 0.55 m, which suggests a strong agreement between the measured shoreline and the model results.

The average absolute difference, *aae*, between the measured and the calculated shorelines is another useful measure of the agreement between the model and the reality, which can be calculated from:

$$aae = \frac{1}{n} \sum_{i=1}^{n} |y_i - x_i| \tag{7.5}$$

Again, a 3.5 m average absolute difference between the measured and the calculated shorelines at 1993 is considered a strong agreement between the modelled and the measured shorelines.

Figure (7.20) shows the measured and calculated shorelines of 1993 after calibration as well as the initial bathymetry at 1986 (Saied and Tsanis, 2004c). The initial contour map of 1986 is shown in grey scale, while the contour map of 1993 is shown as contour lines so that the bathymetric changes can be distinguished. The measured shoreline of 1993 is shown as a thick dotted line. It can be shown that the seabed erodes in the vicinity of the detached breakwater system. This is due to the circulation cells formed behind the breakwaters which move the sediments from the breakwaters vicinity

to the shore where they settle down and build up salients as shown in Figure (7.20). On the other hand, the beach slope in front of the seawalls continues steeping due to the offshore transport of sediments generated by the wave action.

In order to verify the model, the same parameters are used to calculate the shoreline at 1995. Figure (7.21) shows the measured and computed shoreline advance from 1986 to 1995. Again, the error in the total shoreline advance is less than 5%. The root mean square difference *rmse* and the average absolute difference *aae* between the measured and the calculated shorelines at 1995 are calculated using Equations (7.4) and (7.5), respectively. Very small values of 0.94 m and 8.83 m for the *rmse* and the *aae* at 1995, respectively, prove that the model agreement with the measured data is very strong.

Figure (7.22) shows the morphological changes after phase 3, where the contour map of 1986 is shown in grey scale, while the contour map of 1995 is shown as lines. Like phase 2, erosion in the vicinity of the detached breakwater system is reported. At 1995, the overall beach profile seems to reach steady state. Significant erosion occurs behind the first two breakwaters from the West, which suggests some kind of toe protection.

The calibration and verification of the ICEM using Ras El-Bar area with more than 9 years of simulation prove the applicability of the three-dimensional morphological models over the long term. On the other hand, the applicability of this type of models in the short term (several months) is already proven in the preceding literature. Therefore, it can be concluded that the ICEM can be used as a design tool for coastal structures since it can be used for both short and long term coastal-morphology predictions.

7.6. Summary

In this chapter an Integrated Coastal Engineering Model ICEM has been developed. The model simulates waves, currents and sediment transport simultaneously, where waves, currents and sediment transport fluxes are recalculated every morphological time step. The sensitivity of the model's calibration parameters is studied. It was found that the smoothing parameters can be used to control the shape of the beach deformation due to coastal structures. The morphological time step is determined by the most rapid bathymetric evolution inside the model area, where it is not allowed to exceed a certain accuracy which is set by the user and recommended to be of the order of 10%.

The model capabilities are demonstrated through several test cases, which include submerged and emerged detached breakwater systems and groin systems. A case study along the Nile Delta coast in Egypt is used to calibrate and verify the model through comparison with the available field data. The application of the ICEM to Ras El-Bar area proved the model capabilities and applicability to large scales over long terms and suggests that the ICEM can be used as a design tool for coastal structures.

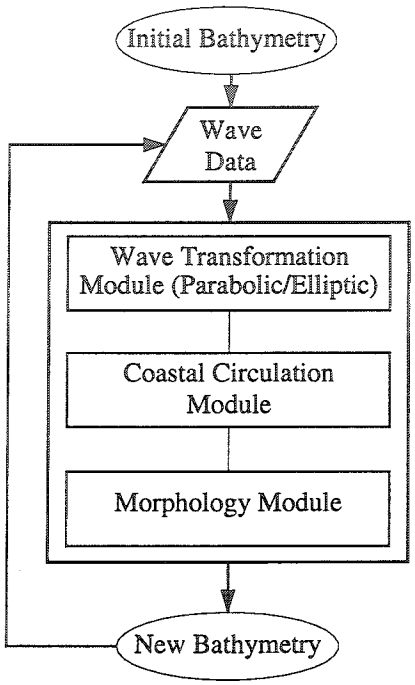

Figure (7.1): Flow chart of the ICEM

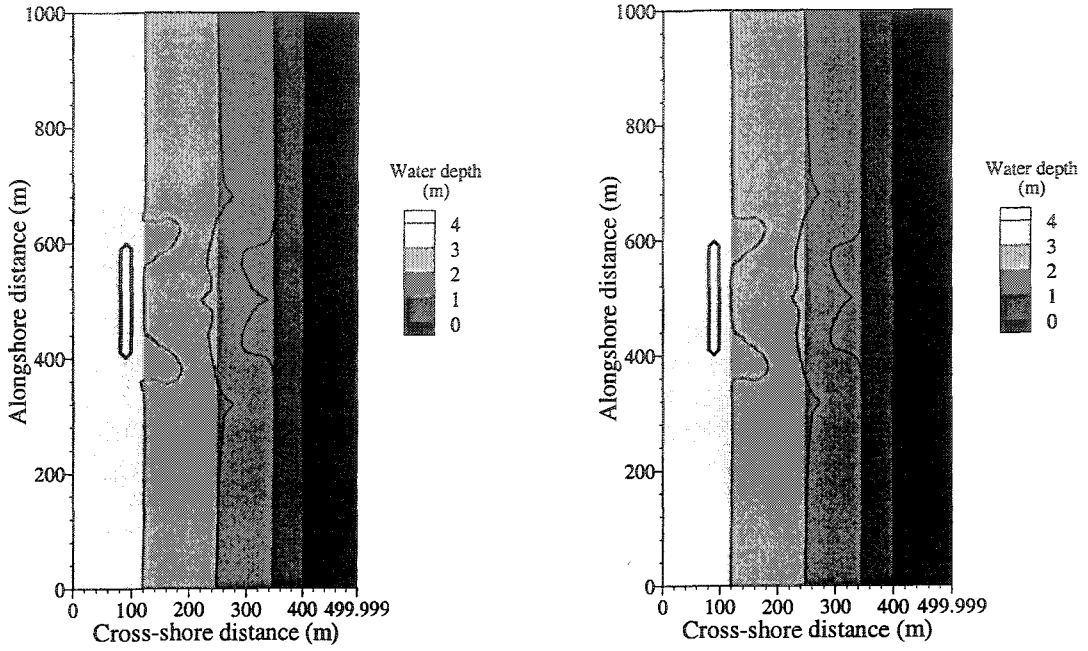

a) $\alpha_x = \alpha_y = 0.0$ b) $\alpha_x = \alpha_y = 0.001$

c) $\alpha_x = \alpha_y = 0.01$ d) $\alpha_x = \alpha_y = 0.05$

Figure (7.2): Effect of the smoothing parameters on the solution.
Grey scale represents the original beach and contour lines represent the deformed beach.

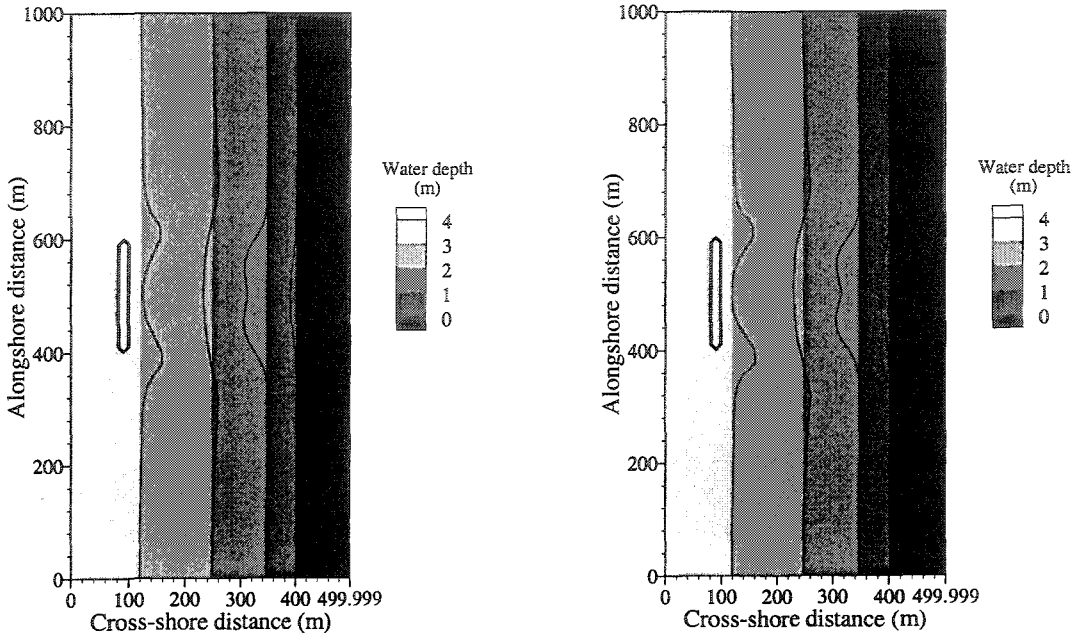

a) $\alpha_x = 0.01$ and $\alpha_y = 0.02$ b) $\alpha_x = 0.02$ and $\alpha_y = 0.01$

Figure (7.3): Effect of distorted smoothing on the solution.
Grey scale represents the original beach and contour lines represent the deformed beach.

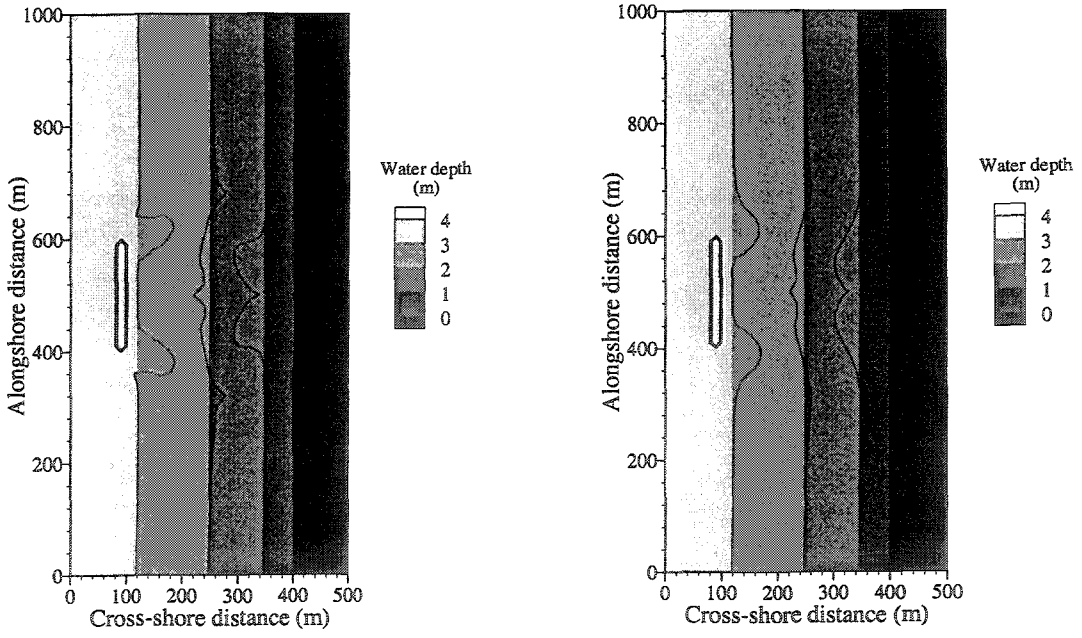

a) $\varepsilon_q = 10.0$ b) $\varepsilon_q = 100.0$

Figure (7.4): Effect of ε_q on the solution without smoothing ($\alpha_x = \alpha_y = 0.0$).
Grey scale represents the original beach and contour lines represent the deformed beach.

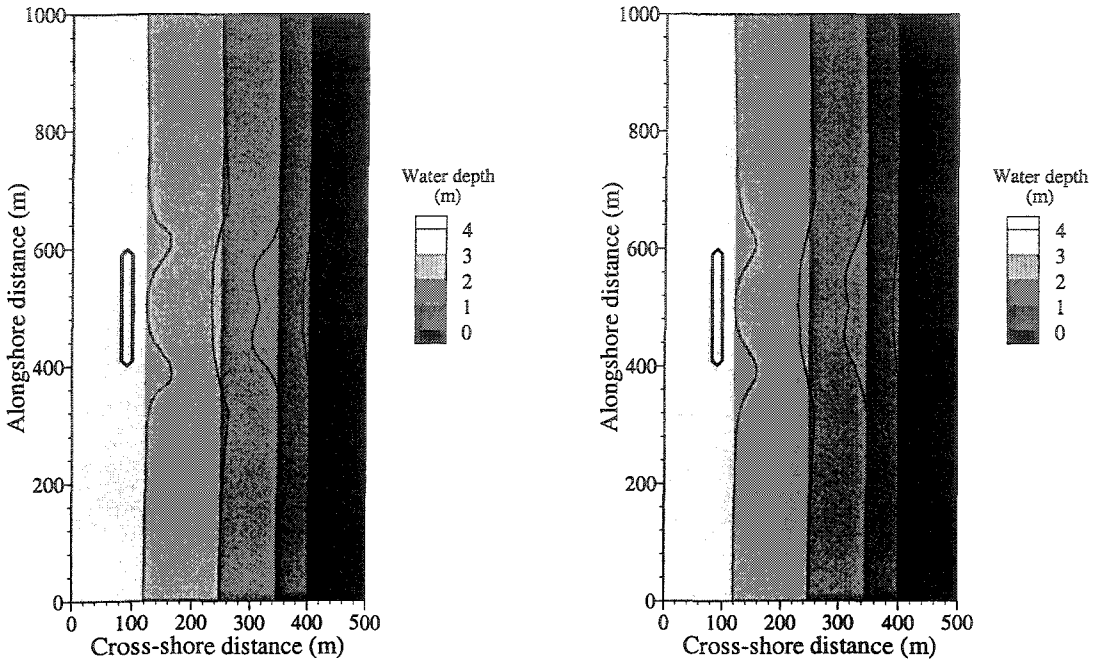

a) $\varepsilon_q = 10.0$ b) $\varepsilon_q = 100.0$

Figure (7.5): Effect of ε_q on the solution with smoothing ($\alpha_x = \alpha_y = 0.01$).
Grey scale represents the original beach and contour lines represent the deformed beach.

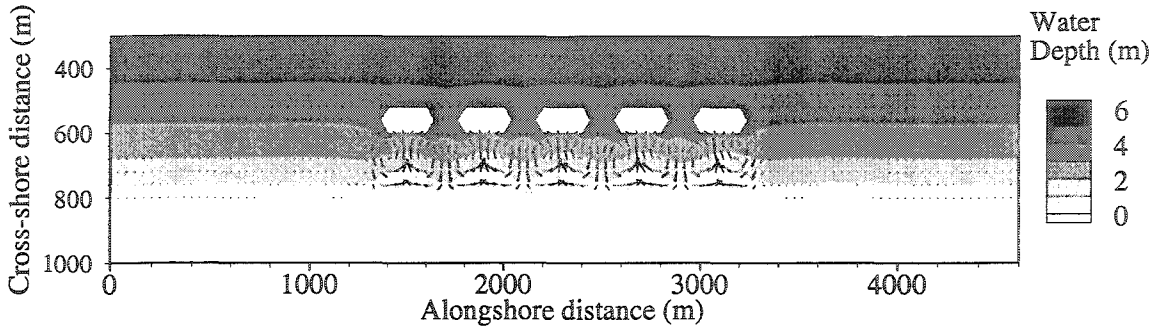

a) $\Delta t_m = 20$ days

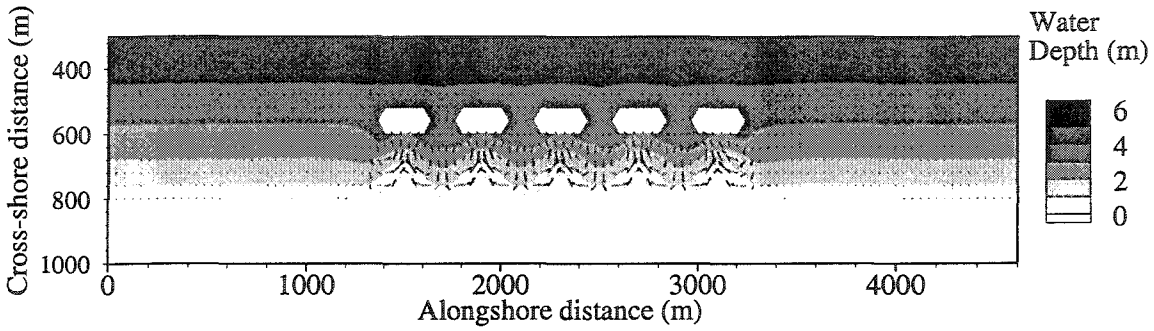

b) $\Delta t_m = 10$ days

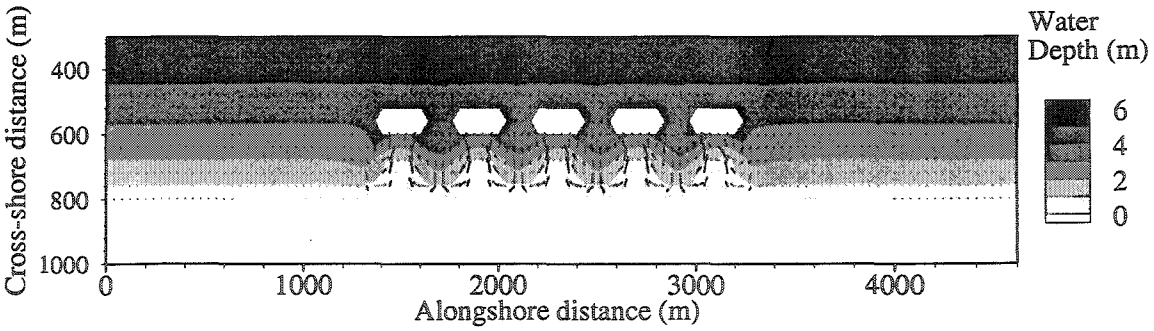

c) $\Delta t_m = 5$ days

Figure (7.6): Circulation behind the detached breakwater system after 40 days.

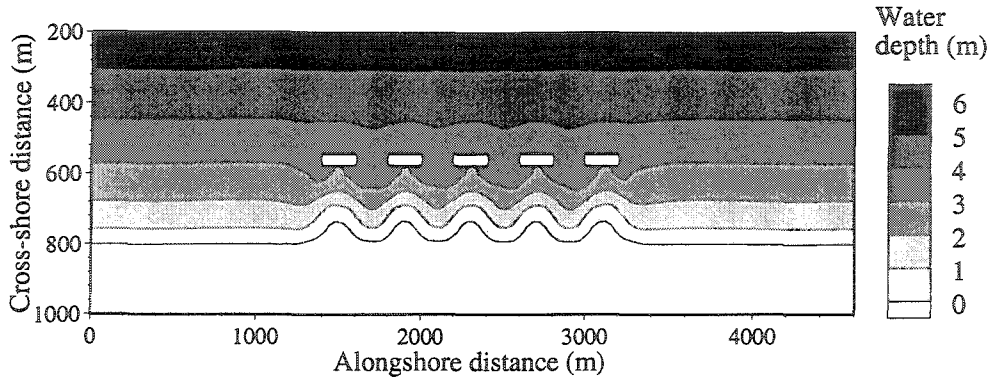

a) $\Delta t_m = 20$ days

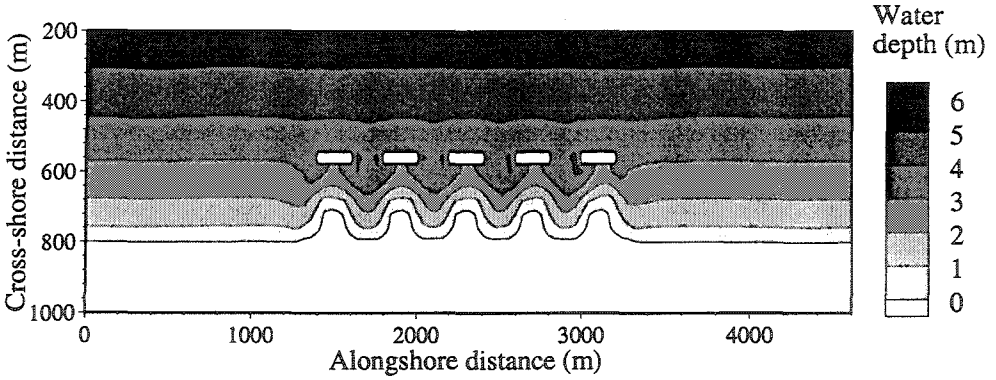

b) $\Delta t_m = 10$ days

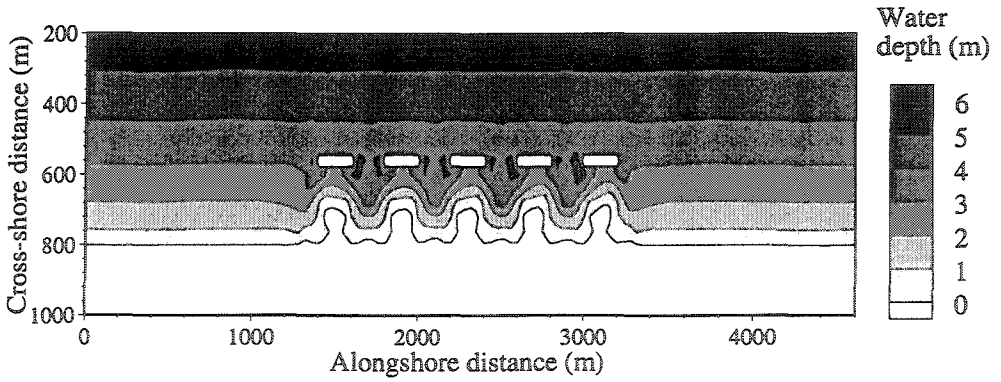

c) $\Delta t_m = 5$ days

Figure (7.7): Morphological changes due to detached breakwater system after 60 days for different values of morphological time step.

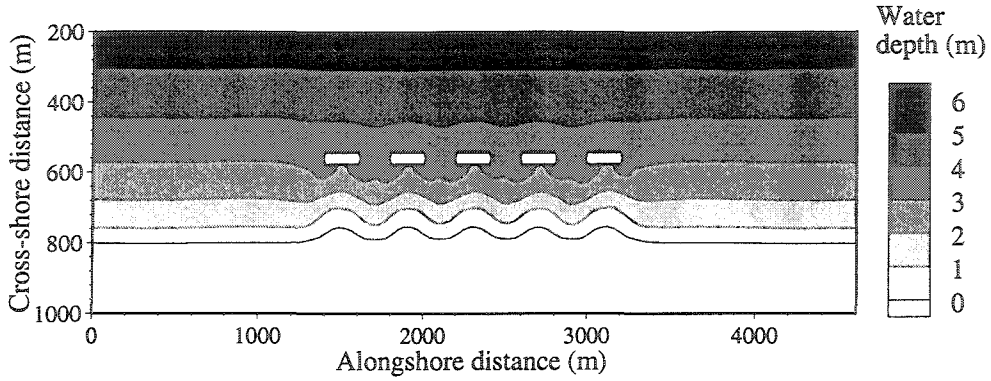

a) Accuracy = 20%

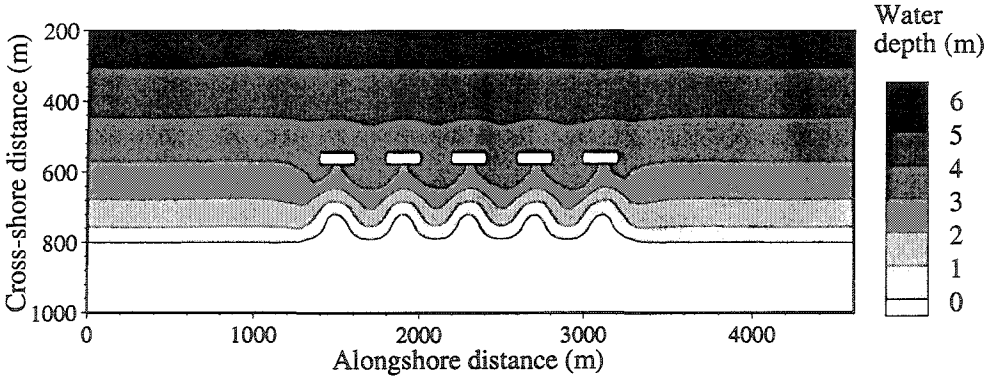

b) Accuracy = 10%

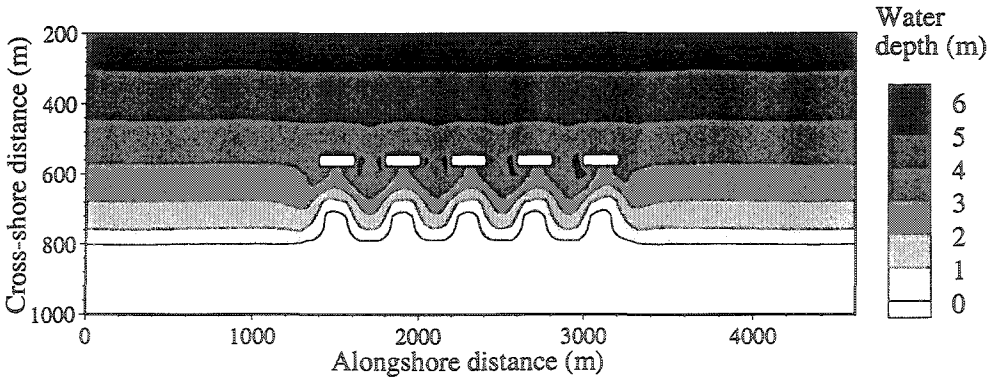

c) Accuracy = 5%

Figure (7.8): Morphological changes due to detached breakwater system after 60 days for different values of the accuracy.

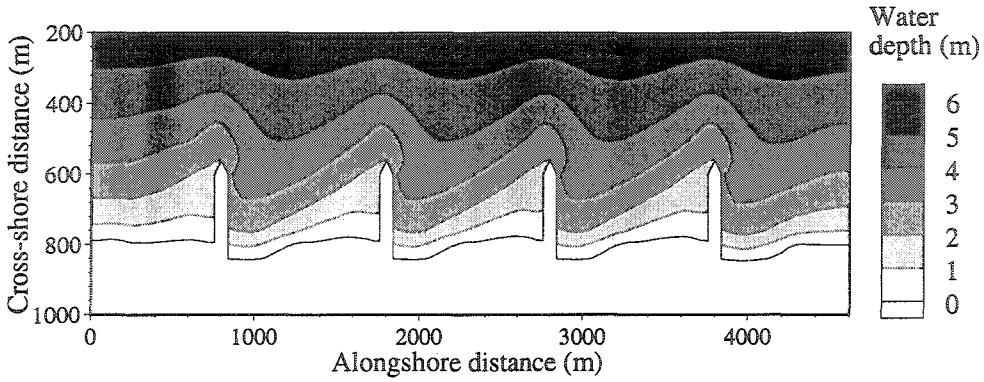

a) Accuracy = 20%

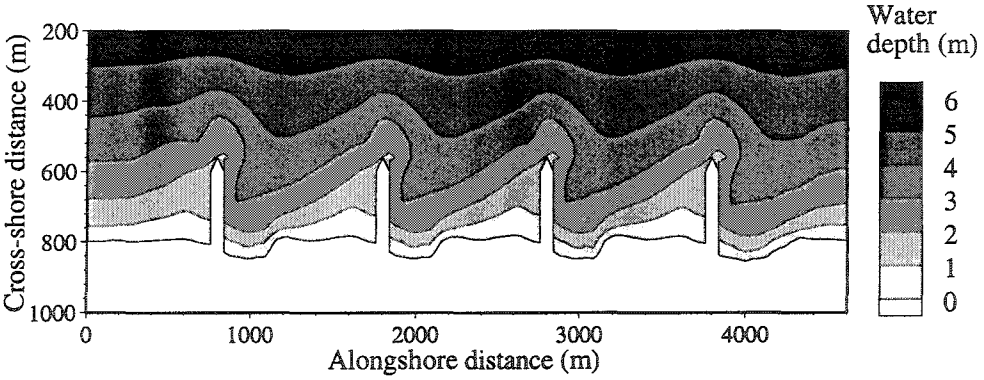

b) Accuracy = 10%

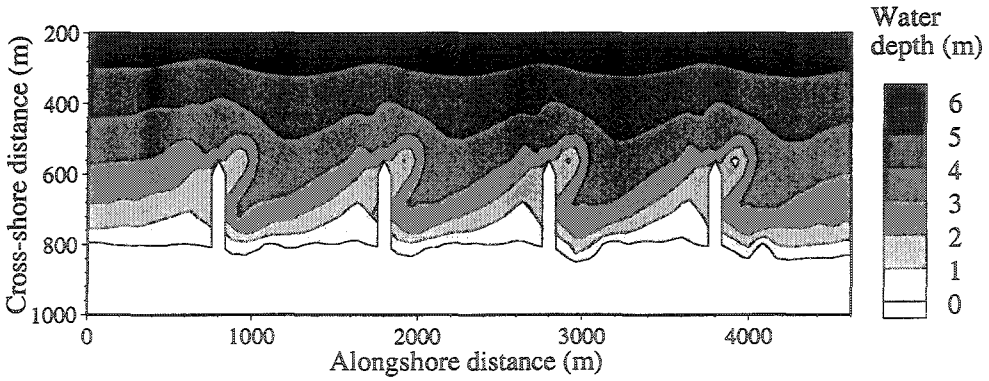

c) Accuracy = 5%

Figure (7.9): Morphological changes due to a system of groins after 90 days for different values of the accuracy.

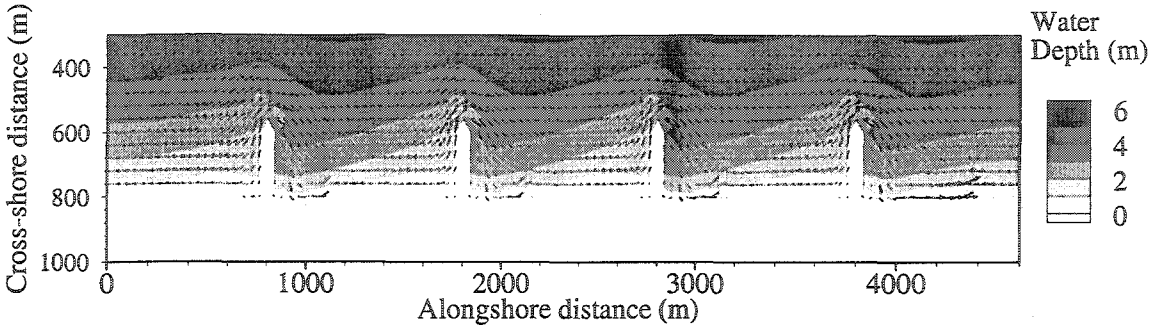

Figure (7.10): Circulation around an emerged groin system after 60 days.

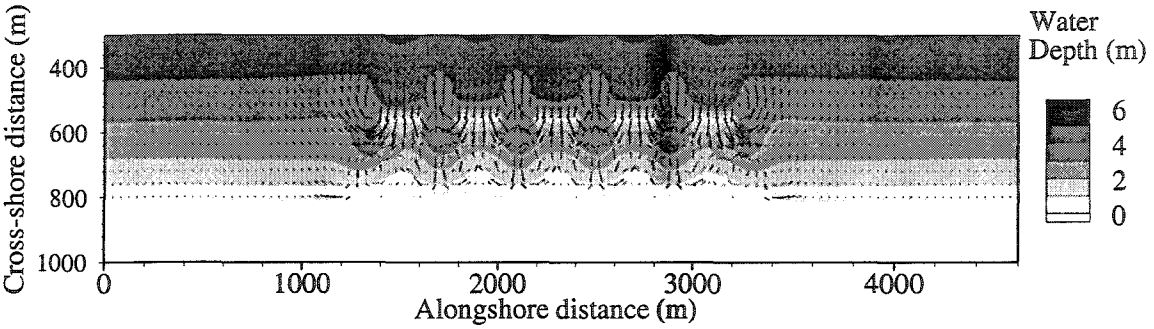

Figure (7.11): Circulation around a system of submerged offshore breakwaters.

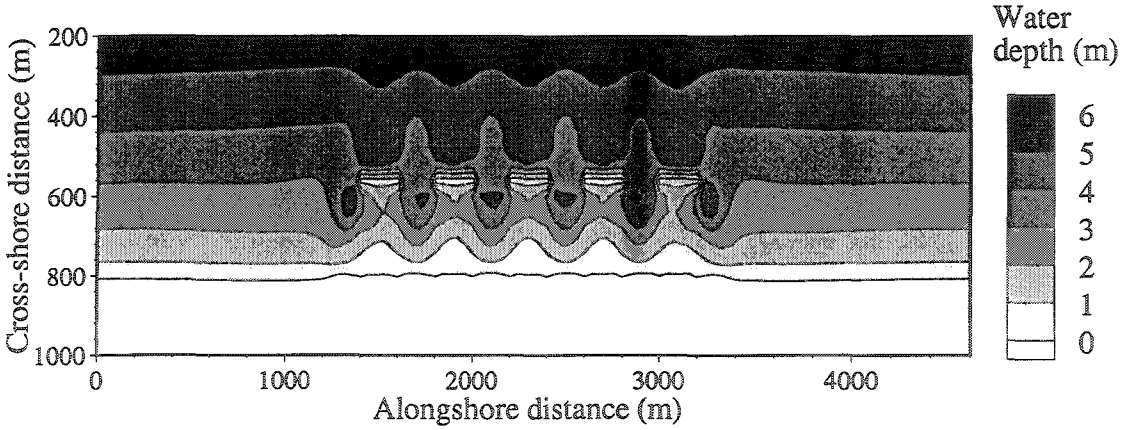

Figure (7.12): Morphological changes due to a system of submerged breakwaters after 60 days of wave attack.

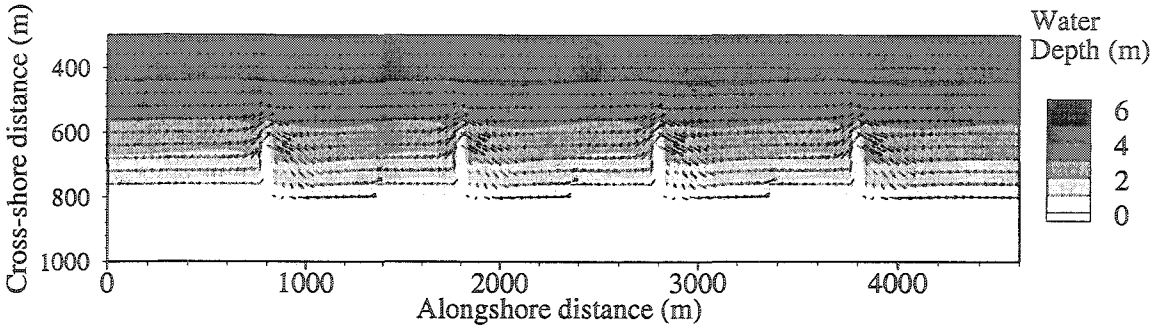

Figure (7.13): Circulation around a system of submerged groins.

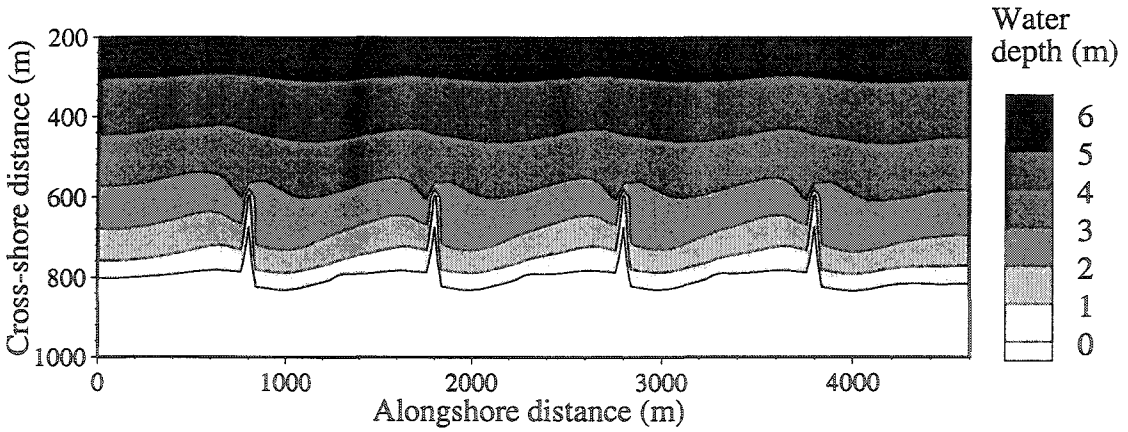

Figure (7.14): Morphological changes due to a system of submerged groins after 90 days of wave attack.

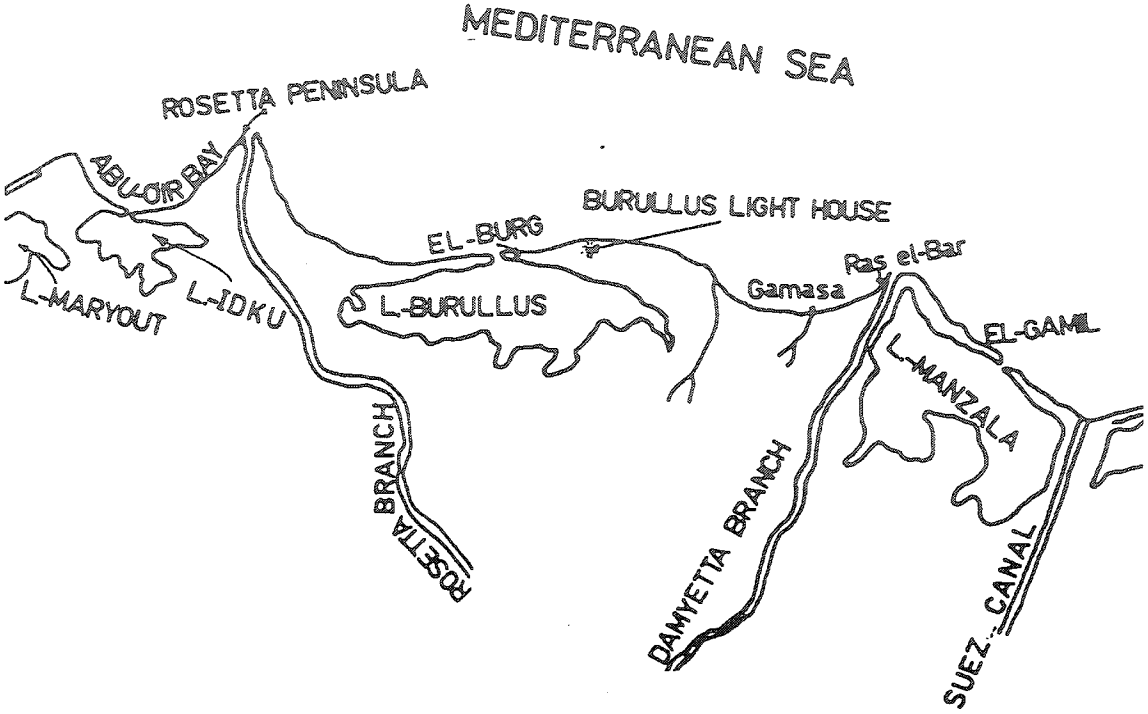

Figure (7.15): The Nile Delta.

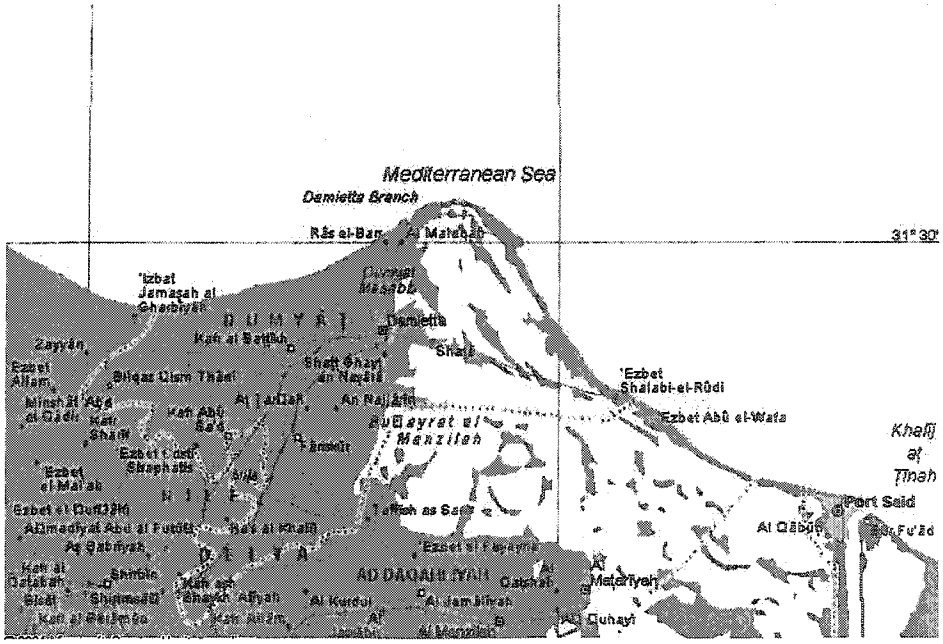

Figure (7.16): Ras El-Bar Area.

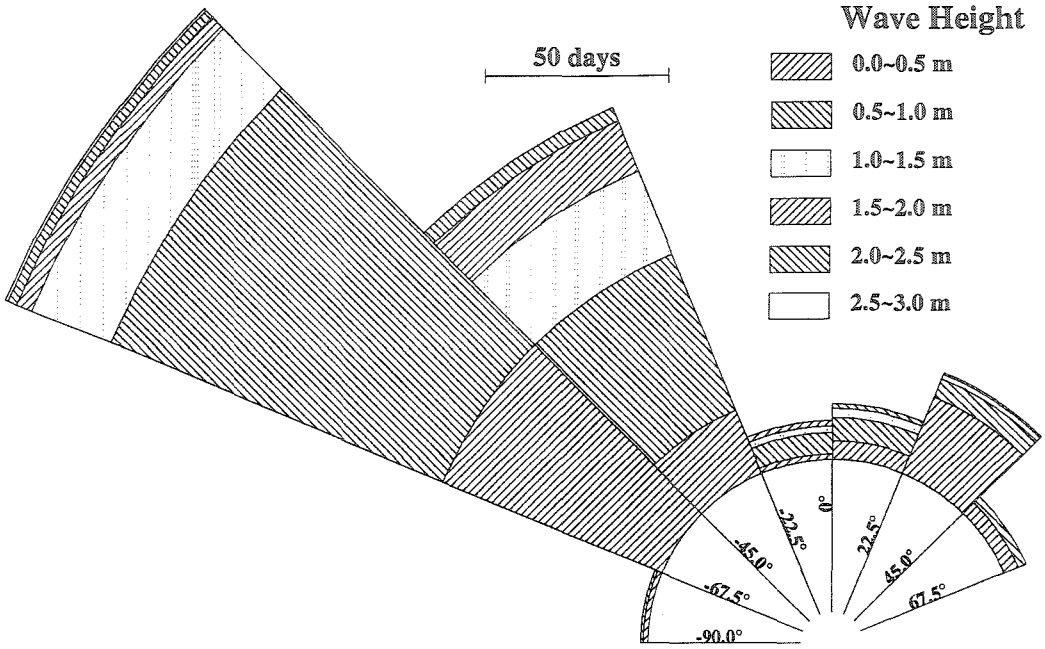

Figure (7.17): Wave rose at Ras El-Bar.

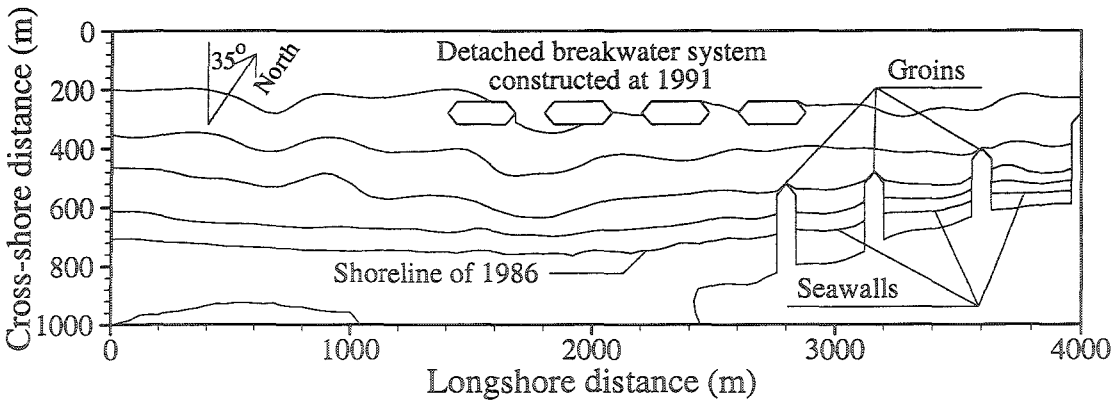

Figure (7.18): Schematic diagram of the modelled region.

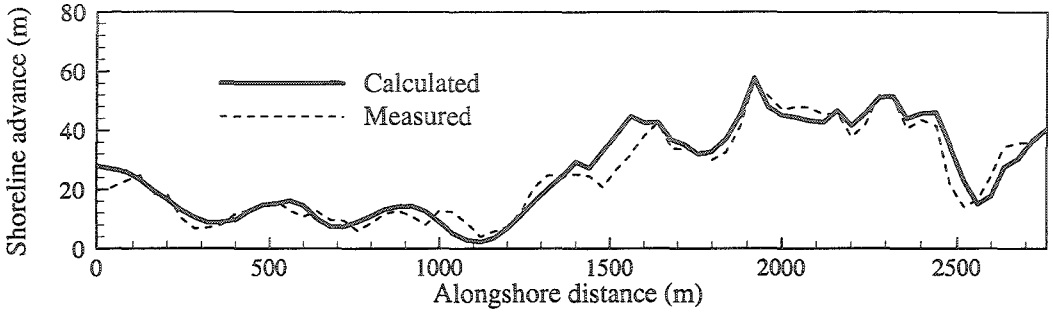

Figure (7.19): Shoreline advance from 1986 to 1993 (measured and calculated).

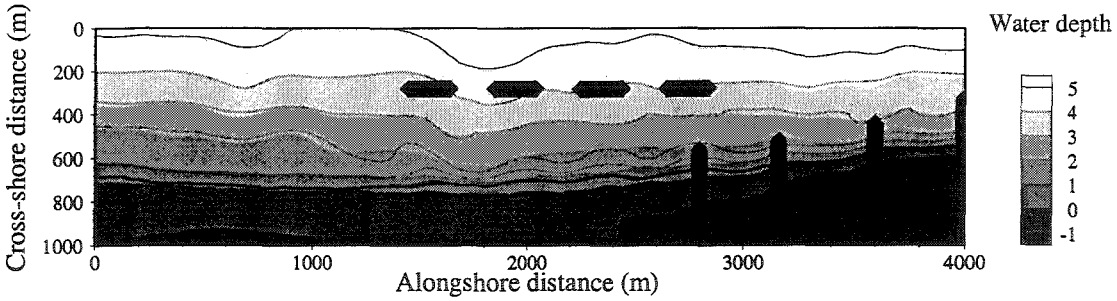

Figure (7.20): Ras El-Bar at November 1986 and July 1993 (measured & calculated).
Grey scale represents the initial contour map of 1986
Contour lines represent the deformed beach at 1993
Thick dotted line represents the measured shoreline at 1993

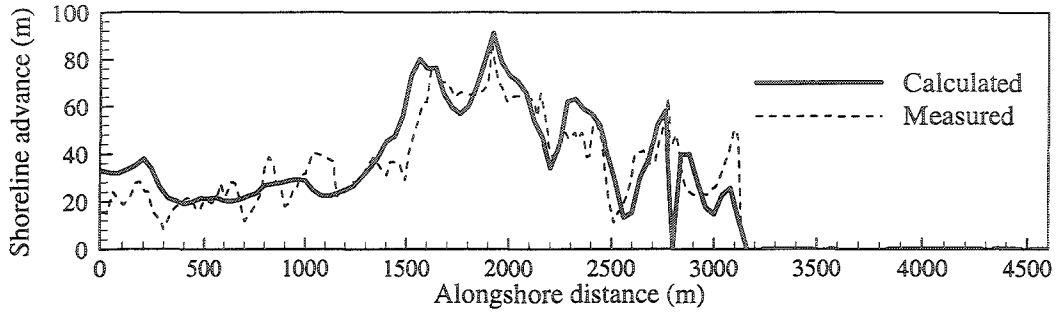

Figure (7.21): Shoreline advance from 1986 to 1995 (measured and calculated).

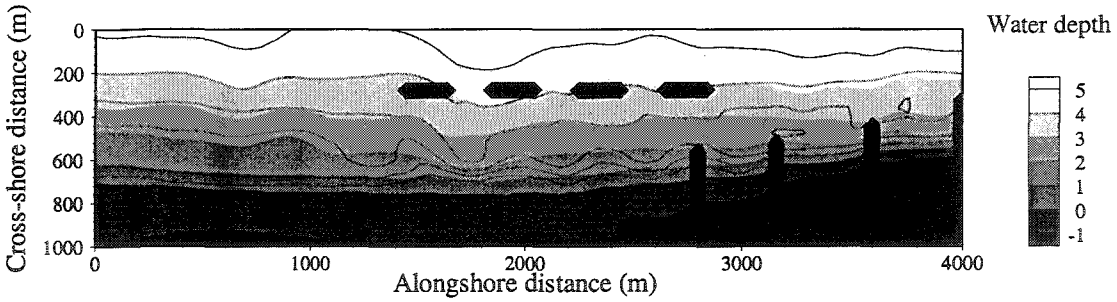

Figure (7.22): Ras El-Bar at November1986 and July 1995.
Grey scale represents the initial contour map of 1986
Contour lines represent the deformed beach at 1995

Chapter 8: Coastal Protection Measures

In this chapter the impacts of several structural types of coastal protection measures will be studied through the application of the ICEM in two case studies in the island of Crete. The non-structural (soft) approaches of beach protection will be reviewed at the end of the chapter for the sake of completeness.

8.1. Study Areas

Two field sites along the island of Crete are studied. Rethymno is the first site, which is located on the Northern shore of Crete, as shown in Figure (8.1). This site represents a typical sandy beach of average slope 1:75. The second field site is the Asfend bay, which is located in the Southern shore of the island and has an average slope of 1:50.

8.1.1. Bathymetric data

The bathymetric data are given on a 20×20 meters grid for both sites. However, the data do not extend to include the shorelines. Therefore, in addition to the interpolation required between the given grid points, extrapolation of data is required to represent shorelines. The gridding is done using Surfer (professional gridding software) with the krigging technique, which is found to yield the most reliable results for both interpolation and extrapolation.

8.1.2. Wave data

The time series wave data over the period from September-99 to October-02 is available, where the significant wave heights and periods are given each 3 hours. Figure (8.2) and Figure (8.3) show the annual wave rose at Asfend and Rethymno, respectively. The monthly wave roses for both sites were studied in order to obtain the design wave time series. It was assumed that over one month, short duration storms which have the same range of wave heights can be grouped into a single prolonged storm.

8.2. Coastal Protection at Rethymno

The dominant direction of waves in Rethymno is from 60° North-West to 30° North-East as shown in Figure (8.3). The beach at Rethymno is composed mainly of medium sand of average grain size 0.27 mm with an average slope of 1:75. A beach of this configuration is quite stable mainly due to the relatively large grain size. The ICEM is applied to a fairly long stretch of Rethymno beach as shown in Figure (8.4), where 5.76 Km of the beach is studied. The whole grid has been rotated by 20° in order to better represent both the shore-parallel and –perpendicular coastal structures and to reduce the wave angles with respect to the grid, although such rotation would not be necessary with the use of the wide angle parabolic model. All the simulations are done over a full year, where waves less than 0.25 m in height are considered calm as they do not affect the sediment movement. Figure (8.5) and Figure (8.6) show the wave heights and vectors of a selected storm of 1.75 m significant wave height, 6.9 s period and -45° anticlockwise from the North. The deformed beach of Rethymno after 1 year of wave attack is shown in

Figure (8.7), where the initial bathymetry is shown in gray scale, while the deformed beach is shown as contour lines. The Rethymno beach is very stable as shown in Figure (8.7) and does not need any kind of coastal protection. In order to study the various impacts of different coastal structures, finer sediment grains of average diameter of 0.12 mm is used (i.e. silty sand beach) so that the Rethymno beach is forced to be an eroding beach as shown in Figure (8.8). In the following sections several structural coastal protection approaches are tested.

8.2.1. Impact of a System of Groins

A groin is a shore protection structure designed to build a protective beach or to retard erosion of an existing or restored beach by trapping littoral drift (U.S. Army, 1984). Groins are usually perpendicular to the shoreline and extend from a point landward of predicted shoreline recession into the water far enough to accomplish their purpose. Since most of the littoral drift moves in the zone landward of the normal breaker zone, the groin maximum extension seaward is not to exceed the breaker line. Groins may be classified as permeable or impermeable, high or low, long or short, submerged or emerged, and fixed or adjustable. Impermeable groins have solid or nearly solid structure, which prevents littoral drift from passing through the structure. Permeable groins have openings through the structure, big enough to permit passage of significant quantities of littoral drift. Some permeable stone groins are made impermeable by heavy marine growth. A series of groins acting together to protect a long section of the shoreline is called groin system or groin field (U.S. Army, 1984). The way a groin modifies the littoral transport rate is about the same whether the groin operates singly or as one of a system, providing

spacing between adjacent groins is adequate. However, a single groin or the updrift groin of a system, may impound less than other individual groins of a system (U.S. Army, 1984). The typical groin, illustrated in Figure (8.9), extends from a point landward of the top of the berm to the normal breaker zone. The predominant direction of wave attack shown by the orthogonals will cause a predominant movement of littoral drift. The groin acts as a partial dam that intercepts a part of the normal longshore transport. As material accumulates on the updrift side, supply to the downdrift shore is reduced, and the downdrift shore recedes. This results in a progressively steepening slope on the updrift side and a flattening slope on the downdrift side, and both slopes reach a common elevation near the end of the groin. When accreted slope reaches ultimate steepness for the available bed material, impoundment stops and all littoral drift passes the groin. If the groin is so high that no material passes over it, all transport must be in depths beyond the end of the groin. Because of the nature of transporting currents, the material in transit does not move directly shoreward after passing the groin, and transport characteristics do not become normal for some distance on the downdrift side of the groin. Thus a system of groins too closely spaced would divert sediment offshore rather than create a widened beach. The accretion filled on the updrift side of the groin creates a departure from normal shore alignment, tending toward a stable alignment perpendicular to the resultant of wave attack. Figure (8.10) shows the general configuration of the shoreline expected for a system of two or more groins. It assumes a well-established net longshore transport in one direction. A general rule is suggested that the spacing between groins should equal two to three times the groin length (U.S. Army, 1984).

The ICEM is capable of modeling the dynamics of sediment transport around the groin system and used as a design tool. Both the emerged and the submerged groin systems will be applied to Rethymno shore in the following sections.

8.2.1.1. Impact of an emerged groin system

Most of the littoral transport in Rethymno moves in the 200 meters close to the shoreline. Therefore, the groins length will not exceed that limit. The first system to be tested is composed of 9 groins equally spaced at 400.0 meters and of 200.0 meters length. Due to the fact that the waves at Rethymno attack the shore nearly perpendicularly as shown in Figure (8.3) and Figure (8.6), the groin system is not effective as shown in Figure (8.11). Comparing Figure (8.8) and Figure (8.11), it is shown that the groins effect is almost nothing. In order to illustrate the effectiveness of the groin system, a different wave climate is imposed on Rethymno beach, where constant wave of 1.0 meters significant offshore height, 6.9 s period and offshore angle of -75° are simulated over a period of 200 days. Figure (8.12) shows the deformed beach of Rethymno, where the groin system stops the erosion and protective beach slowly starts to build up. The effect of the 9-groins system on the littoral transport is shown in Figure (8.13). It is shown that significant amount of the littoral transport is diverted offshore due to the close spacings of the groin system, which suggests that a groin system with wider spacings would behave better in addition to the significant cost saving. Figure (8.14) shows the effect of a 5-groins system of the same length on the littoral transport, where the littoral transport has more space to redevelop between the groins. Figure (8.15) shows the impact of the 5-groins system on the beach. The total accretion for the 5-groins system is found to be

larger than that in the 9-groins system as shown in Figure (8.15) and Figure (8.12), respectively.

8.2.1.2. Impact of a submerged groins system

A system of 5 submerged groins of 2.5 m height above the seabed is tested. The same constant wave climate used to test the groin systems in the previous section is adopted. The advantage of the submerged groins is that they allow the littoral transport to pass over their crests as shown in Figure (8.16). Their impact on the shoreline is almost identical to the emerged groins impact as long as the shoreline advance on the updrift of the groin is less than the length of its emerged-shoreward part, as shown in Figure (8.17). The submerged groin system, on the other hand, has less impact in deep water then the emerged as shown in Figure (8.17). A submerged groin system of less height above the seabed (i.e. 1.5 m) results in a smoother shoreline as shown in Figure (8.18). The downdrift erosion is significantly reduced on the expense of a reduced updrift accretion.

8.2.2. Impact of offshore breakwater system

An offshore breakwater is a structure that is designed to provide protection from wave action to an area or a shoreline located in its leeward side (U.S. Army, 1984). Offshore breakwaters are usually oriented approximately parallel to shore. An offshore breakwater provides protection by reducing the amount of wave energy reaching the water and shore area in its lee. The breakwater structure reflects or dissipates the incoming wave energy impacting directly on the structure and transmits wave energy by means of diffraction into the barrier's geometric shadow. This reduction of wave energy in the shadow area reduces the entrainment and transport of sediments by wave action in

this region. Thus, sand transport from nearby regions will tend to deposit in the lee of the structure. This deposition causes the growth of a cuspate spit (salient) from the shoreline. If the structure's length is long enough in relation to its distance offshore, the salient may connect to the structure forming a tombolo. If the incident breaking wave crests are parallel to the original shoreline (case of no longshore transport), the wave diffracted into the offshore breakwater's shadow will transport sand from the edges of this region into the shadow zone. This process will continue until the shoreline configuration is essentially parallel to the diffracted wave crests and the longshore transport is again zero. In this case the salinet (or tombolo) will have a symmetric shape.

The formation of a tombolo can act as a complete littoral barrier which can trap all the littoral drift until it is filled to capacity at which time sand move around the seaward side of the structure restoring the longshore transport rate. During this process, severe erosion of the downdrift beach would be expected. Therefore, although tombolos increase the length of beach available for recreation use, their formation is not recommended. Tombolo formation can usually be prevented if the structure's length is less than its offshore distance, while tombolo formation becomes almost certain if the structure length is greater than twice the offshore distance.

The detached breakwater system is preferable for cases of waves of nearly normal angle of incidence. Very oblique waves produce a strong longshore current that may prevent tombolo formation and significantly restrict the salient size.

8.2.2.1. Impact of an emerged offshore breakwater system

An emerged offshore breakwater system is tested on the eroding Rethymno silty-sand beach. The system consists of 8 offshore breakwaters of 200.0 meters length each and spaced at 200.0 meters to cover 3.0 Km of the beach. The breakwaters are located 400.0 meters offshore on average so that tombolo formation is prevented. The original wave climate at Rethymno is used in this analysis. Figure (8.19) shows the impact of the breakwater system on Rethymno beach after 1 year. Salients form behind the breakwaters and form a protective beach. Although erosion between the breakwaters still exist, the beach is generally building. Unlike the groin system, the effect of the detached breakwater system on the neighbour areas is minimal due to the fact that the salients do not block the littoral transport.

8.2.2.2. Impact of submerged offshore breakwater system

The impact of a submerged detached breakwater system on the beach is similar to that of an emerged one with smaller amplitudes though. This is due to the fact that significant amount of wave energy is transmitted to the shadow zone of a submerged breakwater. This has the advantage of preventing the tombolo formation. However, the shoreline advance rate is significantly slower than the case of an emerged breakwater system. Therefore, the submerged breakwaters can be placed closer to the shore than the emerged breakwaters. A system of 8 submerged detached breakwaters of 200.0 m length and 200.0 m spacing is tested. The height of the submerged sills (breakwaters) above the seabed is 2.0 meters so that large waves are forced to break at the crests of the breakwaters and therefore dissipate significant amount of their energy there. Small waves,

however, do not break and the whole energy is transformed as if the submerged sills are not present. The breakwaters are placed 200.0 meters away from the shoreline. Figure (8.20) shows both the initial and deformed beaches of Rethymno due to the construction of the submerged sills. The submerged sills do not have a great effect on the shoreline. The reason behind that is that the wave heights at Rethymno are small most of the year.

8.2.3. Impact of T-groins system

The T-groins system is a combination between the groin and the offshore breakwater systems. The shore-connected part of the breakwater acts as a groin, while the offshore-shore-parallel part of the breakwater acts as an offshore breakwater. This system is suitable when the wave climate changes from severe oblique waves, where the groins are preferred, to nearly normal waves, where the offshore breakwaters are preferred. In order to test this kind of system on Rethymno beach, the wave climate has to be modified so that both oblique waves and nearly normal waves are present. A yearly wave climate of 200 active days is assumed where the wave angle changes every 50 days between 75° to 0°. The offshore significant wave height and period is 1.0 m and 6.9 s, respectively. A system of 5 T-groins is tested. Each groin consists of a shore-connected breakwater of 200 m length and a shore-parallel breakwater of 240 m length. The groins are 800 m apart. Figure (8.21) shows the impact of this system on Rethymno beach after one year simulation. The system restores the beach very well as shown in the figure. Figure (8.22) shows the impact of the same system on Rethymno beach using the same wave climate used to test the groin system. The shore-parallel breakwater acts as a littoral barrier, which redirects the littoral transport direction and form a small eddy which helps the

sediments to settle. The erosion on the downdrift sides of the groins is significantly reduced in the case of T-groins because this area lies in the shadow zone of the shore-parallel breakwater, which traps sediments from its vicinity. In conclusion, the T-groins system is an effective system for cases of random wave direction and can be used in cases of dominant wave directions as well.

8.3. Coastal Protection at Asfend Bay

The predominant direction of offshore waves at Asfend is 75° clockwise from the south, as shown in Figure (8.2). The average grain size of the beach material is 0.2 mm. The ICEM is used to investigate the stability of the bay under the wave attack for 1 year. The modeled area extends 4.6 Km alongshore, which includes the whole bay as shown in Figure (8.23). The wide angle parabolic wave model is chosen to model the waves for the bay, where the waves are attacking the beach at a grazing angle (75°). Figure (8.24) shows an example of the wave model output for a selected offshore significant wave of 1.25 m height, 5.8 s period 5.8 and attacking the beach at 75° clockwise from the south. Figure (8.25) shows the transformed wave vectors and rays for the same wave in which the vectors lengths are proportional to wave heights. Figure (8.25) shows the realistic behavior of the wide angle parabolic model, where the wave rays diverges in the bay. Figure (8.26) shows both the initial and deformed beaches of Asfend after one year, where the initial beach is shown in gray scale and the deformed beach is shown as contour line. Note that contour lines of depths more than 6.0 meters have been omitted for convenience. The bay seems to be very stable, where wave energy inside the bay is

relatively small. The Eastern side of the bay is stable as well. The Western side of the bay, however, suffers significant amount of erosion due to the abrupt change in the magnitude and direction of the littoral at the bay entrance as shown in Figure (8.26). Due to the grazing wave angles at the bay, the only choice of a coastal protection regime would be the groin system, which traps significant amount of the littoral drift to build up the beach. Figure (8.27) shows the impact of two groins of 180.0 m length on the Western beach of the bay. The groin system stabilizes the shore and does not cause erosion in the bay.

The other alternative for the beach protection is the submerged groin system. Figure (8.28) shows the impact of a submerged groin system on the beach. The system is composed of two submerged groins of 180.0 m length and 2.5 m height above the sea bed. Comparing Figure (8.27) and Figure (8.28), it is concluded that the emerged groins provide better protection for the shore than the submerged groins.

8.4. Soft Approaches

Beaches can effectively dissipate wave energy and are classified as shore protection structures of adjacent uplands when maintained at proper dimensions (U.S. Army, 1984). Existing beaches are part of the natural coastal system and their wave dissipation usually occurs without creating adverse environmental effects. Since most beach erosion problems occur when there is a deficiency in the natural supply of sand, the placement of borrow material on the shore should be considered as one shore stabilization measure. This can be done either mechanically or hydraulically through sand bypassing.

It is important to remember that the replenishment of sand eroded from the beach does not in itself solve an ongoing erosion problem and periodic replenishment will be required at a rate equal to natural losses caused by the erosion.

Replenishment along an eroding beach segment can be achieved by stockpiling suitable beach material at its updrift end and allow the alongshore process to redistribute the material along the remaining beach. The establishment and periodic replenishment of such a stockpile is termed artificial beach nourishment. Figure (8.29) shows the eroding Lanikai beach (Oahu, Hawaii) before and after nourishment where a wide beach is achieved after nourishment. No matter what the constructed plan shape of the stockpile is, it will spread out (diffuse) and tend toward a straight or slowly curving shoreline as shown in Figure (8.30). Groins may be included in a beach restoration project to reduce the rate of loss and therefore the nourishment requirements, which will produce a great reduction of the annual nourishment costs. When conditions are suitable for artificial nourishment, long reaches of shore may be protected at a cost relatively low compared to costs of other alternative protective structures.

Planning of a protective beach by artificial nourishment requires first the determination of the longshore transport characteristics of the project site and adjacent coast and deficiency of material supply to the problem area. A comparison of surveys of accreting and eroding areas over a long period of time is the best method of estimating the longshore transport rate and therefore the nourishment required to maintain stability of the shore. If these volume measurements surveys are not available, approximations computed from shoreline position as obtained from aerial photography or other suitable

records are often necessary. For such computations, the relation in which 1 square meter of change in beach surface area equals 8 cubic meters of beach material appears to provide acceptable values on exposed seacoasts (U.S. Army, 1984).

After the determination of the volume required for nourishment, it is then necessary to sample and characterize native beach sand in order to obtain a standard for comparing the suitability of potential borrow sediments. During a year at least two sets of samples should be collected from the surface of the active beach profile. Ideally, winter and summer beach conditions should be sampled. The texture properties of all samples are then combined or averaged to form the native composite sample. Based on the native sand properties, the borrow material is selected. The native texture patterns are assumed to be the direct response of sand sorting by natural processes. It is assumed that these same processes will redistribute borrow sand that is placed on the beach in a similar texture pattern as the native sand along the profile considering the differences between native and borrow sand texture. Sorting action by waves will therefore tend to generally transport finer sizes seaward, leave the coarsest sizes slightly shoreward of the plunge point and cover the beach face and remaining offshore areas with the more medium sand sizes. Some sediment sizes that are in borrow material and not in the native beach sand may not be stable in the beach environment. Extremely fine particle sizes are expected ultimately to be moved offshore and lost from the active littoral zone while fragile grains, such as some shells, will be broken, abraded and possibly lost. These kind of changes to the borrow sediment will, through time, make the texture of the beach fill more like the original native sediment but will reduce the original volume of fill placed on the beach.

Therefore, if the fill material is generally finer than the native material, a larger volume of fill is required to achieve the desired beach protection.

Dean and Yoo (1993) offered another explanation for the relationship between the required fill volume and the grain size. They assumed that a stable beach profile (solid line in Figure (8.31)) is represented by Equation (5.66). If the native material is used as nourishment, the beach profile is simply shifted seaward. Since the parameter A in Equation (5.66) increases with D, both the beach profiles and the representative beach slopes will become steeper with grain size. Thus fill material that is coarser than the native sand will result in a steeper profile (dotted line in Figure (8.31)) that intersects the existing profile (Kamphuis, 2000). On the other hand, material that is finer than the native sand produces a flatter profile that does not intersect with the existing profile (dashed line in Figure (8.31)). The volumes of beach fill needed to achieve a certain nourishment width W_n are clearly defined in the case of intersecting profiles. For non-intersecting profiles, it is not clear how far out from shore the nourishment material will migrate and a large volume of the fill material is needed to supply the offshore part of the profile. It is obvious that the non-intersecting profiles must be avoided. Hence, the nourishment material should ideally be coarser than the native material.

After the determination of the borrow material and the required fill volume, the shape of the stockpile is designed. In order to do such design, some surveys have to be done on the original beach in order to determine the berm width and elevation as well as the foreshore slopes. Some beaches have no berms; others have one or several. Figure (8.32) illustrates a beach profile with two berms. The lower berm is the natural or normal

berm and is formed by the uprush of normal wave action during the ordinary range of water level fluctuations. The higher berm, or storm berm, is formed by wave action during storm conditions. During most storms, waves and wave setups will cause an increase in the normal water level on the beach. Beach berms must be carefully considered in planning of a beach fill. If a beach fill is placed to a height lower than the natural berm crest, a ridge will form along the crest and high water may overtop the berm crest causing temporarily flooding the backshore area. The toe of the stockpile should not extend deeper than the effective limiting depth of sediment transport. The initial slope of any beach fill will naturally be steeper than that of the natural profile over which it is placed. The subsequent behaviour of the slope depends on the characteristics of the fill material and the nature of the wave climate.

Another soft shore protection option is the do nothing option. This option would require the evacuation and the relocation of threatened structures. Obviously, this is rarely popular with private homeowners and businesses because of the expense. However, this option poses minimal environmental damage and is usually a one time expense if the relocation is done properly.

8.5. Summary

In this chapter several coastal protection measures have been studied. The ICEM is used to assess the effectiveness of some of the structural measures. It was applied to two coastal areas along the island of Crete. The model is proven to be applicable to large computational domains over the long-term. The analysis showed that the model can be used as a design tool for structural coastal protection measures. The groin system is

shown to be effective in cases of obliquely dominant wave direction, where it acts as littoral barrier. The spacing between the groins is an important parameter, which can be optimized by the model. The model is used to test the impacts of submerged groins as well, which has the same shoreline impact as the emerged groins as long as the emerged part is not filled. The detached breakwater system is mainly used for eroding beaches when the wave angles are generally small. The model can be used to simulate the salients and/or tombolos behind the breakwaters. Submerged sills are used to dissipate the wave energy by forcing the high waves to break over their crests. Therefore, these kind of structures are used to build the shore in cases of storms, while stay ineffective in swell cases. The effectiveness of a system of T-groins is tested by the ICEM. This system can be viewed as a combination between a groin-system and a detached breakwater system. Finally, for the sake of completeness, some non-structural (soft) approaches of shore protection are reviewed.

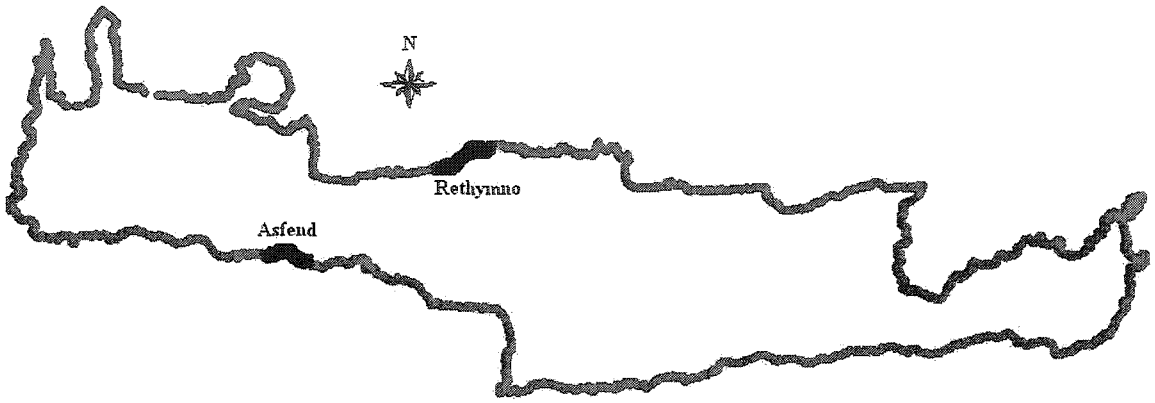

Figure (8.1): The island of Crete.

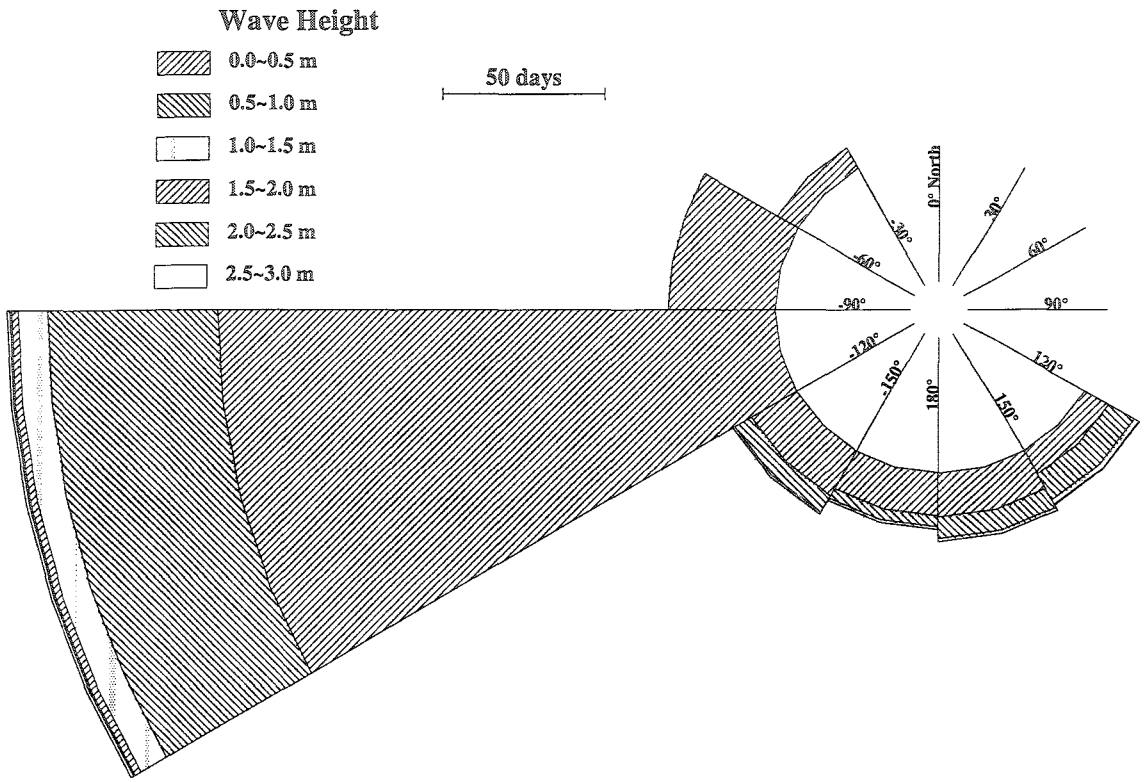

Figure (8.2): Annual wave rose at Asfend bay.

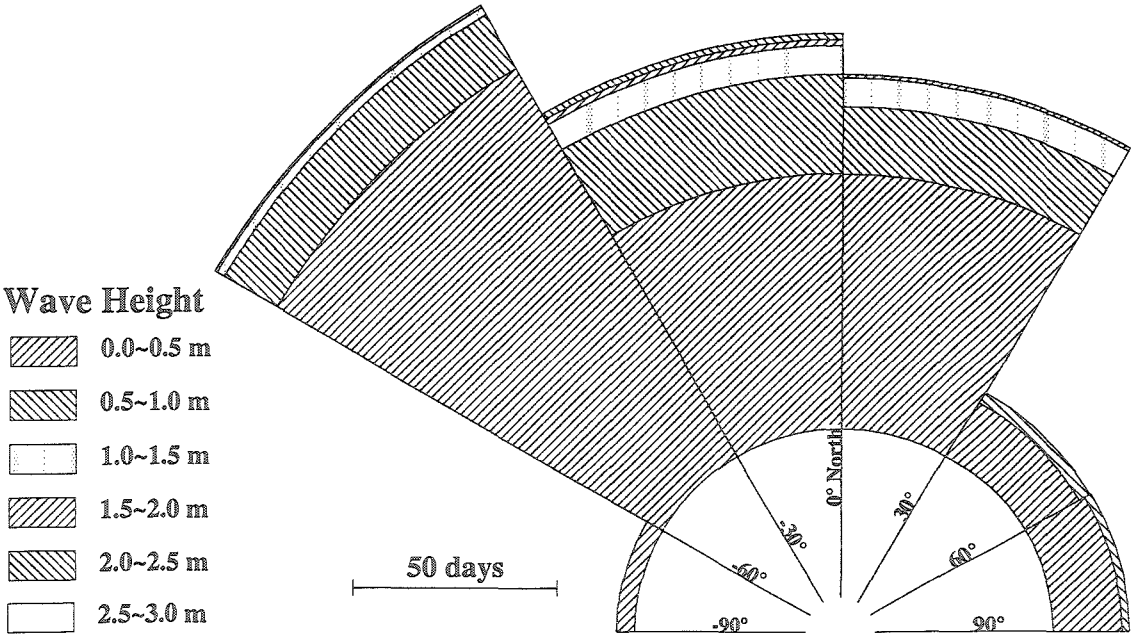

Figure (8.3): Annual wave rose at Rethymno.

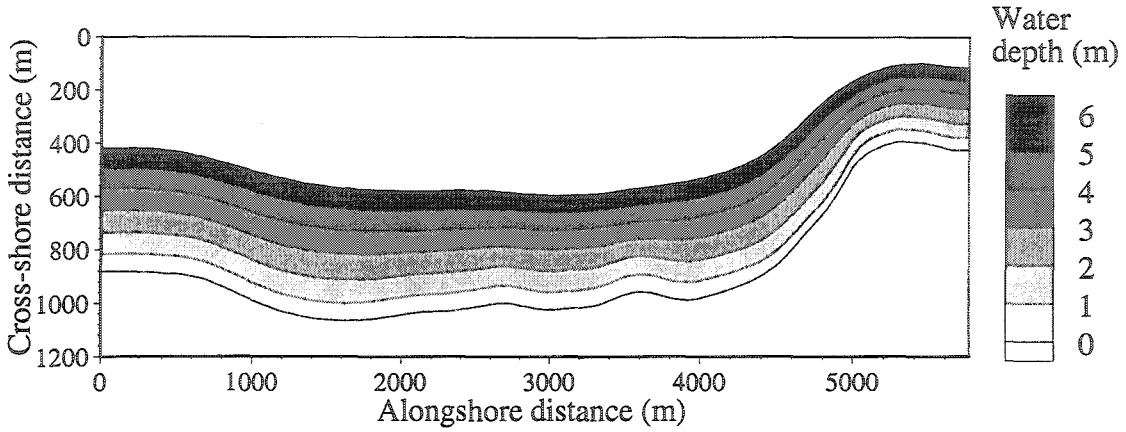

Figure (8.4): Initial bathymetry of Rethymno.

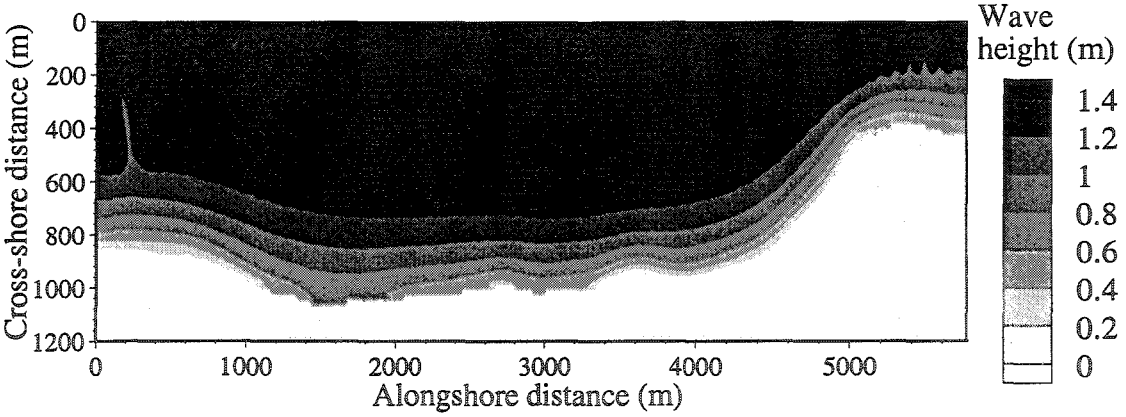

Figure (8.5): Wave heights at Rethymno (H_0 = 1.75 m, T = 6.9 s and θ_0 = 25°).

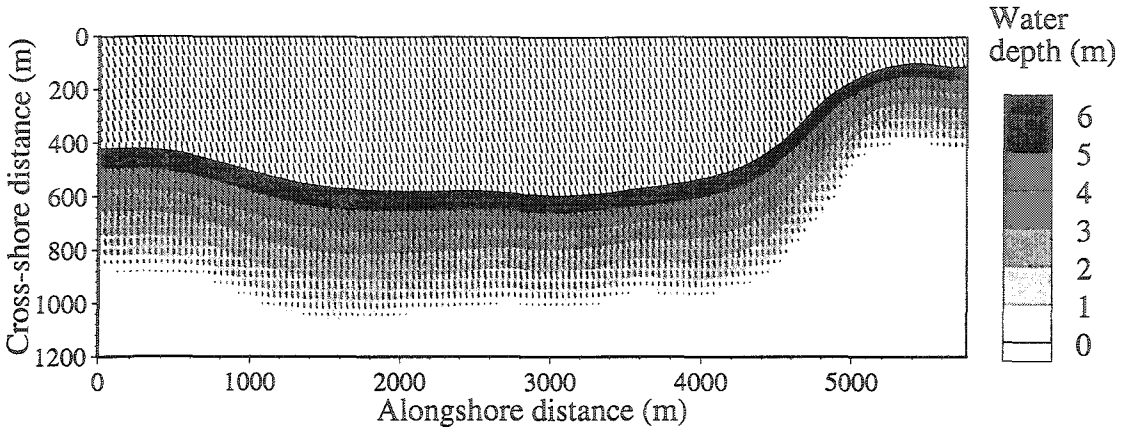

a) Wave vectors.

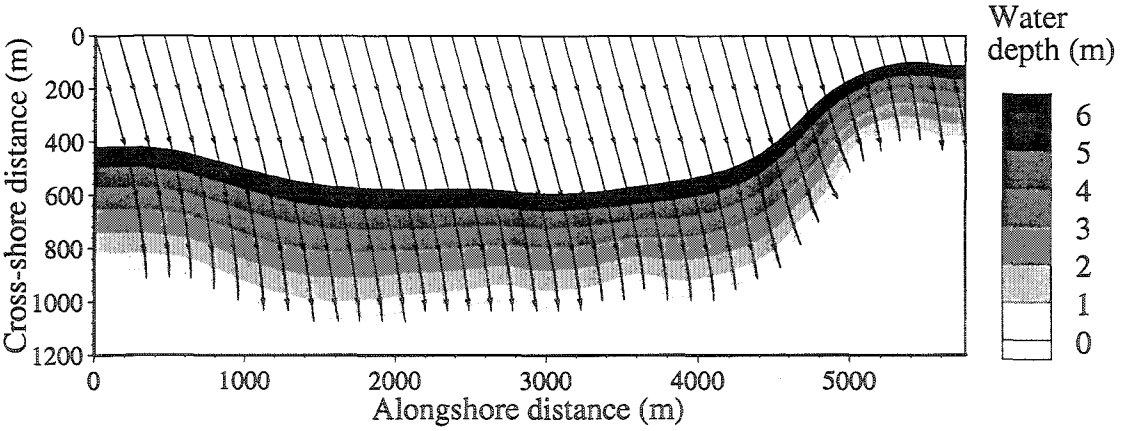

b) Wave rays.

Figure (8.6): Wave vectors and rays at Rethymno (H_0 = 1.75 m, T = 6.9 s and θ_0 = 25°).

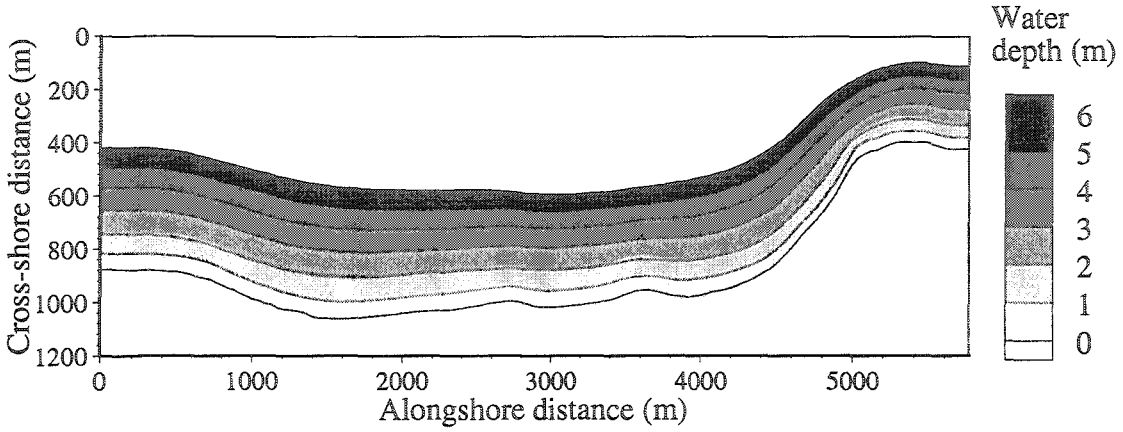

Figure (8.7): Deformed beach of Rethymno after 1 year.

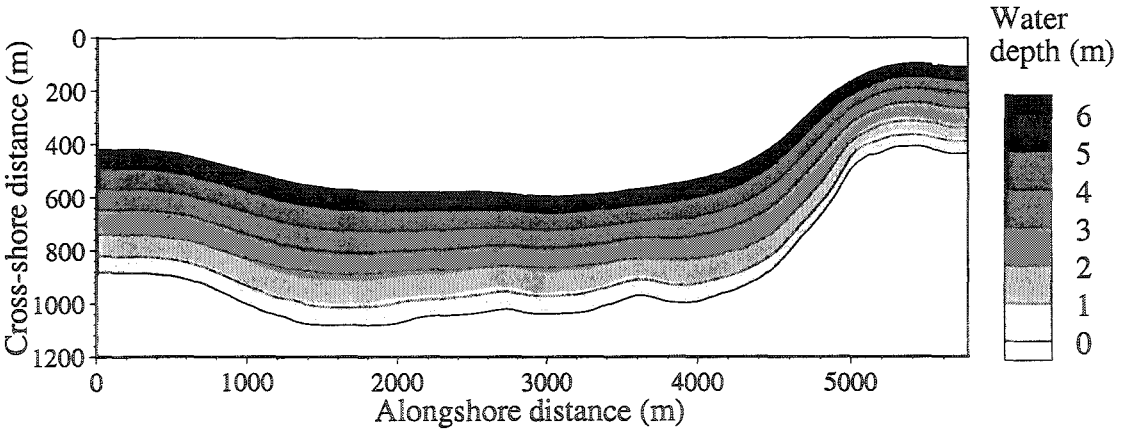

Figure (8.8): Deformed beach of Rethymno after 1 year (D = 0.12 mm).

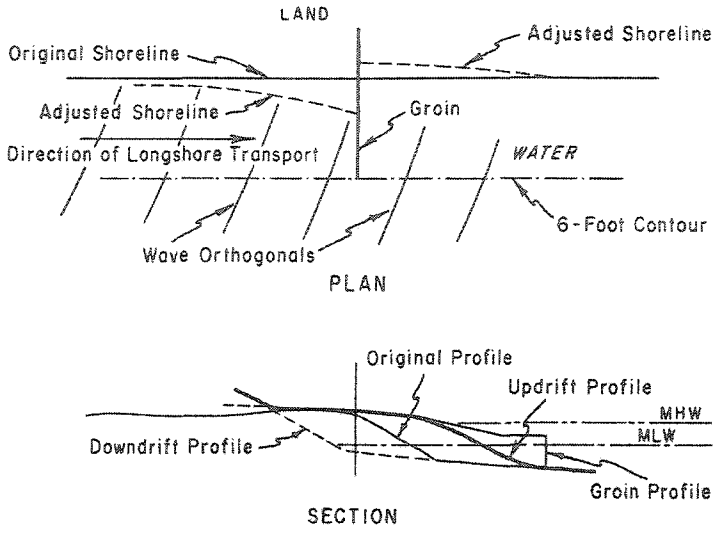

Figure (8.9): Illustration of a typical groin.

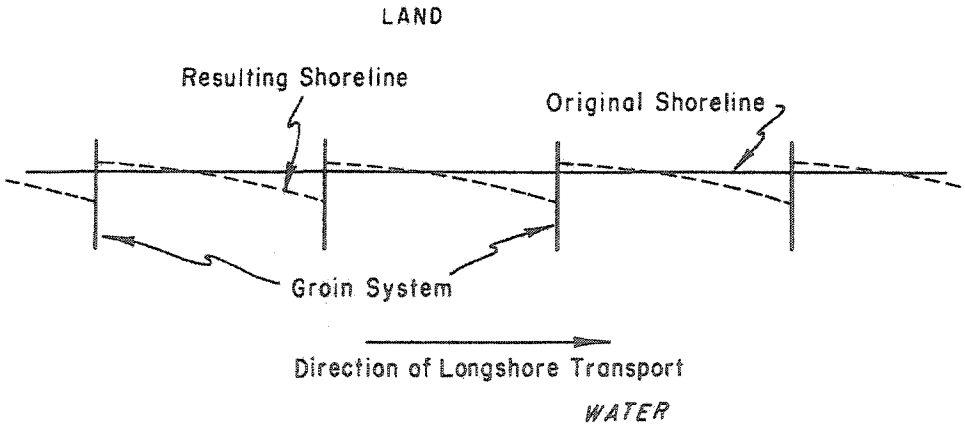

Figure (8.10): Illustration of a typical groin.

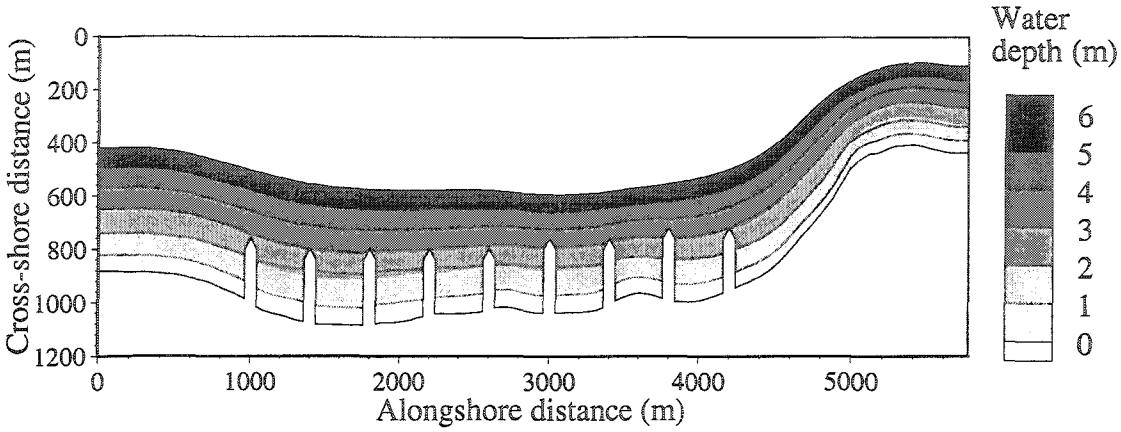

Figure (8.11): Deformed beach of Rethymno with a system of groins.

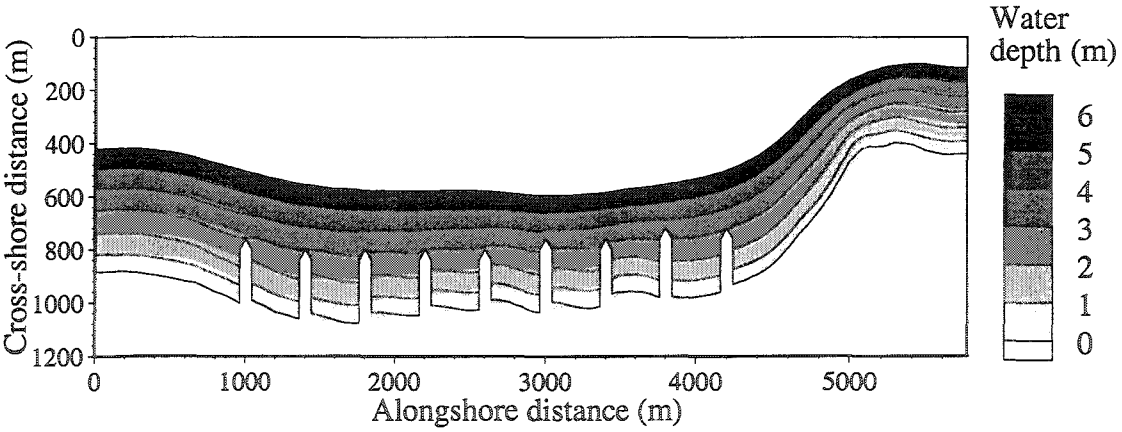

Figure (8.12): Deformed beach of Rethymno with a system of groins (H_0 = 1.00 m, T = 6.9 s and θ_0 = -75°).

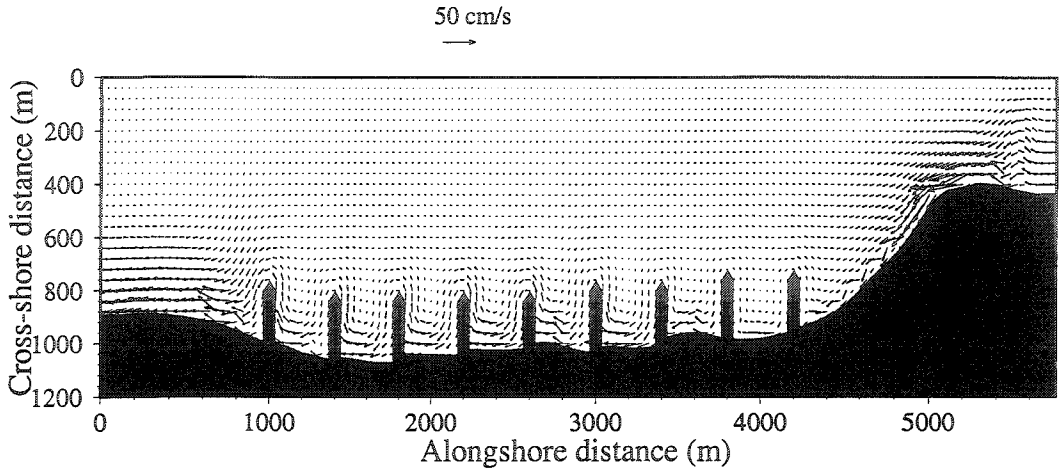

Figure (8.13): Effect of a system of 9 groins on the littoral transport (H_0 = 1.00 m, T = 6.9 s and θ_0 = -75°).

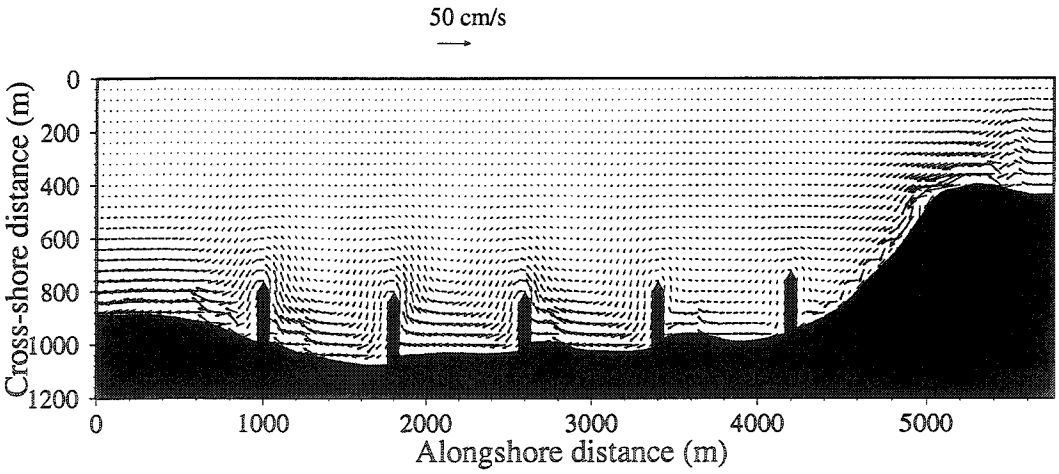

Figure (8.14): Effect of a system of 5 groins on the littoral transport (H_0 = 1.00 m, T = 6.9 s and θ_0 = -75°).

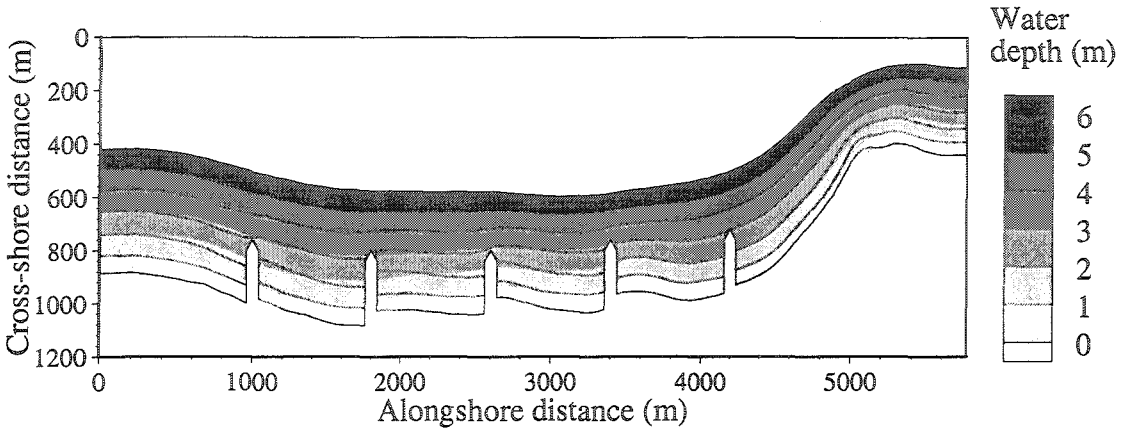

Figure (8.15): Impact of a system of 5 groins on Rethymno beach (H_0 = 1.00 m, T = 6.9 s and θ_0 = -75°).

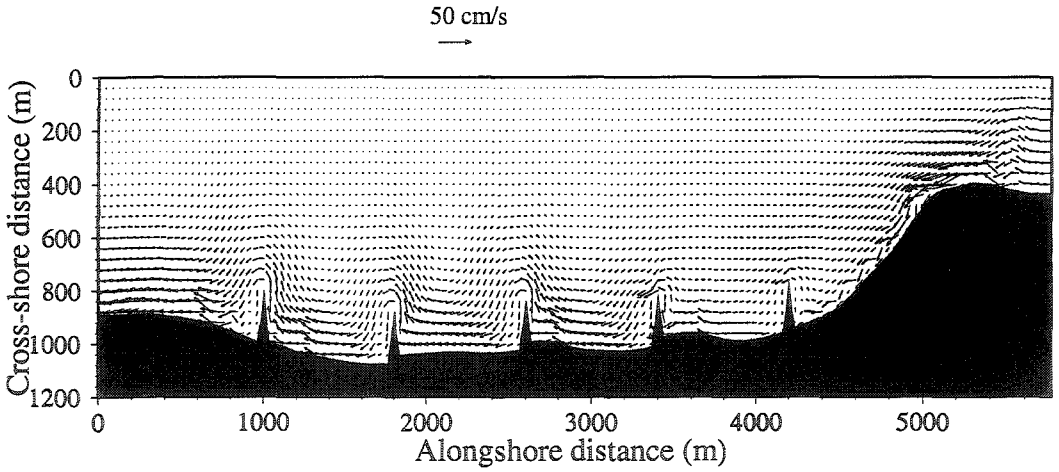

Figure (8.16): Effect of a system of 5 submerged groins on the littoral transport (H_0 = 1.00 m, T = 6.9 s and θ_0 = -75°).

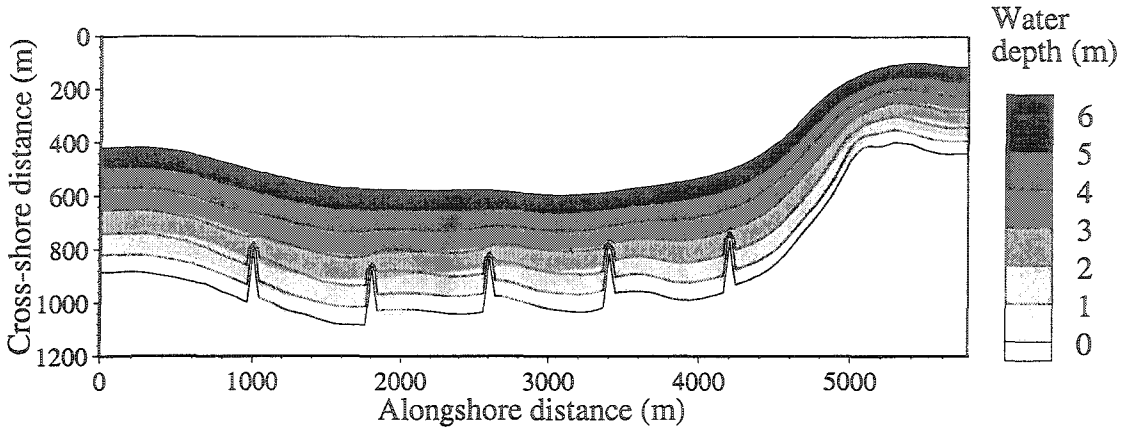

Figure (8.17): Impact of a system of 5 submerged groins of 2.5 m height on Rethymno beach (H_0 = 1.00 m, T = 6.9 s and θ_0 = -75°).

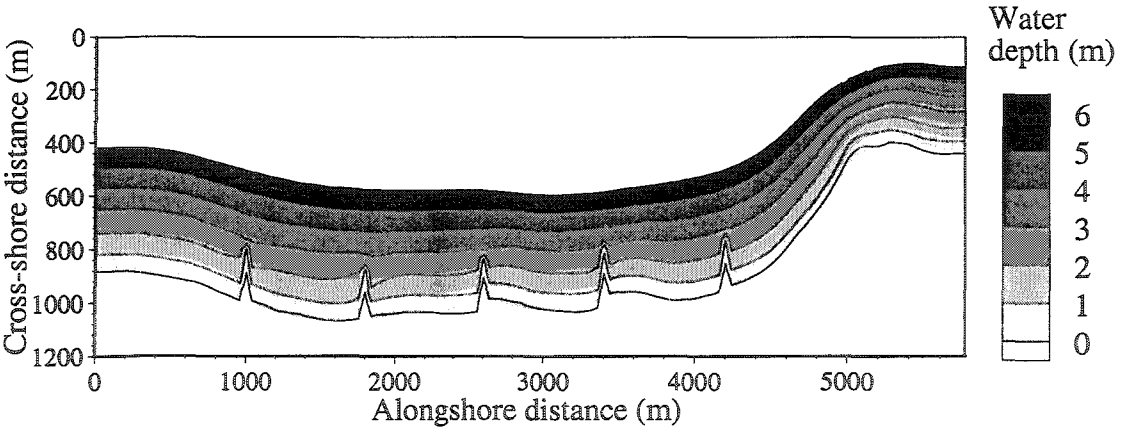

Figure (8.18): Impact of a system of 5 submerged groins of 1.5 m height on Rethymno beach (H_0 = 1.00 m, T = 6.9 s and θ_0 = -75°).

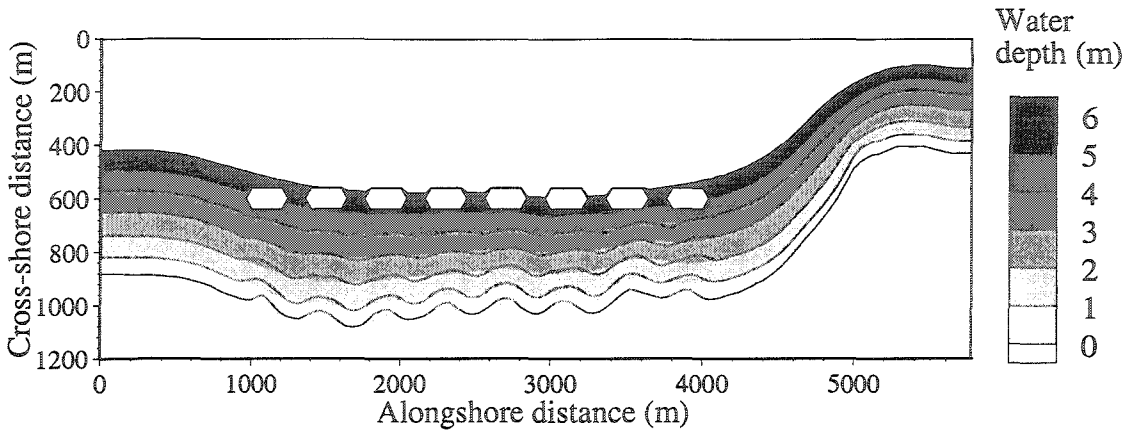

Figure (8.19): Impact of a system of 8 detached breakwaters on Rethymno beach.

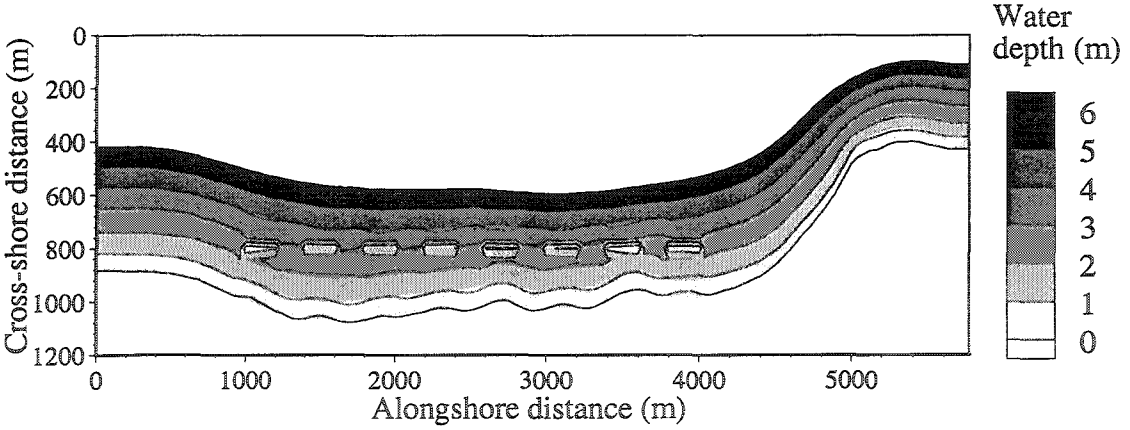

Figure (8.20): Impact of a system of 8 submerged detached breakwaters on Rethymno beach.

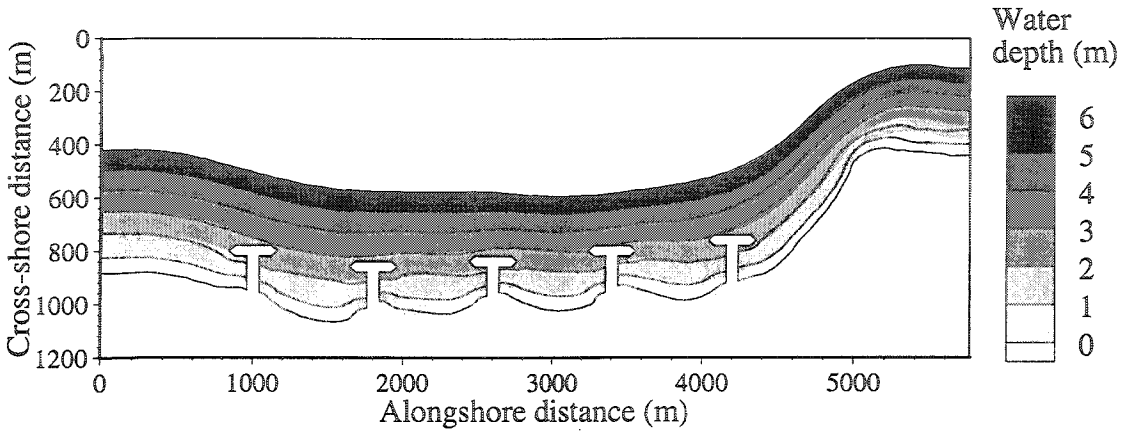

Figure (8.21): Impact of a system 5 T-groins on Rethymno beach.

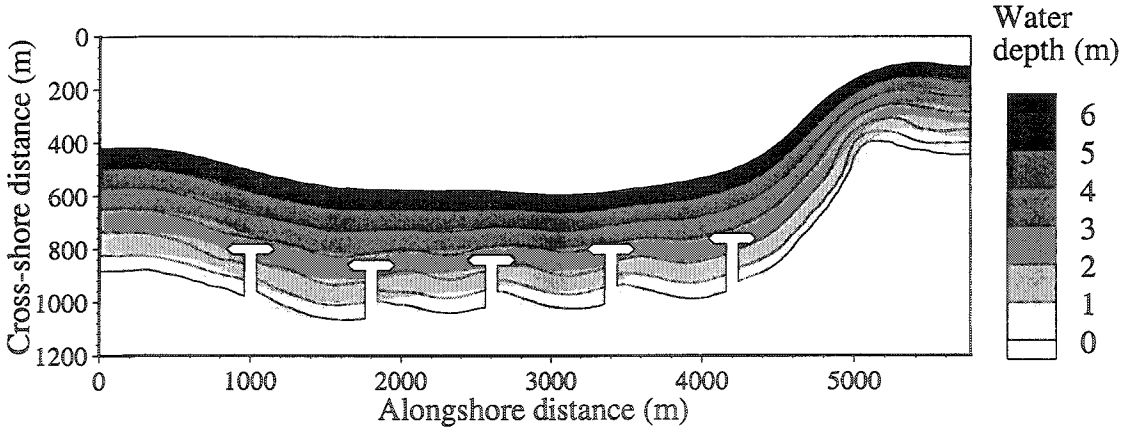

Figure (8.22): Impact of a system of 5 T-groins on Rethymno beach (H_0 = 1.00 m, T = 6.9 s and θ_0 = -75°).

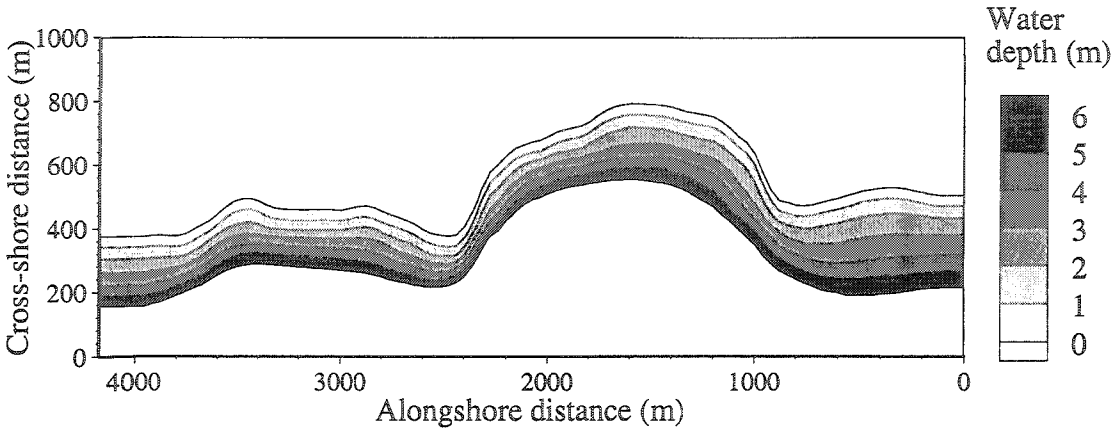

Figure (8.23): Initial bathymetry of Asfend bay.

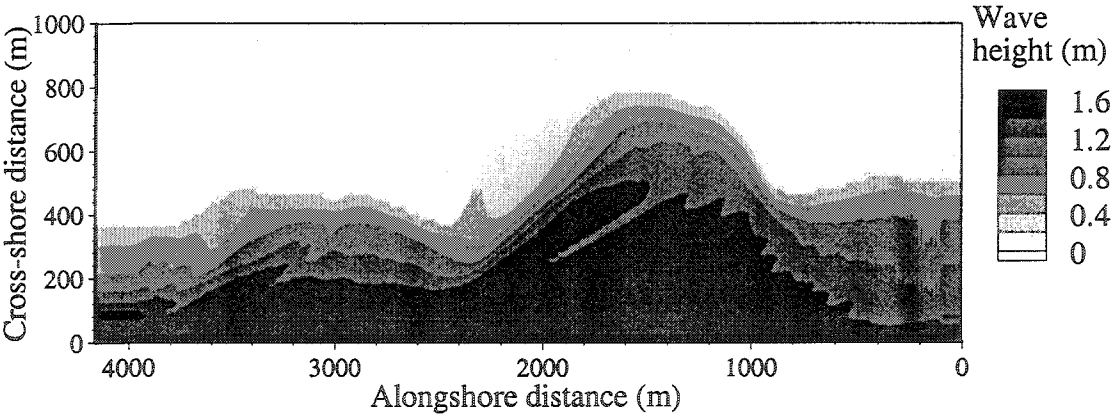

Figure (8.24): Wave heights at Asfend Bay (H_0 = 1.25 m, T = 5.8 s and θ_0 = -75°).

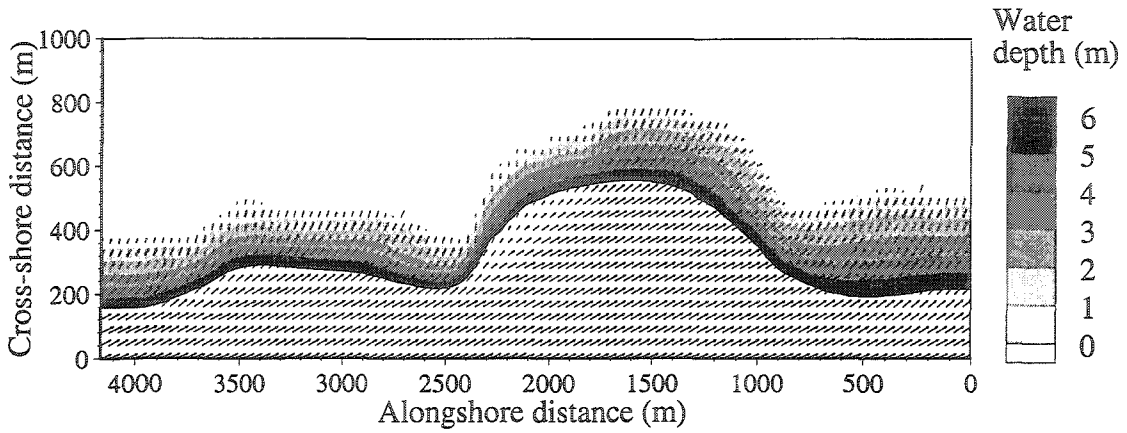

a) Wave vectors

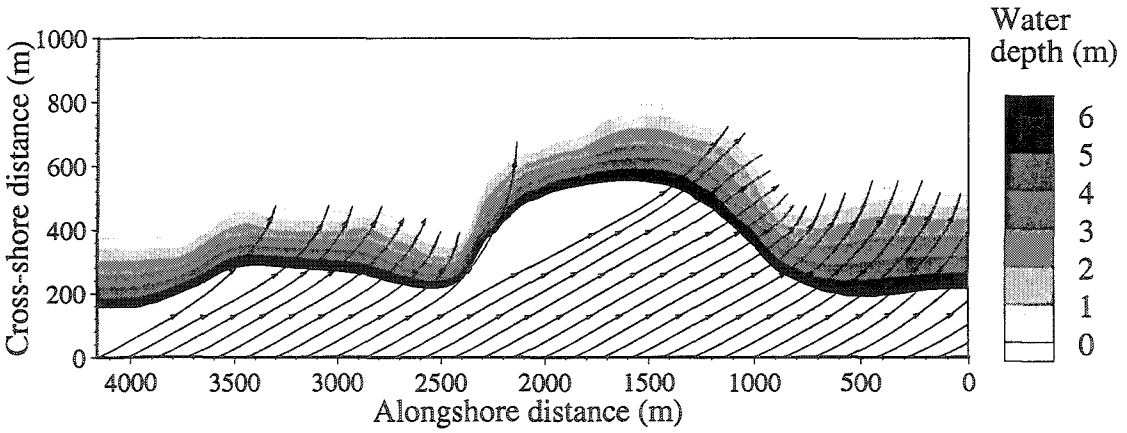

b) wave rays

Figure (8.25): Wave vectors and rays at Asfend Bay (H_0 = 1.25 m, T = 5.8 s and θ_0 = -75°).

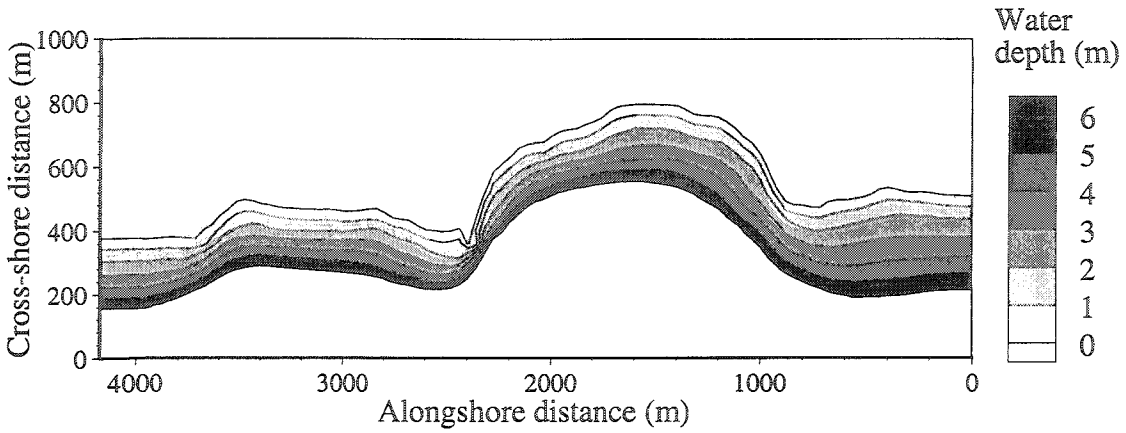

Figure (8.26): Deformed beach of Asfend after 1 year.

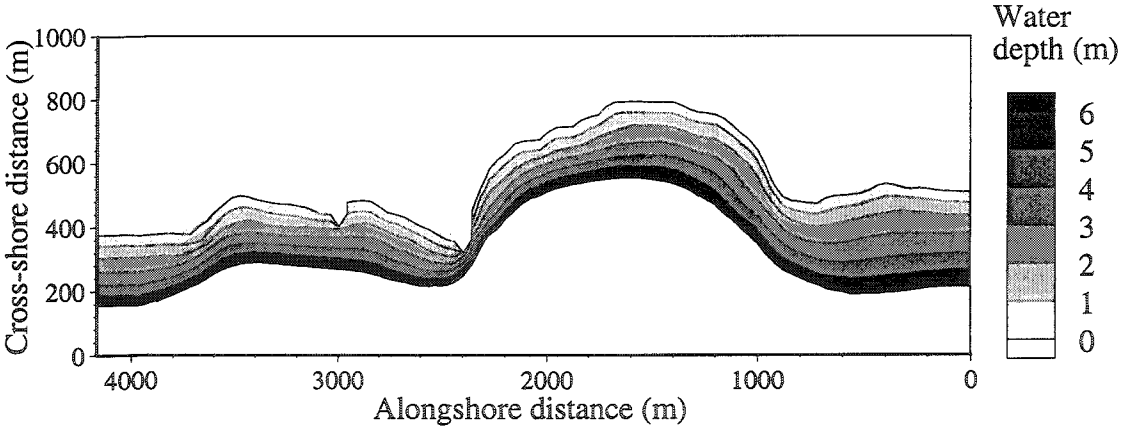

Figure (8.27): Protection of the Western side of Asfend's bay by two emerged groins (1 year simulation).

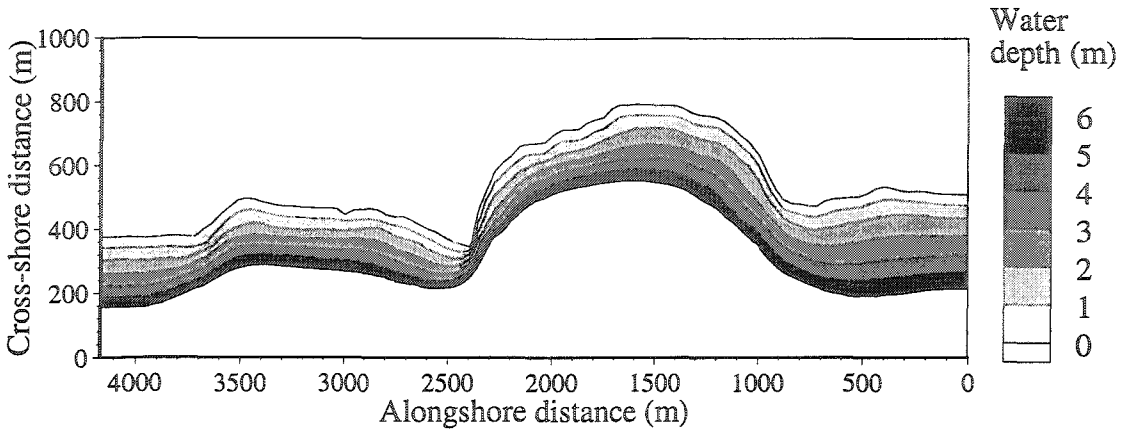

Figure (8.28): Protection of the Western side of Asfend's bay by two submerged groins (1 year simulation).

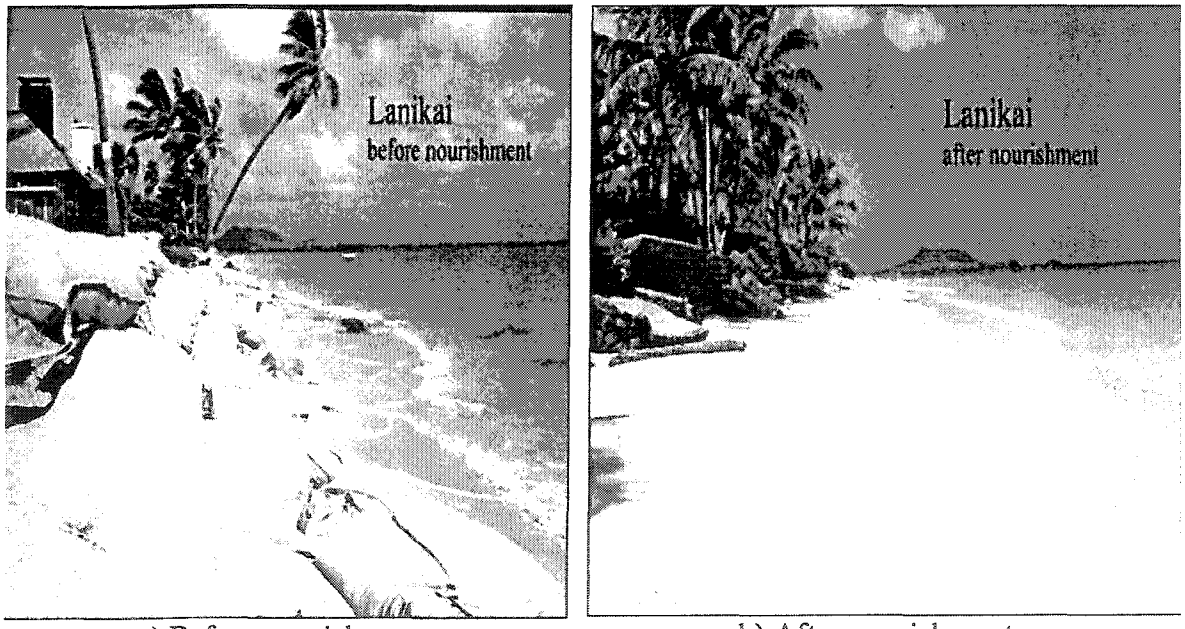

a) Before nourishment b) After nourishment

Figure (8.29): Lanikai beach before and after nourishment.

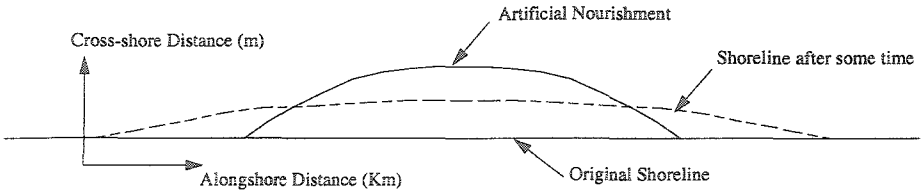

Figure (8.30): Artificial beach nourishment (plan view).

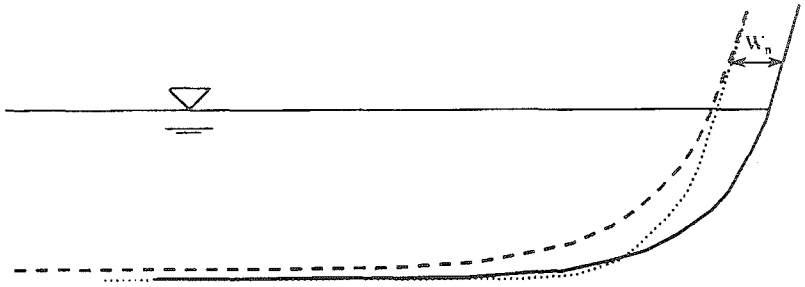

Figure (8.31): Intersecting and non-intersecting profiles.

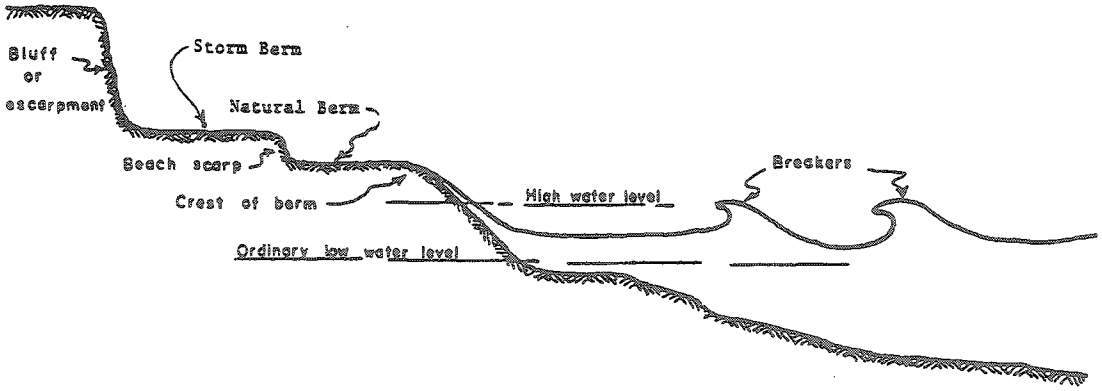

Figure (8.32): Beach berm system.

Chapter 9: Conclusions and Recommendations

9.1. Summary

The main objective of this study was to develop an effective design tool for coastal structures through effectively modelling the various coastal processes. This objective has been achieved through the development of the Integrated Coastal Engineering Model (ICEM). The main modules of this model have been developed over the various chapters of the thesis. Various wave transformation models were developed and verified in chapters 3 and 4. A two-dimensional coastal hydrodynamics model and a coastal morphology model are developed and verified in chapter 5. Sensitivity analysis of the various parameters of the individual modules is done in chapter 6. The ICEM was developed in chapter 7. It was applied to various test cases to show its realistic behaviour. Calibration and verification of the ICEM was done using the field data of the city of Ras El-Bar along the Egyptian Mediterranean coast. Finally, structural impacts of different structures to coastal areas of different characteristics are studied.

9.2. Conclusions

The achievements of the present study can be classified into three components; original, engineering and software components.

9.2.1. Original Components

1. A new set of generalized Padé approximants has been developed and used as absorbing boundary condition for elliptic wave models (chapter 3). It has been theoretically proven

that the new rational approximants are more accurate than all the existing rational approximations.

2. Based on the new set of generalized Padé approximants, a new set of parabolic approximations for the elliptic wave equation (Helmholtz equation) has been developed (chapter 3). The new parabolic equation based on [1/1] generalized Padé approximation is used as an absorbing boundary for elliptic wave models and proven through different applications to be better than all the existing rational approximations. The new [1/1] boundary equation can be applied to cases of wave angles up to 70°. Practically, it has been proven that the [1/1] boundary equation is the best equation in the set, giving the complexity of higher order approximations.

3. A modified generalized conjugate gradient algorithm has been developed to solve the elliptic wave equation with high order boundary equations (particularly [1/1] equation). Compared with the conventional generalized conjugate gradient algorithm, the modified algorithm does need extra iteration to converge, although being two orders higher than the boundaries implemented by the conventional generalized conjugate gradient algorithm.

4. Based on the generalized [1/1] Padé approximation, a new parabolic model for wide wave angles (up to 70°) has been developed (chapter 4). The model is extended to include the effect of nonlinearity on waves in shallow depths and the wave dissipation. The model is proven to be better than all the existing parabolic models.

5. A practical technique is implemented to reduce the total number of iteration required by an elliptic model through using the parabolic model solution as an initial solution. This technique can reduce the total number of iterations up to 80%. In addition, this technique

allows the choice of low accuracy for the elliptic solver without affecting the quality of the solution.

6. Verification of the ICEM using field data will allow the model to be applied to other similar coastal areas as a design and assessment tool for coastal protection structures.

7. The applicability of the 3D morphological models for the long-term prediction is proven through the successful application of the ICEM to Ras El-Bar area over 9 years.

9.2.2. Engineering Components

1. The parabolic model which simulates the combined refraction-diffraction is used to estimate the wave heights and angles over a very wide range of wave angles and bottom slopes. It is effectively used for simulations over very complicated bottom bathymetry.

2. The wave models developed in this study are suited for practical use because their formulation allows the application of the models without having to rotate grids to reduce the wave angles with respect to the grid.

3. The elliptic wave model is used to effectively simulate the wave heights and angles around coastal structures.

4. The depth integrated coastal circulations are estimated by the hydrodynamic model, which allows the study of the hydrodynamic impacts of coastal structures. In addition, it allows the estimation of wave setup along beaches.

5. The sediment transport rates in coastal areas are calculated after the suitable calibration of the different parameters of the sediment transport model.

6. The ICEM allows the study of the morpho-dynamical impacts of different coastal structures.

7. The ICEM is used as an effective design tool for coastal protection works. It is used for both the short and long terms.

8. The ICEM is used to examine the significance of existing coastal structures and propose remedial actions for the existing coastal structures.

9.2.3. Software Components

Through the course of this study, several programs have been developed using FORTRAN 77. Implicit finite-difference schemes are used for all the models except the coastal morphology model. The following summarises the software developed:

1. A new parabolic water wave transformation model. The model effects and facilities include:

   a. Refraction, diffraction and shoaling,

   b. applicable over a very wide range of wave angles,

   c. complicated bathymetry,

   d. nonlinear effects,

   e. wave energy dissipation, and

   f. very fast and stable.

2. A new elliptic water wave transformation model. It's facilities and effects include:

   a. Refraction, diffraction reflection and shoaling,

   b. applicable over a very wide range of wave angles,

   c. complicated bathymetry,

   d. nonlinear effects,

   e. wave energy dissipation, and

f. convergence is guaranteed.

3. A combined parabolic/elliptic water wave transformation model. It overcomes the limitations of the two other models. In addition to the facilities mentioned for the elliptic model, it is relatively fast.

4. A new depth-integrated time-dependent coastal hydrodynamic model. It includes:

a. Convective and cross momentum,

b. bottom shear stress,

c. Coriolis forces,

d. momentum dispersion,

e. wave-induced currents, and

f. Stokes drift and surface rollers effects.

5. Coastal morphology model (uses an explicit finite-difference method), which includes:

a. Sediment transport due to coexisting current and wave,

b. cross-shore transport by the action of waves,

c. effect of induced turbulence in the surfzone, and

d. coastal morpho-dynamics.

6. Integrated Coastal Engineering Model, which groups all the above models. It can simulate both the short and long term coastal morphology changes.

9.3. Recommendations for Future Work

An integrated coastal engineering modelling system has been developed in this study. However, further research and effort is required to improve this modelling system to include more facilities and tools. The following summarises the recommendation for the future work:

1. The wave transformation models developed in this study set the foundation that can be built upon. Although they are very reliable and can model very complicated cases, they only allow the transformation of monochromatic waves. A very useful extension would be the inclusion of random waves without sacrificing the nonlinear effects.

2. The proposed hydrodynamic model does not include the tidal effects, which can be significant in some cases. It is recommended to improve the present hydrodynamic model to include tidal currents and tidal water level variations.

3. It is recommended to study the three-dimensional effect on the hydrodynamic modelling in the surfzone. Although this will restrict the model applicability, it will allow the micro-modelling of different phenomena that take place in the highly turbulent surfzone.

4. In order to study the environmental impacts of different structural approaches, it is recommended to include a pollutant transport module to ICEM.

5. More research is required to improve the existing sediment transport in the surfzone, which are generally based on empirical estimation of parameters, which generally need calibration beforehand. A more general model will allow the portability of sediment transport models.

6. Although the ICEM can be used for the coastal structural design and assessment, in some cases the optimum protection scheme would be a non-structural one. Therefore, it is recommended that further research is to be done to include the inland coastal dynamics to the modelling system ICEM.

7. Adding a one-line based model to the ICEM will allow the simulation of larger coastal domains over longer period of time. The new module can be used as a long-term mode in the improved ICEM.

8. Last but not least, a master plan for coastal protection projects along Canadian Pacific and Atlantic coasts can be developed based on the improved ICEM. This will require large funding and effort to be spent in the data collection which includes wave, sediment and morphological data. After the data collection, the long-term mode (based on the one-line theory) of the improved ICEM can be used to identify areas which suffer from severe erosion. These areas are then studied separately in details using the model and the best protection scheme is identified for each area. The long-term mode of the model is applied again with the proposed protection schemes in order to check the stability of the whole coast. This idea of master planning will enforce the suitable bylaw restrictions upon the development of coastal activities.

BIBLIOGRAPHY

Abbott, M.B. *Computational Hydraulics*. Pitman Advanced Publishing Program, Boston, Mss., 1980.

Abbott, M.B., Larsen, J., and Tao, J. *Modelling Circulations in Depth-Integrated Flows, Part 1: The Accumulation of the Evidence*. Journal of Hydraulic Res. 23 (4), pp. 309-326, 1985.

Airy, G.B. *On Tides and Waves*. Encyclopedia Metropolitan, London, pp. 241-396, 1845.

Ariathurai, C.R. *A Finite Element Model of Cohesive Sediment Transportation*. Ph.D. Diss., Univ. California, Davis, Calif., 1974.

Athow, R.F., Trawle, M.J., and Richards, D.R. *Numerical Evaluation of Training Structures*. Proc. Natl. Conf. Hydraulic Eng., Hydraulics Divs., ASCE, Williamsburg, Va., pp. 345-350, 1987.

Badiei, P., and Kamphuis, J.W. *Physical and Numerical Study of Wave Induced Currents in Wave Basins of Various Sizes*. Coastal Dynamics' 95, ASCE, Gdansk, pp. 337-388, 1995.

Bagnold, R.A. *Mechanics of Marine Sedimentation*. The Sea (ed. By Hill, M.N.), Vol. 3, Interscience, New York, pp. 507-528, 1963.

Bailard, J.A. *A Simplified Model for Longshore Sediment Transport*. Proc. 19th Coastal Eng. Conf., ASCE, pp. 1454-1470, 1984.

Bailard, J.A. An *Energetic Total Load Sediment Transport Model for a Plain Sloping Beach*. J. Geophys. Res., Vol. 86, pp. 10938-10954, 1981.

Bakker, W.T. *The Dynamics of a Coast with a Groin System. Proc.* Of the 11th Coastal Engineering Conf. ASCE, pp. 492-517, 1968.

Battjes, J.A., and Janssen, J.P.F.M. *Energy Loss and Set-up Due to Breaking of Random Waves*. Proc. 16th Int. Conf. on Coastal Eng., ASCE, New York, pp. 569-587, 1978.

Behrendt, L. *A Finite Element Model for Water Wave Diffraction Including Boundary Absorption and Bottom Friction*. Technical University of Denmark, Series paper No. 37. 1985.

Beltrami, G.M., Bellotti, G., De Girolamo, P., and Sammarco, P. *Treatment of Wave Breaking and Total Absorption in a Mild-Slope Equation FEM Model*. Journal of Waterway, Port, Coastal, and Ocean Eng. Vol. 127, No. 5, pp. 263-271, 2001.

Berkhoff, J.C.W. *Computation of Combined Refraction-Diffraction*. Proc. 13th Coastal Eng. Conf., ASCE, pp. 471-490, 1972.

Berkhoff, J.C.W. *Mathematical Models for Simple Harmonic Linear Water Wave Refraction and Diffraction*. Publication No. 163, Delft Hydraulics Lab., 103pp, 1976.

Berkhoff, J.C.W. *Refraction and Diffraction of Water Waves; Wave Deformation by a Shoal, Comparison between Computations and Measurements*. Report on mathematical investigation, Delft Hydraulics Laboratory, Report W 154 part VIII, 1982.

Bijker, E.W. *Longshore Transport Computations*. J. Waterways, Harbors, and Coastal Eng. Division, ASCE, Vol. 97, WW$, pp. 687-701, 1971.

Birkemeier, W.A., and Dalrymple, R.A. Nearshore Water Circulation Induced by Wind and Waves. Proc. Symp. on Modeling Techniques, Modeling'75, ASCE, pp. 1062-1081, 1975.

Bodge, K.R. *Longshore Current and Transport Across Non-Singular Equilibrium Beach Profiles*. Proc. 21st Int. Conf. Coastal Eng., ASCE, pp. 1396-1410, 1988.

Booij, N. *Gravity Waves on Water With Non-Uniform Depth and Current*. Report No. 81-1, Delft University of Technology, Dept. of Civil Eng, 1981.

Bowen, A.J. Simple *Models of Nearshore Sedimentation, Beach Profiles and Longshore Bars*. The Coastline of Canada (ed. By S.B. McCann), Geological Survey of Canada, pp. 1-11, 1980.

Briand, M.H.G., and Kamphuis, J.W. *A Micro Computer Based Quasi 3-D Sediment Transport Model. Proc.* 22nd Int. Coastal Eng. Conf., ASCE, pp. 2159-2172, 1990.

Briand, M.-H.G., Kamphuis, J.W. *Waves and Currents on Natural Beaches: A Quasi 3-D Numerical Model*. Coastal Eng. 33, pp. 11-39, 1993.

Butler, H.L. *Numerical Simulation of Tidal Hydrodynamics*. Great Egg Harbour and Corson Inlets, New Jersey, Technical Rep. H-78-11, Coast. Eng. Res. Centre, U.S. Army Engr. Waterway Experiment Station, Vicksburg, Miss., 1978.

Chen, H.S. *A Storm Surge Model Study, Vol. II: A Finite Element Storm Surge Analysis and its Application to a Bay-Ocean System*. Virginia Inst. Marine Science, Gloucester Point, Va., Spec. Rep. 189, 1978.

Chen, H.S., and Houston, J.R. *Calculation of Water Level Oscillation in Coastal Harbors*. Instructional Rep. 87-2, Coast. Eng. Res. Centre, U.S. Army Engr. Waterway Experiment Station, Vicksburg, Miss., 1987.

Chu, W.-S., and Yeh, E.E.-G. *Calibration of a Two-Dimensional Hydrodynamics Model*. Coastal Eng., 9(4), pp. 293-307, 1985.

Copeland, G.J.M. *A Practical Alternative to the Mild-Slope Wave Equation*. Coastal Eng., 9, pp. 125-149, 1985.

Dabees, M., and Kamphuis, J.W. *ONELINE, A Numerical Model for Shoreline Change*. Proc. 26th Int. Conf. of Coastal Eng., ASCE, pp. 2668-2681, 1998.

Dabees, M.A., and Kamphuis, J.W. *ONELINE: A Numerical Model for Shoreline Change*. Proc. 26th International Conference of Coastal Engineering, Copenhagen, Denmark, ASCE, pp 2668-2681, 1998.

Dabees, M.A., Kamphuis, J.W. *NLINE: Efficient Modelling of 3D Beach Change*. 27th Conf. on Coastal Eng., Sydney, Australia, July 2000.

Dally, W.R., Dean, R.G., and Dalrymple, R.A. *Wave Height Variations Across Beaches of Arbitrary Profile*. J. Geophys. Res., 90, pp. 11917-11927, 1985.

Dally, W.R. and Osiecki, D.A. *The Role of Rollers in Surf Zone Currents*. 24th Int. Conf. on Coastal Eng., Kobe, pp. 1895-1905, 1994.

Dalrymple, R.A., and Kirby, J.T. *Models for Very Wide-Angle Water Waves and Wave Diffraction*. J. Fluid Mech., Cambridge, U.K., 192, pp. 33-50, 1988.

Dalrymple, R.A., Suh, K.D., Kirby, J.T., and Chae, J.W. *Models for Very Wide-Angle Water Waves and Wave Diffraction. 2: Irregular Bathymetry*. J. Fluid Mech., Cambridge, U.K., 201, pp. 299-322, 1989.

Davis, J.C. *Statistics and Data Analysis in Geology*. 2nd edition, John Wiley & Sons, 1973.

de Vriend, H.J., and Stive, M.J.F. *Quasi-3D Modelling of Nearshore Currents*. Coastal Eng., 11, pp. 565-601, 1987.

Dean, R.G., and Yoo, C. *Predictability of Beach Nourishment Performance, Beach Nourishment Engineering and Management Considerations*. Proc. Coastal Zone' 93, ASCE, New Orleans, pp. 86-102, 1993.

del Valle, R., Medina, R., and Losada, M.A. *Dependence of Coefficient K on Grain Size*. Technical Note No. 3062. J. of Waterway, Port, Coastal and Ocean Eng., Vol. 119, No. 5, pp. 568-574, 1993.

Dingemans, M.W. and Radder, A.C. *Surface Wave Propagation over an Uneven Bottom; Wave Deformation by a Shoal*. Delft Hydraulics, Report W301, Part 6, 1986.

Dingemans, M.W. *Verification of Numerical Wave Propagation Models with Filed Measurments; CREDIZ verification Haringvliet*, Delft Hydraulics, Report W488, Part 1, 1983.

Dingemans, M.W. *Water Wave Propagation over Uneven Bottoms, Part 1 – Linear Wave Propagation*. World Scientific, 1997.

Dingemans, M.W., Stive, M.J.F., Kuik, A.J., Radder, A.C., and Booij, N. *Field and Laboratory Verification of the Wave Propagation Model CREDIZ*. Proc. 19th Int. Conf. on Coastal Eng., Houston, pp. 1178-1191, 1984.

Eagleson, P.S. *Theoretical Study of Longshore Currents on a Plane Beach*. Hydrodynamics Lab. Report, No. 82, M.I.T. 1965.

Ebersole, B.A. and Dalrymple, R.A. *Numerical Modelling of Nearshore Circulation*. Proc. 17th Coastal Eng. Conf., ASCE, pp. 2710-2725, 1980.

Ebersole, B.A.,Cialone, M.A., and Prater, M.D. *PCPWAVE: A Linear Wave Propagation Model for Engineering Use*. Technical Rep. 86-4, Coast. Eng. Res. Centre, U.S. Army Engr. Waterway Experiment Station, Vicksburg, Miss., 1986.

Einstein, H.A. *Formulas for the Transportation of Bed Load*. Trans. ASCE, Vol. 107, pp. 561-577, 1942.

Engquist, B., and Majda, *A. Absorbing Boundary Conditions for the Numerical Simulation of Waves*. Math. Comput., 31, pp. 629-652, 1977.

Frihy, O.E., Fanos, A.M., Khafagy, A.A., and Komar, P.D. *Patterns of Nearshore Sediment Transport along the Nile Delta, Egypt*. Coastal Eng., Vol. 15, pp. 409-429, 1991.

Galvin, C.J., and Eagleson, P.S. Experimantal Study of Longshore Currents on a Plane Beach. Technical Memo. No. 10, Coast. Eng. Res. Centre, U.S. Army Engr. Waterway Experiment Station, Vicksburg, Miss., 1965.

Givoli, D. *Numerical Methods for Problems in Infinite Domains*. Elsevier Science Publishers B.V., 1992.

Granat, M. *Numerical Model Evaluation of Advance Maintenance*. Proc. Natl. Conf. Hydraulic Eng., Hydraulics Divs., ASCE, Williamsburg, Va., pp. 321-326, 1987.

Grant, U.S. *Waves as a Transporting Agent*. American Journal of Science, Vol. 241, pp. 117-123, 1943.

Halpern, L. and Trfethen, L.N. *Wide-Angle One-way Wave Equations*. J. Acoust. Soc. Am., 84, pp. 1397-1404, 1988.

Hanson, H., and Kraus, N.C. *GENESIS: Generalized Model for Simulating Shoreline Change*. Miscellaneous Rep. No. 89-19, Coast. Eng. Res. Centre, U.S. Army Engr. Waterway Experiment Station, Vicksburg, Miss., 1989.

Hedges, T.S. *An Empirical Modification to Linear Wave Theory*. Proc. Inst. Civil Eng., Part 2, Vol. 61, pp. 575-579, 1976.

Herbich, J.B. (ed.). *Handbook of Coastal and Ocean Engineering*. Gulf Publishing Co., Huston, Texas, 1991.

Herbich, J.B., Elfiky, A., Elmongy, A., Elbahrawy, A., and Elsaeed, G. *Shore Protection Studies for Ras El-Bar, Egypt*. Proc. Coastal Eng. Conf., ASCE, pp. 3976-3985, 1996.

Hino, M. *Turbulent Flow with Suspended Particles*. Proc. ASCE, Vol. 89, No. HY4, pp. 161-185, 1963.

Hino, M., Yamashita, T., and Yoneyama, S. *Study on Sand Particle Motion on Plane Horizontal and Sloping Bottoms by Water Waves*. Coastal Eng. in Japan, Vol. 25, pp. 65-74, 1982.

Horikawa, K. *Nearshore dynamics and coastal processes*. Tokyo: University of Tokyo Press, 1988.

Horikawa, K., and Watanabe, A. *Turbulence and Sediment Concentration Due to Wave*. Proc. 12th Coastal Eng. Conf., ASCE, pp. 751-766, 1970.

Houston, J.R. *Combined Refraction and Diffraction of Short Waves Using the Finite Element Method*. Appl. Ocean Res., 3, pp. 169-170, 1981.

Inman, D.L., and Quinn, W.H. *Currents in the Surfzone*. Proc. 2nd Coastal Eng. Conf., pp. 24-36, 1951.

Ito, Y., and Tanimoto, K. *A Numerical Wave Analysis Method and its Application*. Proc. 18th Japanese Conf. on Coastal Eng., JSCE, pp. 66-70, 1971.

Ito, Y., and Tanimoto, K. *Refraction in Intersecting Wave-Rays Region*. Proc. 19th Japanese Conf. on Coastal Eng., JSCE, pp. 325-329, 1972.

Jamart, B.M., and Ozer, J. *Comparison of 2-D and 3-D Models of the Steady Wind-Driven Circulation in Shallow Waters*. Coastal Eng., 11, pp. 393-413, 1987.

Kaczmarek, L.M., Harris, J.M. and O'Connor, B.A. *Modeling Movable Bed Roughness and Friction for Spectral Waves*. 24th Int. Conf. on Coastal Eng. Kobe, pp. 300-314, 1994.

Kajima, R., Maruyama, K., Shimizu, T., Sakakiyama, T., Saito, S. *Experimental Study of Waves on Beaches with Prototype Wave Flume*. Proc. 29th Japanese Conf. on Coastal Eng., JSCE, pp. 213-217, 1982.

Kamphuis, J.W. *Alongshore Sediment Transport Rate*. Journal of Waterway, Port, Coastal, and Ocean Eng., 117(6), pp. 624-640, 1991.

Kamphuis, J.W. *Introduction to Coastal Engineering and Management*. Wrold Scientific, 2000.

Kamphuis, J.W., and Readshaw, J.S. *A Model Study of Alongshore Sediment Transport Rate*. Proc. 16th Int. Coastal Eng. Conf., ASCE, pp. 1656-1674, 1978.

Kirby, J.K, and Dalrymple, R.A. *An Approximate Model for Nonlinear Dispersion in Monochromatic Wave Propagation Models*. Coastal Eng., 9, pp. 545-561, 1986.

Kirby, J.T. *A Note on Parabolic Boundary Conditions for Elliptic Wave Calculations*. Coastal Eng., 13, pp. 211-218. 1989.

Kirby, J.T. and Dalrymple, R.A. *Combined Refraction/Diffraction Model, Ref/Diff 1*. CACR report no. 94-22. University of Delaware, Newark, 1994.

Kirby, J.T. *Rational Approximations in the Parabolic Equation Method for Water Waves*. Coastal Engineering, 10, pp. 355-378, 1986a.

Kirby, J.T. *Higher-Order Approximations in the Parabolic Equation Method for Water Waves*. Journal of Geophysical Res. Vol 91, No. C1, 933-952, 1986b.

Komar, P.D. *Beach Sand Transport: Distribution and Total Drift*. J. Waterway, Port, Coastal and Ocean Division, ASCE, Vil. 103(WW2), pp. 225-239, 1977.

Komar, P.D. *Environmental Controls on Littoral Sand Transport*. Proc. 21st Int. Coastal Eng. Conf., ASCE, pp. 1238-1252, 1988.

Komar, P.D. *Relative Quantities of Suspension versus Bed-Load Transport on Beaches*. J. Sedimentary Petrology, Vol. 48, No. 3, pp. 921-932, 1978.

Komar, P.D., and Inman, D.L. *Longshore Sand Transport on Beaches*. Journal of Geophys. Res., Vol. 75 (30), pp. 5914-5927, 1970.

Kostene, J.K., Meijer, K.L., Dingemans, M.W., Mynett, A.E. and van den Bosch, P. *Wave Energy Dissipation in Arbitrary Shaped Harbours of Variable Depth*. Proc. 20th Int. Conf. Coastal Eng., pp. 2002-2016, 1986.

Kraus, N.C., and Dean, J.L. *Longshore Sediment Transport Rate Distribution Measured by Trap*. Proc. Coastal Sediments'87, ASCE, pp. 881-896, 1987.

Kuriyama, Y. *Numerical Model for Longshore Current Distribution on a Bar-Trough Beach*. 24th Int. Conf. on Coastal Eng. Kobe, pp. 2237-2251, 1994.

Larsen, J. and Dancy, H. *Open Boundaries in Short-Wave Simulations – A New Approach*. Coastal Eng., 7, pp. 285-297, 1983.

Larson, M. and Kraus, N.C. *SBEACH: Numerical Model for Simulating Strom-Induced Beach Change*. Technical Rep. 89-9. Coast. Eng. Res. Centre, U.S. Army Engr. Waterway Experiment Station, Vicksburg, Miss., 1989.

Larson, M., Hanson, H., and Kraus, N.C. *Decoupled Numerical Model of Three-Dimensional Beach Change*. Proc. 22nd Int. Coastal Eng. Conf., ASCE, pp. 2173-2185, 1990.

Le Blond, P.H. and Tang, C.L. *On Energy Coupling Between Waves and Rip Currents*. Journal Geophys. Res., 79 (6), 811-816, 1974.

Le Mèhautè, B., and Soldate, M. *Mathematical Modeling of Shoreline Evolution*. CERC Miscellaneous Rep. No. 77-10, Coast. Research Centre, U.S. Army Engr. Waterway Experiment Station, Vicksburg, Miss., 1977.

Leont'yev, I.O. *Modeling of Morphological Changes due to Coastal Structures*. Coastal Engineering, 38, pp 149-166, 1999.

Leont'yev, I.O. *Short-term Shoreline Changes due to Cross-Shore Structure: A One-Line Numerical Model*. Coastal Engineering, 31, pp 59-57, 1997.

Li, B. *A Generalized Conjugate Gradient Model for the Mild Slope Equation*. Coastal Eng., 23, pp. 215-225, 1994a.

Li, B. *An Evolution Equation for Water Waves*. Coastal Eng., 23, pp. 227-242, 1994b.

Li, B. and Fleming, C.A. *A Three Dimensional Multigrid Model for Fully Nonlinear Water Waves*. Coastal Engineering 23: 215-225, 1997.

Li, B. *Parabolic Model for Water Waves*. J. of Waterway, Port, Coastal, and Ocean Eng. Vol 123, No. 4, pp. 192-199, 1997.

Li, B., and Anastasiou, K. *Efficient Elliptic Solvers for the Mild Slope Equation Using the Multigrid technique*. Coastal Eng., 16, pp. 245-266, 1992.

Li, B., Reeve, D.E., and Felming, C.A. *Numerical Solution of the Elliptic Mild-Slope Equation for Irregular Wave Propagation*. Coastal Eng., 20, pp. 85-100, 1993.

Longuet-Higgins, M.S. *Longshore Currents Generated by Obliquely Incident Sea Waves, Part 1 and 2.* , J. Geophys. Res., Vol. 75, No. 33, pp. 6778-6789 and 6790-6801, 1970.

Longuet-Higgins, M.S., and Stewart, R.W. *Changes in the Form of Short Gravity Waves on Long Waves and Tidal Currents*. J. Fluid Mech., Vol. 8, pp. 565-583, 1960.

Longuet-Higgins, M.S., and Stewart, R.W. *Radiation Stress and Mass Transport in Gravity Waves, with Application to "Surf Beat"*. . J. Fluid Mech., Vol. 13, pp. 481-504, 1962.

Longuet-Higgins, M.S., and Stewart, R.W. *Radiation Stress in Water Waves - A Physical Discussion with Applications*. Deep-sea Res., Vol. 11, pp. 529-562, 1964.

Longuet-Higgins, M.S., and Stewart, R.W. *The Changes of Amplitude on Short Gravity Waves on Steady Non-Uniform Currents*. J. Fluid Mech., Vol. 10, pp. 529-549, 1961.

Maa, J. P.-Y. *An Efficient Horizontal Two-Dimensional Hydrodynamic Model*. Coastal Eng., 14, pp. 1-18, 1990.

Maa, J.P.Y., Hsu, T.W., and Hwung, H.H. *RDE Model: A Program for Simulating Water Wave Transformation for Harbour Planning*. Special Scientific Rep. No. 136, Virginia Institute of Marine Science, Gloucester Point, Virginia, 1998.

Maa, J.P.Y., Hsu, T.W., Tsai, C.H., and Juang, W.J. *Comparison of Wave Refraction and Diffraction Models*. Journal of Coast. Res., 16 No. 4, pp. 1073-1082, 2000.

Madsen, O.S. *Sediment Transport outside the Surfzone*. Unpublished Technical Report, U.S. Army Engineering Waterways Experiment Station, Vicksburg, Miss, 1993.

Madsen, P.A., and Larsen, J. *An Efficient Finite-Difference Approach to the Mild-Slope Equation*. Coastal Eng., 11, pp. 329-351, 1987.

McDougal, W.G., and Hudspeth, R.T. *Longshore Current and Sediment Transport on Composite Beach Profiles*. J. Coastal Eng., 12, pp. 315-338, 1989.

McDougal, W.G., and Hudspeth, R.T. *Longshore Sediment Transport on Non-Planar Beaches*. J. Coastal Eng., 7, pp. 119-131, 1983.

Miller, H.C. *Comparison of Storm Longshore Transport Rates to Predictions.* Proc. 26th Int. Conf. on Coastal Eng., ASCE Press, 1998.

Miller, H.C. *Filed Measurements of Longshore Sediment Transport during Storms.* Coastal engineering 36, pp. 301-321, 1999.

Mimura, N., Ohtsuka, Y., and Watanabe, A. *Laboratory Study on Two-Dimensional Beach Transformation Due to Irregular Waves.* Proc. 20th Coastal Eng. Conf. ASCE, pp. 1393-1406, 1986.

Mobarek, I.E. *The Nile Delta Coastal Protection Project.* Proc. 13th Coastal Eng. Conf., ASCE, Vol. 2, pp. 1409-1426, 1972.

Nagai, S. On Coastal Groins. Proc. 1st Japanese Conf. on Coastal Eng., JSCE, pp. 99-104, 1954 (in Japanese).

Nielsen, P. *Coastal Bottom Boundary Layers and Sediment Transport.* World Scientific Pub. Co., 1992.

Nielsen, P., Svendsen, A., and Staub, C. *Onshore-Offshore Sediment Movement on a Beach.* Proc. 16th Coastal Eng. Conf., ASCE, pp. 1475-1492, 1978.

Nishimura, H. *Numerical Simulation of Nearshore Circulations.* Proc. 29th Japanese Conf. on Coastal Eng., JSCE, pp. 333-337, 1982 (in Japanese).

Nishimura, H., Maruyama, K., and Sakurai, T. *On the Numerical Computation of Nearshore Currents.* Coastal Eng. in Japan, Vol. 28, pp. 137-145, 1985.

Nizam. *Numerical Modelling of Three-Dimensional Wave Induced Nearshore Current.* Ph.D. Thesis, Imperial College, University of London.

Nocedal, J. and Wright, S. *Springer Series in Operations Research.* Springer-Verlag New York, Inc., 1999.

Noda, E.K. *Wave-Induced Nearshore Circulation.* J. Geophys. Res., Vol. 79 (27), pp. 4097-4106, 1974.

Ozasa, H., and Brampton, A.H. *Mathematical Modeling of Beaches Backed by Seawalls.* Coastal Eng., Vol. 4, pp. 47-64, 1980.

Panchang, V.G., Cushman-Roisin, B., and Pearce, B.R. *Combined Refraction-Diffraction of Short-Waves in Large Coastal Regions.* Coastal Eng., 12, pp. 133-156, 1988.

Panchang, V.G., Pearce, B.R., Wei, G., and Cushman-Roisin, B. *Solution of the Mild-Slope Wave Problem by Iteration.* Applied Ocean Res., Vol. 13, No. 4, pp. 187-199, 1991.

Park, K.-Y., and Brothwick, A.G.L. Quadtree Grid Numerical Model of Nearshore Wave-Current Interaction. Coastal Eng., 42, pp. 219-239, 2001.

Pèchon, P., and Teisson, C. *Numerical Modelling of Bed Evolution Behind a Detached Breakwater*. Proc. 25th Int. Conf. Coastal Eng., ASCE, pp. 2050-2062, 1996.

Pelnard-Considère, R. *Essai de Theorie de l'Evolution des Formes de Rivage en Plages de Sable et de Galets*. 4th Journees de l'Hydraulique, Les Energies de la Mar, Question III, Repport No. 1, pp 289-298, 1956.

Perlin, M. and Dean, R. *A Numerical Model to Simulate Sediment Transport in the Vicinity of Coastal Structures*. Miscellaneous Rep. No. 83-10, Coast. Eng. Res. Centre, U.S. Army Engr. Waterway Experiment Station, Vicksburg, Miss., 1983.

Putnam, J.A., Munk, W.H., Traylor, M.A. *The Prediction of Longshore Currents*. Trans. Am. Geophys. Union, Vol. 30, No. 3, pp. 337-345, 1949.

Radder, A.C. *On the parabolic equation method for water wave propagation*. J. Fluid Mech. Cambridge, U.K., 91(1), pp. 159-176, 1979.

Roelvink, J.A., Walstra, D.J., and Chen, Z. *Morphological Modeling of Keta Lagoon Case*. Proc. 25th Int. Conf. on Coastal Eng., Orlando, FL, ASCE, pp. 3222-3236, 1994.

Rouse, H. *Modern Conceptions of the Mechanics of Fluid Turbulence*. Trans. ASCE, Vol. 102, pp. 463-543, 1937.

Saied, U.M., and Tsanis, I.K. *Improved Boundary Equations for Elliptic Water Wave Models*. Coastal Eng. Vol 51/1 pp 17-34, 2004a.

Saied, U.M., and Tsanis, I.K. *Improved Parabolic Water Wave Transformation Model*. Coastal Eng., to appear, 2004b.

Saied, U.M., and Tsanis, I.K. *ICEM: Integrated Coastal Engineering Model*. Journal of Coastal Research, to appear, 2004c.

Sanchez-Arcilla, A., Collado, F., and Rodriguez, A. *Vertically Varying Velocity Field in Q-3D Nearshore Circulation*. Proc. 23rd Intr. Conf. on Coastal Eng., ASCE, Venice, pp. 2811-2824, 1992.

Sato, S., and Tanaka, N. *Filed Investigation on Sand Drift at Kashima Harbour Facing the Pacific Ocean*. Proc. 10th Coastal Eng. Conf., ASCE, pp. 595-614, 1966.

Savage, R.P. Laboratory Determination of Littoral Transport Rates. J. Waterway, Port, Coastal and Ocean Division, ASCE, No. WW2, pp. 69-92, 1962.

Schoonees, J.S., and Theron, A.K. Accuracy *and Application of the SPM Longshore Transport Formula.* Proc. 24th Int. Conf. on Coastal Eng., ASCE, pp. 2595-2609, 1995.

Schuepfer, F.E., Lennon, G.P., Weisman, R.N., and Gabriel, R. *Hydrodynamic Model of Great Sound, New Jersey.* Mar. Geol., 82, pp. 1-15, 1988.

Shen, H. *Numerical Analysis of Large-Scaled Flows and Mass Transports in Lakes.* Ph.D. dissertation, Kyoto University, 1991.

Sheng, Y.P. *Mathematical Modeling of Three-Dimensional Coastal Currents and Sediment Dispersion: Model Development and Application.* Technical Rep. 83-2, Coast. Eng. Res. Centre, U.S. Army Engr. Waterway Experiment Station, Vicksburg, Miss., 1983.

Sheng, Y.P. *Three-Dimensional Modeling of Estuarine Circulation and Transport.* Proc. 1987 Natl. Conf. Hydraulic Eng., Hydraulics Div., ASCE, Williamsburg, Virginia, pp. 636-640, 1987.

Shi, F., Svedsen, I.A., Kirby, J.T., and Smith, J.M. *A Curvilinear Version of a Quasi-3D Nearshore Circulation Model.* Coastal Eng., 49, pp. 99-124, 2003.

Shimizu, T., Kumagai, T., and Watanabe, A. *Improved 3-D Beach Evolution Model Coupled with the Shoreline (3D-SHORE).* Proc. 25th Int. Conf. Coastal Eng., ASCE, pp. 2843-2857, 1996.

Shimizu, T., Mimura, N., and Watanabe, A. *Sediment Transport Model for the Wave-Current Coexistent Filed.* Proc. 30th Japanese Conf. on Coastal Eng., JSCE, pp.229-233, 1983.

Shimizu, T., Saito, S., Maruyama, K., Hasegawa, H., and Kajima, R. *Modeling of Onshore-Offshore Sand Transport Rate Distribution Based on Large Wave Flume Experiments.* Central Res. Inst. Electric Power Industry, Civil Eng. Lab. Rep. No. 384028, 1985.

Sorensen, R.M. *Basic Wave Mechanics: For Coastal and Ocean Engineers.* John Wiley and Sons, Inc., 1993.

Sunamura, T. *A Laboratory Study of Offshore Transport of Sediment and a Model for Eroding Beaches.* Proc. 17th Coastal Eng. Conf. ASCE, pp. 1051-1070, 1980.

Sunamura, T.A. *Onshore-Offshore Sediment Transport Rate in the Swash Zone of Laboratory Beaches.* Coastal Eng. in Japan, Vol. 27, pp. 205-212, 1984.

Svendsen, I.A., and Lorenz, R.S. *Velocities in Combined Undertow and Longshore Currents.* Coastal Eng., 13, pp. 55-79, 1989.

Svendsen, I.A., Putrevu, U. *Nearshore Mixing and Dispersion*. Proc. R. Soc. London, Ser. A. 445, pp. 1-16, 1994.

Swart, D.H. *Offshore Sediment Transport and Equilibrium Beach Profiles*. Delft Hydraulics Lab. Publ. No. 131, 1974.

Tanimoto, K., and Kobune, K. *Computation of Waves in a Harbour Basin by a Numerical Wave Analysis Method*. Proc. 22nd Japanese Conf. on Coastal Eng., JSCE, pp. 249-253, 1975.

Thieler, E.R., Pilkey, O.H., Young, R.S., Bush, D.M., and Chai, F. *The Use of Mathematical Models to Predict Beach Behaviour for U.S. Coastal Engineering: A Critical Review*. Journal of Coastal Research, (16) 1, pp 48-70, 2000

Tsay, T.-K. and Liu, P.L.-F. *A Finite Element Model for Wave Refraction and Diffraction*. Appl. Ocean Res., 5, pp. 30-37, 1983.

U.S. Army Corps of Engineers. *Coastal Engineering Manual, Part III*. EC 1110-2-292, U.S. Army Corps of Engineers, Washington, DC, 1998.

U.S. Army Corps of Engineers. *Coastal Engineering Manual*. Part III, EC 1110-2-292, U.S. Army, 1998.

U.S. Army Corps of Engineers. *Shore Protection, Planning, and Design*. Technical Report No. 4, 3rd ed., CERC, U.S. Army Engr. Waterway Experiment Station, Vicksburg, Miss., 1966.

Uda, T., Yamamoto, Y., Itabashi, N., and Yamaji, K. *Filed Observation of Movement of Sand Body Due to Waves and Verification of its Mechanism by a Numerical Model*. Proc. 25th Int. Conf. Coastal Eng., ASCE, pp. 137-150, 1996.

Uda, T., Yamamoto, Y., Itabashi, N., and Yamaji, K. *Predictive Model of Three-Dimensional Development and Deformation of a River Delta by Applying Contour Line Change Model*. Proc. 26th Int. Conf. Coastal Eng., ASCE, 1998.

US Army Corps of Engineers. *Shore Protection Manual. 4th ed.* Washington, D.C.: U.S. Government Printing Office, 1984.

van der Velden, E.T.J.M. *Coastal Engineering*. Delft Univ. of Technology, 1989.

van Dongeren, A.R., Sancho, F.E.., Svendsen, I.A., Putrevu, U. *SHORECIRC: a Quasi-3D Nearshore Model*. Proc. 24th Int. Conf. on Coastal Eng., ASCE, Kobe, pp. 2740-2754, 1994.

Vemulakonda, S.R., Scheffner, N.W., Earickson, J.A., and Chou, L.W. *Kings Bay Coastal Processes Numerical Model*. Technical Rep. 88-3, Coast. Eng. Res. Centre, U.S. Army Engr. Waterway Experiment Station, Vicksburg, Miss., 1988.

Walker, J.R. *Refraction of Finite-Height and Breaking Waves*, Proc. 15th Int. Conf. on Coast. Eng., Hawaii, Vol. 1, pp. 507-524, 1976.

Walker, J.R. *Wave Transformations over a Sloping Bottom and over a Three-Dimensional Shoal*. Dissertation Univ. of Hawaii, James K.K. Look Lab. of Ocean Eng., Report 11, 1974.

Walton, T.L. Hand-*held Calculator Algorithms for Coastal Engineering; Second Series*. CETA 82-4, CERC, U.S. Army Engr. Waterway Experiment Station, Vicksburg, Miss., 1982.

Walton, T.L. *Littoral Sand Transport from Longshore Currents*. Tech. Note, J. of Waterway, Port, Coastal, and Ocean Division, ASCE, Vol. 106, No. WW4, pp. 483-487, 1980.

Wang, H., Dalrymple, R.A., and Shiau, J.C. *Computer Simulation of Beach Erosion and Profile Modification due to Waves*. Proc. Symp. on Modelling Technique, ASCE, pp. 1369-1384, 1975.

Wang, J.D., and Connor, J.J. *Mathematical Modeling of Near Coastal Circulation*. Parsons Lab., Dep. Civil Eng., M.I.T., Cambridge, Mass., Rep. 200, 1975.

Wang, P., Kraus, N.C., and Davis, R.A., Jr. *Total Rate of Longshore Sediment Transport in the Surfzone: Filed Measurements and Empirical Predictions*. J. Coastal Res., 14(1), pp. 269-283, 1998.

Wanstrath, J. *An Open-Coast Mathematical Strom Surge Model with Coastal Flooding for Louisiana, Report 1*. Technical Rep. H-78-4, Coast. Eng. Res. Centre, U.S. Army Engr. Waterway Experiment Station, Vicksburg, Miss., 1978.

Watanabe, A. *Numerical Models of Nearshore Currents and Beach Deformation*. Coastal Eng. in Japan, Vol. 25, pp. 147-161, 1982.

Watanabe, A., Maruyama, K. *Numerical Modelling of Nearshore Wave Field under Combined Refraction, Diffraction and Breaking*. Coastal Eng. in Japan, Vol. 27, pp. 71-82, 1986.

Watanabe, A., Maruyama, K., Shimizu, T., and Sakakiyama, T. *Numerical Prediction Model of Three-Dimensional Beach Deformation Around a Structure*. Coastal Eng. in Japan, Vol. 29, pp. 179-194, 1986.

Watanabe, A., Maruyama, K., Shimizu, T., and Sakakiyama, T. *Numerical Prediction Model of Three Dimensional Beach Deformation Around Coastal Structures*. Proc. 31st Japanese Conf. on Coastal Eng., JSCE, pp. 406-410, 1984.

Watanabe, A., Maruyama, K., Shimizu, T., and Sakakiyama, T. *Numerical Prediction Model of Three Dimensional Beach Deformation Around a Structures*. Coastal Eng. in Japan, Vol. 29, pp. 179-194, 1986.

Watanabe, A., Riho, Y., and Horikawa, K. *Beach Profiles and On-Offshore Sediment Transport*. Proc. 17th Coastal Eng. Conf., ASCE, pp. 1106-1121, 1980.

Westerink, J.J., Stolzenbach, K.D., and Connor, J.J. *A Frequency Domain Finite Element Model for Tidal Circulation*. Energy Lab., M.I.T., Mass., Rep. MIT-EL-85-006, 1985.

White, T.E., and Grandon, J.F. *Longshore Sediment Transport: A Comparison of Energetics-Based Total-Load Models*. (in preparation).

Xu, B., and Panchang, V. *Outgoing Boundary Conditions for Finite-Difference Elliptic Water-Wave Models*. Proc. Math. & Phys. Science., The Royal Society, Vol. 441, pp. 575-588, 1993.

Yamagichi, M., and Nishioka, Y. *Numerical Simulation on the Change of Bottom Topography by the Presence of Coastal Structures*. Proc. 19th Coastal Eng. Conf., ASCE, pp. 1732-1784, 1984.

Yamashita, T., Sawamoto, M., Akiyama, Y., and Yamazaki, T. *Probabilistic Approach to Sand Movement and Bed-Load Transport Rate in Wave Filed*. Proc. 30th Japanese Conf. on Coastal Eng., JSCE, pp. 194-198, 1983 (in Japanese).

APPENDIX 1: ICEM PROGRAM LISTING

Only the main three programs; waves, currents and sediment transport, are listed.

A1.1. Main.For

```
*     FOLDER: ICEM004
*
*     INTEGRATED COASTAL ENGINEERING MODEL VER. 4
*     ICEM004
*
*     THIS MODEL IS DESIGNED BY USAMA M. SAIED (JUNE-2003)
*
*
*
*
      PROGRAM ICEM004
      IMPLICIT NONE
*     MAIN VARIABLES
*
*     H0,TH0,T: DEEP WAVE HEIGHT, ANGLE WITH X-AXIS, PERIOD, AND LENGTH
      RESPECTIVELY (INPUTS)
*     L0: WAVE LENGTH OF THE DEEP WATER WAVE (LINEAR WAVE APPROXIMATION)
*     DX,DY: GRID SIZE IN X & Y DIRECTIONS (M)
*     K(I,J): LOCAL WAVE NUMBER
*     GS(I,J): GRADIENT OF THE PHASE FUNCTION
*     D(I,J): LOCAL WATER DEPTH
*     DA(I,J): APPARENT DEPTH TO THE HYDRODYNAMIC AND SED. TRANSPORT
      MODELS
*     C(I,J): LOCAL ABSOLUTE WAVE CELERITY (LINEAR WAVE APPROXIMATION)
*     CG(I,J): LOCAL GROUP WAVE CELERITY (LINEAR WAVE APPROXIMATION)
*     CC(I,J): THE PRODUCT OF C(I,J)*CG(I,J)
*     TLAST : IS THE TIME IN DAYS WHICH THE MORPHOLOGICAL MODEL IS BEING
      RUN
*     ALSO IS THE TIME THAT THE WAVE AND CURRENTS ARE FIXED
*     THEREFORE, IT IS ESSENTIALLY THE MORPHOLOGICAL TIME STEP
*
*     IMAX,JMAX: MAXIMUM NUMBER OF DISCRETE POINTS IN BOTH DIRECTIONS
*     AP(I,J),AE(I,J),AW(I,J),AN(I,J),AS(I,J),B(I,J): MATRIX
      COEFFICIENTS
*     COMPLEX A(I,J): (REDUCED COMPLEX VELOCITY POTENTIAL FOR THE
      ENVELOPE)
*     ACCURACY: REQUIRED ACCURACY
*
*     ALL INPUT PARAMETERS ARE EXPLAINED IN THE "INPUT.DAT" FILE
*

      INTEGER IMAX,JMAX,JB,JE,DIMX,DIMY,I,J,NOUT
      INTEGER INBNDRY,ISBNDRY,APROX,NONLIN,NN,NOUTER,BRKI
      INTEGER INBNDRYE,ISBNDRYE,NSYM,SSYM,NI,NJ,ELIPREFIN
      INTEGER NXBW,NYBW,IBR,IER,JBR,JER
      INTEGER NIH,NJH
      INTEGER,DIMENSION(20)::IXB,IXE,JXB,JXE,IYB,IYE,JYB,JYE
      PARAMETER(DIMX=800,DIMY=800)
      REAL,DIMENSION(DIMX,DIMY)::D,DA
```

```
      REAL,DIMENSION(DIMX,DIMY)::H,TH,K,C,CG
      REAL,DIMENSION(DIMX,DIMY)::U,V,Z
      REAL DX,DY,DMIN,H0,TH0,T,PI
      REAL RE,RN,RS,CONS,GAMA
      REAL ACCURACY,REE,RNE,RSE
      REAL TIME,TLAST,T1
      CHARACTER*20 AAA
      INTEGER NTIMES
      INTEGER NSUBM
      INTEGER,DIMENSION(20)::IBSUB,IESUB,JBSUB,JESUB

      PI=ACOS(-1.0)


      CALL INPUT(PI,H0,TH0,T,GAMA,IMAX,JMAX,JB,JE,DX,DY,DMIN,INBNDRY,
      +ISBNDRY,APROX,NOUTER,NONLIN,NN,BRKI,RE,RN,RS,CONS,D,DA,DIMX,DIMY,
     +INBNDRYE,ISBNDRYE,NSYM,SSYM,ELIPREFIN,IBR,IER,JBR,JER,NI,NJ,
     +ACCURACY,REE,RNE,RSE,NXBW,NYBW,IXB,IXE,JXB,JXE,IYB,IYE,JYB,JYE,
     +NIH,NJH,NSUBM,IBSUB,IESUB,JBSUB,JESUB)


   OPEN THE WAVE SPECTRUM FILE
      OPEN(UNIT=55,FILE='WAVE SPEC.DAT')
      READ(55,*)AAA
      READ(55,*)NTIMES   ! NUMBER OF TIMES OF WAVE CHANGES OR #MORPHO.
      RUNS
      READ(55,*)AAA

      TIME=0.0           ! TIME IN DAYS
      DO 111 NOUT=1,NTIMES

***
      PRINT*,'*******************************************'
      PRINT*,'*********WAVE CLIMATE CHANGE*****************'
      PRINT*,'*******************************************'
   READ THE WAVE DATA
      READ(55,*)H0,TH0,T,TLAST
      TH0=TH0*PI/180.
      T1=TIME      ! TIME BEFORE THE MORPHOLOGICAL RUN
15    CONTINUE
      PRINT*,'*******TIME   =',TIME,'      DAYS','*************'
      PRINT*,'NOUT = ',NOUT,' H0 =',H0,' TH0 =',TH0*180./PI,' T =',T
      IF(NOUT.GT.1.AND.ELIPREFIN.EQ.1)GOTO 5           ! NO PARABOLIC
      SOLUTION
*
*     PARABOLIC WAVE SOLUTION
      PRINT*,'**************BEGIN PARABOLIC SOLUTION************'
*
      CALL PARAWAVE04(H,TH,K,C,CG,PI,H0,TH0,T,GAMA,IMAX,JMAX,JB,JE,DX,
      +DY,DMIN,INBNDRY,ISBNDRY,APROX,NOUTER,NONLIN,BRKI,NN,RE,RN,RS,
     +CONS,D,DIMX,DIMY,NXBW,NYBW,IXB,IXE,JXB,JXE,IYB,IYE,JYB,JYE,
     +NSUBM,IBSUB,IESUB,JBSUB,JESUB)
*
**************OUTPUT AFTER PARABOLIC SOLUTION*******************
*
*     IF(MOD(NOUT,5).EQ.0)THEN
      CALL TECOUT(H,10,1,IMAX,1,JMAX,DIMX,DIMY,DX,DY,
      +                        'WAVE HEIGHTSp','WAVES.DAT')
*     ENDIF

*
```

```
**********************ELLIPTIC WAVE MODEL*************************
      IF(ELIPREFIN.NE.1)GOTO 10
5     PRINT*,'***************BEGIN ELLIPTIC SOLUTION*************'
*     INTERPOLATION FOR WAVE HEIGHTS AND ANGLES TO GET DOWN TO THE
*     ELLIPTICAL WAVE RESOLUTION
      CALL INTERPOLATE(DIMX,DIMY,IMAX,JMAX,NI,NJ,DX,DY,H,D,TH,K,C,CG)
*
      CALL ELIPWAVE05(IBR,IER,JBR,JER,DIMX,DIMY,H,TH,T,D,K,C,CG,DX,DY,
      +DMIN,INBNDRYE,ISBNDRYE,NSYM,SSYM,ACCURACY,REE,RNE,RSE,CONS,NONLIN
,
     +BRKI,GAMA,NI,NJ,NXBW,NYBW,IXB,IXE,JXB,JXE,IYB,IYE,JYB,JYE)
*
**********************PARABOLIC FINAL SWEEP***********************
*     RETURN TO THE PARABOLIC RESOLUTION FOR THE FINAL SWEEP
      CALL PARARESOL(DIMX,DIMY,IMAX,JMAX,NI,NJ,DX,DY,H,D,TH,K,C,CG)
*
***************OUTPUT AFTER ELLIPTIC SOLUTION********************
*
*     IF(MOD(NOUT,5).EQ.0)THEN
      CALL TECOUT(H,10,1,IMAX,1,JMAX,DIMX,DIMY,DX,DY,
      +                          'WAVE HEIGHTSe','WAVES.DAT')
*     ENDIF

******************OUTPUT FOR HYDRODYNAMIC MODEL*******************
10    CONTINUE
*     SET THE RESOLUTION TO HYDRODYNAMIC RESOLUTION
      CALL PARARESOL(DIMX,DIMY,IMAX,JMAX,NIH,NJH,DX,DY,H,D,TH,K,C,CG)
   SET THE DEPTHS TO -99.99 AT THE WALLS
      CALL WALLS(DIMX,DIMY,IMAX,JMAX,NIH,NJH,NXBW,NYBW,
      +                         IXB,IXE,JXB,JXE,IYB,IYE,JYB,JYE,DA,D)

******************BEGIN THE HYDRODYNAMIC MODEL********************
      CALL ADI003(DIMX,DIMY,IMAX,JMAX,DA,H,TH,K,C,CG,T,DX,DY,U,V,Z)
******************BEGIN THE SEDIMENT TRANSPORT********************
   PRINT THE DEPTHS AT THE VERY BEGINING WITH THE HYDRODYNAMIC
   RESOLUTION
      IF(NOUT.EQ.1.AND.TIME.EQ.0.0)THEN
      CALL TECOUT(D,12,1,IMAX,1,JMAX,DIMX,DIMY,DX,DY,
      +                          'WATER DEPTHS-','BATHYM.DAT')
      CALL TECOUT(DA,12,1,IMAX,1,JMAX,DIMX,DIMY,DX,DY,
      +                          'WATER DEPTHS-','BATHYM.DAT')
      ENDIF

      CALL MORPHOLOGY(DIMX,DIMY,IMAX,JMAX,DX,DY,T,H,TH,K,
      +                                    DA,D,Z,U,V,TIME,TLAST,T1,
     +                              NIH,NJH,NSUBM,IBSUB,IESUB,JBSUB,JESUB)
   UPDATE THE DEPTHS FOR THE WAVE MODEL
      DO 20 I=1,IMAX
      DO 20 J=1,JMAX
      IF(DA(I,J).LT.-80.0)GOTO 20
      D(I,J)=DA(I,J)
20    CONTINUE

****  OUTPUT FILES AT THE END MORPHOLOGICAL STEP (TECPLOT)
      CALL TECOUT(DA,12,1,IMAX,1,JMAX,DIMX,DIMY,DX,DY,
      +                          'WATER DEPTHS-','BATHYM.DAT')
      CALL TECOUT(Z,11,1,IMAX,1,JMAX,DIMX,DIMY,DX,DY,'WATER SURFACE',
      +                                  'WATSURF.DAT')
      CALL TECVEC1(14,1,IMAX,1,1,JMAX,1,DIMX,DIMY,
      +                   DX,DY,U,V,'  CURRENT DIRECTION ','CURRENT.DAT')
      CALL TECVEC(13,1,IMAX,1,1,JMAX,1,DIMX,DIMY,
```

```
      +                    DX,DY,TH,H,D,'   WAVE   VECTORS
','WAVEVEC.DAT')

****  RETURN TO THE PARABOLIC MODEL RESOLUTION
      CALL INTERPOLATE(DIMX,DIMY,IMAX,JMAX,NIH,NJH,DX,DY,H,D,TH,K,C,CG)

      IF(TIME.LT.T1+TLAST)GOTO 15    ! END OF MORPHOLOGICAL TIME STEP B4
THE END OF WAVE INTERVAL

*     DISPLAT THE OUTPUT
      IF(NOUT.EQ.ntimes)THEN
   CALL WALLS2 ONLY TO DISPLAY RESULTS BETTER. IT IS CHANGE THE SOLUTION
      CALL WALLS2(DIMX,DIMY,IMAX,JMAX,NXBW,NYBW,
      +                          IXB,IXE,JXB,JXE,IYB,IYE,JYB,JYE,DA,D)
****  OUTPUT FILES AT THE END MORPHOLOGICAL STEP (TECPLOT)
      CALL TECOUT(DA,12,1,IMAX,1,JMAX,DIMX,DIMY,DX,DY,
      +                          'WATER DEPTHS-','BATHYM.DAT')
      CALL TECOUT(D,12,1,IMAX,1,JMAX,DIMX,DIMY,DX,DY,
      +                          'WATER DEPTHS-','BATHYM.DAT')
      ENDIF


111   CONTINUE

*
      PRINT*,'*******************************************************'
      PRINT*,'****TIME AT THE END OF THE RUN =',TIME
      PRINT*,'*******************************************************'


   WRITE A DEPTH FILE FOR THE NEXT PHASE (IF AT ALL PRESENT)
      OPEN(UNIT=77,FILE='NEWDEPTH.DAT')
      DO I=1,IMAX
      WRITE(77,*)I
      WRITE(77,112)(D(I,J),J=1,JMAX)
      ENDDO
112   FORMAT(20F10.5)



      CLOSE(10)    ! WAVE HEIGHTS FILE
      CLOSE(11)    ! WATER SURFACE FILE
      CLOSE(12)    ! BATHYMETRY FILE
      CLOSE(13)    ! WAVE VECTORS FILE
      CLOSE(14)    ! CURRENTS FILES
      CLOSE(113)   ! KINETIC ENERGY FILE
      CLOSE(114)   ! SCREEN FILE
      CLOSE(55)    ! WAVE SPECTRUM FILE
      CLOSE(77)    ! NEW DEPTH FILE
      CLOSE(777)   ! SEDIMENT TRANSPORT FLUXES

      END
```

A1.2. w-Parawave04.For

```
*
*      PARABOLIC WATER WAVE TRANSFORMATION MODEL
*
*      THIS MODEL IS DESIGNED BY USAMA M. SAIED
*      TO MODEL THE COMBINED REFRACTION-DIFFRACTION WAVES
*
*      THE MODEL USES THE GENERALIZED PADE APPROXIMATION [1/1]
*      DEVELOPED BY USAMA SAIED (2003)
*
*
*      (MONOCHROMATIC WAVE)
*
*
*
*
       SUBROUTINE PARAWAVE04(H,TH,K,C,CG,PI,H0,TH0,T,GAMA,IMAX,JMAX,JB,JE
       +
       ,DX,DY,DMIN,INBNDRY,ISBNDRY,APROX,NOUTER,NONLIN,BRKI,NN,RE,RN,
      +RS,CONS,D,DIMX,DIMY,NXBW,NYBW,IXB,IXE,JXB,JXE,IYB,IYE,JYB,JYE,
      +NSUBM,IBSUB,IESUB,JBSUB,JESUB)
       IMPLICIT NONE
*      MAIN VARIABLES
*
*      H0,TH0,T: DEEP WAVE HEIGHT, ANGLE WITH X-AXIS, PERIOD, AND LENGTH
       RESPECTIVELY (INPUTS)
*      L0: WAVE LENGTH OF THE DEEP WATER WAVE (LINEAR WAVE APPROXIMATION)
*      DX,DY: GRID SIZE IN X & Y DIRECTIONS (M)
*      K(I,J): LOCAL WAVE NUMBER
*      GS(I,J): GRADIENT OF THE PHASE FUNCTION
*      D(I,J): LOCAL WATER DEPTH
*      C(I,J): LOCAL ABSOLUTE WAVE CELERITY (LINEAR WAVE APPROXIMATION)
*      CG(I,J): LOCAL GROUP WAVE CELERITY (LINEAR WAVE APPROXIMATION)
*      CC(I,J): THE PRODUCT OF C(I,J)*CG(I,J)
*
*      IMAX,JMAX: MAXIMUM NUMBER OF DISCRETE POINTS IN BOTH DIRECTIONS
*      AP(I,J),AE(I,J),AW(I,J),AN(I,J),AS(I,J),B(I,J): MATRIX
       COEFFICIENTS
*      COMPLEX A(I,J): (REDUCED COMPLEX VELOCITY POTENTIAL FOR THE
       ENVELOPE)
*      ACCURACY: REQUIRED ACCURACY
*
*      ALL INPUT PARAMETERS ARE EXPLAINED IN THE "INPUT.DAT" FILE
*

       INTEGER I,J,N,IS,IMAX,JMAX,JB,JE,DIMX,DIMY
       INTEGER INBNDRY,ISBNDRY,APROX,NONLIN,NN,NOUT,NOUTER,BRKI
       INTEGER NXBW,NYBW
       INTEGER,DIMENSION(20)::IXB,IXE,JXB,JXE,IYB,IYE,JYB,JYE
       COMPLEX,DIMENSION(DIMX,DIMY)::A
       COMPLEX,DIMENSION(DIMY)::APT,APP,APM,BPT
       COMPLEX,DIMENSION(DIMX)::AGN,AGS
       COMPLEX,DIMENSION(DIMY)::AGW
       REAL,DIMENSION(DIMX,DIMY)::D,K,CC,CG,C,S
       REAL,DIMENSION(DIMX)::KB
       REAL,DIMENSION(DIMY)::W
       REAL,DIMENSION(DIMX,DIMY)::H,TH
       REAL DX,DY,DMIN,H0,TH0,T,PI
       REAL RE,RN,RS,CONS,GAMA
```

```
      INTEGER NSUBM,ISUB,JSUB,III
      INTEGER,DIMENSION(20)::IBSUB,IESUB,JBSUB,JESUB
      REAL HDUM

**********************************************************************
********
*     CALCULATE THE WAVE CHARACTERISTICS AT DISCRETE POINTS
      CALL WAVE(IMAX,JMAX,D,DMIN,T,TH0,H0,K,KB,CC,CG,C,TH,H,DIMX,DIMY)
*     CALL OUT2D(1,1,IMAX,JMAX,10,10,H/H0,DIMX,DIMY,3,'   H/H0 ')
*     CALL OUT2D(1,1,IMAX,JMAX,10,10,TH*180./PI,DIMX,DIMY,3,'   TH    ')

*     INITIAL SOLUTION
*     (INITIAL 1 IS BETTER BECAUSE IT GIVES ACCURATE RESULTS FOR NORTH
      BNDRY)
      CALL INITIAL1(IMAX,JMAX,DIMX,DIMY,H,TH,K,KB,DX,DY,
      +                                    A,AGW,AGN,AGS,CONS)
*     CALL INITIAL2(IMAX,JMAX,DIMX,DIMY,H,TH,K,KB,DX,DY,A,
*     +                                    AGN,AGS,AGW,CONS)

*     NULL THE COEFFICINETS
      CALL NULL1D(APT,JMAX,DIMY)
      CALL NULL1D(APP,JMAX,DIMY)
      CALL NULL1D(APM,JMAX,DIMY)
      CALL NULL1D(BPT,JMAX,DIMY)


*     BEGIN SOLUTION MARCHING IN SPACE STARTING FROM COLUMN # 3
      DO NOUT=1,NOUTER
      PRINT*,'NOUT   =',NOUT
      DO I=3,IMAX
*     PRINT*,'I=',I
      DO N=1,NN
*     PRINT*,'N=',N
      IF(NOUT.EQ.1)THEN  ! GET ESTIMATE FOR THE ANGLES
      IF(N.EQ.1)THEN     ! CALCULATE TH VALUES FROM PREVIOS COLUMN (I-1)
      CALL ANGLES(I-1,I-1,JMAX,DIMX,DIMY,DX,DY,A,KB,D,TH,TH0)
      ELSE               ! CALCULATE TH VALUES AT COLUMN (I-1/2)
      CALL ANGLES(I-1,I,JMAX,DIMX,DIMY,DX,DY,A,KB,D,TH,TH0)
      ENDIF
      ENDIF
      CALL COEFF(I,N,NOUT,JMAX,DIMX,DIMY,DX,DY,T,K,KB,CG,CC,W,
      +
      D,A,H,TH,AGN,AGS,NONLIN,APROX,INBNDRY,ISBNDRY,APT,APP,APM,BPT)

*     UPDATE COEFFICINTS FOR THE PRESENCE OF A BREAKWATER
*     GROINS (X-PARALLEL BREAKWATERS)
      DO IS=1,NXBW
      IF(I.GE.IXB(IS).AND.I.LE.IXE(IS))THEN
      CALL BREAKY(JXB(IS),JXE(IS),DIMX,DIMY,APT,APP,APM,BPT,D)
      ENDIF
      ENDDO
*     DETACHED BREAKWATERS
*     (Y-PARALLEL STRUCTURES)
      DO IS=1,NYBW
      IF(I.GE.IYB(IS).AND.I.LE.IYE(IS))THEN
      CALL BREAKX(JYB(IS),JYE(IS),DIMX,DIMY,APT,APP,APM,BPT,D)
      ENDIF
      ENDDO

      CALL TDMACY(A,APT,APP,APM,BPT,1,JMAX,I,DIMX,DIMY,DIMY)
```

```
      CALL HEIGHTS(I,I,JMAX,DIMX,DIMY,A,CONS,H,S)
*     CALL THE BREAKING MODEL
      IF(BRKI.EQ.1)CALL WAVBRK(I,JMAX,DIMX,DIMY,T,H,D,K,GAMA,W)
      ENDDO
*     UPDATE THE WAVE HEIGHTS OVER THE SUBMERGED STRUCTURES
      DO III=1,NSUBM
      DO ISUB=IBSUB(III),IESUB(III)
      DO JSUB=JBSUB(III),JESUB(III)
      HDUM=GAMA*D(ISUB,JSUB)
      IF(HDUM.LT.H(ISUB,JSUB).AND.H(ISUB,JSUB).GT.0.0)THEN
      A(ISUB,JSUB)=A(ISUB,JSUB)*HDUM/H(ISUB,JSUB)
      H(ISUB,JSUB)=HDUM
      ENDIF
      ENDDO
      ENDDO
      ENDDO

*     UPDATE THE GIVEN A FROM PREVIOUS COLUMN
*     IF(I.EQ.30)PRINT*,AGS(31)
      IF(NOUT.EQ.1)THEN
      CALL AGIVEN(I,JMAX,DIMX,DIMY,H,TH,S,K,KB,DX,CONS,A,AGS,AGN)
      ENDIF

      ENDDO
*     CALCULATE THE ANGLES AT (I-1/2) FOR INTERNAL POINTS
*     AND AT (I) FOR BOUNDARY POINTS
      CALL ANGLES2(IMAX,JMAX,DIMX,DIMY,DX,DY,A,KB,D,TH,TH0)
      CALL AGIVEN2(IMAX,JMAX,DIMX,DIMY,H,TH,S,K,KB,DX,CONS,A,
     +                                        AGS,AGN)

      ENDDO


*     CALCULATE THE SOLUTION
10    CONTINUE
*     EXTRAPOLATE THE SOLUTION FROM THE SMALL DOMAIN TO THE BIG DOMIAN
      CALL EXTRPOL(IMAX,JMAX,JB,JE,DIMX,DIMY,H,TH)
*     RELOCATE THE THETA VAIABLES TO BE ON THE GRID POINTS
      DO 20 J=1,JMAX
      DO 20 I=2,IMAX
      IF(D(I,J).LE.0.0)THEN
      TH(I,J)=TH(I-1,J)
      GOTO 20
      ENDIF
      IF(D(I+1,J).LE.0.0)GOTO 20
*     FROM SUBROUTINE ANGLES2, THE WAVE ANGLES, FOR INTERNAL POINTS,
*     WERE CALCULATED AT (I-1/2)... NOW WE NEED THEM AT "I"
      TH(I,J)=(TH(I,J)+TH(I+1,J))/2.
20    CONTINUE

*     FILTER THE WAVE HEIGHTS (TO BE SMOOTHED ARROUND STRUCTURES)
*     THE NUMBER APPERAING IN THE ARRGUMENTS IS THE FILTRATION PARAMETER
(0.1~0.3)
      CALL FILTER(H,D,0.2,IMAX,JMAX,DIMX,DIMY)
      CALL FILTER(TH,D,0.1,IMAX,JMAX,DIMX,DIMY)



      RETURN
      END
```

A1.3. w-Elipwave05.For

```
*
*
*
*     THIS MODEL IS DESIGNED BY USAMA M. SAIED
*     TO MODEL THE COMBINED REFRACTION-DIFFRACTION WAVES
*
*     IN THIS MODEL WE TRY TO GET THE WAVE ANGLE AT THE BOUNDARIES
      BEFOREHAND
*     USING THE ITERATIVE PROCEDURES OF RCPWAVE1 AND SNELS LAW
*
*     THIS VERSION IS THE SAME AS ELIPWAVE4b BUT IT ALLOWS THE INCLINED
      WAVE
*     INCIDENCE AT THE WEST BOUNDARY...
*
*
*
*     (MONOCHROMATIC WAVE)
*
*
*
*
      SUBROUTINE ELIPWAVE05(IB,IE,JB,JE,DIMX,DIMY,H,TH,T,D,K,C,CG,DX,DY,
      +DMIN,INBNDRY,ISBNDRY,NSYM,SSYM,ACCURACY,RE,RN,RS,CONS,NONLIN,
     +BRKI,GAMA,NI,NJ,NXBW,NYBW,IXB,IXE,JXB,JXE,IYB,IYE,JYB,JYE)
      IMPLICIT NONE
*     MAIN VARIABLES
*
*     H0,TH0,T: DEEP WAVE HEIGHT, ANGLE WITH X-AXIS, PERIOD, AND LENGTH
      RESPECTIVELY (INPUTS)
*     L0: WAVE LENGTH OF THE DEEP WATER WAVE (LINEAR WAVE APPROXIMATION)
*     DX,DY: GRID SIZE IN X & Y DIRECTIONS (M)
*     K(I,J): LOCAL WAVE NUMBER
*     GS(I,J): GRADIENT OF THE PHASE FUNCTION
*     D(I,J): LOCAL WATER DEPTH
*     C(I,J): LOCAL ABSOLUTE WAVE CELERITY (LINEAR WAVE APPROXIMATION)
*     CG(I,J): LOCAL GROUP WAVE CELERITY (LINEAR WAVE APPROXIMATION)
*     CC(I,J): THE PRODUCT OF C(I,J)*CG(I,J)
*
*     IMAX,JMAX: MAXIMUM NUMBER OF DISCRETE POINTS IN BOTH DIRECTIONS
*     AP(I,J),AE(I,J),AW(I,J),AN(I,J),AS(I,J),B(I,J): MATRIX
      COEFFICIENTS
*     COMPLEX EP(I,J): EPSAY (COMPLEX VELOCITY POTENTIAL FOR THE
      ENVELOPE)
*     ACCURACY: REQUIRED ACCURACY
*
*     ALL INPUT PARAMETERS ARE EXPLAINED IN THE "INPUT.DAT" FILE
*

      INTEGER I,J,IMAX,JMAX,DIMX,DIMY,DIM,IB,IE,JB,JE
      INTEGER INBNDRY,ISBNDRY,NSYM,SSYM,NONLIN,BRKI
      INTEGER IS,NXBW,NYBW,I1,I2,J1,J2,NI,NJ
      INTEGER,DIMENSION(20)::IXB,IXE,JXB,JXE,IYB,IYE,JYB,JYE
      PARAMETER(DIM=90000)
      COMPLEX,DIMENSION(DIMX,DIMY)::EP,EPG
      COMPLEX,DIMENSION(DIMX,DIMY)::AP,AE,AW,AN,AS,BP
      COMPLEX,DIMENSION(DIMY)::AEB1,AEB2
      COMPLEX,DIMENSION(DIMX)::ANB1,ANB2,ASB1,ASB2
      REAL,DIMENSION(DIMX,DIMY)::D,K,KEX,KNY,KX,KY,CC,CG,C,S
```

```
      COMPLEX,DIMENSION(DIMX,DIMY)::KC
      REAL,DIMENSION(DIMX,DIMY)::H,TH,SS,W
      REAL DX,DY,T,ACCURACY,PI
      REAL RE,RN,RS,CONS,DMIN,GAMA


      PI=ACOS(-1.)

      OPEN(UNIT=4,FILE='CNVRGNC.DAT')
      WRITE(4,*)('ZONE = "CONVERGENCE OF THE GENERALIZED CG"')

      IMAX=IE+1
      JMAX=JE+1
   CALCAULATE THE DISSIPATION 'W'
      CALL NULL2DR(W,IE+1,JE+1,DIMX,DIMY)
      IF(BRKI.EQ.1)THEN
      CALL WAVBRKe(IB,IE,JB,JE,DIMX,DIMY,T,H,D,K,GAMA,W)
      ENDIF
*     CALCULATE THE WAVE CHARACTERISTICS AT DISCRETE POINTS
*     THE NON-LINEARITY IS INCLUDED TO MODIFY THE CELERITY FOR THE
*     SHALLOW DEPTHS
      CALL WAVENL(IB,JB,IE,JE,DIMX,DIMY,D,H,T,K,KC,CC,CG,C,W,DX,DY,DMIN,
      +                                NONLIN)

*     CALCULATE THE VALUES OF SS(I,J)=-M^2=-(SIN (TH(I,J))^2
      CALL BNDRYANG(IB,JB,IE,JE,DIMX,DIMY,TH,SS)
*     INITIAL SOLUTION (BIG FACTOR)
      CALL INITIALMOD3(H,T,TH,K,DX,DY,IB,JB,IE,JE,DIMX,DIMY,CC,EPG,EP,
      +                                        CONS)

*     THE ELLIPTICAL MODEL
*     NULL THE COEFFICIENT MATRICIES
      CALL NULL2D(AP,IE+1,JE+1,DIMX,DIMY)
      CALL NULL2D(AE,IE+1,JE+1,DIMX,DIMY)
      CALL NULL2D(AW,IE+1,JE+1,DIMX,DIMY)
      CALL NULL2D(AN,IE+1,JE+1,DIMX,DIMY)
      CALL NULL2D(AS,IE+1,JE+1,DIMX,DIMY)
      CALL NULL2D(BP,IE+1,JE+1,DIMX,DIMY)
      CALL NULL1D(AEB1,JE+1,DIM)
      CALL NULL1D(AEB2,JE+1,DIM)
      CALL NULL1D(ANB1,IE+1,DIM)
      CALL NULL1D(ANB2,IE+1,DIM)
      CALL NULL1D(ASB1,IE+1,DIM)
      CALL NULL1D(ASB2,IE+1,DIM)
*
10    CONTINUE


*     CALCULATE THE INTERNAL COEFFICIENTS  (IB~IE AND JB~JE)
      CALL COEFFE(IB,JB,IE,JE,DIMX,DIMY,KC,DX,DY,AP,AE,AW,AN,AS,BP)
   CALCULATE THE BOUNDARY COEFFICIENTS
      CALL XBNDRY(IB,JB,IE,JE,DIMX,DIMY,KC,K,CC,EPG,TH,SS,DX,DY,
      +
      RE,AP,AW,AE,AN,AS,AEB1,AEB2,BP)
      CALL YBNDRY(IB,JB,IE,JE,DIMX,DIMY,KC,K,TH,SS,DX,DY,EPG,CC,RN,
      +RS,INBNDRY,ISBNDRY,NSYM,SSYM,AP,AW,AE,AN,AS,ANB1,ANB2,ASB1,
     +ASB2,BP)
      CALL CORNERS(IB,JB,IE,JE,DIMX,DIMY,EP,AP,BP)
*
```

```
*       UPDATE FOR THE PRESENCE OF BREAKWATERS
*       BREAKAWTERS PARALLEL TO X-AXIS (GROINS)
*
        DO IS=1,NXBW
        J1=(JXB(IS)-1)*NJ+1
        J2=(JXE(IS)-1)*NJ+1
        I1=(IXB(IS)-1)*NI+1
        I2=(IXE(IS)-1)*NI+1
        DO I=I1,I2
        CALL BREAKYE(I,J1,J2,DIMX,DIMY,CC,AP,AE,AW,AN,AS,BP)
        ENDDO
        ENDDO
*
*       BREAKAWTERS PARALLEL TO Y-AXIS (DETACHED BREAKWATERS)
*
        DO IS=1,NYBW
        J1=(JYB(IS)-1)*NJ+1
        J2=(JYE(IS)-1)*NJ+1
        I1=(IYB(IS)-1)*NI+1
        I2=(IYE(IS)-1)*NI+1
        DO J=J1,J2
        CALL BREAKXE(J,I1,I2,DIMX,DIMY,CC,AP,AE,AW,AN,AS,BP)
        ENDDO
        ENDDO


    SOLVE FOR THE EPSAY
        CALL SPARSEGCG(DIM,DIMX,DIMY,IMAX,JMAX,DIM,ACCURACY,AP,AE,AW,
        +            AN,AS,BP,AEB1,AEB2,ANB1,ANB2,ASB1,ASB2,EP)

    CALCULATE THE SOLUTION
        CALL PHASE(IB,JB,IE,JE,DIMX,DIMY,EP,S)
        CALL WAVENO1(IB,JB,IE,JE,DIMX,DIMY,DX,DY,EP,KEX,KNY,CC,K)
        CALL SOLUTION(IB,JB,IE,JE,DIMX,DIMY,K,KEX,KNY,KX,KY)
        CALL TRANSFORM(IB,JB,IE,JE,DIMX,DIMY,KX,KY,EP,T,S,CC,H,TH,CONS)


100     CONTINUE



        RETURN
        END
```

A1.4. h-main.For

```
c     Program ADI003
c     This program models the hydrodynamics in coastal areas
c     ------------------------------------------------------------------
------------------
c     By: Usama Saied (Ph.D. student at McMaster University)
c     ------------------------------------------------------------------
------------------
c     Main variables definition
c     ------------------------------------------------------------------
------------------
c     um,vm(i,j)   = velocity components along x and y directions
c     d(i,j)       = water depth in meters at center of each grid.
c     h(i,j)       = water depth  PLUS  free-water elevation
c     hw(i,j)      = wave heights
c     ang(i,j)     = wave angle
c     c(i,j)       = wave celerity
c     k(i,j)       = wave number
c     cg(i,j)      = wave group velocity
c     t            = wave period
c     is,ie        = calculation  domain   provided by  this program
c     dt           = time step
c     dx(i)        = mesh size in x-direction
c     dy(j)        = mesh size in y-direction
c     tlast        = simulation time
c     th           = smooth factor (horizontal diffusivity)
c     imax,jmax    = max grid number in x and y directions
c     dimx,dimy    = array sizes
c     phi          = mean geographical latitude of the area
c     ------------------------------------------------------------------
      SUBROUTINE ADI003(DIMX,DIMY,IMAX,JMAX,H,HW,ANG,K,C,CG,T,DXW,DYW,U,
     +                                V,Z)
c     ------------------------------------------------------------------
c     Declaration
c     ------------------------------------------------------------------
      implicit none
      integer dimx,dimy,dim,imax,jmax,n,i,j,ii,jj
      parameter(dim=900)
      real,dimension(dimx,dimy)::un,u,vn,v,z,zn,h
      real,dimension(dimx,dimy)::hw,ang,k,c,cg
      real,dimension(dimx,dimy)::DXXX,DYYY,DXYX,DXYY,UM,ZR
      real,dimension(dim)::apt,app,apm,bp
      integer,dimension(dimy)::is,ie
      real,dimension(dimy)::thb
      real t,ax,ay,cf,dxw,dyw,dt,time,tlast
      real rho,phi,cb,cs,th,keold
      integer isteady
      REAL D50


c     ------------------------------------------------------------------
c     Calculate the Wave Forcing


*
*     read input data file
      call inputh(dimx,dimy,ax,ay,rho,cf,cb,cs,dt,tlast,phi,d50,hw,t)

*     DETERMINE THE CALCULATION DOMAIN
```

```
      CALL DomBoun(dimx,dimy,imax,jmax,dxw,dyw,h,is,ie,thb)
   EXTRAPOLTE THE WAVE HEIGHTS
      CALL WAVEDEF(DIMX,DIMY,IMAX,JMAX,H,HW,ANG,C,CG)
      do i=1,imax
      do j=1,jmax
      IF(HW(I,J).GT.(0.7*H(I,J)).AND.H(I,J).GT.0.0)HW(I,J)=0.7*H(I,J)
      enddo
      enddo

*     CALCULATE THE RADIATION STRESSES
*     CALL RADIATION1(IMAX,JMAX,DIMX,DIMY,IE,C,CG,HW,ANG,
*     +                                          DXW,DYW,DXXX,DYYY,DXYX,DXYY)
      CALL RADIATION2(IMAX,JMAX,DIMX,DIMY,IE,C,CG,HW,ANG,H,K,
      +
      T,DXW,DYW,DXXX,DYYY,DXYX,DXYY,UM)

   NULL THE WORKIN MATRICES
      call nullall(dimx,dimy,imax,jmax,un,vn,zn,u,v,z)

      DO I=1,DIM
      APT(I)=0.0
      APP(I)=0.0
      APM(I)=0.0
      BP(I)=0.0
      ENDDO


c     Initializing the model
*     BEGIN MARCHING IN TIME
      print*,'*****Begin Hydrodynamic Solution Marching in Time****'
      n=0
      time=0.0
      keold=0.0          ! kinetic energy at the •eginning
      isteady=0          ! assumed to be not in the steady state
100   n=n+1
***********FIRST FRACTION *** SWEEPING IN X-DIRECTION *********
      time=time+dt/2.
*****************C.O.MASS SWEEPING IN X**********************
      DO J=1,JMAX
      CALL COEFFMSX(J,DIMX,DIMY,DIM,IMAX,JMAX,IE,DXW,DYW,DT,APT,
      +                                        APP,APM,BP,U,V,Z,H)
      CALL TDMAX(ZN,APT,APP,APM,BP,1,IE(J),J,DIMX,DIMY,DIM)
      ENDDO
*****************X - MOMENTUM SWEEPING IN X******************
      DO J=2,JMAX-1
      CALL COEFFXMOMX(J,DIMX,DIMY,DIM,IMAX,JMAX,IE,DXW,DYW,DT,AX,AY,
      +
      CF,CB,RHO,DXXX,DXYY,APT,APP,APM,BP,U,V,ZN,H,ANG,UM)
      CALL TDMAX(UN,APT,APP,APM,BP,1,IE(J)+1,J,DIMX,DIMY,DIM)
      ENDDO
      CALL BNDRYUX(DIMX,DIMY,JMAX,IE,UN)
*****************Y - MOMENTUM SWEEPING IN X******************
   PRINT*,'HELLO'
      DO J=2,JMAX
      CALL COEFFYMOMX(J,DIMX,DIMY,DIM,IMAX,JMAX,IE,DXW,DYW,DT,AX,AY,
      +
      CF,CB,RHO,DYYY,DXYX,APT,APP,APM,BP,U,V,ZN,H,ANG,UM)
      CALL TDMAX(VN,APT,APP,APM,BP,1,IE(J)+1,J,DIMX,DIMY,DIM)
      ENDDO
      CALL BNDRYVX(DIMX,DIMY,JMAX,IE,VN)
```

```
**********SECOND FRACTION *** SWEEPING IN Y-DIRECTION *********
******UPDATE THE VALUES OF Z,U&V
      CALL NEWSTEP(DIMX,DIMY,IMAX,JMAX,U,UN,V,VN,Z,ZN)
      time=time+dt/2.
******************C.O.MASS SWEEPING IN Y**********************
      DO I=1,IMAX
      CALL COEFFMSY(I,DIMX,DIMY,DIM,IMAX,JMAX,IE,DXW,DYW,DT,APT,
      +                                    APP,APM,BP,U,V,Z,H)
      CALL TDMAY(ZN,APT,APP,APM,BP,1,JMAX,I,DIMX,DIMY,DIM)
      ENDDO
******************X - MOMENTUM SWEEPING IN Y******************
      DO I=2,IMAX-1
      CALL COEFFXMOMY(I,DIMX,DIMY,DIM,IMAX,JMAX,IE,DXW,DYW,DT,AX,AY,
      +
      CF,CB,RHO,DXXX,DXYY,APT,APP,APM,BP,U,V,ZN,H,ANG,UM)
      CALL TDMAY(UN,APT,APP,APM,BP,1,JMAX,I,DIMX,DIMY,DIM)
      ENDDO
      CALL BNDRYUY(DIMX,DIMY,JMAX,IE,UN)
******************Y - MOMENTUM SWEEPING IN Y******************
      DO I=2,IMAX-1
      CALL COEFFYMOMY(I,DIMX,DIMY,DIM,IMAX,JMAX,IE,DXW,DYW,DT,AX,AY,
      +
      CF,CB,RHO,DYYY,DXYX,APT,APP,APM,BP,U,V,ZN,H,ANG,UM)
      CALL TDMAY(VN,APT,APP,APM,BP,1,JMAX+1,I,DIMX,DIMY,DIM)
      ENDDO
      CALL BNDRYVY(DIMX,DIMY,JMAX,IE,VN)
******UPDATE THE VALUES OF Z,U&V
      CALL NEWSTEP(DIMX,DIMY,IMAX,JMAX,U,UN,V,VN,Z,ZN)



      IF(MOD(N,100).EQ.0)THEN
      print*,'time   =',time
      CALL maximum(time,dimx,dimy,imax,jmax,dxw,dyw,un,vn,zn,h,
      +                          keold,isteady)
      if(isteady.eq.1)then           ! steady state (stop the run)
      print*,'Steady State*********************'
      goto 550
      endif

      endif


      if(time.le.tlast)goto 100
*     the run has ended
550   CONTINUE

*     RELOCTE THE VELOCITY VECTORS AT THE GRID POINTS
      CALL RELOCATE(DIMX,DIMY,IMAX,JMAX,U,V)
*     extrapolate the water surface elevations for the shore
      call watsurf(dimx,dimy,imax,jmax,ie,z,h)
*     calculate the near bottom vel
*     call NEARBED01(DIMX,DIMY,IMAX,JMAX,RHO,D50,Z,H,U,V,
*     +                                HW,ANG,CG,C,K,T,DXW,IE,UN,VN,UM,ZR)

*     write the output file
*     call outputh(dimx,dimy,imax,jmax,h,z,u,v,hw,ang,k,dxw,dyw,t)

*     CALL TECVEC(1,IMAX,1,1,JMAX,1,DIMX,DIMY,
*     +                          DXW,DYW,U,V,'   CURRENT DIREC     ')
```

```
*     CALL TECVEC(1,IMAX,1,1,JMAX,1,DIMX,DIMY,
*     +                          DXW,DYW,UN,VN,'  NEAR-BED VELOCITY ')
*     OPEN(UNIT=10,FILE='SURFACE.DAT')
*     OPEN(UNIT=11,FILE='DEPTHS.DAT')
*     CALL TECOUT(10,Z,1,IMAX,1,JMAX,DIMX,DIMY,DXW,DYW,
*     +                          ' WATER SURFAC')
*     CALL TECOUT(11,H,1,IMAX,1,JMAX,DIMX,DIMY,DXW,DYW,
*     +                          ' WATER DEPTHS')

      write(*,560)
560   format(/,'*** end of hydrodynamic run ****',/)


      RETURN
      end
```

A1.5. s-Main.For

```
*
*
*     SUBROUTINE MORPHOLOGY... DESIGNED BY: USAMA M. SAIED
*
*
*     MAIN INPUT PARAMTERES
*
*     IMAX,JMAX: MAXIMUMX INDICEIS IN I AND J DIRECTIONS
*     H(I,J): WATER DEPTH
*     HE(I,J) :EFFECTIVE WATER DEPTH (WITHOUT STRUCTURES)
*     HW(I,J): WAVE HEIGHT
*     Z(I,J): WATER SURFACE ELEVATION
*     VEL(I,J): CURRENT ABSOLUTE VELOCITY
*     ANGC(I,J): CURRENT ANGLE WITH RESPECT TO X-AXIS (POSITIVE IN THE
      SHALLOWING DIREC.)
*     ANG(I,J): WAVE ANGLE WITH RESPECT TO X-AXIS
*     K(I,J) : WAVE NUMBER
*     TM : MORPHOLOGICAL TIME STEP
*
      SUBROUTINE MORPHOLOGY(DIMX,DIMY,IMAX,JMAX,DX,DY,T,HW,ANG,K,
     +                                      H,HE,Z,U,V,TIME,TLAST,T1,
     +
      NIH,NJH,NSUBM,IBSUB,IESUB,JBSUB,JESUB)
      IMPLICIT NONE
      INTEGER DIMX,DIMY,IMAX,JMAX,I,J,N,IC
      INTEGER,DIMENSION(DIMY)::IE
      REAL,DIMENSION(DIMX,DIMY)::H,HE,Z,D,DE,VEL,ANGC,HW,ANG,K,ZB
      REAL,DIMENSION(DIMX,DIMY)::QX,QY
      REAL,DIMENSION(DIMX,DIMY)::U,V
      REAL UBM,T,DX,DY,DT,TIME,TLAST,TEND,TM,T1,ACC
      REAL ALFA,UC,QSTX,QSTY
      REAL D50,EQ,AX,AY,DEPTH
      REAL PI
      INTEGER NOUT
      REAL AC,AW,KC,KD,RRC,XSZ,L,L0,PHIC
      REAL XCLOSE

      INTEGER NSUBM,ISUB,JSUB,III,NIH,NJH,I1,I2,J1,J2
      INTEGER,DIMENSION(20)::IBSUB,IESUB,JBSUB,JESUB
```

```
      PI=ACOS(-1.)
      L0=9.81*(T**2.)/2./PI                    ! OFFSHORE WAVE LENGTH

      PRINT*,'*************START THE MORPHOLOGICAL RUN*****'

*     CALCULATE THE CURRENT ANGLE WITH RESPECT TO X-DIRECTION
      (ANTICLOCKWISE)
      DO I=1,IMAX
      DO J=1,JMAX
      VEL(I,J)=SQRT(U(I,J)**2.+V(I,J)**2.)
      ANGC(I,J)=ACOS(ABS(U(I,J))/(VEL(I,J)+1.e-20))
      IF(U(I,J).GE.0.0.AND.V(I,J).GE.0.0)THEN
      ANGC(I,J)=ANGC(I,J)
      GOTO 10
      ENDIF
      IF(U(I,J).LE.0.0.AND.V(I,J).GE.0.0)THEN
      ANGC(I,J)=PI-ANGC(I,J)
      GOTO 10
      ENDIF
      IF(U(I,J).LE.0.0.AND.V(I,J).LE.0.0)THEN
      ANGC(I,J)=PI+ANGC(I,J)
      GOTO 10
      ENDIF
      IF(U(I,J).GE.0.0.AND.V(I,J).LE.0.0)THEN
      ANGC(I,J)=2.*PI-ANGC(I,J)
      GOTO 10
      ENDIF

10    CONTINUE

      ENDDO
      ENDDO

*     COMPLETE THE PARAMETERS
      CALL INPUTM(DT,NOUT,D50,EQ,AX,AY,AC,AW,KC,KD,RRC,ACC)

*     NULL THE WORKING MATRICIES
      CALL NULL(DIMX,DIMY,IMAX,JMAX,QX)
      CALL NULL(DIMX,DIMY,IMAX,JMAX,QY)
      CALL NULL(DIMX,DIMY,IMAX,JMAX,ZB)

*     CALCULATE THE WATER DEPTHS
      DO I=1,IMAX
      DO J=1,JMAX
      D(I,J)=H(I,J)+Z(I,J)
      DE(I,J)=HE(I,J)+Z(I,J)
      ENDDO
      ENDDO

*     IDENTIFY THE SHORELINE
      CALL DOMBOUNM(DIMX,DIMY,IMAX,JMAX,DX,DY,DE,IE)


*     CALCULATE THE FLUXES
      DO 100 J=1,JMAX
      DO 100 I=1,IE(J)

*     CALCULATE THE NECCESSARY PARAMETERS FOR THE TOTAL SEDIMENT FLUXES
      CALCULATIONS
      IF(D(I,J).LE.0.00)THEN
```

```
      QX(I,J)=0.0
      QY(I,J)=0.0
      GOTO 100
      ENDIF

      CALL PARAMETERS(I,J,DIMX,DIMY,H,D,HW,T,K,UBM)

*     CALCULATE THE FLUXES IN THE DIRECTION OF WAVE PROPAGATION AND
      PERPENDICULAR
      ALFA=ANG(I,J)                          ! WAVE ANGLE ANTICLOCKWISE
      PHIC=ANGC(I,J)                         ! CURRENT ANGLE ANTICLOCKWISE
      UC=VEL(I,J)                            ! CURRENT VELOCITY
      DEPTH=D(I,J)
      L=2.*PI/K(I,J)                         ! LOCAL WAVE LENGTH

*     print*,i,j,D(I,J),UBM,UC

      CALL TOTALLOAD(DIMX,DIMY,I,J,XSZ,IE,DX,
      +                  UBM,T,ALFA,L0,PHIC,UC,DEPTH,QSTX,QSTY,D50,
     +                   AC,AW,KC,KD,RRC,XCLOSE)


*     CALCULATE THE SEDIMENT FLUXES AT THE NODES IN THE X AND Y
DIRECTIONS
      QX(I,J)=QSTX              ! M^2/S
      QY(I,J)=QSTY              ! M^2/S
100   CONTINUE

      CALL TECVEC1(777,1,IMAX,1,1,JMAX,1,DIMX,DIMY,
      +            DX,DY,QX,QY,'SEDIMENT TRAN FLUXES','FLUXES.DAT')

*     CALCULATE THE FLUXES AT THE FACES OF CONTROL VOLUMES
      CALL FLUXES(DIMX,DIMY,IMAX,JMAX,QX,QY,D,IE)

*     CALCULATE THE MORPHOLOGICAL TIME STEP "TM" IN SECONDS
      CALL TMORPHO(DIMX,DIMY,IMAX,JMAX,IE,DX,DY,QX,QY,D,ACC,TM)



*     BEGIN SOLUTION MARCHING IN TIME
      PRINT*,'Begin Marching Solution'
      N=0
      TEND=TM+TIME
      IF(TEND.GT.(TLAST+T1))TEND=TLAST+T1
*     PRINT*,'**************START THE MORPHOLOGICAL RUN*****'
20    N=N+1
*     IF(MOD(N,4000).EQ.0)PRINT*,'N     =',N
      TIME=TIME+DT/3600./24.
*     CALCULATE THE NEW BED ELEVATION
      CALL MORPHO(DIMX,DIMY,IMAX,JMAX,IE,DX,DY,DT,QX,QY,D,ZB,EQ,AX,AY)
*     UPDATE THE WAVE HEIGHTS OVER THE SUBMERGED STRUCTURES
      DO III=1,NSUBM
      J1=(JBSUB(III)-1)/NJH+1
      J2=(JESUB(III)-1)/NJH+1
      I1=(IBSUB(III)-1)/NIH+1
      I2=(IESUB(III)-1)/NIH+1
      DO I=I1,I2
      DO J=J1,J2
      ZB(I,J)=0.0
      ENDDO
      ENDDO
```

```
      ENDDO

      IF(TIME.LT.TEND)GOTO 20

30    PRINT*,'***********END MORPHOLOGICAL RUN*************'
      WRITE(*,560)
560   FORMAT(/,'*************************************************',/)


*     UPDATE THE DEPTHS
      DO I=1,IMAX
      DO J=1,JMAX
      H(I,J)=H(I,J)-ZB(I,J)
      ENDDO
      ENDDO

*     SMOOTH THE DEPTHS AT THE LATERAL ENDS OF THE DOMAIN
*     DO I=1,IMAX
*     DO J=1,13
*     H(I,J)=H(I,14)
*     ENDDO
*     DO J=JMAX,JMAX-3,-1
*     H(I,J)=H(I,JMAX-4)
*     ENDDO
*     ENDDO

      RETURN
      END
```

APPENDIX 2: SAMPLE INPUT FILES

The following input files are used to model 8 submerged offshore detached breakwaters on the Rethym beach in Crete island.

A2.1. Input.dat

This file defines the parameters required by the wave model as well as all the geometric parameters.

```
0.7          GAMA : BREAKING CRITERIA FOR THE SHALLOW ZONE
61 578       IMAX, JMAX
11 568       JB, JE: INDICES OF IMPORTANT SOLUTION (required for
extrapolation)
20.0 10.0          DX ,DY
0.2          DMIN : MINIMUM DEPTH USED IN ORDER TO KEEP THE WAVE MODEL
RUNNING
0      INBNDRY = 1 IF NORTH BOUNDARY IS ALWAYS PASSING THROUGH, 0 ELSE
0      ISBNDRY = 1 IF SOUTH BOUNDARY IS ALWAYS PASSING THROUGH, 0 ELSE
1      APROX = 1 IF UNCENTRED PADE APPROXIMATION IS USED, 2 FOR CENTERED
PADE [1/1],  = 50 FOR MINIMAX 50, = 80 FOR MINIMAX 80
2      NOUTER= NUMBER OF OUTER ITERATIONS FOR WAVE ANGLES
1      NONLIN= 1 (IF NONLINEARITY IS INCLUDED, REFINE SHOULD BE SET 1),
0 ELSE
3      NN     = NUMBER OF ITERATIVES AFTER THE LINEAR SOLUTION (INNER
ITERATIONS)
1      BRKI   = 1 IF WAVE BREAKING IS INCLUDED, OTHERWISE NO BREAKING
0.0    RE =   REFLECTION COEFF. FOR THE EAST BOUNDARY (shore line)
0.0    RN =   REFLECTION COEFF. FOR THE NORTH BOUNDARY
0.0    RS =   REFLECTION COEFF. FOR THE SOUTH BOUNDARY
100.   CONS =       CONSTANT MULTIPLIED BY EPSAY(I,J) IN ORDER TO REDUCE
THR ROUND OFF ERRORS
EMERGED STRUCTURES
0      NXBW = NUMBER OF X-PARALLEL (GROINS) STRUCTURES; next lines are as
IXB,IXE,JXB,JXE
0      NYBW = NUMBER OF Y-PARALLAEL (SHORELINE PARALLEL) STRUCTURES
SUBMERGES STRUCTURES
8      NSUBM = NUMBER OF SUBMERGED STRUCTURES; next lines are as
IB,IE,JB,JE, HEIGHT
41 41 101 121 2.0
41 41 141 161 2.0
41 41 181 201 2.0
41 41 221 241 2.0
41 41 261 281 2.0
41 41 301 321 2.0
41 41 341 361 2.0
41 41 381 401 2.0
ELLIPTIC MODEL INPUT PARAMETERS (Imax=(Imax-1)*NI+1)
0      ELIPREFIN = 1 IF ELLIPTIC REFINMENT IS REQUIRED
2 90 2 80    IBR IER JBR JER = INDICIES THAT IDENTIFY DOMAIN OF
REFINEMNT (ELLIPTIC INDICES)
4 4    NI AND NJ : NUMBER OF ADDITIONAL GRID POINTS IN BETWEEN THE
ORIGINAL GRID POINTS
```

```
1.E-7 ACCURACY = REQUIRED ACCURACY FOR THE CONJUGATE GRADIENT METHOD
0     INBNDRYE = 1 IF NORTH BOUNDARY IS ALWAYS PASSING THROUGH
0     ISBNDRYE = 1 IF SOUTH BOUNDARY IS ALWAYS PASSING THROUGH
0     NSYM = 1 IF NORTH BOUNDARY IS ALWAYS SYMMETRIC
0     SSYM = 1 IF SOUTH BOUNDARY IS ALWAYS SYMMETRIC
0.0   REE = REFLECTION COEFF. FOR THE EAST BOUNDARY
1.0   RNE = REFLECTION COEFF. FOR THE NORTH BOUNDARY
0.0   RSE = REFLECTION COEFF. FOR THE SOUTH BOUNDARY
HYDRODYNAMIC MODEL OUTPUT
2 4   NIH AND NJH = NUMBER OF SPACINGS BETWEEN THE PARABOLIC RESOL. AND
HYDRO. RESOL
```

A2.2. Wavespec.dat

This file defines the wave climate.

```
WAVE SPECTRUM DATA (ASFEND BAY - REPRESENTATIVE YEAR)

17    = NTIMES : NUMBER OF CHANGES IN DEEP WAVE
THE WAVE DATA IN THE FORM H0, TH0, T, TIME IN DAYS
0.25  -35.0 4.6   30.0  1
0.25  -35.0 3.5   32.4  2
0.75  -35.0 4.6   16.4  3
1.25  -35.0 5.7   7.0   4
1.75  -35.0 6.9   0.9   5
0.25  25.0  3.5   50.0  6
0.25  25.0  3.5   59.5  7
0.75  25.0  4.6   15.0  8
1.25  25.0  5.7   2.0   9
1.75  25.0  6.9   0.6   10
0.25  -5.0  3.5   30.0  11
0.25  -5.0  3.5   32.5  12
0.75  -5.0  4.6   24.1  13
1.25  -5.0  5.7   7.0   14
1.75  -5.0  6.9   1.5   15
2.25  -5.0  8.1   0.5   16
2.75  -5.0  9.2   0.4   17
```

A2.3. Inputh.dat

This file defines the parameters required by the hydrodynamics model.

```
3.5   DT = TIME STEP IN SECONDS
1.0   TLAST = SIMULATION TIME IN HOURS
0.01  bed friction coefficint (combined wave current)
0.0000018   wind drag coeff (divided by rho)
00.0  PHI = MEAN GEOGRAPHIC LATITUDE OF THE AREA WITH X-AXIS TO THE
SOUTH AND Y-AXIS TO THE EAST
0.12E-3     D50 (METERS)
```

A2.4. Inputm.dat

This file defines the parameters required by the sediment transport and morphology models.

```
1000.0DT IN SECONDS
10    NOUT= NUMBER OF OUTPUT ZONES REQUIRES
0.12E-3      D50 IN METERS
10.0  EQ  EMPIRICAL CALIBRATION CONSTANT TO ACCOUNT FOR TRANSPORT ON
SLOPES
0.01  AX  SMOOTHING PARAMETER IN X-DIRECTION
0.015 AY  SMOOTHING PARAMETER IN Y-DIRECTION
CALIBRATION PARAMETERS
0.25  AC = 0.1~1 (CURRENT TRANSPORT DIMENSIONLESS PARAMETER)
0.05  AW = 0.1~1 (WAVE TRANSPORT DIMENSIONLESS PARAMETER)
1.0   KC = ARROUND 1 (PARAMETER INVOLVED IN THE IDENTIFICATION OF
CRITICAL SHEAR STRESS)
0.2   KD = ARROUND 1 (CONTROLS THE DEGRRE OF CHANGE IN THE CROSS-SHORE
TRANSPORT)
3.0   RRC = ARROUND 1 (CRITICAL VALUE AT WHICH WAVE TRANSPORT REVERSES
DIRECTION)
50.0  Accuracy used to determine the morphological time step
```

A2.5. Depth.dat

This file includes the initial bathymetry of the area. The file contains an exact number of IMAX × JMAX of data points. They are arranged as rows starting from the farthest offshore row (of maximum depth) to the last onshore row. The row number appears before the data. The following shows part of row number 33 as an example.

```
         33
   3.1403300   3.1403300   3.1403300   3.1403300   3.1403300   3.1403300
3.1403300   3.1403300   3.1403300   3.1403300   3.1403300   3.1287000
3.1261700   3.1273500   3.1289600   3.1298900   3.1309700   3.1325000
3.1345500   3.1336900
   3.1362200   3.1364300   3.1384200   3.1372200   3.1377500   3.1393000
3.1408200   3.1439600   3.1466100   3.1489000   3.1516500   3.1555900
3.1581100   3.1637800   3.1665000   3.1702200   3.1711600   3.1768100
3.1811700   3.1886700
   3.1930900   3.1990300   3.2045700   3.2116100   3.2210000   3.2318600
3.2374200   3.2468800   3.2539200   3.2643500   3.2798700   3.2932200
3.3013900   3.3166900   3.3289900   3.3414300   3.3584800   3.3704700
3.3853500   3.4014400
   3.4141900   3.4330500   3.4559800   3.4731100   3.4893700   3.5105600
3.5293800   3.5526000   3.5764500   3.5949900   3.6177800   3.6408300
3.6639900   3.6868400   3.7056800   3.7308200   3.7490300   3.7705500
3.7930200   3.8160800
   3.8350900   3.8579800   3.8783900   3.8984800   3.9216100   3.9181100
3.9414100   3.9624400   3.9863100   4.0099100   4.0303000   4.0558900
4.0809900   4.1033500   4.1259100   4.1521700   4.1426500   4.1653700
4.1913900   4.2086700
   4.2329600   4.2536200   4.2730200   4.3025300   4.3261300   4.3465500
4.3688800   4.3905200   4.4161000   4.4376500   4.4573500   4.4768200
4.5013000   4.5225400   4.5437300   4.5645400   4.5852800   4.6055200
4.6237900   4.6465200
   4.6648800   4.6818900   4.6987600   4.7182900   4.7341700   4.7510900
4.7631800   4.7778600   4.7914700   4.8066300   4.8213300   4.8359600
4.8514700   4.8626400   4.8774700   4.8876300   4.8967100   4.9106500
4.8952400   4.9059700
   4.9138100   4.9231200   4.9336200   4.9465400   4.9610500   4.9710600
4.9774700   4.9818500   4.9966000   5.0066200   5.0161300   5.0234900
5.0348400   5.0281700   5.0550900   5.0653600   5.0740000   5.0818600
5.0874600   5.09354
```